Femtosecond Pump-Probe Spectroscopy on Corroles, Phytochromes, Channelrhodopsins and Ground-state Reactions

Till Stensitzki

2018

Im Fachbereich Physik der Freien Universität Berlin eingereichte Dissertation Erlangung des akademischen Grades eines Doktors der Naturwissenschaften (Dr. rer. nat.)

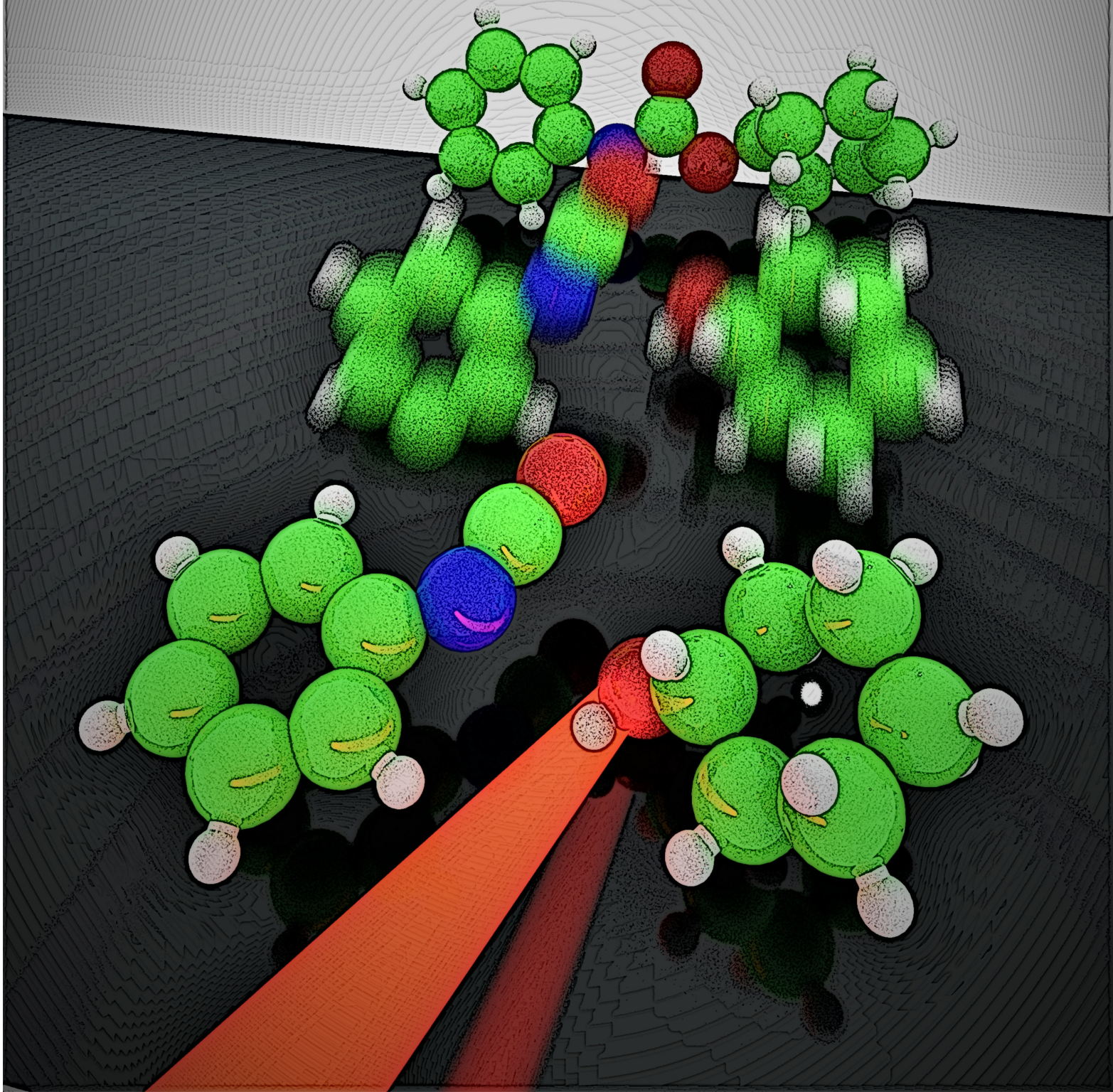

Datum der Disputation: 22.10.2019
1. Gutachter: Prof. Dr. Karsten Heyne
2. Gutachter: Prof. Dr. Ulrike Alexiev

Abstract

Photoreactions are ubiquitous and the foundation of life. The outcome of a photoreaction is mostly determined by its first steps, which happen within few picoseconds. Therefore the study of the initial part of a photoreaction is indispensable for its full understanding. This thesis presents the results of femtosecond pump-probe spectroscopy, the tool of choice for observing photoreactions on an ultrashort timescale, on four different systems: Corrole, Channelrhodopsin 1, Cph1-Phytochrome and a bimolecular ground-state reaction.

Corroles are cyclic tetrapyrroles similar to porphyrins. They show promising characteristics as photosensitizers in photodynamic therapy for cancer. Here, a high triplet yield is crucial. My results show that the addition of bromine to the macrocycle induces efficient intersystem crossing on a 100 ps timescale with a yield near unity. Observation of the ISC in the mid-infrared reveals a distinct spectrum of the triplet state, useable as a marker for the spin-state.

Phytochromes are an omnipresent class of photoreceptor proteins initially found in plants. Phytochromes have two semi-stable states, the red and the far-red absorbing state. Recent studies show that these states itself are heterogeneous, but whether this heterogeneity influences the photoreaction was still unknown. Using Vis-pump IR/Vis-probe spectroscopy, we show that this is the case. The transient spectra expose two different bleaching bands of the ring-D carboxyl stretching vibration, which we assign to sub-states with different ring-D orientation. Since these two bands show different transient changes, we conclude that the heterogeneity indeed influences the photoreaction.

Channelrhodopsin 1 is a transmembrane protein which functions as a light-activated cation channel. Channelrhodopsins variants are the primary tools in the new field of Optogenetics. Visible pump visible probe spectroscopy reveals an unusually fast 100 fs all-trans to 13-cis photo-isomerization of the retinal photoreceptor and excitation wavelength dependent dynamics. In the mid-IR fingerprint region, we find evidence that the isomerization depends on the conformation of the ground-state. Using polarisation resolved Vis-pump IR-probe spectroscopy, we assign several priorly unassigned bands in the amide region. Comparision of our results with the C1C2-chimaera- and a homology-structure suggests that ultrafast appearing amide I band, which is strong in *Ca*ChR1, has its origin in one of the tryptophans belonging to the retinal cage. Moreover, my data excludes the existence of protonated carboxylic groups coupled to the retinal in ground-state, since no corresponding bands are observed.

Bimolecular *ground-state reactions* are the most common reactions in chemistry. They can be described by transition state theory, in which the reaction is described by a potential energy surface. The initial and the product state are minima separated by a barrier and the shortest path over the barrier only depends on a subset of coordinates, called reaction coordinates. Since they can be represented by normal modes, it is generally believed that IR-excitation of the correct modes can initiate the reaction. However, this idea was not yet experimentally proven.

To find the missing proof and make selective laser-chemistry possible, we applied fs IR-pump IR-probe spectroscopy to a mixture of cyclohexanol and isocyanate, which react to Cyclohexylcarbanilate at room temperature. We observe the rise of vibrational bands belonging to the product and the rise of bleaching bands belonging to the reagents on a 10 ps scale, which shows that the reaction is initiated by the IR-excitation. We support this finding by comparing the reaction rates with and without IR-illumination, showing a 24 % increase. This finding offers entirely new ways to optimize low yield reactions.

Kurzfassung

Photoreaktion sind allgegenwärtig und bilden das Fundament des Lebens. Das Ergebnis einer Photoreaktion wird größtenteils innerhalb der ersten Schritte auf einer sub-Pikosekunden Zeitskala bestimmt. Für ein genaues Verständnis einer Photoreaktion ist es daher unerlässlich, diese ersten Schritte im Detail zu Untersuchen. Die Standardmethode zur Untersuchung des ultraschnellen Teils einer Photoreaktion ist die femtosekunden Pump-Probe Spektroskopie. Diese Arbeit präsentiert die Ergebnisse der Methode auf vier verschiedene Systeme: Corrole, Phytochrome, Channelrhodopsin und auf eine bimolekulare Grundzustandsreaktion.

Corrole sind Porphyrin ähnlichen zyklischen Tetrapyrole. Dank der speziellen Eigenschaften von Corrolen eignet es sich als Photosensibilisator in Photodynamischer Therapie zur Krebsbehandlung. Hierbei ist eine hohe Triplett-Ausbeute unerlässlich. Wir zeigen, dass die Addition von Brom zu einem effizienten Intersystem Crossing auf der 100 ps Zeitskala im Corrole führt. Im Infraroten hat der entstehende Triplett Zustand ein typisches Spektrum, welches als Marker für dem Spin-Zustand genutzt werden kann.

Phytochrome ist ein allgegenwärtiger Photorezeptor welcher zuerst in Pflanzen gefunden wurde. Charakteristisch für Phytochrome sind seine zwei semi-stabilen Zustände, der rot und der tiefrot absorbierende Zustand. Neuere Studien zeigen, dass diese Zustände selbst heterogen sind. Allerdings ist bisher nicht geklärt, ob die Heterogenität einen Einfluss auf die Photoreaktion hat. Mittels fs Pump-Probe Spektroskopie zeigen wir, dass die unterschiedlichen Unterzustände unterschiedliche Photoreaktion vollführen. Dazu beobachten wir die Streckschwingung der Carboxylgruppe am Ring-D. Diese zeigt zwei Bleichbanden mit unterschiedlicher Orientierung und verschiedenen Dynamiken. Daraus folgt, dass die Heterogenität einen Einfluss auf die Photoreaktion hat.

Channelrhodopsine (ChR) sind lichtaktivierte Ionenkanäle, die in der Zellmembran bestimmter einzelliger Algen vorkommen. ChR bilden die Basis der Optogentik, da es durch Genexpression in Neuronen eingebracht werden kann, welche daraufhin mittels Licht aktiviert werden können. Durch sichtbare Pump-Probe Spektroskopie zeigen wir, dass die initiale all-*trans* zu 13-*cis* Photoisomerisierung unerwartet schnell mit 100 fs stattfindet. Desweitern zeigt sich eine von der Anregungswellenlänge abhängige Dynamik. Im IR Fingerprint Bereich finden wir erstmals Beweise dafür, dass der Ausgang der Isomerisierung von der anfänglichen Geometrie des Retinals abhängt. Mittels polarisationsaufgelöster Vis-Pump IR-Probe Spektroskopie ordnen wir mehrere Banden im Amide I Bereich zu. Insbesondere zeigt der Vergleich unserer Spektren mit der C1C2-Struktur und einen Homology-Model, dass die im untersuchten ChR besonders starke ultraschnelle Amide I Bande zu einen der am Retinal liegenden Trypthophane gehört. Aus unseren Daten folgt, dass die zum Gegenion gehörenden Asp und Glu im Grundzustand deprotoniert sind.

Bimolekulare *Grundzustandsreaktion* bilden die Grundlage der Chemie. Sie können durch die Theorie des Übergangszustandes beschrieben werden, in der die Reaktion durch eine Potentialoberfläche beschrieben wird. Der Initial- und Endzustand sind dabei durch eine Barriere getrennte lokale Minima. Der kürzeste Pfad über die Barriere involviert nur einen Teil aller Koordinaten. Diese Koordinaten werden Reaktionskoordinaten genannt und können durch Normalmoden dargestellt werden. Es wird daher im allgemeinen angenommen, dass es eigentlich möglich sein sollte eine Reaktion mittels IR-Anregung zu starten. Der experimentale Beweis dafür fehlte bisher.

Um den fehlenden Beweis zu finden und selektive Laserchemie möglich zu machen, wenden wir fs IR-Pump IR-Probe Spektroskopie auf eine Cyclohexanol-Isocyanat Lösung an. Eine solche Lösung reagiert bei Raumtemperatur zu Cyclohexyl-carbanilate. Die Observierung der Produkt- und der Reagenzbanden zeigt eindeutig eine durch dem IR-pump verursachte Produktbildung innerhalb von 10 ps. Des Weiteren zeigt ein Vergleich der Reaktionsrate zwischen beleuchteter und nicht beleuchteter Probe einen Anstieg der Rate von bis zu 24%. Dabei wurde darauf geachtet lichtinduzierte Erwärmung als Grund des Anstiegs auszuschließen. Dieses Ergebnis eröffnet völlig neue Wege Reaktionen mit niedriger Ausbeute zu optimieren.

Publications

This dissertation is accumulative and contains the following manuscripts which all have been published in a peer-reviewed journal:

1. Stensitzki, T., Muders, V., Schlesinger, R., Heberle, J. & Heyne, K. The Primary Photoreaction of Channelrhodopsin-1: Wavelength Dependent Photoreactions Induced by Ground-State Heterogeneity. *Frontiers in Molecular Biosciences* **2.** ISSN: 2296-889X. pmid: 26258130 (July 22, 2015)

2. Stensitzki, T., Yang, Y., Berg, A., Mahammed, A., Gross, Z. & Heyne, K. Ultrafast Electronic and Vibrational Dynamics in Brominated Aluminum Corroles: Energy Relaxation and Triplet Formation. *Structural Dynamics* **3.** ISSN: 2329-7778. pmid: 27226980 (May 12, 2016)

3. Stensitzki, T., Yang, Y., Muders, V., Schlesinger, R., Heberle, J. & Heyne, K. Femtosecond Infrared Spectroscopy of Channelrhodopsin-1 Chromophore Isomerization. *Structural Dynamics* **3,** 043208. ISSN: 2329-7778 (July 1, 2016)

4. Stensitzki, T., Yang, Y., Wölke, A. L., Knapp, E.-W., Hughes, J., Mroginski, M. A. & Heyne, K. Influence of Heterogeneity on the Ultrafast Photoisomerization Dynamics of Pfr in Cph1 Phytochrome. *Photochemistry and Photobiology* **93,** 703–712. ISSN: 1751-1097 (May 1, 2017)

5. Stensitzki, T., Yang, Y., Kozich, V., Ahmed, A. A., Kössl, F., Kühn, O. & Heyne, K. Acceleration of a Ground-State Reaction by Selective Femtosecond-Infrared-Laser-Pulse Excitation. *Nature Chemistry* **10,** 126–131. ISSN: 1755-4349 (Feb. 2018)

Additionally, I co-authored the following peer-reviewed publication:

6. Zahn, C., Stensitzki, T., Gerecke, M., Berg, A., Mahammed, A., Gross, Z. & Heyne, K. Ultrafast Dynamics of Sb-Corroles: A Combined Vis-Pump Supercontinuum Probe and Broadband Fluorescence Up-Conversion Study. *Molecules* **22,** 1174 (July 13, 2017)

In the course of my work, I contributed to the following scientific open-source software:

7. Newville, M., Stensitzki, T., Allen, D. B. & Ingargiola, A. *LMFIT: Non-Linear Least-Square Minimization and Curve-Fitting for Python* Zenodo, Sept. 21, 2014

Contents

Chapter 1

Introduction

The field of photochemistry describes chemical reactions initiated by the absorption of light. Light-induced reactions are the backbone of life, as they convert the sunlight into chemical energy usable by living organisms. Therefore the absorption of light is the starting point of numerous important processes in nature, including photosynthesis, vision, plant signaling and the formation of vitamin D.

Hence, studying photoreactions is indispensable. This field is interdisciplinary. It involves physics, chemistry, and (when working with on proteins) biology. Physics gives us the framework to describe the interaction of the electromagnetic field with the quantum-mechanical states of the molecule; chemistry links the photoreaction to the molecular structure, and biology is necessary to understand the function.

In this work I present the result of my studies on four different reactions, focussing on their physical properties.

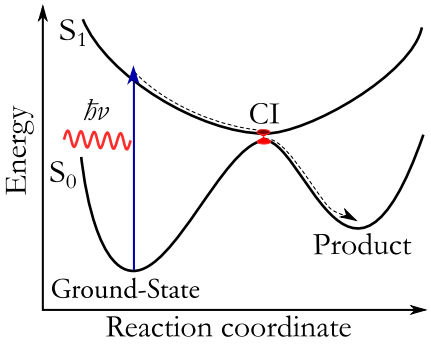

FIGURE 1.1: Schematic of a photoreaction. The dashed line shows the reaction pathway. After excitation, the molecule follows the potential energy surface downwards. It reaches the product state by passing through a so called *conical intersection* (CI), thereby converting potential electronic energy into kinetic energy of the atoms.

1.1 Photoreactions

Photo-induced reactions differ from temperature driven ground-state reactions in that a photon provides their activation energy and, therefore, the energy is initially confined to a single degree of freedom.

In most reactions, this degree of freedom is not identical to the reaction coordinate, and the energy must first relax into the correct modes. This normally involves the conversion of the electronic energy into nuclear motion, which then leads to structural changes (see Fig. 1.1).

For instance the photoreaction in many photoreceptor proteins starts with the isomerization of the chromophore, which then induces further changes later. Therefore, evolution optimized the structure of proteins to funnel the energy of the light into the corrected vibrational modes which facilitate the isomerization. As part of this work, two of such reactions in proteins, Channelrhodopsin and Phytochrome, are studied in detail.

However, the reaction coordinate of ground-state reactions is primarily built up from nuclear coordinates too. Hence the question arises: Is it possible to start such a reaction similarly? Can we start a ground-state reaction by exciting a vibrational mode?

While this is generally believed to be true, it has not yet been shown directly. The most significant result of this thesis – the initiation of a synthesis

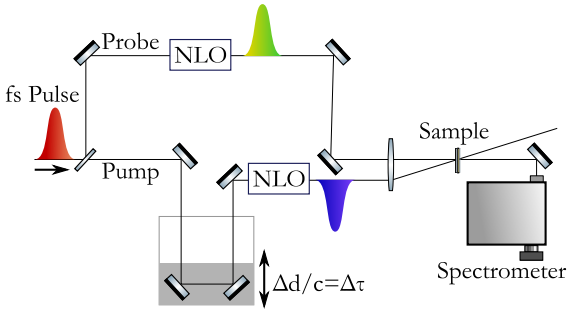

FIGURE 1.2: The basic concept of fs pump-probe spectroscopy. A fs- pulse is split into the pump, which starts the photoreaction, and probe, which examines the reaction and is detected by a spectrometer. The time-delay between pulses is varied by changing the path length d of one beam. Non-linear optics (NLO) are used to convert each beam to the needed wavelength.

reaction in solution with IR-light – shows that this indeed is possible.

If the energy of the excited state cannot be converted to vibrational energy, relaxation continues via other channels. For single molecules, a lower state can be reached by spontaneous emission (fluorescence) or by radiation-less inter-system crossing. In applied photochemistry, it can be useful to tune the ratio between these two, since applications can make use of either. As part of this thesis, I show that small alterations to an aluminum corrole can drastically change the triplet yield of its photoreaction.

Chapter 2 gives a more detailed look at relaxation dynamics of excited molecules.

1.2 Pump-probe spectroscopy

The timescale on which the initial steps of the photoreaction happen is incredibly short: after absorption of the photon, the first reaction steps are finished after few picoseconds at most. Hence to study these reactions, ultrafast techniques with a time-resolution in femtosecond (10^{-15} s) range are necessary. In this thesis, we use femtosecond pump-probe spectroscopy. The basic idea behind fs pump-probe spectroscopy, as is shown Fig. 1.2, is simple:

A femtosecond laser pulse is split into two parts by a beam-splitter, the pump- and the probe pulse. Both pulses pass through the same sample volume, the pump is used to excite the sample and the probe is used to track the changes induced by the pump. For that, the intensity of the probe pulse with- and without the pump-pulse excitation are compared. The delay between both pulses can be varied by changing the path-length of one beam with a motor-controlled stage. By spectrally resolving the probe this gives the transient spectra of the sample.

The peak-power of fs-pulses is very high; therefore non-linear optical processes can be used to generate almost any wavelength from a given pulse. In this work, we mainly pump electronic transitions located in the visible region of the electromagnetic spectrum. The majority of biological photo-active systems absorb in this range to make use of sunlight which has its peak-power around 530 nm.

We observe the pump-induced changes in the visible and the mid-infrared part of the electromagnetic spectrum. The former allows us to track the electronic state of the system. The latter probes molecular vibrations, which are sensitive to changes in the structure, the protonation state, the electronic state and of the temperature. The combination of the two regions is particularly useful for proteins since the transient spectra only show changes to the photoreceptor while the IR-spectra allow us to observe changes in the protein itself.

To simplify the interpretation of the crowded IR-spectra in proteins, we perform the pump-probe experiments polarization resolved. The ensemble excited by linear polarized light is anisotropic because the probability of the excitation depends on the angle between the electronic field and the transition dipole moment (tdm). The same is true for interactions with the probe field. Hence it is possible to extract information about the relative angle between the pumped and probed tdm. Together with a given structure, this information can be used to assign bands to specific residues.

More information about femtosecond pump-probe spectroscopy and an introduction to non-linear optics is given in chapter 2, where I list possible signal contributions and discuss the effect of using polarized light in more detail. In chapter 3, I lay down experimental details of used fs pump-probe spectrometer. Since the software to control the experiment and to analyze the data is as necessary as the setup itself, I commit chapter 4 to software. It explains the design of MessPy, the software which

controls the experiment, and gives an overview of the methods employed to analyze the experimental results.

1.3 Studied Systems

As mentioned before, I examined four different photoreactions for this thesis: Corroles, phytochromes, channelrhodopsins and ground-state reactions.

1.3.1 Corroles

Corroles are a class of cyclic tetrapyrroles with distinct properties which make them prime candidates for many chemical and medical applications. An efficient synthesis reaction of corroles was only recently discovered. Hence, the exact properties of their photoreaction and how it changes between different corroles is yet unknown. Knowing these properties can guide further development of corrole variants tailored for specific applications.

My presented study, introduced in chapter 5, is about the effect of adding bromine to an aluminum corrole. While this has been known to rise the triplet-yield, the exact increase and the influence on the initial dynamics were not yet quantified. A hight triplet yield is vital for applications which need photo-sensitizers, like photo-dynamic therapy for cancer treatment.

1.3.2 Phytochromes

Phytochromes are photoreceptor proteins which play an important role in many organisms. In plants, they control the germination of seeds, the chlorophyll synthesis, the elongation of seedlings, the growth and many other things. In cyanobacteria, they are responsible for the chromatic adoption of the composition of the photosynthesis apparatus. The chromophore of phytochromes is a linear tetrapyrrole, which initiates the photoreaction by isomerization.

One specialty of phytochromes is that they are dichromatic sensors, meaning that they have two stable states, Pr (red) and Pfr (far red), with different absorption spectra, which can be inter-converted via light. Recent studies show that these states itself are heterogeneous. The impact of these sub-states on the photoreaction was not known.

In our in chapter 6 presented study on the Pfr-state of Cph1 we use polarization resolved Vis-pump IR-probe spectroscopy in combination with quantum chemical calculations to answer this question.

1.3.3 Channelrhodopsin

Channelrhodopsins are also photoreceptor proteins. They were the first discovered light-gated cation channels. Their discovery enabled the field of optogenetics: By expressing channelrhodopsin in cells, the activity of the cells can be controlled by light. A better understanding of the function is essential to guide the design of application-specific mutants. Like in other rhodopsins, the initial photoreaction induces the isomerization of the retinal chromophore.

Chapter 7 presents the first studies on the photoreaction of *Ca*ChR1. Prior to our studies, only the photoreaction of *Cr*Chr2 has been studied on an ultrafast time-scale. It was entirely unclear, how similar the two reactions are and if there is any heterogeneity in the ground-state. If so, does the heterogeneity influences the photoreaction? Another question we can answer by Vis-pump IR-probe spectroscopy is the protonation state of the counterion in ground-state of *Ca*ChR1. Using polarization resolved spectra, we can tentatively assign the ultrafast amide response found in most rhodopsins to a specific residue.

1.3.4 Ground-state Reactions

At last, I present my results on initiation of a synthesis reaction by IR-excitation. Bimolecular ground-state reactions are the foundation of chemistry. As previously mentioned, the reaction coordinate of these reactions is built from vibrational degrees of freedom. Yet it has not been shown, that vibrational excitation via IR-excitation can activate such a reaction.

In chapter 8 I introduce my paper which proves that such an activation is possible by using IR-pump IR-probe spectroscopy on the urethane synthesis reaction of phenylisocyanate and cyclohexanol. The experimental results are supported by the first calculations which successfully predict the activation energy of such a reaction.

Chapter 2

Theoretical Principles

This chapter gives a brief introduction to theoretical concepts behind the physics used in the thesis. The chapter starts with a short introduction of nonlinear optics. Nonlinear optics are necessary to describe the frequency conversion process used in the experiment and provide a frame-work to explain pump-probe spectroscopy, which is treated afterwards. Finally, the chapter discusses the possible relaxation pathways of excited molecules.

2.1 Nonlinear Optics

The short duration of femtosecond pulses has an advantage other than just the short time resolution. The high peak power, in the range of gigawatts, gives us the option to use nonlinear processes. This section will shortly describe the physics behind the nonlinear process used in the experiment. A full treatment can be found in Boyds "Nonlinear Optics"[1], which the description given below closely follows.

In optics, the electric field $\vec{\mathbf{E}}(t)$ and the induced polarization per volume $\vec{P}(t)$ in a material are connected by the susceptibility χ of the medium:

$$\vec{\mathbf{P}}(t) = {}_0\chi\vec{E}. \tag{2.1}$$

If the driving electric field is large, the response of the medium is nonlinear and the equation above has to be extended. For that, we do a Taylor expansion

$$\vec{\mathbf{P}}(t) = {}_0\chi^{(1)}\vec{\mathbf{E}}(t) + {}_0\chi^{(2)}\vec{\mathbf{E}^2}(t) + {}_0\chi^{(3)}\vec{\mathbf{E}^3}(t) + \ldots, \tag{2.2}$$

where $\chi^{(n)}$ are the n-th-order susceptibility tensors. In isotropic media, the second order vanishes and can only be observed in anisotropic situations, e.g., in birefringent crystals or at interfaces.

Starting from Maxwell's equations, it can be shown, under the assumption that there are no free charges, that

$$\boldsymbol{\nabla}^2\mathbf{E} - \frac{n^2}{c^2}\frac{\partial^2}{\partial t^2}\mathbf{E} = \frac{1}{{}_0c^2}\frac{\partial^2}{\partial t^2}\mathbf{P}^{\mathbf{NL}}. \tag{2.3}$$

$\mathbf{P}^{\mathbf{NL}}$ is the nonlinear part of the polarization density. This equation is called the standard nonlinear wave equation. Generally, the n-order susceptibility leads to n+1 interacting waves. For example, inserting $E(t) = \sin(\omega_1 t) + \sin(\omega_2 t)$ into 2.2 results in:

$$\begin{aligned} P_{\chi^{(2)}}(t) &= (\sin(\omega_1 t) + \sin(\omega_2 t))^2 && (2.4)\\ &= \sin(\omega_1 t) + \sin(\omega_1 t) && (2.5)\\ &\quad + 2\sin(\omega_1 t)\sin(\omega_2 t) && (2.6)\\ &= \cos((\omega_1-\omega_2)t) - \cos((\omega_1+\omega_2)t) && (2.7)\\ &\quad + \frac{1-\cos(2\omega_1 t)}{2} && (2.8)\\ &\quad + \frac{1-\cos(2\omega_2 t)}{2} && (2.9) \end{aligned}$$

Hence, the interaction of two plane waves in a nonlinear medium with a non-zero second-order susceptibility generates oscillations with the frequencies $2\omega_1$, $2\omega_2$, $2\omega_1+\omega_2$ and $2\omega_1-\omega_2$. The first two terms are called second harmonic generation (SHG), the third is called sum-frequency generation (SFG) and the last is called difference frequency generation (DFG). We will describe SHG and DFG in more detail in the next sections.

[1] (8) Boyd, R. W. *Nonlinear Optics.* 2008.

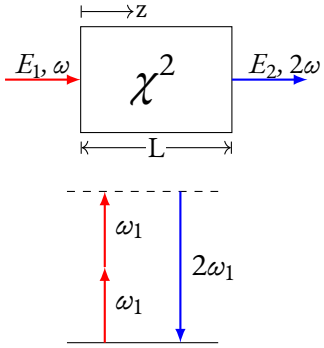

FIGURE 2.1: *Top:* Shematic describing the SHG-model. In a medium of length L with a non-vanishing second order susceptibility, we have the pump wave E_1 at the frequency ω, which we assume to be undepleted by the nonlinear interaction, and the generated wave E_2 at the frequency 2ω. *Bottom:* Energy conservation commands that for every generated photon with the energy $\hbar 2\omega$ two photons with $\hbar\omega$ are annihilated.

2.1.1 Second-Harmonic Generation (SHG)

The most commonly used nonlinear optical effect is second harmonic generation. It is even used in laser pointers, where the output of a near-infrared (NIR) laser-diode is converted into visible light by SHG. Similarly, most fs-femtosecond laser-systems deliver pulses in the NIR range, either centered at 800 nm or at 1030 nm, and SHG is used to generate light in the visible region. To describe SHG, we use the one-dimensional model shown in Fig. 2.1.

Let

$$\tilde{E}_1(z,t) = E_1(z)e^{-i\omega t} + c.c. \tag{2.10}$$
$$= A_1 e^{i(k_1 z - \omega t)} + c.c. \tag{2.11}$$
$$\tilde{E}_2(z,t) = E_2(z)e^{-i2\omega t} + c.c. \tag{2.12}$$
$$= A_2(z)e^{i(k_2 z - 2\omega t)} + c.c., \tag{2.13}$$

where $k_1 = n_1\omega/c$ and $k_2 = n_2 2\omega/c$. A_2 is a function of z since the SH amplitude changes with z. The aim is to calculate $A_2(L)$, the amplitude of the generated field at end of the medium. For that we also introduce

$$\tilde{P}_2(t) = P_2 e^{-i2\omega t}, \tag{2.14}$$

with

$$P_2 = {}_0\chi^{(2)} E_1^2 = {}_0\chi^{(2)} A_1^2 e^{i2k_1 z}.$$

As mentioned above, the generation of E_2 is governed by the nonhomogeneous wave equation

$$\boldsymbol{\nabla}^2\tilde{\mathbf{E}}_2 - \frac{n^2}{c^2}\frac{\partial^2}{\partial t^2}\tilde{\mathbf{E}}_2 = \frac{1}{{}_0c^2}\frac{\partial^2}{\partial t^2}\tilde{\mathbf{P}}_2. \tag{2.15}$$

By evaluation of the terms and applying the *slowly varying amplitude approximation*, which drops the term $\frac{\partial^2 A_2}{\partial z^2}$, we obtain

$$2ik_2\frac{\mathrm{d}A_2}{\mathrm{d}z} = \frac{-4\omega^2}{c^2}\chi^{(2)}A_1^2 e^{i\Delta k z}. \tag{2.16}$$

The quantity $\Delta k = 2k_1 - k_2$ is called phase mismatch. If the phase mismatch is not near zero, the fields generated at different positions in the medium are not in phase and will destructively interfere. A phase mismatch of zero is equal to $n_1 = n_2$.

Phase matching is important in all nonlinear processes where different wavelengths interact with each other. Phase matching is ordinarily achieved by a using birefringent crystal, where the index of refraction seen by one polarization can be tuned by adjusting the angle of the crystal. In the so-called type I phase matching the generated field is polarized perpendicular to the pumping field which is aligned with the ordinary axis.

The general solution for the equation at the end of medium is

$$|A_2(L)|^2 = \frac{4\omega^2}{n_2^2 c^2}\left[\chi^{(2)}\right]^2 |A_1|^4 L^2 \,\mathrm{sinc}^2(\Delta k L/2). \tag{2.17}$$

One sees that the intensity of the generated wave is proportional to the squared intensity of driving wave and the squared length of the medium. However, since the sinc^2 function decreases with increasing L for non-zero phase match (see Fig. 2.2), a comprise for the length has to be chosen. Because the refractive index n is depended on the wavelength, thicker crystals have a smaller frequency range where phase matching is archived. Thus, to generate short SHG-pulses from intrinsically spectrally board fs-pulses, thin crystals have to be used.

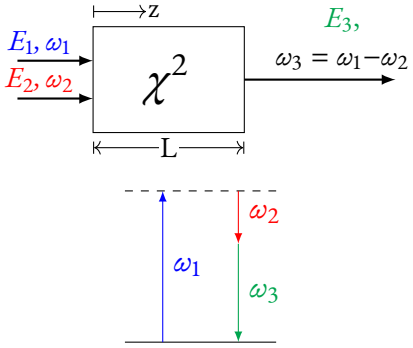

FIGURE 2.3: Top: Shematic of the DFG model. The input fields E_1 and E_2 generate the wave E_3 at the frequency $\omega_3 = \omega_1 - \omega_2$. Here we assume $\omega_1 > \omega_2$. Bottom: Energy-level diagramm of the interacting photons. For each ω_1 photon consumed, photons are emitted at ω_2 and ω_3.

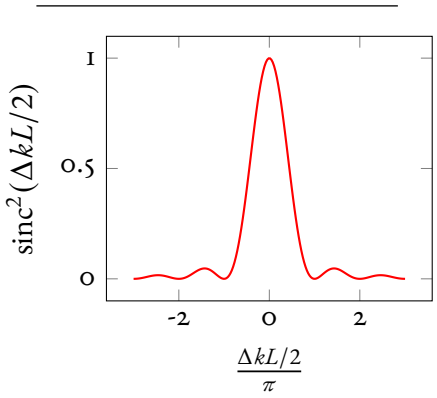

FIGURE 2.2: SHG intensity as a function of $\Delta kL/2$. The product of the phase mismatch and interaction length has to be smaller than π for efficent SHG.

2.1.2 Difference Frequency Generation (DFG)

DFG is another second-order process, which is described by the driving nonlinear polarization

$$P(\omega_1 - \omega_2) = 2_0 \chi^{(2)} E_1 E_2^*. \tag{2.18}$$

The process is illustrated in Fig.2.3. On a first glance, it looks very similar to sum frequency generation, but the photon-energy scheme reveals a difference: for every photon created at the frequency ω_3, a photon of higher input frequency ω_1 is annihilated and a photon at lower input frequency ω_2 is created.

Hence, DFG can be used to amplify light by generating the difference of a weak field (called seed) with a strong pump field at a higher frequency. This process is also called optical parametric amplification and is one of the standard tools in ultrafast spectroscopy. It can be seen as stimulated emission from the virtual energy level populated by ω_1. Like for SHG, phase matching is crucial for efficient amplification.

The phase-mismatch is given by

$$\Delta k = k_1 - k_2 - k_3.$$

Phase matching is again achieved by using birefringent crystals.

So far we showed how to generate visible light from our NIR fs-pulse source by SHG and how to use it as a pump to amplify light with a lower frequency via DFG. We still need a way to generate the seed for the DFG. The common way to generate the necessary seed from our fundamental beam is to generate a super-continuum, which is eluded in the next section.

2.1.3 Super-Continuum Generation (SCG)

Since SCG (or white light generation) is a product of different nonlinear processes, only a short description of its main contribution, *self-phase modulation*, will be given.

Self-phase modulation (SPM) differs from the so far described processes since it is a third order process and requires a modulated amplitude of the input wave (e.g., an optical pulse). The field of a pulse can be written as

$$\tilde{E}(z,t) = \tilde{A}(z,t) e^{i(k_0 z - \omega_0 t)} + c.c. \tag{2.19}$$

where $A(\tilde{z},t)$ is the pulse envelope and ω_0 the center frequency. Assuming the refractive index of the medium is changed by a strong external field, it can be characterized by

$$n(t) = n_0 + n_2 I(t) \tag{2.20}$$

where $I(t) = 2n_{00}c\left|\tilde{A}(z,t)\right|^2$. The change of the refractive index with time leads to time depended phase change of the transmitted pulse:

$$\varphi_{NL}(t) = -n_2 I(t) \omega_0 L/c \tag{2.21}$$

By defining the instantaneous frequency

$$\omega(t) = \omega_0 + \delta\omega(t) \tag{2.22}$$

$$= \omega_0 + \frac{\mathrm{d}}{\mathrm{d}t}\varphi_{NL}(t) \tag{2.23}$$

we directly see that non-linear phase leads to spectral broadening proportional to the intensity change. As is shown in Fig.2.4 for a Gaussian pulse, the front edge of a pulse experiences a red-shift, while the trailing edge of the pulse experiences a blue-shift. Additionally, the intensity-dependent refractive index leads to self-focussing.

For a more realistic modeling of SCG, additional effects like self-steepening, four-wave mixing and self-focussing have to be considered[2]. Practically, it is easily implemented: simple focussing with enough power in a suitable medium leads to SCG. The resulting output spectrum is very sensitive to the input power, the medium, the characteristics of the generating pulse, and the numerical aperture used to focus the beam. A comparison of SCG in different bulk media is given by Dubietis et al[3].

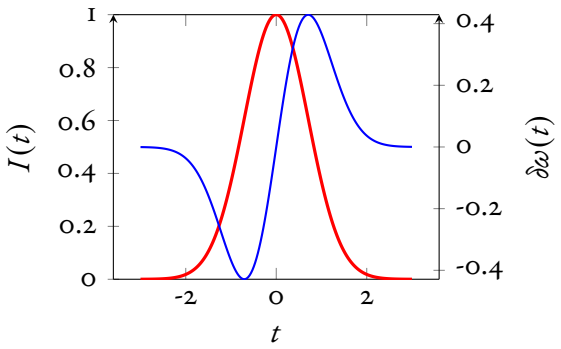

FIGURE 2.4: Frequency shift due to SPM. The intensity of the pulse is plotted in red, while the resulting frequency shift is plotted in blue. The frequency shift near the maximum is well approximated by a linear function.

2.2 Pump-Probe Spectroscopy

Femtosecond pump-probe spectroscopy is a non-linear spectroscopy. Non-linear spectroscopy is most commonly described in a semi-classical picture where the driving field is treated classically and the sample quantum-mechanically[4]. A full QM-treatment is given by Kowaleski and co-workers[5]. In the semi-classical picture, pump-probe spectroscopy can be viewed as a third order effect, where the pump pulses induce transient changes to the probe pulse via the medium of interest.

$$P^{(3)}(t) = \int_0^t \mathrm{d}t_3 \int_0^t \mathrm{d}t_2 \int_0^t \mathrm{d}t_1 \, S_3(t_3, t_2, t_1) \cdot \mathbf{E}(t - t_3)\mathbf{E}(t - t_3 - t_2)\mathbf{E}(t - t_3 - t_2 - t_1) \tag{2.24}$$

Here the $S^3(t_3, t_2, t_1)$ is the *third-order nonlinear response function*, which is the sum of all allowed response functions. The response functions each describe a path in the Liouville space. A full treatment of the response functions is outside the scope of this work.

Summarized, the state of matter is described by the density matrix

$$\rho = \sum_{i,j} |c_{ij}|^2 \, |i\rangle\langle j| .$$

Assuming an N level system starting in its ground state $|0\rangle\langle 0|$, interactions with a light pulse either increases or decreases (if not zero) the bra or the ket side. The probability of an interaction is given by the transition dipole moment

$$\mu_{ab} = \langle a|q\hat{x}|b\rangle$$

between the states.

Between the interactions with the fields, the time evolution of the system is given by the unperturbed Hamiltonian. Since the pump pulse leads to the population of an excited state, two simultaneous interactions with the pump-pulse are necessary to get the populated density matrix $|1\rangle\langle 1|$. Assuming, without any loss of generality, that the final remaining polarization is on the left, the following probe pulse can generate either generate $|2\rangle\langle 1|$ or $|1\rangle\langle 0|$. The remaining off-diagonal polarization oscillates

[2](9) Zheltikov, A. M. „Let There Be White Light: Supercontinuum Generation by Ultrashort Laser Pulses“. 2006.

[3](10) Dubietis, A., Tamošauskas, G., Šuminas, R., Jukna, V. & Couairon, A. „Ultrafast Supercontinuum Generation in Bulk Condensed Media (Invited Review)“. 2017.

[4](11) Hamm, P. & Zanni, M. T. *Concepts and Methods of 2d Infrared Spectroscopy*. 2011.

[5](12) Kowalewski, M., Fingerhut, B. P., Dorfman, K. E., Bennett, K. & Mukamel, S. „Simulating Coherent Multidimensional Spectroscopy of Nonadiabatic Molecular Processes: From the Infrared to the X-Ray Regime“. 2017.

with the frequency ω_{21} or ω_{10}, which generates an electric field which interferences with the field of the probe itself (this is called homodyne detection).

Neglecting coherent effects, pump-probe experiments can be described in a simpler picture in which the pump-pulse simple promotes part of the initial population into an excited state. The three signal contributions are explained below.

2.2.1 Signal Contributions

The observed signal in pump-probe experiments is the sum of the following three contributions:

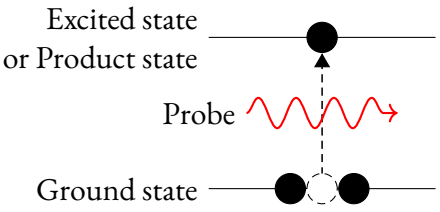

Bleach: The initial pump excitation depopulates the ground state. Hence, compared due to the unpumped sample, the sample has less ground state absorption (dashed arrow), and more probe light is transmitted. While bleaching is typically assigned to the depopulation due to the initial excitation, later process can also depopulate the ground-state after the excitation. For example, if the excitation initiates a reaction which consumes non-excited molecules in the sample.

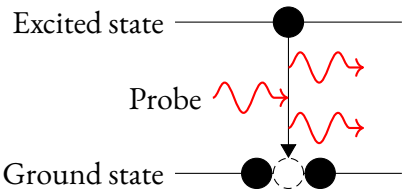

Stimulated emission: If the probe light is resonant with an allowed transition between a populated excited state and a lower state, the excited system will drop to the lower level by emitting a photon (solid arrow). The direction, polarization and phase of the emitted photon are identical to the stimulating field.

Since SE depends on the existence of an excited state, it's not seen in slower time-resolved spectroscopy. While the existence of SE requires an excited state, the absence of it does not mean the system is in the ground state: structural changes in the excited state could make a transition quasi-forbidden since the transition dipole moment also depends on nuclear coordinates.

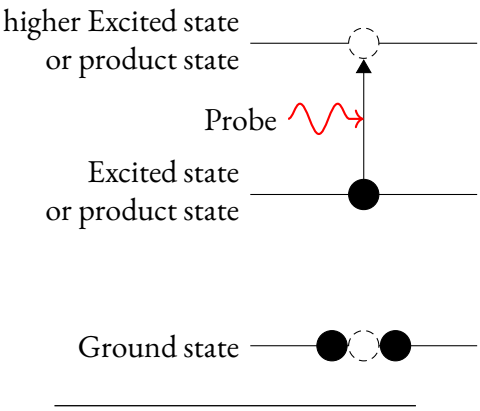

Photoinduced Absorption Newly populated states have different absorption spectra from the initial state. Hence, the probe light is absorbed by these transitions (solid arrow), reducing the transmittance of the excited sample. The absorption of an excited state to a higher excited state is called excited state absorption (ESA), the absorption of a product is called product absorption (PA).

2.2.2 Polarization

For dipole transitions, the transition probability between to states interacting with an external field is proportional to

$$P_{in} \propto \left| \cdot \vec{\mu}_{in} \right|^2 \tag{2.25}$$

$$\propto \cos^2(\varphi). \tag{2.26}$$

Here, is the field vector of the electric field and μ is the transition dipole moment (tdm) associated with the transition between the states, φ is the angle between them. In solution, the initial distribution of the tdms is isotropic. The interaction with a linear polarized field leads to anisotropic sub-ensemble of the tdms, with a preferred μ orientation parallel to .

The tdms of the pumped and probed transition can be different. If both belong to the same molecule and the geometry of the molecule does not change, the angle between both tdms is fixed. Hence, the resulting distribution of the probed tdm is a cone around the direction of the pumped tdms. Therefore the ratio of the signals measured with parallel and perpendicular polarizations of

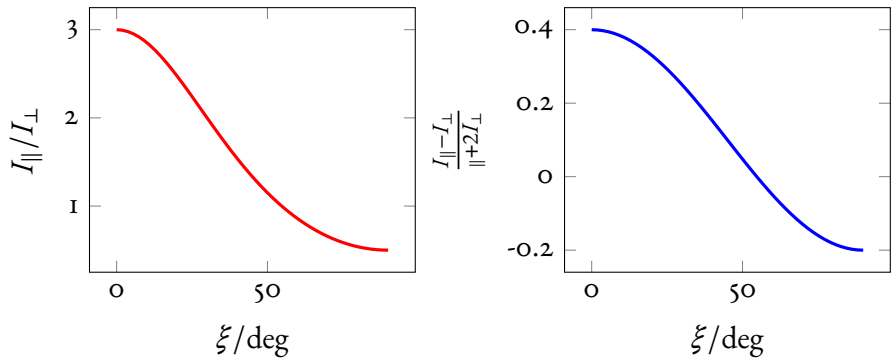

FIGURE 2.5: *Left:* The dichroic ratio for a given relative angle ξ between the pump- and probe-tdm. The signal for parallel tdms is 6 times heigher then for perpendicular tdms. The signals are equal if the angle is the so-called magic angle with 54.73°. *Right:* The anisotropy for a given angle.

the pump and probe depend on the angle between the tdms. Following Parson[6], assuming the pump-polarization lays in x-plane the so-called *dichroic ratio* is given by

$$\frac{I_\parallel}{I_\perp} = \frac{\overline{(\hat{x}\cdot\hat{\mu_{pu}})^2(\hat{x}\cdot\hat{\mu_{pr}})^2}}{\overline{(\hat{x}\cdot\hat{\mu_{pu}})^2(\hat{y}\cdot\hat{\mu_{pr}})^2}} \tag{2.27}$$

$$= \frac{(1+2\cos^2(\xi))/15}{(2-\cos^2(\xi))/15} \tag{2.28}$$

$$= \frac{1+2\cos^2(\xi)}{2-\cos^2(\xi)}, \tag{2.29}$$

with ξ being the angle between the tdms and $\overline{f}$ being defined as averaging over all orientations of f. Fig. 2.5 shows the dichroic ratio for a given angle. Instead of dichroic ratio the *anisotropy* defined as

$$r = \frac{I_\parallel - I_\perp}{I_\parallel + 2I_\perp} \tag{2.30}$$

is often used. Here the sum in the denominator is the scaled isotropic signal $3I_{iso}$, which can also directly measured by setting the angle between pump- and probe polarisation to 54.7°[7]. For a given angle ξ this results in

$$r = \frac{2}{5}\left(\frac{3\cos^2(\xi)-1}{2}\right) \tag{2.31}$$

The anisotropy and dichroic ratio are time-depended. In addition to changing with state transitions and geometry changes of the excited molecule, they also decay due to rotational diffusion. While the anisotropy decays to zero, the dichroic ratio decays to one. The decay, which depends on the solvent, the molecule and the temperature, can be directly measured by polarization resolved pump-probe experiments.

Polarization resolved measurements can be very useful when analysing transient spectra. They can help to disentangle spectra and to attribute bands to specific transitions. E.g. if a spectra has zero-crossings which are not at the same position for both polarizations, one can conclude that the band is made-up from at least two transitions with differently orientated tdms.

IR-spectroscopy itself is already structural sensitive, since the band-position and strength of the observed transition depends on the associated bonds and atoms. Unlike electronic transitions, mid-IR vibrations tend also to be localized. Therefore we can almost directly translate the calculated angle from the dichroic ratio to an bond-angle.

If a structure is available, it can be used to assign bands to specific groups with the correct orientation of the tdm. Similarly, one can calculate the orientation of the excited tdm[8] from the dichroic ratio of three different probed transitions with known orientation. Likewise, one can use Vis-pump IR-probe spectroscopy to differentiate between a vibronic progression and a second electronic tran-

[6](13) Parson, W. W. *Modern Optical Spectroscopy: With Examples from Biophysics and Biochemistry*. 2007.

[7]The isotropic signal is very useful since the signal is not impeded by rotational diffusion.

[8](14) Linke, M., Theisen, M., von Haimberger, T., Madjet, M. E.-A., Zacarias, A., Fidder, H. & Heyne, K. „Determining the Three-Dimensional Electronic Transition Dipole Moment Orientation: Influence of an Isomeric Mixture“. 2010.

sition, under the condition that directions of the electronic tdms are different.

2.3 Relaxation dynamics

In a sense ultrafast pump-probe spectroscopy is the study of relaxation dynamics: a sample in equilibrium with its surroundings is suddenly perturbed by the absorption of energy. In the beginning, the energy is restricted to the few degrees of freedoms which were accessible by direct excitation. In the case of a narrow excitation in the infra-red, we have a single excited vibration, while a visible excitation leads to a electronically excited state and possible excited vibrational bands which are Franck-Condon active a therefore couple to the electronic transition. In both cases, assuming no stable product is formed, the localized energy will be redistributed over time until a statistical equilibrium is reached again.

2.3.1 Vibrational Relaxation

For vibrational modes, this process is called *vibrational energy relaxation* (VER) and consists of two effects: Intramolecular vibrational redistribution (IVR) and vibrational cooling (VC). IVR describes how the energy from one mode flows into other modes while conserving the total energy. Vibration cooling, also called external vibrational relaxation (EVR), describes how the energy dissipates from molecule to the solvent.

While there is no clear boundary between these two, as a VC can happen in a very IVR fashion and even excite solvent modes coherently, there are some general guidelines. For a medium-sized molecule with an excited high-frequency mode, the molecule first relaxes via IVR into a combination band or a higher harmonic of a lower frequency mode. This continues until mostly low-frequency modes are populated, which contribute a channel to deposit energy into the solvent bath. At room temperature the modes up to 200 cm^{-1} are populated according to the Boltzmann distribution.

The size of the molecules is of importance because the number of vibrational modes in a molecule is $3N - 6$, with N being the number of atoms of the molecule. More modes lead to a higher state density per energy, hence making IVR more likely since there are more possible acceptor states. For the extreme case of a diatomic molecule, there is only one mode, and therefore IVR is not possible.

This picture presented here is simplified, since it only accounts for energy conservation. But both IVR and VC can only populate modes which couple to the excited vibration. Two kinds of couplings dominate the relaxation process: dipole-dipole coupling and mechanical coupling. Both have coupling strengths which scale strongly with distance, inducing locality to the IVR process. Therefore, the excess energy dissipates from its origin similar to heat diffusion in macroscopic materials[9]. In larger molecules vibrational energy relaxation can also have ballistic behavior, e.g., the energy distributes over the volume with a constant velocity. This was shown by observing the frequency shift of spatially distributed observer mode at different positions over time. These modes shift when coupled low-frequencies modes get populated. Comparison of the rise time of the different observer modes gives a mean velocity of the energy transfer in the molecule.

If the relaxation is faster than the period of an accepting mode, coherent contributions of the acceptor mode are observed[10]

In solution at room temperature, vibrational lifetimes are generally in the range of 0.1 ps to 20 ps, since the mean time between collisions with surrounding molecules is also in same range.

2.3.2 Electronic Relaxation

So far the discussion here was restricted to vibrational modes. Including electronic excitations makes the picture even more complicated. An electronically excited molecule can lose energy by internal conversion, light radiation, intersystem crossing and via energy transfer to another system. An example of a typical relaxation pathway is shown in

[9](15) Rubtsova, N. I. & Rubtsov, I. V. „Vibrational Energy Transport in Molecules Studied by Relaxation-Assisted Two-Dimensional Infrared Spectroscopy". 2015.

[10](16) Heyne, K., Huse, N., Nibbering, E. T. J. & Elsaesser, T. „Coherent Vibrational Dynamics of Intermolecular Hydrogen Bonds in Acetic Acid Dimers Studied by Ultrafast Mid-Infrared Spectroscopy". 2003; (17) Heyne, K., Huse, N., Dreyer, J., Nibbering, E. T. J., Elsaesser, T. & Mukamel, S. „Coherent Low-Frequency Motions of Hydrogen Bonded Acetic Acid Dimers in the Liquid Phase". 2004.

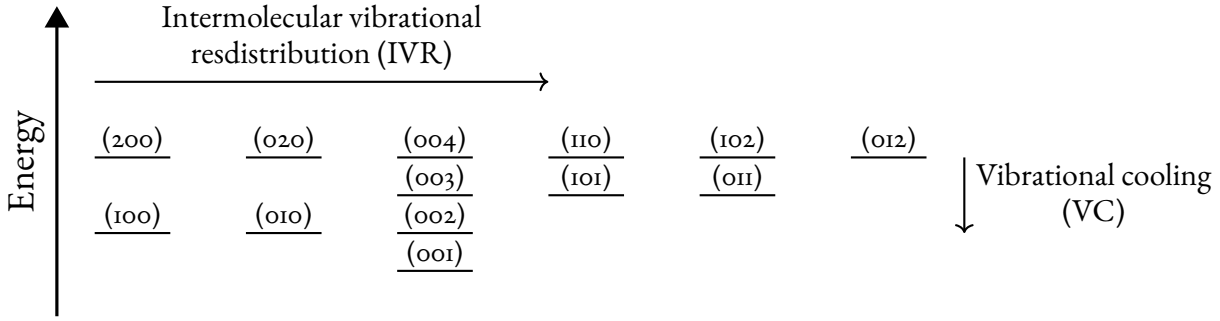

FIGURE 2.6: Energy levels of a triatomtic molecoule where two modes have the same frequency and the third half the frequency. If the (200) state would have been populated, the energy could be transfered to five other isoenergetic states due to IVR. VC leads to lower states via dumping energy into the surounding.

Fig. 2.7.

The most common decay path and normally the fastest is internal conversion (IC). IC describes the process where the electronic energy is converted to vibrational energy via a conical intersection (CI). A CI represents the intersection of the potential energy surfaces (PES) of two electronic states. The passing of the conical intersection hence leads to conversion of electronic to vibrational energy in the form of kinetic energy of the nuclei.

The second way to lose energy is to emit light acompanied with a transition to a lower state. If the transition is between two singlet states, it is called fluorescence. In most molecules, even fluorophores, only the fluorescence of the lowest excited state is observed (This is known as Kashas rule.), regardless of the initially excited state. This a consequence of the fast internal conversion between the higher excited states: as a rule of thumb, the higher the energy difference between two states, the slower the internal conversion: The intersection will be further away from the PES minimum. Similarly, the displacement between the minima of the PES is inversely proportional to the distance between the Franck-Condon region and the CI. This is all visualized in Figure Fig. 2.7. Hence, fluorescence is mostly observed in molecules with a small displacement.

Another transition to an electronically lower state is intersystem crossing (ISC). Ultrafast ISC can be seen as internal conversion between states with different multiplicity. Slower ISC not involving a CI can be described by tunneling and often has a similar rate as emission. Additional coupling between the states, e.g., by spin-orbit coupling due to heavy atoms, accelerate ISC.

Excess energy can also be lost by an electron transfer (ET). Here the excited electron moves to a suitable acceptor. Slow ET is well modelled by the Marcus theory, which is very similar to the transition state theory for reactions. The difference lies in the composition of the reaction coordinate, which is dominated by the solvents electronic dipole orientation for the Marcus theory. For an ultrafast ET, the wavefunctions of the donor and accepter-states need to overlap, and the spectra of both states need to be similar. The ET is typically followed by a back electron transfer (BET). If the BET occurs not from the highest occupied orbital, the process is called Dexter Energy Transfer, since the excitation energy of the donor was transferred to the acceptor without a lasting change in the oxidation state of the molecules.

The energy can also be transferred to another molecule by Förster Resonance Energy Transfer (FRET). Here, dipole-dipole coupling leads to deexcitation of the initially excited state by exciting the accepting molecule. Therefore it is sensitive to the distance and the relative orientation of both donor and acceptor.

2.4 Summary

- Non-linear optics are required to describe the light-matter interaction for ultra-short pulses. In birefringent crystals with a phase-matched orientation, the second-order susceptibility can be used for second harmonic generation

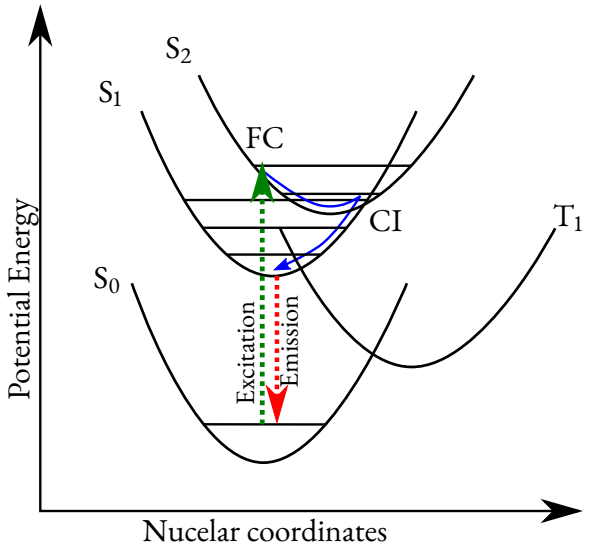

FIGURE 2.7: Relaxation after electronic excitation. Shown are the potential energy surfaces (PES) of the electronic states along the 1D-representation of the reaction coordinate. The blue line shows the relaxation path: The initial S_0- to the S_2 excitation promotes the molecule to the so-called Franck-Condon region (FC). The system then follows the PES downwards until it reaches the conical intersection (CI) with the vibrationally excited S_1 state. Here, the part of the electronic energy is converted to vibrational energy. After passing the CI, the system relaxes to the minimum of the PES via vibrational cooling. Since further internal conversion is not possible, the system either emits light - the fluorescence - or does inter-system crossing to the lower triplet state T_1.

(SHG) and difference frequency generation (DFG).

- DFG can be used to amplify a given seed wavelength. To generate a broadband seed, a high-power pulse is focussed into a medium. There, self-phase modulation, a third-order effect, leads to strong spectral broadening of pulse.

- Pump-probe spectroscopy is also described by third-order process. However, the simpler picture where the pump-pulse promotes part of the ground-state population to an excited state is enough to explain most observations: The signal is comprised of three contributions: bleaching, stimulated emission and excited-state absorption.

- A linear polarized pump-pulse generates an anisotropic population of excited molecules. By probing this distribution with two different polarizations, one can retrieve information about the relative angle between the probed and pumped transition dipole moment. With a given structure, this can be used to assign IR-bands to specific groups.

- Energy relaxation of excited molecules can be divided into electronic and vibrational relaxation. Vibrational relaxation consists of intra- and intermolecular relaxation, with the former being generally faster. High frequency modes relax into multiple modes with lower frequencies. Low-frequency modes can couple well to the solvent and therefore transfer energy to it. Electronic excited states can convert their energy to vibrational energy by passing through a conical intersection. Other decay channels for electronically excited states are fluorescence, intersystem crossing, electron transfer, and resonance energy transfer.

Chapter 3

Experimental Methods

This chapter will shortly explain the experimental setups used. Since the setups varied in between the different studies and the details are already given by the accompanying papers, the chapter concentrates on the implemented improvements to the setups.

The chapter starts with simplified description of modern commercial fs-laser sources. Next, it explains the basics of a pump-probe setup before giving an overview of the capabilities of the used fs pump-probe spectrometer. The details on the different spectrometers parts follow.

3.1 fs-Laser Source

This section explains the basic design of commonly available commercial femtosecond laser sources.

The actual source of the ultrashort pulses is the oscillator, a laser with a broad gain bandwidth and a high number of phase-locked modes. The mode-locking is most commonly achieved by using the optical Kerr-Lens effect. The optical Kerr-Lens effect leads to self-focussing in a medium, if the laser power goes over a threshold. By inserting the combination of a Kerr-medium and an aperture in the laser cavity, only the high powered (mode-locked) part is self-focused and passes the aperture while the low powered cw-part is blocked. After several passes, only locked modes participate in the lasing, resulting in a pulse train with a frequency in the MHz range. The pulse train is used as a seed for a chirped pulse amplifier (CPA).

In a chirped pulse amplifier, a grating stretcher first lengthens the seed by inserting chirp via an inverted grating compressor. The lengthened seed pulse is then amplified in a birefringent Ti: Sa crystal by a high-powered nanosecond pump pulse. After several passes through the amplifier, a single pulse leaves the amplification cavity and is compressed again by a grating compressor. Fast switching pocket-cells in combination with polarizers control the injection and the exit of the oscillator pulses. A grating compressor shortens the amplified pulse back to tens of femtoseconds.

3.2 fs Pump-Probe Spectroscopy

The most common ultrafast spectroscopy setup is the pump-probe setup. Here, a short laser pulse is divided by a beam-splitter. One part, the pump, is used to excite the sample. The other, called the probe, passes through the sample at the same spot and is detected directly. The signal is given by the change of the absorption when comparing the probe intensity with and without prior excitation by the pump pulse. The delay between both pulses can be varied by changing the path-length of one beam. Therefore $\Delta\tau$ is given by $\Delta l/c$. Today, the detection of the probe done in a spectrally resolved way. The signal at the frequency ω and the delay time τ is than given by

$$\Delta \mathrm{abs.}(\omega, \tau) = -\log_{10}\left(\frac{I_{pu}(\omega, \tau)}{I_{nopu}(\omega)}\right). \qquad (3.1)$$

Here, *pu* is short for pump and *no pu* is short for no pump. For noise reduction, every second pump is blocked mechanic chopper. The light modulation limits the noise to high-frequency contributions, which strongly decreases systematic errors.

The attenuation of light passing through the material is given by Beer-Lamberts law

$$\log_{10}(I_{pass}/I_0) = \lambda cd,$$

where λ is the wavelength depended extinction coefficient, c the sample concentration and d the length of the light path. Hence we need to take the logarithm to get the pump-induced change of the absorbance.

3.3 The Pump-Probe Spectrometer

All presented results in this work were performed with a commercial femtosecond laser system from *Coherent*, named Legend. The system delivers 80 fs pulses with a pulse energy of about 2.5 mJ with a repetition rate of 1088 kHz.

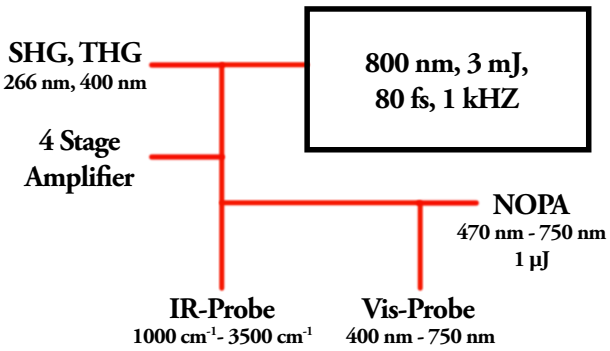

FIGURE 3.1: Overview of the Vis-IR femtosecond pump-probe spectrometer.

The current setup, schematically shown in Fig. 3.1, is divided into two probe beams with corresponding detection hardware: the simpler visible probe which is using a supercontiuum detected by a high-resolution CCD and the IR-probe beam which consists of a home-build three stages OPA and a 2x32 MCT array.

Two different conversation and amplification stages exists to generate the desired pump-pulse. Visible pulses with a power of about 1 µJ in the range of 470 nm to 750 nm can be generated by a non-linear optical parametric amplifier.

For other wavelengths ranges, a flexible three to four stage OPA setup is available. While it always starts by generating NIR pulses in the first stage, the other stages depends on wished output range. For example, visible pulses at 530 nm can be produced by amplifying the NIR output of the first stage two times and generating the second harmonic in the fourth stage.

The laser fundamental centered at 800 nm and its second and third harmonics at 400 nm and 266 nm can also be used for excitation.

3.4 IR-Probe

Only a short summary of the IR-probe setup will be given, since details are given in the dissertations of Y. Yang and M. Linke.[1] The generation of the mid-IR pulses follows the amplification scheme proposed by Kaindl et al[2]. The scheme consists of three stages. The first stage OPA amplifies the near IR part, around 1400 nm, of a sapphire supercontiuum. The second OPA stage is used to amplify the output of the first stage. In the last stage, mid-IR pulses are generated by DFG of the signal and idler of the second state.

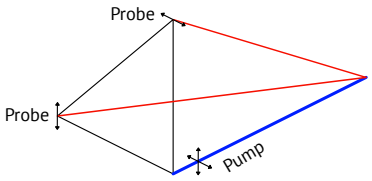

FIGURE 3.2: Balanced polarisation resolved setup to minimize errors due to the angle between pump and probe beams. The polarisation of the pump is switched after every scan.

The generated IR-pulse passes through a telescope and the optical delay-line. Two different variations of the setup were used for the remaining parts. In the first variant, the probe is first split into three parts by a ZnS window. The transmitted beam is only used for referencing, while the two reflections are used as two separated probe beams. A periscope rotates the polarisation of one of the beams. Two 80 mm lenses focus the two beams into the sample.

[1](18) Yang, Y. „Echtzeitverfolgung der ultraschnellen Strukturänderungen der Pr und Pfr Photoisomerisierungen in Phytochrom“. 2017; (19) Linke, M. „Analyse von Photorezeptoren und Antennenpigmenten mit Ultraschneller Polarisationsaufgelöster Infrarotspektroskopie“. 2012.

[2](20) Kaindl, R. A., Wurm, M., Reimann, K., Hamm, P., Weiner, A. M. & Woerner, M. „Generation, Shaping, and Characterization of Intense Femtosecond Pulses Tunable from 3 to 20 Mm“. 2000.

In order to minimize systematic errors in measuring the dichroic ratio, the polarisation of each probe beam is perpendicular to the plane given by the pump and probe, as is shown in Fig. 3.2. This setup was used in the studies of corrole, phytochrome and channelrhodopsin.

In the second variation, which was used in the IR induced reaction study, the probe is split into two beams by an IR-beamsplitter. By increasing the length of one beam path, a time difference of several nanoseconds between the two pulses is introduced. Both beams are passing through the same spot in sample, but the pulse of the leading beam is always arriving before the pump-pulse and therefore can be used as a frequency resolved reference.

In both variants, the probe beams are collimated after the sample and focussed into a *Triax 320* grating spectrometer, equipped with two 32-elements MCT arrays.

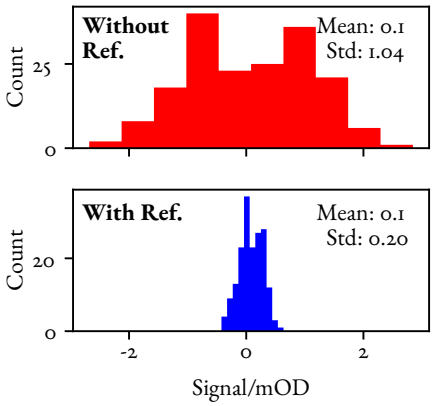

FIGURE 3.3: Histograms of measured signals without (*top*) and with (*bottom*) referencing. The histograms are calculated from 180 measurements from a single channel. Each measurement used 600 shots. The data was taken from IR-pump IR-probe experiments on Cyclohexanol. Here the referencing leads to a reduction of the standard deviation by a factor of five.

3.4.1 Improvements to IR-Probe Setup

The performance of IR-probe was improved by several changes. The next subsections describe these changes.

3.4.2 Referencing

Two different referencing schemes for the IR-probe were added to the software and to the setup.

In first scheme, a single element MCT-detector is used to record the total intensity of a part of the probe beam not passing the sample. In the signal calculation, the spectrum of every shot is dived by the total intensity, cancelling out the noise due to power variations. Since the probe is generated by a three stage OPA, this works remarkable well, since the random variations between different frequencies is much smaller. The scheme doesn't require a full MCT-array, so it allows for simultaneous recording of two different polarized beams. The scheme, as it was implemented, had a drawback: the referencing beam didn't pass sample. For proteins and other samples, small signals are measured against a high background absorption. Due to sample heterogeneity and thickness variations, the background fluctuates strongly when the sample is moved, which leads to large baseline noise.

Since the large baseline noise impacts negatively on the detection of small signals, we introduced another referencing scheme. As explained above, we split the pulse in two parts and add a delay to one of the pulses. The pulse arriving several nanoseconds earlier is used as reference. Since the reference pulse is passing through the same sample spot as the probe, only at an earlier time, large parts of the baseline noise are eliminated. This is exemplified in Fig. 3.3. The drawback of this scheme is the lack of the simultaneous detection of both polarisations.

In both cases, the referencing improves the stability over time. A carefully aligned probe OPA can produces pulses with less the 0.5 % noise, but the stability is very sensitive to the laser system. In practice, the probe only remains in the low-noise region for up to two hours. It has to be tested if a combination of both variants can address the drawbacks of both variants by leading the reference beam of the first variant through the sample spot.

3.4.3 MessPy

The old Labview software was replaced by the python software used on visible probe setup, called "MessPy". In addition to more user comfort, this change also reduced the measurement time. The reduction is mostly due to faster data acquisition: the

legacy software unnecessarily resets the ADC hardware before every reading, a behaviour copied from included reference code[3]. This adaptation also allowed MessPy to be used on the IR-pump IR-probe setup of our other laser-system.

The software is described in more detail in the next chapter.

3.4.4 ADC Voltage drops

I could also pin-down the reason for erratic voltage drops in the output of the IR-detection hardware. These drops were caused by grounding problems of the MCT-detector: By replacing metal clutch holding MCT-array with a non-conducting plastic version the issue was solved.

3.4.5 Stepper Motor driven Sample Holder

The sample scanner used to move the sample is already described in PhD thesis of M.Linke. It consists of two spindles controlled by two stepper motor. The old software was only able to send precalculated paths to the motor controller. Therefore, the area of sample was fixed to discrete sizes. The updated control software is more flexible, which has the its downsides: While it is easy to calculate arbitrary paths, the motor itself can only follow very specific paths. The usable path files of the old software were tested to work for specific baud-rates to result in the requisite path, something which is yet missing in the new software. Therefore, for movement of the sample the old software is still useful.

Another avenue not explored by the prior software is the automatic determination of the focus size. This can be achieved in two ways, both are involving a light blocking element in focal plane.

The first way uses a pinhole: One maximizes for maximal transmission through the pinhole. The intensity is recorded while scanning the position of pinhole. This results in a intensity map roughly proportional to the convolution of the pinhole with focal spot.

The second way involves a sharp edge. The sharp edge is moved to block parts of the beam while the resulting intensity is recorded. Doing this for two perpendicular direction we get x- and y-FWHM values of an assumed gaussian focus spot. We only used the latter method, since it requires less alignment, fewer measurement time and does not need beam adjustment through a very small pinhole.

[3] This changed in the newer versions.

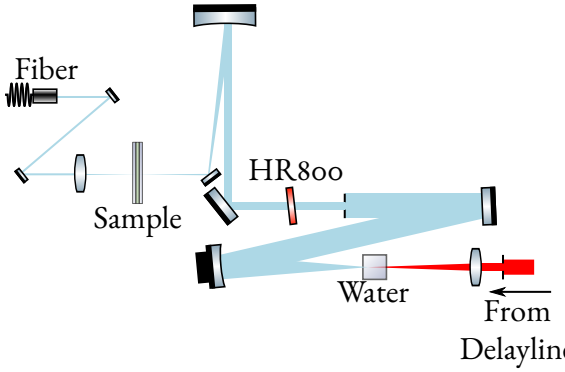

FIGURE 3.4: Schematic of the visible probe setup. The 800 nm pulse coming from the delay line is focused into a 1 cm water cell. A spherical mirror collimates the SC and a HR800 mirror filters out the residual part of the fundamental. A second spherical mirror focusses the beam into the sample, after which it is collimated again and coupled into spectrometer via a fiber.

3.5 Vis-Probe

The current setup of the visible probe, which uses a super-continuum generated in water, is shown in Fig. 3.4. The setup is an improved version of the prior setup, which is described in my diploma thesis[4].

3.5.1 Improvements of the Vis-Probe Setup

The visible probe setup was improved in several points to decrease the necessary measurement time.

3.5.2 Delay-Line

Instead of varying the pathlength of the pump beam, which has poor spatial mode, we vary the pathlength of the probe. To further minimize the influence of the pathlength variation, the 800 nm laser fundamental passes the delay-line before the supercontinuum generation (SCG). This has two advantages: First, the mode quality should be decent and the beam should be collimated, since no collimating optics are passed except the telescope

[4] (21) Stenstitzki, T. „Polarisationsaufgelöste Femtosekundenspektroskopie an Aluminium-Corrolen“. 2010.

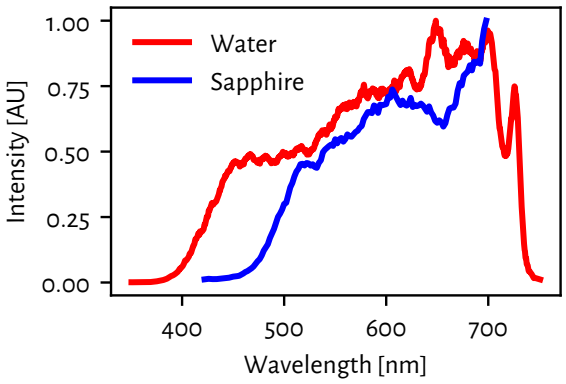

FIGURE 3.5: Spectra of the supercontinuum generated in sapphire and water. The shown water spectrum is measured is filtered by Schottglass for a flatter shape and not corrected for the wavelength depended quantum efficiency of the CCD.

directly at the laser exit. Delay induced changes are further filtered out by the whitelight generation, which starts with a small pinhole selecting only a small part of fundamental beam. Since the mode is assumed to be gaussian and centered at the pinhole, small beam displacements due delay-line movements are not critical.

This setup proved itself quite resistant even with our non-ideal laser mode: After careful alignment it was possible to record transient absorption spectra over the full 2 ns range, despite a very divergent laser mode.

3.5.3 Water supercontinuum

Another improvement was the change from sapphire to water as the medium for SCG. It is often believed, that SCG in water is quite unstable. Despite this, we were able to generate a stable supercontinuum in 1 cm water cell. The advantage of water is that the lower wavelength limit of the light generation is shifted down to 390 nm from 470 nm in sapphire. In Fig. 3.5 the SCG spectra generated in sapphire and water are compared. Unlike CaF_2, which generates a SC also going down to 400 nm, there is no need for mechanical movement of the SC medium to avoid photo-damage.

To get stable SCG in water, we focussed the beam in the second half of the cell[5]. The SCG in water can be roughly dived into three regimes, depending on the input power: The low power regime, where an unstable red continuum is generated, the medium power regime, where a very blueish spectrum is generated and the high power regime, where a very white continuum is generated. The medium regime seems to be the most stable. It is not always possible the differentiate between stable and unstable by eye, hence minimizing the standard deviation of the CCD-signal is recommended. While it is possible to generate a continuum with less than one percent standard deviation over most of the observed spectral range, the water continuum has sometimes short periods of unstable behaviour. If these are caused by laser fluctuations or due to thermal convection in the water-cell is not clear. Recorded data from these periods are easily removed in postprocessing via outlier detection.

3.5.4 Detection

Light induced sample degradation can be a real issue for certain samples, e.g. channelrhodopsin, hence a reduction in measurement time is very useful. The used Shamrock-spectrometer had three 600 lines/cm gratings installed by default, differing only in their blaze wavelengths. Together with the 512 pixel from CCD (binned down from 2048) and ignoring deviations resulting from the imaging this resulted in a nominal spectral resolution of 0.13 nm per pixel. Even assuming an error of one magnitude, the resolution is still unnecessary high for spectrography in solution, where all spectral bands have an FWHM of at least 20 nm.

Therefore I replaced one of the gratings with a 150 lines/cm grating. This change allows us to record almost the whole spectral range of the SC at once, decreasing the measurement time by a factor of three to five. The spectrum shown in Fig. 3.5 was recorded with the described grating. The calibration was done with an argon calibration pencil lamp.

So far our setup was limited to around 1000 nm due to quantum efficiency drop of Si-based CCDs over 900 nm. For broader coverage into the NIR

[5] We think that chirp (and by that the duration) of the input pulse strongly affects the generation, it could be that a too short pulse leads to unstable SCG.

region, we acquired a prism spectrometer equipped with an InGaS-based CCD array. Since these don't work below 500 nm, this system is not a replacement of our Si-based CCD system. The NIR region is very interesting for all studied systems in this work. For corroles and phythochromes, the Q-band to Soret-band transition is located in the NIR. For retinal proteins, both stimulated emission and excited state absorption of the relaxed photoexcited state are also located in the near IR region.

Calibration of NIR spectrometer was done with a combination of aluminium corrole, chloroform and the laser fundamental. I also tried to use green laser pointer, which normally works by frequency doubling of a NIR-laser at 1050 nm, which is not filtered out. This didn't work very well, because the pixel positions of a wavelength is very sensitive to the alignment of the input beam.

The usefulness of the NIR spectrometer is hampered by the lack of a good NIR supercontiuum source. Sofar, the tested SCG of sapphire and YAG only produced light up 1100 nm under stable conditions

The NIR spectrometer was used in examining the photoreaction of brominated Al-corrole and of Cph1.

3.6 Noncollinear Optical Parameteric Amplifier

An additional noncollinear OPA[6] was added back to the setup. With a second variable visible pump source available, both probe setups can be operated simultaneously. A schematic of the NOPA is shown in Fig. 3.6. The advantage of the noncollinear setup is a broader spectrum, since the geometry allows for phasematching over a broader range. For that, a chirped seed is required.

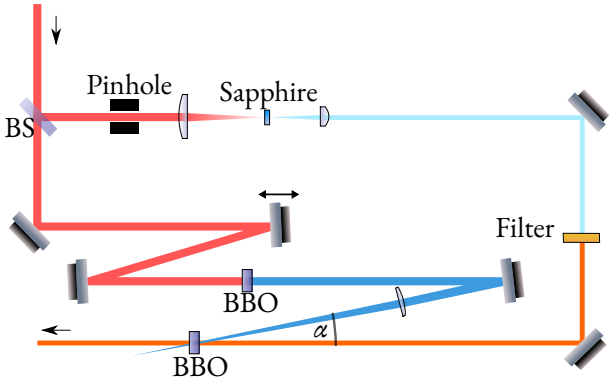

FIGURE 3.6: Schematic of the noncollinear optical parametric amplifier. The beam is spilt into two parts: 10 % are used for SCG in sapphire (SAPH) after passing a pinhole (PH). The SC is used as the seed. A bandpass filter can be placed in the path of seed SC to generate spectrally narrow pulses at a given wavelength. The remaining 90 % are used for SHG in a BBO crystal, generating the pump-pulses. Both the pump and the seed are focussed and overlapped with an small angle in another BBO, generating the signal.

3.7 Summary

- The setup is based on commercial fs-laser system, consisting of a seed laser and an chirped pulse amplifier.
- The spectrometer is able to generate sub-picosecond pulses in the range from 266 nm up-to 10 000 nm (1000 cm^{-1}).
- The Vis-pump Vis-probe setup was improved: A NIR spectrometer was installed to extend the spectral window into the near infra-red. The medium for super-continuum generation was changed from sapphire to water, extending the spectral window down to 390 nm. To decrease the measurement time the grating in the visible spectrometer was changed and now allows to record the whole range of 390 nm to 750 nm at once.
- The IR-probe now uses a same-spot referencing scheme, strongly improving the signal to noise ratio.
- With the motorized sample holders it is now possible to measure the focal spot size of the pump- and probe beams automatically.

[6](22) Wilhelm, T., Piel, J. & Riedle, E. „Sub-20-Fs Pulses Tunable across the Visible from a Blue-Pumped Single-Pass Noncollinear Parametric Converter". 1997.

Chapter 4

Software Methods and Design

This chapter is - in part - an opinionated chapter. First, I will discuss software in science and suggest a minimum set of best-practices I deem necessary for usable and maintainable software. Secondly, this chapter will describe the general design of MessPy, the software now used in all of our ultrafast spectroscopy setups in the lab. Subsequently, I will give a survey of the methods used to analyze our experimental time-resolved data in the self-written python package skultrafast.

4.1 Software in Science

Today's science is impossible without software.

This still holds true for experimental science: For controlling the experiment, analyzing the data and visualizing the result, software is required. A number of commercial software suites with graphical user interfaces are available to solve the latter two points. These work well for simple cases, but for more complex cases, hand-tailored solutions are frequently necessary. While the commercial solutions have scripting capabilities, these often lack the numerical algorithms required for state of the art data analysis. Additionally, using closed source proprietary software for science is problematic, since not every step done in the analysis is reproducible easily since the source code of the software is not available.

Due to the high variability of experiments and the need for customizations, there is no stand-alone commercial solution for controlling scientific experiments. Instead, the proprietary visual programming language LabView tries to ease the complexity of software engineering in this domain.

LabView is the only widely used visual language. The most prominent advantage of LabView is the support by the hardware manufacturers; almost all lab equipment comes with LabView drivers. Due to the visual aspect of LabView, the drivers also function as small GUI which can be easily connected to other devices. However, it has several drawbacks, most of which it shares with other visual languages: it does not work with standard version control software, it has an unclear separation of the GUI- and Logic-layer, and larger projects get confusing fast[1]. Additionally, it is quite expensive and has almost no users outside the domain of automation.

Software in science has another problem: It seldom produces papers on its own. Hence, it does not generate funding directly. Thus, software in science is mostly seen as necessary busy work, which in turn leads to bad software practices which then results in unmaintained programs. Often, a working program is considered finished, regardless of its maintainability and expandability, and the reproducibility of results is only an afterthought.

Besides, capable programmers are sought for by the industry, whom can offer higher wages and a more secure career path than science currently does. This leads to situations, where the single programmer knowing the code leaves and due to the bad software practices mentioned above it is almost impossible for an outsider to change or improve the program for his or her successor.

Despite all of this, software for developed for science now powers the world, as they are the fundament of all modern data science.

[1] This may not be true for experienced LabView developers, but even examples which are delivered with hardware are often unnecessarily hard to follow.

4.2 Minimal Software Practices

A lot is written about good software practices[2], but it is seldom applied for scientific software for the reasons mentioned above. In an ideal world, testing, reproducibility, and documentation would be as important as new features. However, in the real world, getting experiment/analysis running without delay is crucial. Even under the constraint of delivering working software fast, time should be taken to make the result maintainable. I propose the following guidelines.

Programming Language Only use a very common and popular programming language. If possible, it should be a language which is used as part of the curriculum. Else, the already small pool of potential contributors gets even smaller. A healthy ecosystem of scientific packages, including visualization solutions, is a big plus. It allows a rapid application of novel methods. Lab-equipment almost always supports C via dynamic link libraries (DLL). Therefore the language should have good interoperability with C-libraries.

Version Control Always use a version control (VCS) system like *git*, *svn* or *mercurial*. Using one of the modern distributed version control systems also serves as a backup solution, because the code is saved in different locations. There is no excuse for not using a VCS.

Modularity Modularization is necessary for maintainable software and increases reusability. One of the most common mistakes in scientific software is the missing separation between the graphical user interface (GUI) and the actual logic. This entanglement of the layers leads to unmaintainable code and prohibits code reuse.

A very pragmatic choice of language and VCS fulfilling the mentioned requirements would be Python and Git. Git is the clear winner of the new generation of VCS. Python is now very common, has a low entry barrier and a very healthy scientific ecosystem and good interoperability with C and C++. I would defer the use of strongly typed languages like C and C++ since programs in these languages tend to be hard to change if not well designed. These two languages also lack a real module system.

[2](23) Wilson, G. *et al.* „Best Practices for Scientific Computing“. 2014.

4.3 MessPy

MessPy is now the software which now controls all pump-probe setups in the lab. It was at first a replacement for the old Messnetz software coming from Max-Born Institute. A student job for maintaining and improving the software was my introduction to Prof. Heyne group. Another replacement for Messnetz written/drawn in LabView was also successfully replaced by *MessPy*.

MessPy is written in Python for the CPython, the Python reference interpreter written in C. It can be divided into three layers: the instruments packages, the control/plan packages, and the GUI layer.

The instrument package contains standalone modules for controlling and communicating with the lab equipment.

4.3.1 Controller and Plans

Two parts make up the middle layer, the controller and the plans.

The Controller initiates and holds references to the different instruments and does some common data processing which is used for the diagnostics which are displayed in the GUI. It also controls the main loop which runs the current plan.

A plan is a class containing the actual logic and state necessary to run an experiment. It is also responsible for saving the recorded data. It must supply a `make_step()` method, which is looped by the controller until it returns false. It should not contain logic for displaying results. This is handled in the third layer.

An exemplary plan which scans the spectrum in a given range is shown in Listing 1. In each step, it moves the spectrometer grating to a new wavelength position, reads the CCD and saves the middle channel of the detector to the memory. When reaching the last requested wavelength, it writes the recorded data to a file. I want to emphasize again,

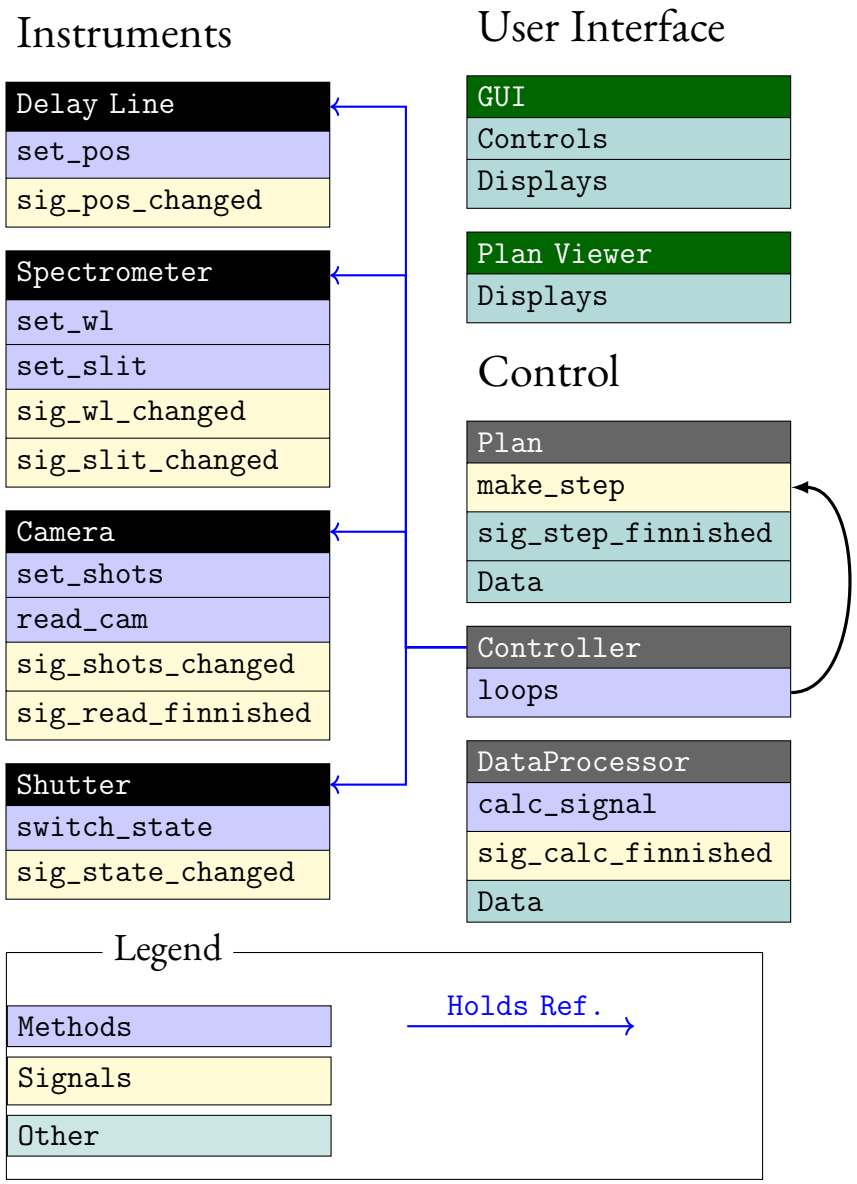

FIGURE 4.1: Simplified presentation of the structure of MessPy program. It can be roughly dived into three parts.

```
class SpectrumPlan:
  def __init__(self, fname, from_wl, to_wl, n):
    self.fname = fname
    self.wls = np.linspace(from_wl, to_wl, n)
    self.wl_idx, self.out = 0, []
    self.sigStepFinished = Signal()

  def make_step(self):
    c = controller
    if self.wl_idx == len(self.wls):
      tmp = np.hstack((self.wls, self.out))
      np.savetxt(fname, tmp)
      return False
    self.wl_idx += 1
    next_wl = self.wls[self.wl_idx]
    c.spectrometer.set_wl(next_wl)
    c.cam.read()
    self.out.append(c.data_processor.detA_mean[16])
    self.sigStepFinished.emit()
```

Listing 1: Example plan which scans the spectrum in a given range for a number of given points.

that the plan itself has no responsibility in visualizing results.

4.3.2 GUI Layer

The third layer is the GUI layer. It has two parts: The first part, the main GUI, offers control widgets for the instruments and displays several basic plots: the detector means, their standard deviation, and the calculated signal. The second part of GUI are the plan views - custom windows visualizing the results of a plan while running - and plan configurations - dialogs in which the parameters of a plan are set. Communication of the GUI layer with other layers happens only through signals, e.g., when the spectrometer changes the wavelength it will emit its *sigWavelengthChanged* signal. The widget which displays the wavelength is subscribed to the signal and will update itself when the signal is emitted. Similarly, plans will emit a signal when a step is done to tell their subscribed plan view to update themselves.

Using this design makes MessPy portable and extensible, it is now used as the control program for four different ultrafast spectrometer setups. Only small per setup adjustments were necessary and design seems robust to extensions.

4.3.3 Supported Hardware

The drawback of Python when it comes to automation and control of lab equipment is the missing Python support by the manufacturers. While recently some manufacturers started to deliver Python modules, the majority still supplies only LabView- and C-APIs.

Shared C libraries, DLL-files in windows, can easily be called from Python, only a small wrapper module is enough. These wrappers either use the *cytpes*- or *cffi*-module to call the DLL. Both work by generating Python-callable functions from supplied function declarations of the C functions. The newer *cffi* can automatically parse C-header files[3] and has better error handling than *cffi*. Hence it is the now preferred way for new wrappers. Since there is no automatic memory management in C, necessary memory allocations have to be handled by the python code.

Surprisingly, a huge amount of equipment is still controlled via a serial connection, either via a hardware COM-port or by providing a Virtual COM port. Latter is commonly done by new USB based hardware. Serial-communication in Python is easily done with the *Serial*-package.

A list of the MessPy supported hardware is given in Table 4.1. Every device wrapper can be used outside of MessPy.

Table 4.1: Python packages included in MessPy to control lab hardware. The type annotates which package is used to communicate with the driver or the hardware.

Device Driver	Type
PI translation Stage	ctypes/cffi
Ocean Optics spectrometer	ctypes
Stresing CCDs	ctypes/cffi
Thorlabs CCD spectrometer	cffi
Thorlabs Shutter	Serial
Newport rotation stage	Serial
Faulhaber motor controller	Serial
Triax spectrometer	Serial
Shamrock spectrometer	Serial
Thorlabs CCD cam	cffi
CRI Shaper	Serial
NIDaqmx	package

[3] After they passed the C pre-processor or are manually prepared.

4.3.4 Signal Calculation

For the signal calculation in pump-probe, various schemes are proposed in the literature. The signal $S(\lambda, \tau)$ is wavelength and delay depended. Hence we calculate the signal for each channel and each delay point independently. In the following discussion, we drop the λ and τ arguments for readability.

The induced absorbance change is defined (Eq. (3.1)) as

$$S = -\log_{10}(I_p/I_0) + \log_{10}(I_u/I_0) = -\log_{10}(I_p/I_u), \tag{4.1}$$

where I_0 is the probe intensity without the sample, I_u the probe intensity with the sample and I_p is the probe intensity with the sample illuminated by the pump pulse. Assuming we record N-shots and the pump pulse is blocked every second shot, we have $N/2$-pumped and $N/2$-unpumped shots to calculate the signal. By taking the means, we get:

$$\langle I_p \rangle = \sum_{i=1,3,5,\dots}^{N-1} I[i]/\tfrac{N}{2} \tag{4.2}$$

$$\langle I_u \rangle = \sum_{i=2,4,6,\dots}^{N} I[i]/\tfrac{N}{2} \tag{4.3}$$

$I[i]$ here means the intensity of the i-th shot. If a reference detector is used, we divide each shot by the reference before taking the mean. By inserting the means into Eq. (4.1) we can calculate the averaged signal.

If often suggested to calculate the signal from every sequential pulse-pair independently and then taking the average of these values. Next I will show that this is not necessary, since the chopper already acts as a lock-in amplifier. This can be easily seen by expressing the intensity means above in terms of FFT-terms. The zero frequency component of an FFT is simple given by the mean

$$I_0 = \sum_{i=1,2,3,\dots}^{N} I[i]/N. \tag{4.4}$$

which equals to $I_0 = \langle I_u \rangle + \langle I_p \rangle$.

The fastest component has a frequency of N/2. Therefore it is given by

$$I_{N/2} = \sum_{i=1,2,3,\dots}^{N} I[i](-1)^i/N. \tag{4.5}$$

Similar to the mean this can be written as $I_{N/2} = 2(\langle I_u \rangle - \langle I_u \rangle)$. It follows directly that $\langle I_p \rangle$ and $\langle I_u \rangle$ can be expressed in terms of these two frequency components, therefore using a windows does not help since we already apply Fourier-filtering by using the chopper.

To test the hypothesis, I recorded the raw data of a mid-IR probe with a blocked pump-pulse, causing a known zero signal. Multiple schemes were tested on this dataset and neither did outperform the direct signal calculation presented above. Even for a medium amount of data all resulting signals look identical.

4.4 skultrafast

This section will be about the skultrafast package which contains a plethora of different approaches to fit and analyze data from ultrafast experiments. Because the package is not in a publishable state yet and may never be, this section will only describe the used algorithms instead of the describing the package in detail. Latter should be placed inside the package documentation, which is quite sparse.

4.4.1 Data Preprocessing

Part of package deals with preprocessing the data as is produced by MessPy. An array with the shape

(central wavelengths, channels, time points, detectors, scans)

is saved by *MessPy* . The array-shape is explained in Fig. 4.2, the colors of the axis captions are as in the description of the array dimensions above. The datasets for different central wavelengths will be merged as the last step. Hence the following steps are done for each of them in isolation. If the second detector was used for referencing, the detector signal is replaced by the referenced signal.

When doing polarization resolved measurements, we switch the pump polarization between every scan. This combined with simultaneous detection of both polarization allows for what we are calling *Iso-correction*.

Iso-correction is used to correct for two systematic error sources: the varying overlap of each probe beam with the pump (see Fig. 4.3) and the signal decay over multiple scans due to sample degradation.

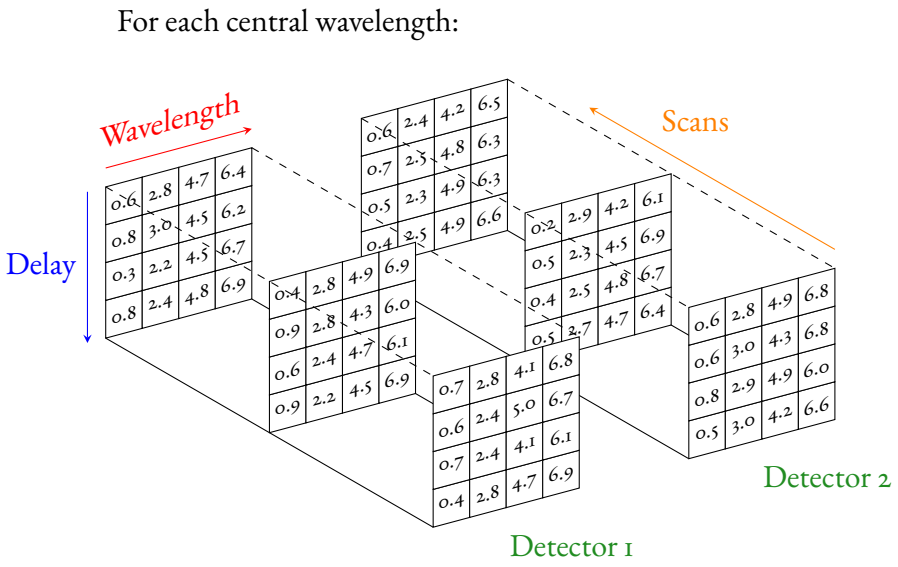

FIGURE 4.2: Graphical representation of the array as it is saved by MessPy. In the experiment, one full scan before switching to the next central wavelength. In polarisation resolved measurements, the pump-polarization is switched after finishing one scan for each central wavelength.

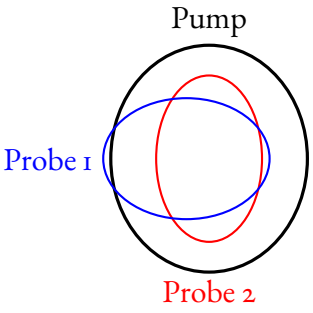

FIGURE 4.3: Schematic of the focal spots of the pump and two probe beams. Differences in the overlap of the probe spots with pump spots lead to differences in recorded signal strengths.

As the first step, we generate a characteristic spectrum for each scan, by taking the trimmed mean over a large time range. If no correction would be necessary, these spectra should be identical for equivalent polarizations. Now since we have two polarisation and two detectors, we end with n/2-scans for each of the four combinations:

$$\mathrm{det}_{1\parallel},\ \mathrm{det}_{1\perp},\ \mathrm{det}_{2\parallel},\ \mathrm{det}_{2\perp}.$$

To correct for sample degradation, we can scale each scan to the first scan of the set by simple using least squares to calculate c:

$$\min_c \left|\det(scan = i) - c \cdot \det(scan = 0)\right|^2$$

The subtraction here means that we subtract the spectra element wise. After scaling, we calculate the robust mean of scans for each dataset. With these, we construct the isotropic signal for each detector:

$$\mathrm{det}_{1\mathrm{iso}} = \frac{1}{3}\overline{\mathrm{det}_{1\parallel}} + \frac{2}{3}\overline{\mathrm{det}_{1\perp}}$$

$$\mathrm{det}_{2\mathrm{iso}} = \frac{1}{3}\overline{\mathrm{det}_{2\parallel}} + \frac{2}{3}\overline{\mathrm{det}_{2\perp}}$$

With these, we can determine the scaling factor d necessary to correct for the different overlap conditions of the two probe beams. With that, we can calculate of polarization depended signals by

$$\mathrm{sig}_{\parallel} = \mathrm{det}_{1\parallel} + d \cdot \mathrm{det}_{2\parallel}$$

$$\mathrm{sig}_{\perp} = \mathrm{det}_{1\perp} + d \cdot \mathrm{det}_{2\perp}$$

4.4.2 Chirp Correction

The Vis-pump Vis-probe setup uses a non compressed super continuum as the probe. This octave spanning probe already generated with a chirp and it acquires more when passing through optics and windows, causing different arrival times at sample for different wavelengths as is shown Fig. 4.4. The chirp is well described by a polynomial function of the frequency. Assuming a quadratic chirp, the time-zero for given wavelengths can be written as

$$t_0(\omega) = c_2\omega^2 + c_1\omega + c_0.$$

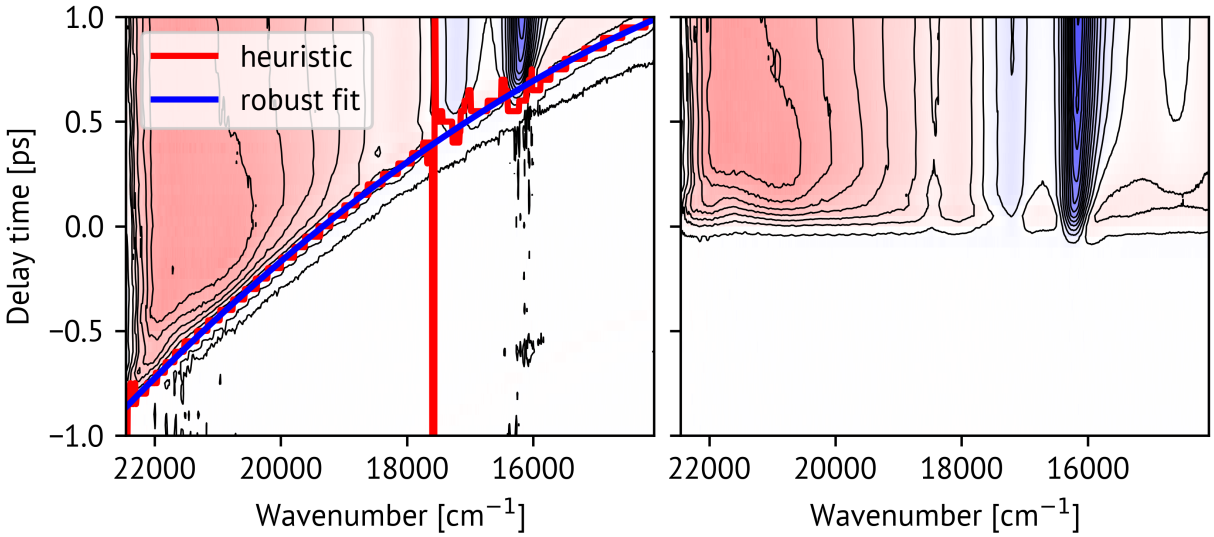

FIGURE 4.4: *Left*: Contour map of the non chirp correct data of Al-corrole probed by strongly chirped super-continuum generated in water. The applied heuristic (shown in red) selects the earliest point where the absolute signal above a given threshold. The robust quadratic fit (blue) also corrects for the discrete times found by the heuristic. *Right*: The resulting chirp corrected data. The time-zero is found with an error below 70 fs.

All relevant methods for the time-zero correction are found in the skultrafast sub-package *zero_finding*. The approach to find the unknown coefficients is the same as is presented in my diploma thesis:[4], To determine the polynomial coefficients, we will first use a heuristic to find a correct time-zero for all channels, resulting in a frequency versus time-zero point dataset. Since we are only using a heuristic which will fail for some channels, the polynomial has to be fitted to the dataset using a robust method which insensitive to outliers.

There are various choices for heuristic which work well for different data sets. E.g. if a pure solvent signal is measured, just determining the position of the signal maximum for each trace works well since the signal is dominated by coherent effects. I found that for regular samples with an reasonable SNR, using smallest time point where the absolute signal is over a given small value is solid heuristic. Using this heuristic systematically underestimates the time zero since it detects the beginning of the interaction and the resulting curve has to be shifted by a small amount.

In total skultrafast comes with four different functions to estimate the time-zero from a given trace: the already mentioned *use_first_abs*, returns the smallest index where signal is greater than a given limit. *use_diff* finds the index where the difference between to adjacent values is largest. Similarly, *use_gaussian* finds the index where the convolution with first derivative of a Gaussian has it biggest value. *use_fit* fits the trance with a convoluted exponential sum and optionally a gaussian and its derivatives, which simulate the coherent contributions when the pulses are overlapping. The time-zero is a free parameter of the fit. In addition to the given heuristic the user can supply its own.

For determining the polynomial coefficients from the heuristic time-zero estimates, I switched from the *RANSAC*-algorithm[5] to the robust fitting methods provided by the python package *statsmodels*[6]. Instead of minimizing the sum of squares of the residuals, in which outliers have a strong in-

[4](21) Stenstitzki, T. „Polarisationsaufgelöste Femtosekundenspektroskopie an Aluminium-Corrolen“. 2010.

[5](24) Fischler, M. A. & Bolles, R. C. „Random Sample Consensus: A Paradigm for Model Fitting with Applications to Image Analysis and Automated Cartography“. 1981.

[6](25) Seabold, S. & Perktold, J. „Statsmodels: Econometric and Statistical Modeling with Python“. 2010.

fluence on the fit, it minimizes the Huber-norm. The Huber norm is quadratic for small residuals and linear for large residuals. The advantage over *RANSAC* are an increase of speed and stability.

The resulting coefficients can be used in two ways: Either use them to rebin or interpolate the 2D-spectra, as is shown in the Fig. 4.4, or treat the dispersion coefficients as parameters of the global fit and use the found values as their initial guess.

4.4.3 Exponential Modelling

The most common approach to fit time resolved spectroscopy data is to use an exponential model. The rationale to use an exponential model is the assumption, that the observed data is a product of n-distinct states where the spectra and transition probabilities between the states are assumed to be time independent and unidirectional. Hence, the problem is described by first order differential equations:

$$\vec{c} = K\vec{\mathbf{c}} \tag{4.6}$$

$\vec{\mathbf{c}}$ represents the population of the states, while K is the matrix which elements K_{ij} describe the transition rates between the states. For a given starting point $\vec{\mathbf{c}}_0$, the solution of such ODE problem is always given by the matrix exponential:

$$\vec{\mathbf{c}}(t) = \exp(Kt) \cdot \vec{\mathbf{c}}_0 \tag{4.7}$$

The elements of the solution vector are built from expontial decay terms. There are at most dim(K)-different exponential terms. For complicated models direct computation of the matrix exponential is not straight forward, hence it best done by a computer[7] or solve the ODE numerically.

To model the finite system response, the exponential model function, which is zero for negative delay times has to been convoluted with the instrument response function (IRF).

$$f(\omega, \tau) = \sum_{i=0}^{n} C(\omega, \tau) IRF \otimes \exp^{\frac{-(t-t_0)}{\tau_i}} \tag{4.8}$$

In fs-pump-probe experiments a Gaussian function is commonly used to model the IRF. This choice has two main advantages: First, the result of the convolution can be expressed in terms of the error function, which can be directly computed, therefore making a full convolution computation unnecessary:

$$\text{folded}\exp(t, A, \tau, \sigma) = A \exp\left(\sigma^2/\tau^2 - t/\tau\right) \cdot \frac{1}{2}\operatorname{erfc}(-t/\sigma + \frac{\sigma}{2\tau}) \tag{4.9}$$

Secondly, the IRF is determined by a single parameter ω, which can be treated as a free parameter of the function.

Variable Projection

For a N pixel detector, the model described above has at least $N \times k + k$ free parameters, where k is number of exponentials. For modern CCD detectors, N can easily go above 1000, which for $k = 4$ gives 4004 free parameters. This is above the capabilities of normal fitting routines, which with some trickery, can solve up to 1600 parameters in several minutes. By using the variable projection (also called separable nonlinear least squares), even the problem with 4004 free parameters can be solved in few seconds. A full introspection of application of this method for the modelling of time-resolved spectra can be fund in Kate Mullen Thesis[8].

The method works by fitting the linear and nonlinear parts independently: For given decay times, the least squares problem reduces to a linear least squares problem, since only the determination of the coefficients $C(\omega, \tau)$ is left open: If we define the Matrix A as

$$A_{ij} = \exp\left(t_i, tau_j\right) \tag{4.10}$$

the problem of fitting the given exponentials to a single transient can now ne reformulated as

$$\min_{c} \quad \left|\vec{\mathbf{y}} - \mathbf{A}\vec{\mathbf{c}}\right|^2, \tag{4.11}$$

where the $\vec{\mathbf{y}}$ is defined with $y_i = y[t_i]$ is the recorded data. The method generalizes for every regression problem where the model function can be expressed as a sum of terms:

$$y(\vec{\mathbf{x}}, \vec{\mathbf{c}}, \vec{\theta}) = \sum_i c_i f(\vec{\mathbf{x}}, \vec{\theta}),$$

[7] (26) Moler, C. & Van Loan, C. „Nineteen Dubious Ways to Compute the Exponential of a Matrix, Twenty-Five Years Later". 2003.

[8] (27) Mullen, K. M. „Separable Nonlinear Models: Theory, Implementation and Applications in Physics and Chemistry".

with $\vec{\mathbf{x}}$ being the independent variable (e.g. the delay times), $\vec{\mathbf{c}}$ the linear coefficients and $\vec{\theta}$ the non-linear variables of the function. The generalized form of Eq. (4.10) is then

$$A_{ij} = f_j(x_i, \vec{\theta}). \tag{4.12}$$

Notice that each term can depend on an arbitrary nonlinear parameters and parameters can be shared between multiple terms.

While a nonlinear least squares problem can only be solved by iterative approaches, a linear least squares solution can be calculated directly. Hence, only the nonlinear parameters will be minimized by a iterative algorithm. From these, the basis matrix A can be calculated and the coefficients c can be determined in addition to the resulting residuals, which are returned to the nonlinear minimization algorithm as residuals of the current nonlinear parameter set.

Assuming that the matrix of the k exponentials doesn't change between different transients, the full linear least squares problem of all transients is solved computational cheaply by calculation of the pseudo-inverse $A^\dagger$. With given pseudo-inverse, solving the problem for a single channels reduces to matrix multiplication with $A^\dagger\vec{\mathbf{y}}$. The assumption above is valid when a) the time-points and time-zeros of the channels is identical and b) the IRF is the same. We can achieve a) by re-binning or interpolation after chirp correction, for b) we just use the approximation that the IRF is mostly determined by the pump-duration, hence the changes for different wavelengths should be negligible.

The least squares problem with a sum of exponentials as fitting function is numerical unstable since the matrix containing the exponential matrix is almost singular. The solver regularly finds minima where two decay constants are converging to a single value while the corresponding amplitudes explode. Normally, this is circumvented by carefully tuning the starting parameters, which takes its time. By using a L1-penalized solver for the linear least squares eliminates the problem almost completely. Only if too many exponentials are chosen, it shows up, but even in this case the fit routine aborts much earlier than without regularization.

A summary of the minimized function is given in Listing 2. Various steps are taken in skultrafast to accelerate the function. Most importantly, the resulting basis array is cached and only necessary columns are updated. This feature is very useful since we are not supplying a derivative of the function to the solver. Instead, the solver estimates the derivative by finite differences, which are calculated by just changing one variable. If the changed variable is a decay constant, only one column needs to be updated. Skultrafast can use different backends for the calculation of the basis functions: while the default backend just uses numpy functions, the OpenCL backend provides GPU[9]-accelerated functions. Depending on the system, this can result in a tenfold speed increase. Also, instead of using the provided complementary error functions (*erfc*-), we use a less accurate but faster version, giving a twofold speed increase in the evaluation. The error of less than 0.0001 is negligible for our purpose. The acceleration steps are only crucial when modelling the dispersion explicitly.

```
alpha = 0.00001
def fit_function(non_linear_parms, data):
    basis = update_basis(non_linear_params)
    all_residuals = [] #empty list
    for trans in data:
        coef = solve_lstsq(trans, basis,
                           alpha)
        model = np.dot(basis, coef)
        resiudals = model - trans
        all_residuals.append(residuals)
    return all_residuals
```

Listing 2: Pseudo-code describing the fit function given to the nonlinear minimizer. The function which calculate the exponentials from the nonlinear parameters is called `update_basis` to emphasize the use of caching. If the dispersion is modelled explicitly, the basis calculation has to be done in the for-loop, since each transient has its own time-zero.

Advantages and Disadvantages

There are good reasons exponential modelling is the standard method for analysing time-resolved spectra. It is straightforward to do and computationally cheap and it gives a sensible summary of the whole dataset. The downsides are that the number

[9] Graphical Processing Unit

of components is not known a priori and that the necessary conditions for exponential modelling are violated in ultra-fast spectroscopy, since the spectra itself evolve in time and processes can have ballistic behaviour.

The downsides can amplify each other, as the processes which are not modelled perfectly by exponentials resulting in bogus extra exponentials[10]. The problem is exemplified in Fig. 4.5. Here, I simulated a dataset consisting of a stationary negative-band and a shifting positive band (both gaussian). The positive band is exponentially red-shifting with a time-constant of 10 ps. The amplitude of the shift is 10 cm^{-1}. Shown are the residuals and the decay-associated spectra for fits with one and two exponentials. The single exponential fit has clearly systematic errors, which only vanish if we add another exponential. For larger shifts, even more exponentials would be necessary. The last row shows that the problem is not visible for lower SNRs. From the singular values we see that at least 2 components are necessary (the constant component can be added two one of them) if we want model the two dimensional spectrum as an outer product of a spectrum and a transient.

While it is possible to fit a kinetic model to data, it is also important to emphasize that this model is not unique solution and there other models fitting the data equally well. Therefore we only use decay associated spectra (DAS), which can be taught of a parallel decay model since they describe the data without additional assumptions.

4.4.4 Lifetime Density Map

Another approach to fit an exponential sum onto a dataset is the so-called lifetime density map (LDM). Basically it uses the same idea as the Discrete Fourier Transformation,but instead of determining the amplitudes of oscillations we calculate the amplitudes of exponential decays.

The one dimensional DFT can be thought of as the least squares (LSQ) problem:

$$\min_x (\mathbf{A}\vec{\mathbf{x}} - \vec{\mathbf{y}})^2 \tag{4.13}$$

Here, A is the so called DFT-matrix. Every column contains a different sinusoid:

$$\mathcal{A}_{k,n} = e^{i2\pi kn/N}$$

For the DFT, the data is assumed to be equidistant, hence n/N can be interpreted as a time $t[n] = n$ and $2\pi k/N$ as a frequency $\omega[k]$. The vector $\vec{\mathbf{y}}$ is the dataset we want to express as a sum of sinusoid, which amplitudes $\vec{\mathbf{x}}$ we want to find. In the case of standard DFT N is equal $\dim\vec{\mathbf{x}}$. If N is smaller than $\dim\vec{\mathbf{x}}$, only the least squares formulation is valid since the problem is overdetermined. The solution to this forumlation is called Lomb-Scargle periodogram.

For the LDM, every row-vector is a different exponential decay.

$$\mathcal{A}_{k,n} = \exp(-t[n]/\tau[k])$$

In the case of the DFT, the column vectors form a complete orthonormal basis, hence the coefficients can be directly calculated by simple multiplication. This is not the case for a matrix build from exponential vectors: neither is their spanned space complete, nor is the basis orthogonal. Actually such a matrix is very badly conditioned. Therefore, simply solving the LSQ-problem does not work. To make the problem solvable one has to add penalty terms to the objective:

$$\min_x \qquad \left|\mathbf{A}\vec{\mathbf{x}} - \vec{\mathbf{y}}\right|^2 + \alpha_{L2}|\vec{\mathbf{x}}|^2 + \alpha_{L1}|\vec{\mathbf{x}}|$$

This technique is known as regularization. Using only the first term corresponds to Tikhonov-regularization, also called ridge-regression or L2-regression. The second term is associated with L1-regression, also known as Lasso. The combination of both terms is called elastic net. In the following we will use the terms L1- and L2-regression.

The introduction of penalty terms to least squares objective can be interpreted as a prior on the solution space. L2-regression equals to the assumption of a Normal distribution of coefficients, while L1-regression assumes a Laplace prior. Both distributions are compared in Fig. 4.6. As can be seen in the figure, the Laplace distribution prefers sparse solutions more than the normal distribution, while both prohibit large solutions.

[10] (28) Marciniak, H. & Lochbrunner, S. „On the Interpretation of Decay Associated Spectra in the Presence of Time Dependent Spectral Shifts“. 2014.

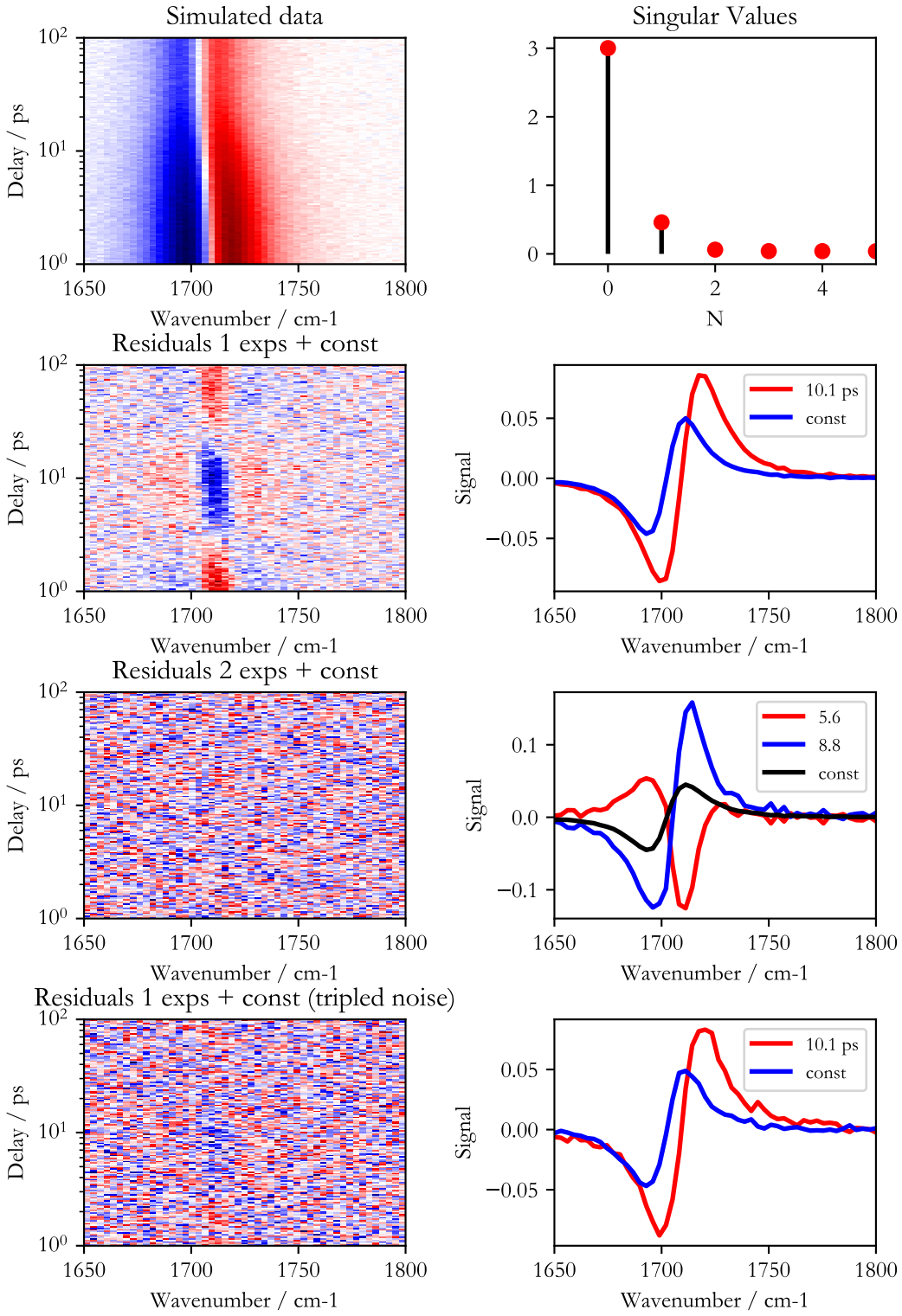

FIGURE 4.5: Exponential modelling of a shifting peak. *Top left*: Colormap of the simulated data set. *Top right*: First singular values of the dataset. *Second row*: Residuals and DAS for a single exponential. *Third row:* The the same for two exponentials. *Bottom row*: The same as in the second row, but for a dataset with additional noise.

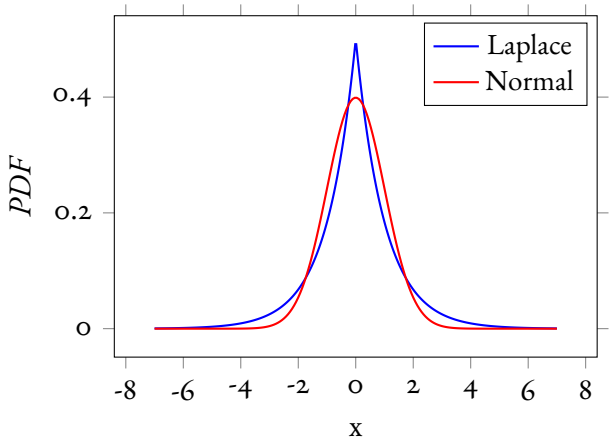

FIGURE 4.6: Probability density functions of the Normal- and Laplace-distribution. The main difference is the behavior near zero, where the normal distribution is flat and the Laplace is the steepest. Therefore, an exact zero is more likely in L1- than in L2-regression.

The choice of the regularization value is important: Too small, the data gets overfitted and the solution has meaningless coefficients. Too large, the resulting fit is bad. Both is shown in Fig. 4.7. Hence, we are looking for largest alpha which still generates good fit to the data. For the shown dataset, one would select the alpha value belonging to the black curve, since smaller values don't increase the quality of the fit, while larger values clearly tend to have systematic errors. There are various methods to automate the process via cross-validation by comparing the root-squared residual sum for different alphas. In practice, simply trying out few value works very well. If the SNR is similar for all channels, the same value can be applied.

In summary, to generate a lifetime density map, we first have to generate an array of exponential decays[11]. Their decay times should be equally distributed on a logarithmic scale spanning the observed time range. Next, we solve the regularized linear model with an appropriate value of alpha. This is repeated for all wavelength. The resulting solution vectors build up the lifetime density map.

As mentioned above, in Fig. 4.7 the results of L1 and L2-regression are compared for a single simulated dataset. One can easily see that the advantages of the L1-regression: it is easier to when overfitting starts and the actual solution is simpler to interpret because it is sparser. The main drawback is the different speed of the methods: L2 regression can be formulated as a standard least squares problem, therefore it can be solved directly. For solving a L1 problem, a slower iterative method has to be used instead.

Originally, the first application of Tikhonov-regularization for fitting time-resolved spectroscopic data was developed by the Holzwarth[12], the same group which also proposed exhaustive search for calculating error bars on time constants. Being critically, the original paper is very hard to reproduce since it presents the procedure as a modification of the Levenberg-Marquardt algorithm, which adds a lot of unnecessary complexity. Positively, they added a smoothness condition to their approach by penalizing differences between to neighbouring channels.

A closed implementation from is available in Optimus[13]. Recently, the group of van Thor published their own open source implementation, the accompanying paper gives a good overview over the history of the development and application of LDM[14]. My inspiration came from Groma et al.[15], who applied L1-regularized LDM to time-resolved fluorescence data.

Like global analysis, they share their own set of problems: a spectral shift is still not well modelled. Multiple exponentials can merge into one, when the SNR is not good enough and the time constants are in a similar range. Shifting peaks can be identified by diagonal lines in the map.

4.5 Summary

- A short opinion piece about the problem of software in sciences was given.

[11] Of course, one also can use exponentials convoluted with the IRF.

[12] (29) Holzwarth, A. R. „Data Analysis of Time-Resolved Measurements". 1996.

[13] (30) Slavov, C., Hartmann, H. & Wachtveitl, J. „Implementation and Evaluation of Data Analysis Strategies for Time-Resolved Optical Spectroscopy". 2015.

[14] (31) Dorlhiac, G. F., Fare, C. & van Thor, J. J. „PyLDM - An Open Source Package for Lifetime Density Analysis of Time-Resolved Spectroscopic Data". 2017.

[15] (32) Groma, G. I., Heiner, Z., Makai, A. & Sarlós, F. „Estimation of Kinetic Parameters from Time-Resolved Fluorescence Data: A Compressed Sensing Approach". 2012.

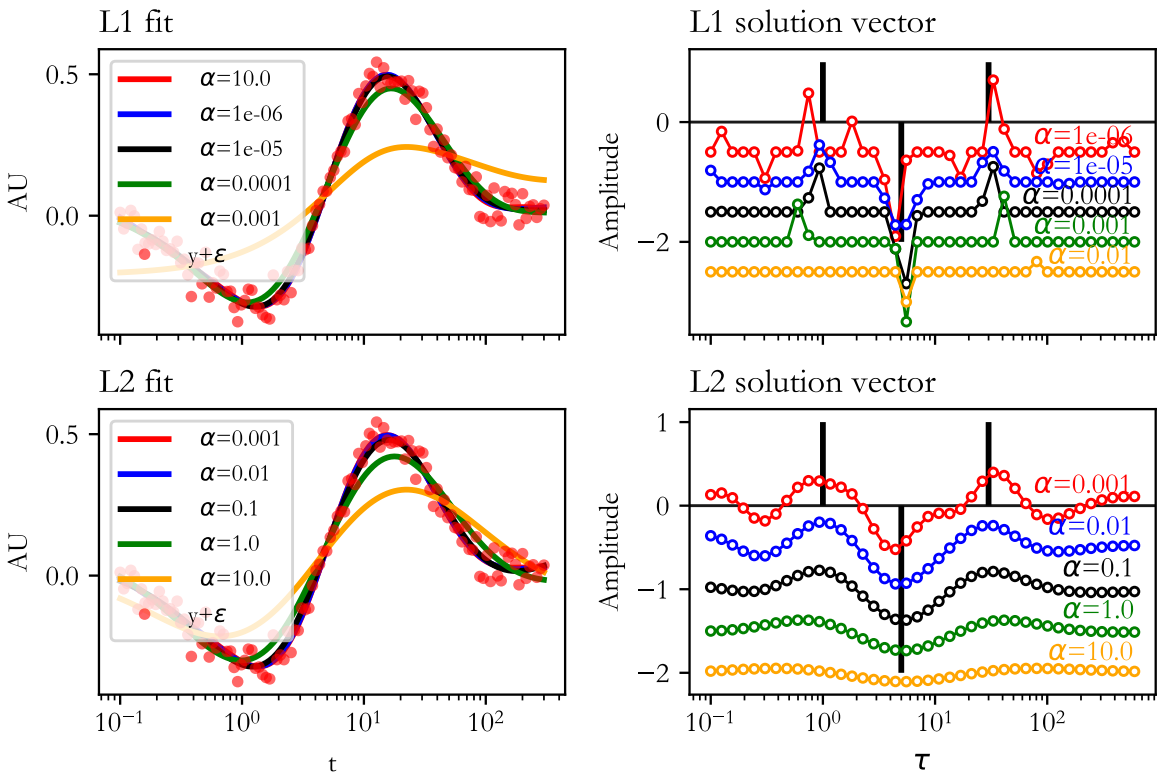

FIGURE 4.7: Comparison of lifetime extraction by L1- and with L2-penalized regression. On the left, a simulated dataset (red points) and fits of it (colored lines) for different values of α are shown. The resulting coefficients, offset for clarity, are shown left. In this graph, the black bars show the true values of exponential amplitudes used in the simulation. It can be seen, that using a penalty too large leads to poor fit and using a penalty too small leads to additional model complexity without improving the fit.

- Proposal of minimal set of best-practices for software in sciences, consisting of a popular programming with a strong scientific ecosystem, a modern version control system, and a strong focus on modularity of the code. A pragmatic choice of tools are Python as the programming language with Git as the version control system.
- Overview of the design of MessPy, the software which controls the different spectrometers in the group. It is separated into three layers: the instrument driver layer, the control layer and the GUI layer.
- The signal calculation and data preprocessing pipeline is summarized.
- An exponential sum is used to the fit data. Variable projection and other simplifications are used to accelerate the computation.
- The exponential model is not ideal for ultrafast spectroscopy since it neither models band-shifting or band-narrowing well.
- Lifetime-density mapping via regularized least-squares is an alternative approach.

Chapter 5

The Initial Photoreaction of Aluminium Corrole

This chapter is about our results on the photoreaction of brominated aluminum corrole[1]. Of the different photoreactions studied in the thesis, corrole has the simplest one. It completely follows the example reaction shown in Fig. 2.7.

The work presented in the article is a continuation of my previous work on corroles, which begun in my diploma thesis[2]. I found that the addition of Br to Al-corrole induced an intersystem crossing with a time constant of approx. 100 ps. The Soret to Q-band transition, due to overlapping coherent artifacts was not fully resolved.

Hence, we repeated the Vis-pump Vis-probe measurements with an extended spectral window and did complementary Vis-pump IR-probe measurements, observing the full region of the ν(C=C)-bands. To get a complete picture, femtosecond broadband fluorescence upconversion measurements were done at Ernstings group in collaboration with Mario Gerecke. While these didn't make it into the paper, they were helpful to confirm our findings.

The same collaboration resulted in another paper, where we combined time-resolved fluorescence and absorption data to elude the photo-physics of antimony corrole[3].

The chapter starts with a description of corroles before dicussing their possible applications. Most of these applications tightly depend on the photophysics of corroles, which are introduced next. The chapter ends with a description of the goals of experiments and a summary of the paper.

5.1 Corroles

Corroles are a class of inorganic cyclic aromatic tetrapyrroles. The name is based on its similarity to Corrin, the core of vitamin B12. The skeletal structure of corrin is almost identical to corrole, but the small differences lead to entirely different conjugated systems. The aromatic corrole is, therefore, more alike porphyrin. All three structures are compared in Fig. 5.1.

Compared to porphyrin, corrole is missing one carbon atom between two of the pyrrole-rings, leading to a smaller cavity in middle and to a reduced D_{4H}-symmetry of corrole compared to the C_{2v}-symmetry of porphyrin. Additionally, the shorter ring increases the number of hydrogen atoms in the cavity from two to three.

While corroles were discovered half a century ago - in 1960 by Johnson and Kay[4] - their research progressed only slowly until the turn of the mil-

[1] (2) Stensitzki, T., Yang, Y., Berg, A., Mahammed, A., Gross, Z. & Heyne, K. „Ultrafast Electronic and Vibrational Dynamics in Brominated Aluminum Corroles: Energy Relaxation and Triplet Formation". 2016.

[2] (21) Stenstitzki, T. „Polarisationsaufgelöste Femtosekundenspektroskopie an Aluminium-Corrolen". 2010.

[3] (6) Zahn, C., Stensitzki, T., Gerecke, M., Berg, A., Mahammed, A., Gross, Z. & Heyne, K. „Ultrafast Dynamics of Sb-Corroles: A Combined Vis-Pump Supercontinuum Probe and Broadband Fluorescence Up-Conversion Study". 2017.

[4] (33) Johnson, A. & Price, R. „The Synthesis of Derivatives of Corrole (Pentadehydrocorrin)". 1960.

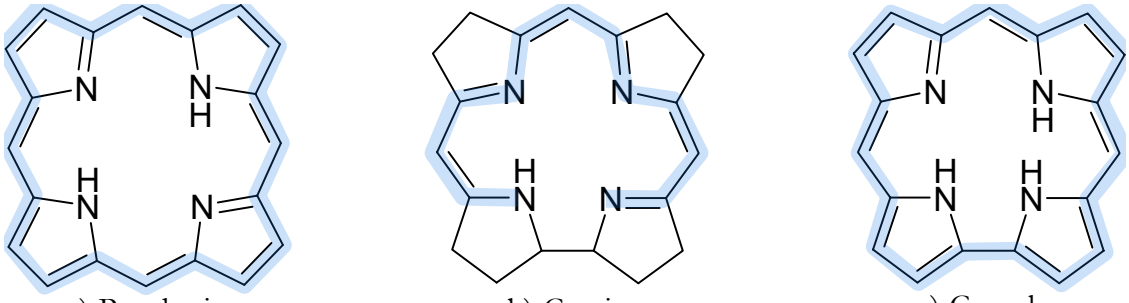

a) Porphyrin b) Corrin c) Corrole

FIGURE 5.1: The basic ring structures of porphyrine, corrin and corrole. The conjugated systems are marked in blue.

lennium, since no effect synthesis path was known. This changed in 1999: efficient synthesis-reactions were found simultaneously by Gross[5] and Paolesse[6].

The discovery renewed the interest in corroles, which lead to the development of a plethora of corrole based applications, which will be discussed below. Even before 1999, research revealed many of the exciting properties of corroles. Most importantly, they can stabilize unusually high oxidation states of their metal ion ligands, like iron(IV), cobalt(IV) and cobalt(V), compared to porphyrin. This makes corrole an interesting and promising platform for organometallic chemistry. Their strong excitation coefficient and high fluorescence yield combined with their versatility to additions to the ring make them attractive candidates for many photo-based applications.

Recently, the generation of air-stable corrole radicals was reported.[7]

5.2 Corrole Applications

The review from Aviv and Gross gives a good overview of corrole based applications[8]. Broadly, they can be divided into two classes: either they make use of their transition-metal ligands as a catalyst, or they make use of their optical properties. The former includes oxidation reactions, reduction catalysis, group transfer catalysis. The latter include the use of corrole as an optical sensor, as a dye for sensitized solar cells and as a photosensitizer for cancer treatment.

So far, Corrole based optical sensors mostly use cobalt- or free-base corroles, since their fluorescence and absorption spectra are sensitive to their surroundings. The free-base corroles have a pH-dependent visible spectrum, because the number of H-atom in cavity influences the electronic structure and changes with the pH. Cobalt-corroles can react reversibly with CO and other small molecules, which agains lead to spectral changes.

In dye-sensitized solar cells, the dye is used as an electron donor for a titan dioxide semiconductor. In combination with an electrolyte – usually iodide/triiodide - connected to the TiO_2, from which the dye can be reduced back into the ground-state, light is converted into an electric current. The critical parameters of the dye are their absorption strength, the HOMO to LUMO-gap and the coupling between the acceptor and donator-states.

The few published experiments on corroles used a dye in solar cells are not yet very promising: the reported photo-currents are low. Here, femtosecond time-resolved studies could help to dissect the problem: the time-resolution must be high since the charge injection is believed to happen on a sub-ps timescale.

Lastly, corroles are a promising photosensitizer (PS) for cancer treatment via photodynamic ther-

[5](34) Gross, Z., Galili, N. & Saltsman, I. „Erste Direkte Synthese von Corrolen Aus Pyrrol". 1999.

[6](35) Paolesse, R., Mini, S., Sagone, F., Boschi, T., Jaquinod, L., Nurco, D. J. & Smith, K. M. „5,10,15-Triphenylcorrole: A Product from a Modified Rothemund Reaction". 1999.

[7](36) Schweyen, P., Brandhorst, K., Wicht, R., Wolfram, B. & Bröring, M. „The Corrole Radical". 2015; (37) Yadav, P., Rathi, P. & Sankar, M. „Facile Generation of A2B Corrole Radical Using Fe(III) Salts and Its Spectroscopic Properties". 2017.

[8](38) Aviv, I. & Gross, Z. „Corrole-Based Applications". 2007.

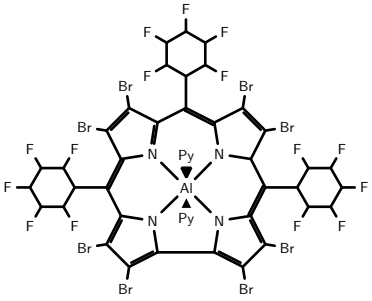

FIGURE 5.2: Structure of hexacoordinated brominated Aluminum Corrole.

apy (PDT)[9]. In PDT the PS is accumulated in cancer affected cells. The PS in the cells is then illuminated to generate singlet-oxygen, which kills the unhealthy cell by its reactivity. Therefore, the PS must have a low toxicity and must be amphipolar (solvable in polar and non-polar solvents). For corroles, latter can be archived by adding SO_3-groups to the corrole. Important photophysical parameters of the sensitizers are the absorption wavelength, the triplet yield, and the singlet-oxygen yield. All three parameters can be modified via changes to the corrole.

As these examples show, corroles are tuneable for a specific application. Designing the ideal corrole for a particular application is only possible when the effect of additions and substitutions is well known. Consequently it is necessary to study and compare the photophysics of different corroles.

5.3 Photophysics of Corroles

In contrast to porphyrins, the photoreactions of different corroles are only covered by few studies (see the references in the paper). Research so far is mostly concentrated on gallium- and aluminum-corroles, which can be seen as "model" corroles, similar to the status of Zinc-porphyrin.

Two bands describe the visible spectrum, the weaker Q-band around 600 nm and the strong Soret-band around 440 nm. In corroles, the reduced symmetry compared to porphyrin lifts the degeneracy of the two Q-band transitions[10]. Additionally, the Q-bands shows visible vibronic progression with a frequency of 1350 cm^{-1}.

Excitation of the Soret-band is often followed by a relatively slow internal conversion to the Q-band, resulting in detectable Soret-band fluorescence. The fluorescence decay times for these corroles are in the nanosecond range, in some cases limited by a co-occurring intersystem crossing. The transient absorption spectra of corrole in the visible show a strong and broad excited state absorption located between the Soret- and Q-band. This broad excited state absorption only shows minuscule changes on state-transitions. Time-resolved IR measurements on corroles are almost not existent outside of our group.

5.4 Aim of the Study

The subject of the presented study was brominated Al-corrole, as is shown in Fig. 5.2. The aim of the study was two folded:

a) The photoreaction of normal Al-corrole after excitation in the Soret-band is well researched by visible transient spectroscopy. Hence, if we see differences in the brominated corrole photoreaction, we can attribute them directly to the bromination of the corrole macrocycle and therefore characterize the effects of the addition.

b) The application of Vis-pump IR-probe spectroscopy to a corrole with an known observable intersystem crossing: From comparison of the triplet and singlet spectra, we wanted to identify marker bands sensitive to the spin state. We hope to apply our findings to the non-brominated Al-corrole, where the decay channel into the triplet manifold is not yet identified, despite being able to produce singlet oxygen.

5.5 Summary

- We applied femtosecond Vis-pump Vis-probe and Vis-pump IR-probe spectroscopy to brominated Al-corrole.
- The addition of Br leads to faster conversion from the Soret-band to Q-band. Instead of the

[9] (39) Teo, R. D., Hwang, J. Y., Termini, J., Gross, Z. & Gray, H. B. „Fighting Cancer with Corroles". 2017.

[10] (40) Yang, Y. *et al.* „Assignment of Aluminum Corroles Absorption Bands to Electronic Transitions by Femtosecond Polarization Resolved VIS-Pump IR-Probe Spectroscopy". 2012.

500 fs it takes for non brominated Al-corrole, it only needs 200 fs.

- The Soret- to Q-band transition is followed by cooling dynamics on a picosecond timescale. They show as shifting and narrowing of the stimulated emission in the visible and of the excited state absorption in the IR.
- The addition of the Br leads to a decay of the stimulated emission with 100 ps, which can be safely attributed to ISC, resulting in a triplet yield near 1.
- The triplet state has characteristic vibrational bands at 1480 cm^{-1} and 1505 cm^{-1} usable a marker bands of the triplet state.

Chapter 6

The Initial Photoreaction of the Phytochrome Cph1

This chapter is about the photoreaction of phytochrome, a very import photosensor protein found in almost all plants and in many bacteria. In the included article[1], we elude the photoreaction of Cph1 in Pr-state.

The chapter begins with an introduction of the phytochrome protein, followed up by a slightly deeper introduction to the photoreaction of the phytochrome. Next, the aim of the included paper will be listed, before ending the chapter with a summary.

6.1 Phytochrome

Phytochrome is a ubiquitous photosensor protein found in many organisms. They are responsible for mediating the photo-response. In plant, phytochromes are believed to regulate seed germination, seedling deetiolation, shade avoidance responses and flowering[2]. In bacteria, phytochrome was among other things found to be part of the phototaxis and regulating the accumulation ratio of red and green pigments[3].

Commonly conserved over the different phytochromes are the PAS-, GAF- and the PHY-domain, which are the photo-sensory core of the protein. The structure of Cph1[4], consisting of these three domains, is shown in Fig. 6.1. The exact interplay between these domains is still not clear. Recent studies[5] suggest that the photoreaction triggers a folding of beta-sheets connecting the GAF and PHY-domain, shorting the distance between the two domains.

A commonly shared feature of phytochromes is its covalently attached bilin photoreceptor in GAF- or PAS-domain, absorbing at the red edge of the visible spectrum. The exact structure of the chromophore varies slightly between plant-, fungi- and bacterial phytochromes. In all cases, it is believed that initial photoreaction involves rotation of the ring D around the C15=C16 double bond of the chromophore[6] (see Fig. 6.2). It is believed that the rotation induces changes to the hydrogen-bond network which facilitate further changes in protein.

Most phytochromes have two thermodynamically stable states, the red-absorbing Pr-state and the far-red-absorbing Pfr-state. Normally, one of the states is the signalling state, which slowly re-

[1] (4) Stensitzki, T., Yang, Y., Wölke, A. L., Knapp, E.-W., Hughes, J., Mroginski, M. A. & Heyne, K. „Influence of Heterogeneity on the Ultrafast Photoisomerization Dynamics of Pfr in Cph1 Phytochrome". 2017.

[2] (41) Rockwell, N. C. & Lagarias, J. C. „A Brief History of Phytochromes". 2010.

[3] (42) Sharrock, R. A. „The Phytochrome Red/Far-Red Photoreceptor Superfamily". 2008.

[4] Phytochrome of Cyanobacterium Synechocystis Stamm PCC6803

[5] (43) Takala, H. *et al.* „Signal Amplification and Transduction in Phytochrome Photosensors". 2014; (44) Nagano, S. „From Photon to Signal in Phytochromes: Similarities and Differences between Prokaryotic and Plant Phytochromes". 2016.

[6] (45) Yang, Y. *et al.* „Real-Time Tracking of Phytochrome's Orientational Changes During Pr Photoisomerization". 2012.

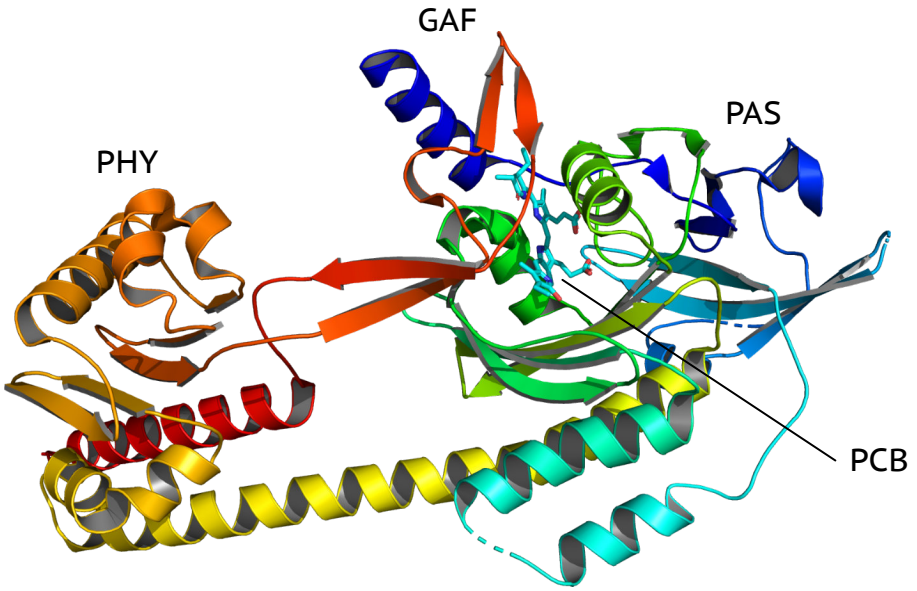

FIGURE 6.1: Cartoon of the 2VEA structure of Cph1 in the Pr-state. Shown are the three domains of the sensor-module, PAS-GAF-PHY. The photoreceptor phycocyanobilin (PCB) is cyan coloured. Recent studies suggest that the Pr to Pfr reaction leads to folding of the β-sheets between the GAF- and PHY-domain.

verts back to the non-signaling state. As shown in Fig. 6.2, interconversion between the two states can be induced by light-absorption, hence the signaling of phytochrome is sensitive to the relative intensity of red and far-red light.

However, the yield of the photoreaction is generally low in phytochromes compared to retinal proteins. If the low yield is due to heterogeneity of the two ground-states or due to the nature of excited state reaction-pathway is still heavily debated.

6.2 Aim of the Study

It is now general consensus that the Cph1 Pfr-state is heterogeneous. This was shown by resonance-raman, pump-probe-, pump-dump-probe-, NMR- and IR-spectroscopy. These subpopulations are called Pfr-I and Pfr-II. However, it remains unclear whether the spectroscopic variations due to structural heterogeneity influence the photoreaction. To elude the question we applied femtosecond polarization resolved Vis-pump IR-probe and Vis-pump Vis-probe spectroscopy to isotopically labeled Cph1 combined with quantum chemical calculations. In contrast, most published ultrafast spectroscopic studies on phytochrome relied on visible spectroscopy, which is not very sensitive to structural differences. In addition, attribution of the electronic spectral features is difficult through overlapping contributions. To combat this problem, we expanded our spectral window up to 1000 nm.

The aim of the study of was to detect signs of heterogeneity in the Pfr-state. If so, can we attribute specific dynamics to the different sub states and does the heterogeneity influences the reaction yield. Can the data be explained by theoretical calculations?

6.3 Summary

- We successfully applied Vis-pump IR-probe and Vis-pump Vis-probe spectroscopy to isotopically labelled Cph1.
- Comparable time constants where found in the electronic and the vibrational spectra.
- In the IR-data, a picosecond decay component could be attributed to single sub-state. Since the DAS of the component shows bleach recovery, we conclude that the yield

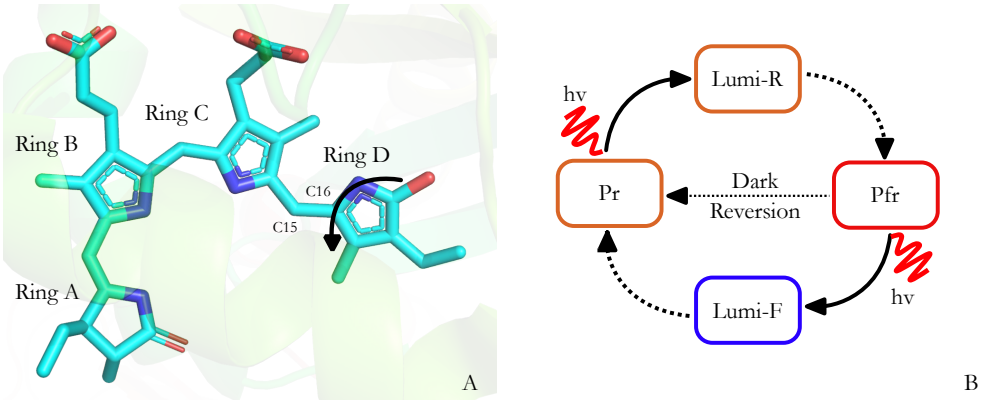

FIGURE 6.2: A) The photoreceptor PCB of Cph1 in more detail. Upon light absorption, ring D rotates. B) The photocycle of Cph1. The Pr-state is the non signaling state populated in the Dark. Light excitation of Pr-state leads to photoproduct Lumi-R, which further develops into the Pfr-state. The signaing Pfr-state dark-reverts into the Pr-state. The reversion can be accelerated by illumination with far-red light.

differs between the sub-states. The two states most likely differ in the orientation of ring D.

- Through band fitting of the polarization resolved DAS spectra and comparison of the result with the theoretical models we assign the two different states to an active and an inactive state. Latter can be converted to the former by light.

Chapter 7

The Initial Photoreaction of Channelrhodopsin 1

7.1 Introduction

This chapter describes the work we have done to elucidate the primary photoreaction of Channelrhodopsin I (ChR1)[1] from *Chlamydomonas augstea*. The chapter start by introducing channelrhodopsin and its potential applications, before summarizing the prior work done on the photoreaction of ChR. It than follows up with explaining the aims of included papers, before presenting additional unpublished work.

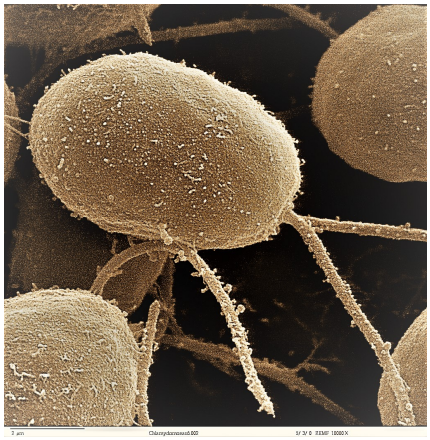

FIGURE 7.1: Scanning electron microscope picture of *Chlamydomonas reinhardtii*.

7.2 Channelrhodopsin

Channelrhodopsins are sensory photoreceptor proteins in unicellular algae functioning as light-gated ion channels and are controlling the light response of the organism[2].

The protein was discovered simultaneously by three the groups of Takahashi, Spudich and Hegemann around the end of the last millennium (a more detailed history is given by Hegemann[3]).

Soon after their discovery, ChR had already gathered a huge interest in the scientific community due to their application as an optogenetic tool[4]: ChR can be expressed in cells and therefore in neurons, where it acts as a photo-switch for neuronal activity by opening its channel for sodium. Combined with a cation channel absorbing at a different wavelength, the activity of a neuron can be turned on and off by light. This has a lot potential in Neuroscience since the activation and deactivation of a neural path can be localized in space and time.

The proteins can be delivered to the target cells via repurposed viruses in-vivo. The neural activity of the host is then sensitive to light. By illuminating

[1] (1) Stensitzki, T., Muders, V., Schlesinger, R., Heberle, J. & Heyne, K. „The Primary Photoreaction of Channelrhodopsin-1: Wavelength Dependent Photoreactions Induced by Ground-State Heterogeneity". 2015; (3) Stensitzki, T., Yang, Y., Muders, V., Schlesinger, R., Heberle, J. & Heyne, K. „Femtosecond Infrared Spectroscopy of Channelrhodopsin-1 Chromophore Isomerization". 2016.

[2] (46) Hegemann, P. „Algal Sensory Photoreceptors". 2008.

[3] (47) Hegemann, P. & Nagel, G. „From Channelrhodopsins to Optogenetics". 2013.

[4] (48) Boyden, E. S. „A History of Optogenetics: The Development of Tools for Controlling Brain Circuits with Light". 2011.

specific areas and recording the response of the host, it is possible to map neural areas of the brain to specific functions.

Together with fluorescent voltage-sensitive dyes, it is possible to use ChR to map the neural network in organisms.[5].

Mapping the neural network is essential for an understanding of the brain. It is believed that optogenetic tools could be helpful in treating Alzheimer, Epilepsy, Parkinson and other neuronal disorders. Since different optogenetic applications have different requirements, various ChR-variants are explored and engineered. Initially, applications almost exclusively used ChR2, since the its photocurrent is much higher than the one of the earlier discovered ChR1.

Recently proposed variants have all kinds of wt-ChR as a basis. Due to the limited understanding of the function, the engineering of new ChR-variants is done via random mutations; various random mutants are tested until one has favourable characteristics. Therefore better knowledge about the mechanism in ChR translates to a better targeting of the mutations.

Two important characteristics are already determined in the initial photoreaction: the upper limit of the quantum yield and the the absorption wavelength. The yield gives a upper limit of the photocurrent. The absorption should be as far in the red as possible, since longer wavelength allow for deeper light penetration in tissue.

7.3 Structure of Retinal Rhodopsins

Like other rhodopsins, the protein consists of seven transmembrane alpha helices and a protonated retinal photoreceptor, which is covalently bound to a lysine residue. and is stabilized by several aromatic residues nearby. The positive charge, located at the Schiff base, is stabilized by the counter-ion. In rhodopsins, the counter-ion consists of a water, a glutamate and a aspartate.

So far, only the structure of an artificial chimera of CrChR1 and CrChR2 is available[6]. Fig. 7.2 shows the binding pocket of the all-*trans* retinal photoreceptor along with several essential side-chains from the structure. Fig. 7.3 shows the Schiff base and the counter-ion in more detail, using a homology model as a basis.

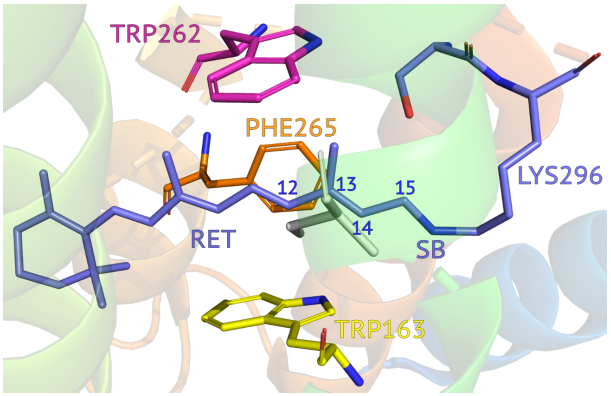

FIGURE 7.2: Structure of the retinal binding pocket in the C1C2-structure from Kato et al. Only selected aromatic amino acids are shown. The relevant retinal carbon atoms are numbered. SB marks the Schiff base connecting the retinal covalently to the lysine. The crystal structure shows the ground-state all-*trans* configuration. Photoisomerization leads to rotation around the $C_{13}-C_{14}$-bond, leading into the 13-*cis* configuration.

In ChR, the initial retinal reaction is mainly an all-*trans* to 13-*cis* reaction, like in Bacteriorhodopsin, a light-driven hydrogen pump, or Sensory Rhodopsin II, a protein controlling the photo-axis via structural changes. The photoisomerization leads to a twisting of polyene chain which moves the Schiff-base of the protonated retinal closer to the counter-ion complex. How changes to retinal is related to later developments in the protein is not entirely solved.

7.4 Prior Work

The photoreaction of retinal rhodopsins is well studied. The reaction of the proton pump Bacteriorhodopsin, which also starts with a *all-trans* to *13-cis* isomerization, has one of the best-researched photocycles of all proteins, especially the initial pho-

[5](49) Lim, D. H., LeDue, J., Mohajerani, M. H., Vanni, M. P. & Murphy, T. H. „Optogenetic Approaches for Functional Mouse Brain Mapping“. 2013.

[6](50) Kato, H. E. *et al.* „Crystal Structure of the Channelrhodopsin Light-Gated Cation Channel“. 2012.

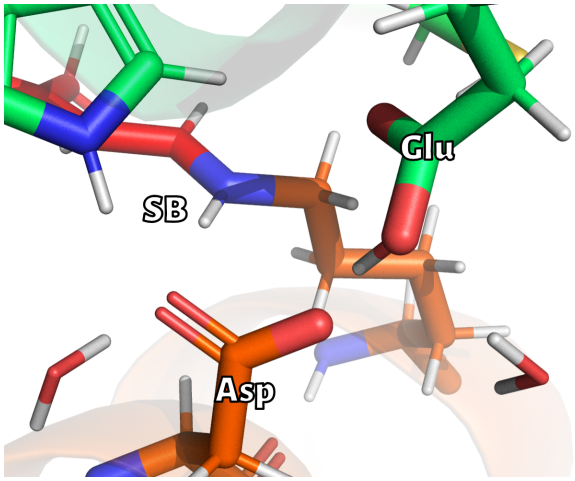

FIGURE 7.3: The geometry of the Schiff base (SB) and the counter-ion. The structure is from a homology model of *Ca*ChR1, for which the Glu was manually protonated. The counter-ion stabilizes the positive charge of the SB in the ground-state and is the initial proton acceptor of the SB after excitation.

toreaction was the subject of a great number of studies[7].

Despite this effort, the exact nature of the primary photoreaction is still under debate, and, in my personal opinion, still not solved. Most of the discussion is based on visible spectroscopy, which by its nature is not very sensitive to small structural changes in the protein. The similarity of the excited state spectrum with product spectrum is also problematic, especially because the product band has the same spectral position as a red-shifted hot ground-state. The quantum yield of most retinal reactions is normally around 65 %, therefore 35 % of the initially excited population are expected to end in such a hot-state.

When working with retinal proteins, one has to be careful about the composition of the ground state. For retinal proteins with an all-*trans* to 13-*cis* reaction, there are at least two different configurations of the retinal, the all-*trans* , 15-anti and 13-*cis* , 15-syn isomer. Usually, the dark-state has a different composition of the two configurations. For *Ca*ChR1 the question of the exact composition is still open: Latest NMR-studies report a pure all-*trans* dark state, in conflict with earlier Resonance Raman studies. However, the NMR studies were done under magic-angle spinning, which puts the sample under high pressure and are known to change the ground-state composition of retinal Proteins[8].

Since our experiments need many repetitions and we only can guarantee no rapid re-excitation, our data generally describes the light-adapted species. This may lead to differences with other publications, which may have a stricter protocol for illumination of the sample.

Notwithstanding its recent discovery, the photocycle of Channelrhodopsin is quite well researched. The majority of the research is centered on CrChR2, since it was and still is the primary tool of the optogenetic community.

Prior our publications, the initial photoreaction of CrChR2 was already eluded in the lab of Wachtveitl in three publications[9]. They observed an all-*trans* to 13-*cis* reaction involving a conical intersection with 400 fs, followed by changes on the picosecond range. The visible transient spectra need two components with time constants of 2.7 ps and 200 ps to describe the picosecond changes. In the mid-IR, a single component of 10 ps was enough to model the picosecond dynamic.

[7](51) Herbst, J. „Femtosecond Infrared Spectroscopy of Bacteriorhodopsin Chromophore Isomerization“. 2002; (52) Moltke, S., Alexiev, U. & Heyn, M. P. „Kinetics of Light-Induced Intramolecular Charge Transfer and Proton Release in Bacteriorhodopsin“. 1995; (53) McCamant, D. W., Kukura, P. & Mathies, R. A. „Femtosecond Stimulated Raman Study of Excited-State Evolution in Bacteriorhodopsin“. 2005; (54) Schenkl, S., van Mourik, F., van der Zwan, G., Haacke, S. & Chergui, M. „Probing the Ultrafast Charge Translocation of Photoexcited Retinal in Bacteriorhodopsin“. 2005.

[8](55) Kawamura, I., Degawa, Y., Yamaguchi, S., Nishimura, K., Tuzi, S., Saitô, H. & Naito, A. „Pressure-Induced Isomerization of Retinal on Bacteriorhodopsin as Disclosed by Fast Magic Angle Spinning NMR†“. 2007.

[9](56) Verhoefen, M.-K., Bamann, C., Blöcher, R., Förster, U., Bamberg, E. & Wachtveitl, J. „The Photocycle of Channelrhodopsin-2: Ultrafast Reaction Dynamics and Subsequent Reaction Steps“. 2010; (57) Neumann-Verhoefen, M.-K., Neumann, K., Bamann, C., Radu, I., Heberle, J., Bamberg, E. & Wachtveitl, J. „Ultrafast Infrared Spectroscopy on Channelrhodopsin-2 Reveals Efficient Energy Transfer from the Retinal Chromophore to the Protein“. 2013; (58) Scholz, F., Bamberg, E., Bamann, C. & Wachtveitl, J. „Tuning the Primary Reaction of Channelrhodopsin-2 by Imidazole, pH, and Site-Specific Mutations“. 2012.

Like in other microbial rhodopsins, an ultrafast rising amide I band was observed. The band is located at 1665 cm^{-1} and is unusually strong in CrChR2, it is even stronger than the retinal C=C stretching band. Unlike other bands, it shows no decay after its initial rise. The transient spectra of CrChR2 were independent of the excitation wavelength. Therefore the authors concluded that the ChR2 ground-state is pure all-*trans* .

For *Ca*ChR1, only steady-state results from Resonance Raman and IR difference spectroscopy were available.[10]. Despite identical methods, these authors came to different conclusions concerning the ground-state composition. Ogren et al. argued that it is strictly all-*trans* , while Muders et al. argued for a 70:30 mixture of the all-*trans* and 13-*cis* . The disagreement stems from different interpretations of the shoulder of the ν(C=C)-stretching vibration.

7.5 Aim of Study

Prior our work, ultrafast spectroscopic methods were only applied to the photoreaction of the ChR2. Hence, the primary objective of our study was to see if and how the reaction in *Ca*ChR1 is different from the reaction CrChR2. Notably, it was of interest to see if the reaction depends on the excitation wavelength, which would be an indicant for ground-state heterogeneity.

The experiments in the fingerprint region were done to confirm the assignment of the prior results: Is the 100 fs component truly the all-*trans* to 13-*cis* isomerization? Can we say more about the two slower decay components? Additionally, since there is less overlap in the vibrational spectrum, we hoped to estimate the quantum yield of the isomerization reaction.

[10](59) Muders, V., Kerruth, S., Lórenz-Fonfría, V. A., Bamann, C., Heberle, J. & Schlesinger, R. „Resonance Raman and FTIR Spectroscopic Characterization of the Closed and Open States of Channelrhodopsin-1". 2014; (60) Ogren, J. I., Mamaev, S., Russano, D., Li, H., Spudich, J. L. & Rothschild, K. J. „Retinal Chromophore Structure and Schiff Base Interactions in Red-Shifted Channelrhodopsin-1 from Chlamydomonas Augustae". 2014.

7.6 Unpublished Results

The Vis-pump IR-probe data presented in our second paper was only a subset of the recorded data. Firstly, the actual recorded data was polarisation resolved. Secondly, we also probed the complete amide range of the IR-spectrum of 1520 cm^{-1} to 1750 cm^{-1} polarization resolved. Next, I will summarize these results.

7.6.1 Fingerprint Region: Polarization Resolved Spectra

As shown in Section 2.2.2, the use of polarization resolved spectroscopy allows the determination of relative angle between the pumped transition dipole moment (tdm) and the probed transition dipole moment, which is particularly useful if the orientation of either is known. An exact determination of the tdm requires theoretical calculations of the transitions, which are still costly and difficult to do for medium sized molecules, especially when they are embedded in proteins. Instead, since the retinal is almost linear and we are exciting the lowest transition, we assume that the electronic tdm is along the retinal polyene-chain. This was also shown by several studies, which determined the tdm angle relative to the membrane. Together with known crystal structures, this shows that the taken approximation is justified.

In Fig. 7.4 two polarization resolved transient spectra are shown. Since the fingerprint region is dominated by modes containing C-C stretching motions, their tdm is aligned with the retinal backbone. Since the excited tdm is also along the same axis the tdms are almost parallel. Therefore we observe ratios near 3:1 between the parallel and perpendicular signal for the bleaching bands. It clearly visible that the signal ratio for the bleach *all-trans* $C_{14}-C_{15}$ stretching band at 1200 cm^{-1} is 3:1 and while the ratio in of the 13-*cis* $C_{14}-C_{15}$ stretching band at 1194 $cm^{-1}$is smaller, around 2:1. This is caused by the geometry change due to the isomerization, in which the $C_{14}-C_{15}$ bond and the associated tdm change their orientation.

The spectra in the fingerprint region consist of multiple overlapping bands. For a more accurate determination of the angle, the decomposing of the difference spectra into single peaks is necessary. Fit-

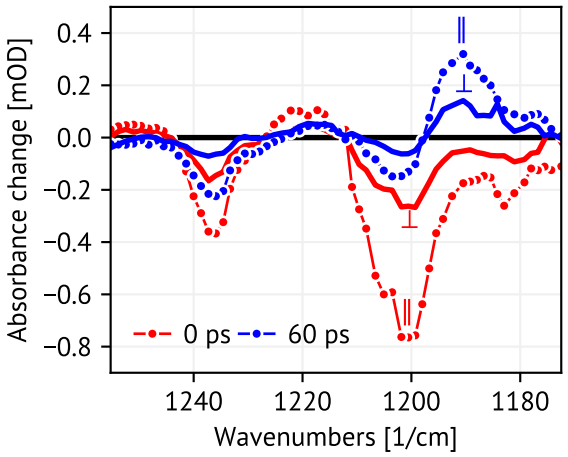

FIGURE 7.4: Polarization resolved difference spectra for 0 ps (red), before isomerization, and 60 ps (blue), after isomerization and cooling. Lines with markers are the spectra for parallel polarization of pump and probe. Thick lines without marker are the spectra for perpendicular polarization of pump and probe.

ting difference spectra is notoriously tricky since the positive and negative amplitudes can cancel each other out. Using polarization resolved data can constrain the solution space by requiring a solution which fits both polarizations well, therefore making useful fitting more probable.

I tried this on the data of fingerprint region: First, the dataset was binned down to 11 spectra. The only parameter allowed to vary between the different spectra is the amplitude, the position, width and angle of a peak are shared between all spectra. The result is shown in Fig. 7.5. It seems that noise in the data is much for the complexity of the spectra, especially at edges of the observed spectral region, where the broad peaks seem to be used for fitting baseline noise. Still, the fit clearly shows the necessity of using two peaks for the bleaching band at 1200 cm^{-1}. These bands have a slight differences in their orientation. Also the fit suggests, that the dip in the product band at 1182 cm^{-1} is due to a bleaching band. This position is often assigned to 13-*cis* , 15-*syn*retinal. It will be interesting to apply the fitting procedure to data with a better signal to noise ratio.

7.6.2 Protonation State of the Counter-Ion

As mentioned above, we also did polarization resolved Vis-pump IR-probe experiments on CaChR 1 in D_2O covering the amide region. Here I will shortly discuss the results.

The initial aim of the experiment was to detect early signals of protonated carboxylic acids and using the resulting relative tdm for the assignment of these bands. These groups are typical proton donors and accepters and play an important role in the functionality of ChR[11] and other retinal proteins. Assigning band changes to a single residue is very useful since these are indicative of possible proton-pathways in the protein.

Since we are doing difference spectroscopy, one of the following conditions has to be fulfilled to detect signals of carboxylic sidechains on our timescale: Either there is a (de)protonation event on our timescale or there is frequency shift due to the electrostatic changes. If the former is true, we expect a bleaching band on the ground-state position and a positive band on the product position, for the latter we would expect signature of bandshift. One can distinguish the two conditions easily, since the bands itself are well separated: The CO-stretching vibration of the protonated carboxyls is located between 1690 cm^{-1} and 1800 cm^{-1} while the asymmetric stretching vibration of the COO^--group lays between 1550 cm^{-1} and 1600 cm^{-1}.

In retinal proteins, the counter ion which stabilizes the protonated Schiffs base (SB) of the retinal is a group of Asp, Glu and a water. The protonation state of the residues varies between different proteins. For *Ca*ChR1, Orgen and coworkers[12] concluded that the Glu169 is likely protonated and the

[11](61) Lórenz-Fonfría, V. A. *et al.* „Transient Protonation Changes in Channelrhodopsin-2 and Their Relevance to Channel Gating“. 2013.

[12](62) Ogren, J. I., Mamaev, S., Russano, D., Li, H., Spudich, J. L. & Rothschild, K. J. „Retinal Chromophore Structure and Schiff Base Interactions in Red-Shifted Channelrhodopsin-1 from *Chlamydomonas Augustae*“. 2014; (63) Ogren, J. I. *et al.* „Comparison of the Structural Changes Occurring during the Primary Phototransition of Two Different Channelrhodopsins from Chlamydomonas Algae“. 2015; (64) Ogren, J. I., Yi, A., Mamaev, S., Li, H., Spudich, J. L. & Rothschild, K. J. „Proton Transfers in a Channelrhodopsin-1 Studied by Fourier Transform Infrared (FTIR) Difference Spectroscopy and Site-Directed Mutagenesis“. 2015.

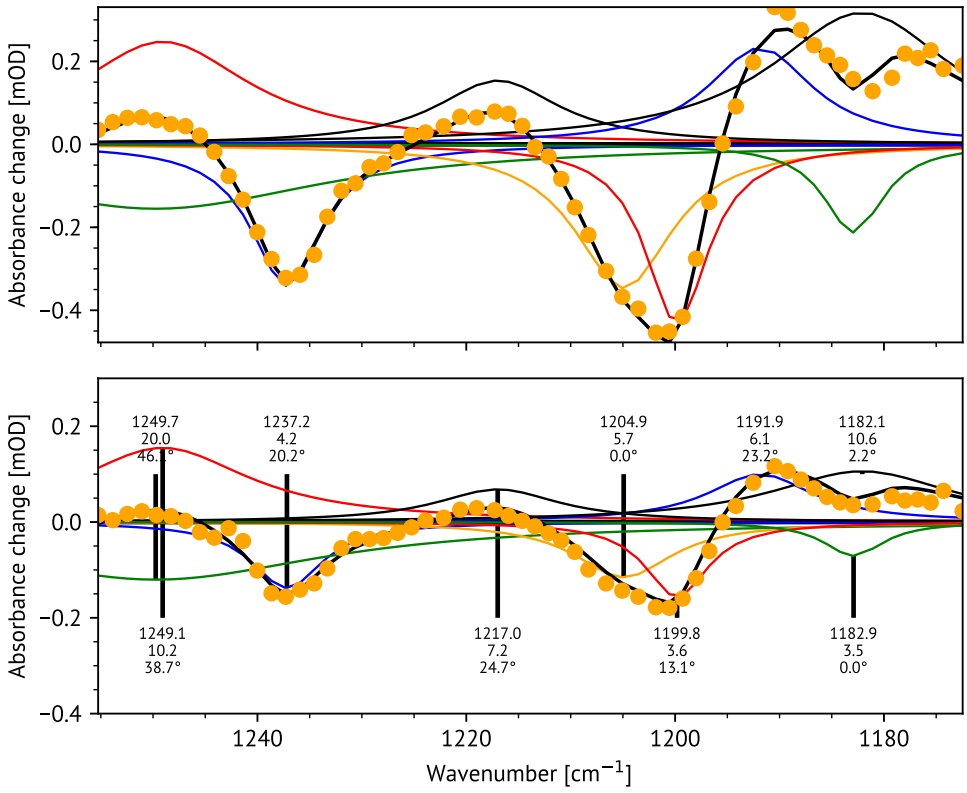

FIGURE 7.5: Fit result of the polarisation resolved data. *Top:* Spectra for parallel polarization of pump and probe (points), fit (black line) and single peaks (coloured lines), shown for the earliest averaged spectra, around 500 fs, *Bottom:* The same for perpendicular polarizations, with annotated peaks. The annotation lists position, width and the relative tdm-angle of the peak.

Asp is deprotonated. Since one effect of the isomerization is a small shift of SB, we would expect at a small change in the frequencies of the residues located close to the SB. These should show up as a signal as explained above. Therefore , if the assignment of Ogren et al. is correct, we should see signals in both spectral windows.

But despite investing a lot of effort and time, I was not able to detected a signal in spectral window of 1690 cm^{-1} to 1800 cm^{-1}. All the following hypothesises could explain the absence of a signal:

i) Something in our setup was wrong, e.g. misaligned. Unlikely, since we detected signals in the amide region under the identical conditions. In addition, I made several attempts to detected a signal in the aforementioned region.

ii) The signal is too weak for us to detect. Since we looked for signals only up to 300 ps, protonation events of the sidechains are unlikely, therefore the hypothetical signal would have been caused by a band-shift due to the different electrostatic interaction before and after photoexcitation. These induced changes are smaller compared to changes due a hydrogen transfer, which is the origin for the signal on the longer timescale.

iii) The protonation state only fully recovers late in the photocycle. Since the photocycle of *Ca*ChR1 takes almost one minute, the mean waiting time-between two excitations may not be long enough and we instead observe an intermediate where the protonation state of the counter ion did not yet return to its initial state.

iv) The assignment of Ogren may be incorrect. However, this would be surprising since they assigned the protonation state by isotopic labelling, pH-studies and site-specific mutations.

To verify that the experimental conditions were not the cause for the absence of a signal, experiments with R82A-mutant of BR are planned. Arg 82 is located near the counter-ion Asp 85. The mutations changes to pK-value of the Asp to around 7[13],

[13](65) Heyne, K., Herbst, J., Dominguez-Herradon, B.,

therefore it is partly protonated at pH 7. Therefore, we expect to see a signal around 1720 cm^{-1}, since the band-position is sensitive to its environment. If a signal is still absent, we know the sensitivity of our setup is lacking.

7.6.3 Amide Region

Fig. 7.6 shows the result of the Vis-pump IR-probe measurements. Since the sample was short-lived under measurement conditions and the signals were weak, we only recorded data with the pump-wavelength centered at the absorption maxima of 530 nm. Fig. 7.7 shows a coarse designation of the band origins in different regions. The earliest spectra still show coherent artifacts, partly caused by dynamics faster than the time resolution.[14]

At 1661 cm^{-1}, a strong negative signal is observed. In D_2O the position can be assigned unequivocally to the amide I band since C=ND-stretch of the chromophore is shifted down to approximately 1630 cm^{-1}. I will discuss the origin of the amide I band in detail later. The region around 1630 cm^{-1} is dominated by two bleaching signals at 1635 cm^{-1} and 1625 cm^{-1}, the already mentioned retinal band, and another band, which is often attributed to the C=N-stretch of an arginine sidechain.

Surprisingly, the stronger changes of the 1625 cm^{-1} at earlier times mirror the changes of the retinal C=C-stretching band located around 1540 cm^{-1}. This indicates that the band belongs to the C=ND-stretch, which is additionally supported by the high dichroic ratio, which is a result from an almost parallel orientation of the electronic tdm and the vibronic tdm, which is true for the C=ND-stretch. Also supporting this assignment is that the PFID-signal in this region seems to be concentrated on the 1625 cm^{-1} position and the Resonance Raman results from Muders et al.

Hence the other band at 1635 cm^{-1} has to be assigned to a side-chain. According to homology structures of *Ca*ChR1, there is no arginine in direct contact to the retinal; the nearest arginine is about 7 Å away. Therefore another residue is likely responsible for the peak. According to Barth, other possible contributions in this region can be the ring-modes of tryptophan, phenylalanine and tyrosine. The former is known to strongly react to the retinal excitation.

The positive band around 1606 cm^{-1} likely belong to one of the former bands. The visible peak is likely from the 13-*cis* C=ND-stretching vibration. The small amplitude could be explained by bleaching bands at same position.

Two small negative bands can be recognized at 1597 cm^{-1} and 1587 cm^{-1}, which were not resolved as bleaching bands in prior studies due to a stronger positive signal at the same position. The polarization resolved data clearly shows that these are real peaks and not signal dips of the positive band. Possible band-origins in the region are the antisymmetric carboxylate stretching vibrations Asp 195 and Glu 162.

The Asp carboxylate group is located near the retinal and likely influences the retinal π-system[15]. Hence it is expected to be very sensitive to the retinal conformation, leading to a shift in frequency after excitation.

Glu 162 is near the protonated Schiff-base, which moves during the isomerization. This change will affect the glutamate as discussed previously. When comparing the antisymmetric carboxylate stretching frequencies, the frequency of Asp is generally higher than the frequency of Glu.

Therefore we tentatively assign the 1597 cm^{-1}-bleaching band to the Asp 195 and the 1587 cm^{-1}-bleaching band to the Glu 162. If this assignment is correct, it would explain the absence of a signal above 1700 cm^{-1}, since both residues in the counterion would be deprontonated.

The assignments of the bands between 1580 cm^{-1} to 1560 cm^{-1} is difficult. It seems that the positive signal obscures some smaller negative signals

Alexiev, U. & Diller, R. „Reaction Control in Bacteriorhodopsin: Impact of Arg82 and Asp85 on the Fast Retinal Isomerization, Studied in the Second Site Revertant Arg82Ala/Gly231Cys and Various Purple and Blue Forms of Bacteriorhodopsin". 2000; (52) Moltke, S., Alexiev, U. & Heyn, M. P. „Kinetics of Light-Induced Intramolecular Charge Transfer and Proton Release in Bacteriorhodopsin". 1995.

[14] (12) Kowalewski, M., Fingerhut, B. P., Dorfman, K. E., Bennett, K. & Mukamel, S. „Simulating Coherent Multidimensional Spectroscopy of Nonadiabatic Molecular Processes: From the Infrared to the X-Ray Regime". 2017.

[15] (50) Kato, H. E. *et al.* „Crystal Structure of the Channelrhodopsin Light-Gated Cation Channel". 2012.

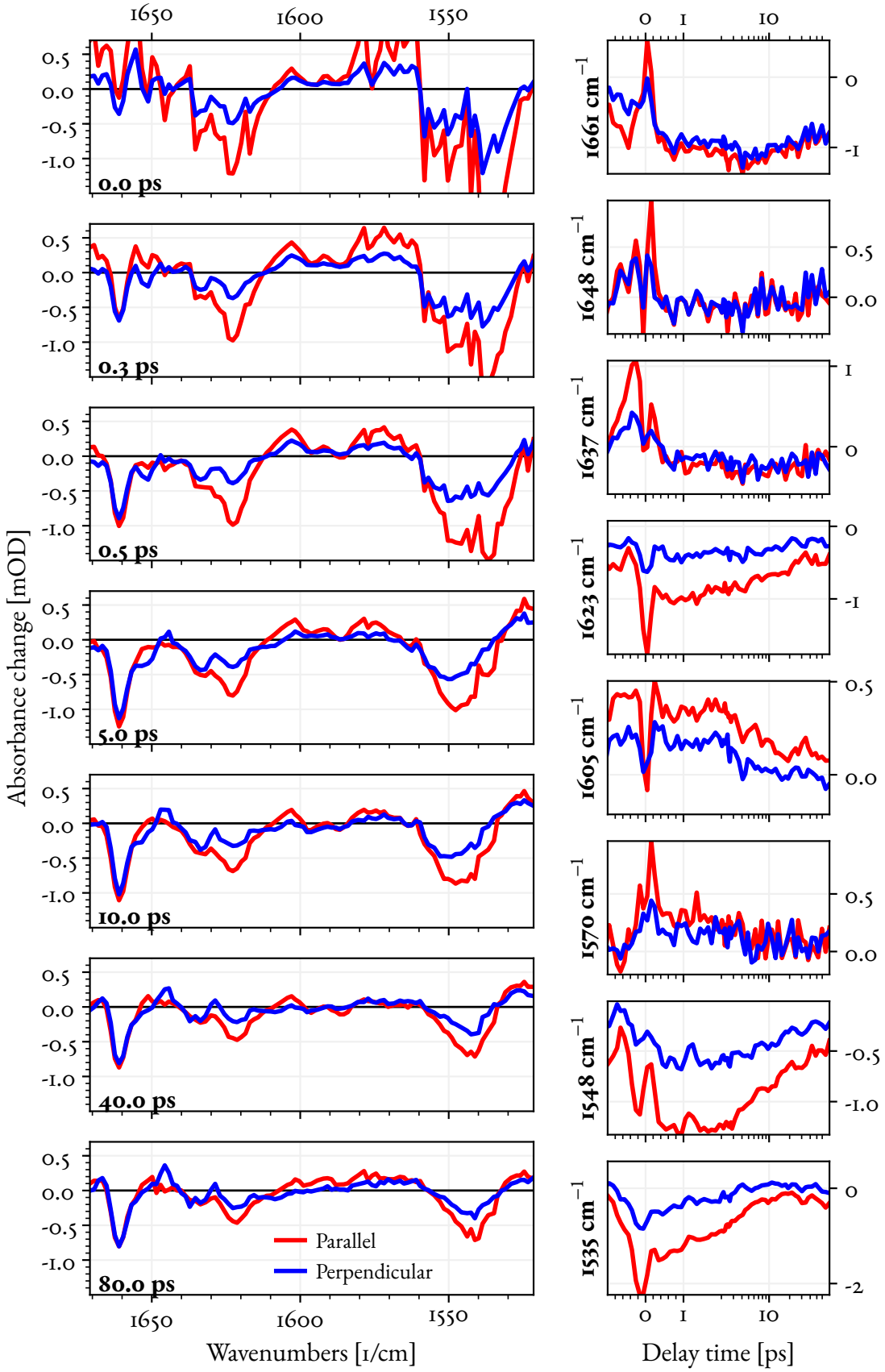

FIGURE 7.6: *Left:* Selected Vis-pump IR-probe difference spectra of *Ca*ChR1 in D_2O. Spectra with parallel polarizations are shown in red, perpendicular in blue. The delay time is shown in the lower left of each panel. *Right:* Selected transients for both polarizations from the dataset. The time axis is linear from −1 ps to 1 ps and logarithmic elsewhere.

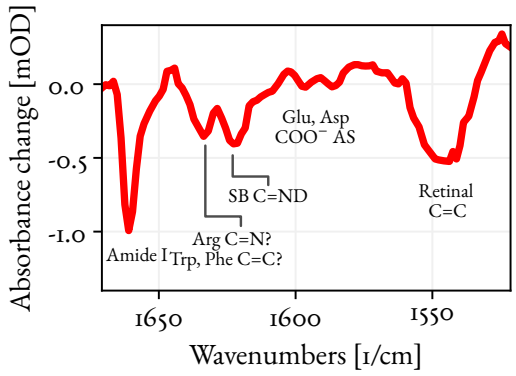

FIGURE 7.7: Tentative assignment of the ground-state IR-bands in the observed window.

at 1576 cm^{-1} and 1563 cm^{-1}. While the former one could be a product of the poor SNR in the region, the latter one seems to be real. It could be attributed to phenylalanine ring-modes, most likely originating from Phe 265. The positive bands could belong to the bleaching bands around 1590 cm^{-1} mentioned before. The assignment to a hot υ(C=C) stretching mode of the retinal is more probable since large parts of the signal decay within several picoseconds, similar to the observations in the fingerprint region. It follows from our Vis-pump Vis-probe data that excited state contributions can be dismissed after 200 fs. In the fingerprint region, we attributed changes on this timescale mainly to the non-reacting population.

The Resonance Raman spectrum of *Ca*ChR1 shows a broad and structured υ(C=C) band around 1530 cm^{-1}, attributed to the retinal ethylenic stretch. Further band-fitting decomposes the mode into three peaks 1548 cm^{-1}, 1533 cm^{-1} and 1525 cm^{-1}. Hence, we assign the strong negative signals to the bleaching of the ground-state ethylenic stretching bands. The spectra at time-zero have a similar structure as the Raman bands: a strong peak located at the red-edge with a smaller shoulder towards the blue edge. Later signals still show a broad bleaching signal, but the visible shoulder is lost, supporting the assignment of the shoulder to 13-*cis* ground-state retinal.

We assign the positive peak at 1520 cm^{-1} to the 13-*cis* band of the non-relaxed retinal in the photoproduct. After its creation outside our observation window, the band shifts blue and overlaps with the bleaching bands, resulting in the signal loss.

7.6.4 Origin of the Amide I Response

Next, I want to discuss the strong negative peak at 1661 cm^{-1}. From the position of the peak, it is likely associated with an amide I vibration since the retinal has no vibration which could absorb at this position.

Two facts about the band are quite puzzling: Firstly, the signal appears almost immediately, even faster than the very fast retinal isomerization where we could observe the rise of the associated signals and secondly, that the signal is missing a corresponding positive peak. Such amide I response bands where also reported for Bacteriorhodopsin, Sensor Rhodopsin II[16] and Channelrhodopsin II[17]. By isotopic labeling, the group of Diller could exclude retinal contributions entirely. However, the question remains which part of the protein is the origin of the response and what causes it.

In this section, I want to argue that the source of the ultrafast protein is the tryptophan 262: From the peak position it is clear that the source has to be a carbonyl stretching vibration of the protein backbone. Since the response is very rapid, only amino acids near the retinal need to be considered. Additionally, the peak is quite strong, having almost the same amplitude as the retinal υ(C=C) stretching band, hence the causing amino acid has to be tightly coupled to the retinal, e.g., by dipole-dipole coupling. For this to be the case, the amino acids should have an aromatic group near the polyene-chain. From these constraints, we can reduce the number of suspects down to three: the two tryptophans above and below the retinal (163 and 262) and the phenylalanine 265 (tyrosin in BR) next to the retinal. All three are shown in Fig. 7.2.

Next, we estimate the relative angle between the amide tdm and electronic tdm from our polarization resolved data. Since parallel and perpendicular peaks are of near equal strength, the relative angle should be near the magic angle of 54.2°. For an amide vibration in a rhodopsin, this is quite surprising, as the majority of amide-carbonyl groups

[16] (66) Gross, R. *et al.* „Primary Photoinduced Protein Response in Bacteriorhodopsin and Sensory Rhodopsin II“. 2009.

[17] (56) Verhoefen, M.-K., Bamann, C., Blöcher, R., Förster, U., Bamberg, E. & Wachtveitl, J. „The Photocycle of Channelrhodopsin-2: Ultrafast Reaction Dynamics and Subsequent Reaction Steps“. 2010.

follow the direction of the alpha helices with an angle of 70° to retinal tdm.

To estimate the relative angle of the tdms from the structure, we use the dot-product of the vector between the C=O and a vector along the polyene chain. For most backbone carbonyl groups this results in something near the expected 70°. Only one exception is encountered: the alpha helices containing the Trp 262 makes a small turn near the retinal, leading to an angle of 52°, well in agreement with the angle resulting from the polarization resolved data.

Since the crystal structure stems not from the same protein, our assignment has to be taken with care. Using a homology model of *Ca*ChR1 instead did not alter our assignment. Additionally, for SR II we estimated an angle of 70° from our polarization resolved data, which is in agreement with the SR II structure, where the helix bend is missing, and all three candidate residues have the same angle.

Our assignment differs from the results by S.Haacke et al. Using ultrafast Vis-pump UV-probe spectroscopy on BR; he showed by mutation of the tryptophan residues that the observed non-retinal signal belongs to Trp 86, corresponding to Trp 163 in ChR. Whether this difference is due to differences in the proteins or due to the method is not clear. Since the amide I signal is much stronger in ChR than in BR or SRII, it is reasonable to expected different processes to be involved.

The question about the nature of the purely negative signal still remains. Pure bleaching IR band are either caused by vanishing of the band due to structural changes or due changes in the oxidation state of the molecule. Since a structural change to the C=O-group is very unlikely, the pure bleaching band is mostly a result of some charge change. If amide band bleach would be caused by the vibrational Stark effect due to change of the electrostatic interaction induced by the excitation, the signal change should be mostly proportional to the first and second derivative of the initial band[18]. This is not the case since these changes conserve the total strength of the band.

However, it is noteworthy that the peak does not change within the first 10 ps and only shows changes slightly afterwards. Since we observe the back-reaction of the non-isomerazing population with a time-constant of about 5 ps, the peak is either visible in both populations or is connected to a successful isomerization.

7.7 Summary

- For the first time, the initial photoreaction of ChR I was observed by femtosecond Vis-pump Vis-probe and Vis-pump IR-probe spectroscopy.
- The reaction consists of all-*trans* to 13-*cis* isomerization of the retinal, which happens with a time constant of 100 fs, the fastest reported all-*trans* to 13-*cis* isomerization to date. Additionally, time constants of 0.5 ps and 5 ps are needed to model the data.
- The quantum yield of the reaction was estimated to be 60 %.
- Excitation wavelength depended behavior was observed, supporting the hypotheses of a heterogeneous ground.state. The signal difference could be extracted by subtraction after normalization to later delay-times . It completely decayed triexponentially within 100 ps.
- Identical time-constants were found in the fingerprint region and the visible data. From the IR DAS, the 5 ps-component is assigned to the back-reaction of the non-reacting population.
- The bleaching bands of the 5 ps- and constant-component differ, indicating that structural differences in the ground-state are responsible for the successes of the isomerization reaction.
- Several bands in the amide region could be assigned. Particularly, we could pin down the origin of the unusually strong amide I band to Trp 162.
- Since no signal could be detected above 1690 cm^{-1}, we conclude that both Asp and Glu of the counter-ion are deprotonated. This contradicts prior publications, therefore more work is necessary.

[18] (67) Chattopadhyay, A. & Boxer, S. G. „Vibrational Stark Effect Spectroscopy“. 1995.

Chapter 8

Acceleration of Reactions by IR-Excitation

8.1 Introduction

This chapter introduces the paper[1] which proves, that direct initiation of bimolecular chemical ground-state reactions in solution via mid-IR light is possible.

The general idea is sketched in Fig. 8.1. An IR-photon with $E(\omega) > E_{act}$ excites a vibration of a reagent with a energy greater than the activation energy. The energy in the vibration gets redistributed, populating modes belonging to reaction coordidate in the process, which allows the passing of the transition state barrier leading to product formation.

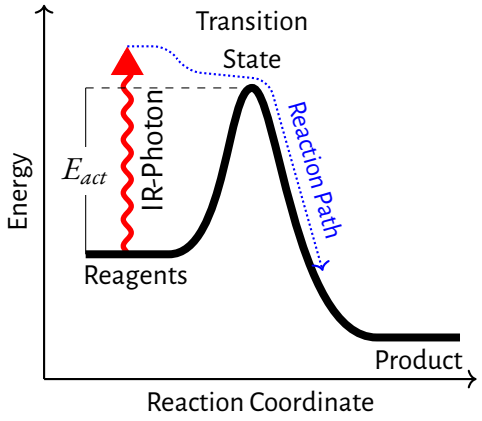

FIGURE 8.1: General idea behind the acceleration of ground-state reactions with IR-light. IR-excitation of modes connected to the reaction coordinates leads to crossing of the barrier.

To prove our hypothesis, we monitored vibrations of the excited reagents and the forming product by femtosecond IR-pump IR-probe spectroscopy in real-time. To our knowledge, this is the first time a ground-state bimolecular synthesis in solution was observed in real time.

Observation of bimolecular reactions in solution is demanding: only if molecules of both reagents have the correct conformation, they can react and contribute to the signal.

In 2015 Dunning and co-workers[2] successfully observed a bimolecular reaction in solution. In their study, they used a UV pulse to photolysis XeF_2 for generation of F-radicals which then react with deuterium of the solvent to produce DF. Their study also confirmed the need for a very high signal to noise ratio: the observed signals were in the range of 0.5 mOD; to capture the dynamics a sub 0.1 mOD sensitivity is necessary.

The chapter first describes our concept of the laser induced chemistry, before detailing the reaction we used to test our idea. Next it explains the goal of the experiment before explaining the methods used.

[1] (5) Stensitzki, T., Yang, Y., Kozich, V., Ahmed, A. A., Kössl, F., Kühn, O. & Heyne, K. „Acceleration of a Ground-State Reaction by Selective Femtosecond-Infrared-Laser-Pulse Excitation“. 2018.

[2] (68) Dunning, G. T. *et al.* „Reaction Dynamics. Vibrational Relaxation and Microsolvation of DF after F-Atom Reactions in Polar Solvents“. 2015; (69) J. Orr-Ewing, A. „Taking the Plunge: Chemical Reaction Dynamics in Liquids“. 2017.

8.2 Influencing Chemical Reactions by Laser-light

For a bimolecular ground-state reaction in solution to happen, the two reagents have (a) to collide with each other, (b) at the right relative orientation and (c) have enough vibrational and kinetic energy in the participating vibrational modes. Because the occurrence of all three prerequisites depend on the temperature, acceleration of chemical reaction is easily obtained by heating.

Heating has downsides: The acceleration is not reaction specific. If one could instead deposit energy into a single reaction coordinate, only the corresponding reaction would be sped up. This could dramatically increase the yield of reactions when the desired reaction competes with other unwanted reactions.

Of course, the idea of using laser radiation to control chemical reactions is not new. Already in 1980 the later noble prize winner Ahmed H. Zeweil wrote a paper which title posed the question "Laser selective chemistry — Is it possible?"[3]. He concluded, that *"With sufficiently brief and intense radiation, properly tuned to specific resonances, we may be able to fulfill a chemist's dream, to break particular selected bonds in large molecules."*

Only a few years later it was indeed shown that by excitation with visible light, dissociation reactions in the gas phase could be accelerated. A decade later it was also shown, that weakening a bound by excitation of the corresponding vibration mode prior a collision also increase the output of specific reactions. Again, this was shown using molecular beams in a vacuum. The development of pulse shaping techniques in combination with optimization algorithms in a feedback-loop can now produce specific pulses optimizing the reaction pathway. The field which does these experiments is now called coherent control. While this lead to countless successful scientific studies, it had not yet lead to real applications.

The major reason for the non applicability of coherent control in the industry is that most reactions used in applications are synthesis reactions in the liquid phase. Here the approach used in coherent control has several obstacles: The initial configuration is not as narrowly defined as in the gas-phase, inhabiting the use of complicated schemes depending on a specific geometry. The increased interaction between molecules – 10^{10} collisions per s – leads to much shorter dephasing and relaxation times. Already in the gas phase, intra-molecular vibrational relaxation via anharmonic coupling is a strong obstacle for preparation of higher vibrational states. The shortend lifetime in solution also limits the potential influence of the light pulse to reagents in the right orientation at the moment the pulse arrives.

Here we use a simpler and more straightforward approach. We are using an IR-photon to deposit energy near or into the reaction coordinate. A massive advantage of this approach is that it does not depend on a short or complicated laser pulse. In fact, nothing in this approach impede the usage of a continuous wave laser for the acceleration, which, considering the recent development of high powered quantum cascade IR-lasers, is helpful for potential applications.

While a short pulse is likely not necessary to use IR-light for reaction acceleration, it is a requirement for studying the cause of acceleration. As already mentioned above, thermal relaxation happens within picoseconds. Hence to separate acceleration due to energy deposited directly into or near the RC from acceleration due to increased temperature after relaxation, time-resolved experiments with sub-ps time resolution are required.

8.3 The Urethane Reaction

First, a suitable reaction has to be chosen: It has to be slow enough, that over the timespan of the experiment the concentration does not change too much. The activation energy should not exceed the mid-IR region, which gives an upper limit of approximately 0.5 eV $\approx$ 3500 cm^{-1}. Additionally, the reaction should be simple, and the participants should have strong and seperated marker bands for identification.

From an earlier study from our group in cooperation with O. Kühn[4] we knew that Urethane for-

[3] (70) Zewail, A. H. „Laser Selective Chemistry—Is It Possible?" 1980.

[4] (71) Kössl, F., Lisaj, M., Kozich, V., Heyne, K. & Kühn, O. „Monitoring the Alcoholysis of Isocyanates with Infrared Spectroscopy". 2015.

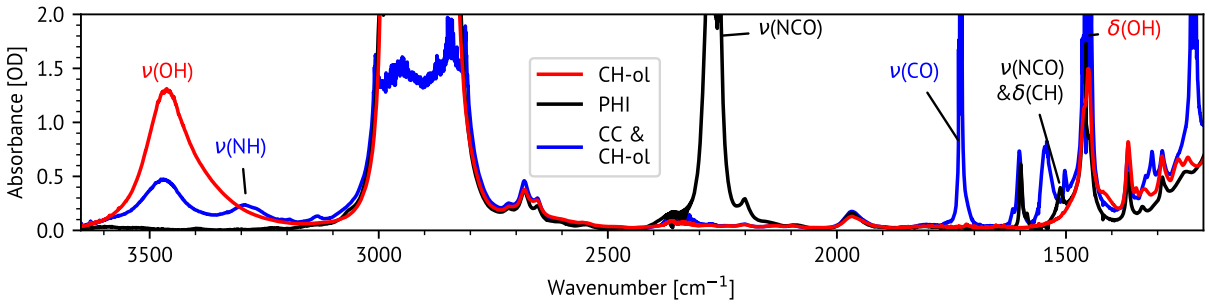

FIGURE 8.2: Infrared spectra of cyclohexanol (CH-ol), phenylisocynat (PHI) and a mixture of CH-ol and Cyclohexyl-carbanilate (CC), all solved in THF. Details are given in the Text.

mation fulfills the requirements perfectly. The reaction consists of an alcohol-group and a cyanate-group forming an amide group, connecting the alcohol with the cyanate.

In the article, the activation energies of the alcoholysis of mono-urethane (2340 cm^{-1}) and of poly-urethane (1000 cm^{-1}) where measured and calculated. While the activation energy of the mono-urethane reaction is higher as the poly-urethane reaction, the synthesis of mono-urethane is advantageous for our experiment as the monomers do not scatter light, unlike long poly-urethane chains.

Thus, the focus of our study was the formation of the mono-urethane Cyclohexyl-carbanilate from Cyclohexanol and Phenylisocynat which are shown below in Fig. 8.3.

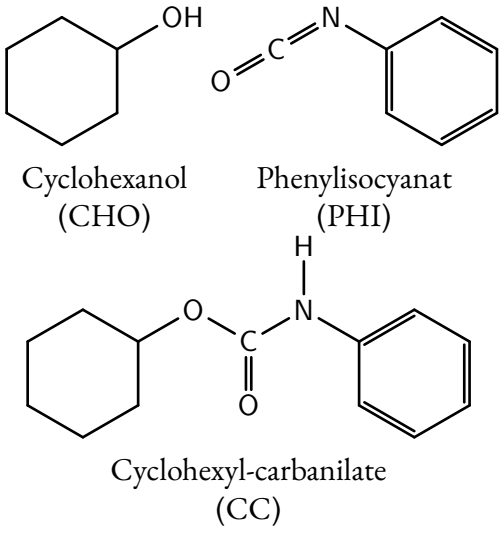

FIGURE 8.3: Structures. Top, the starting material; bottom: the product.

The involved groups all have strong vibrational bands: the alcohol group has the OH-stretching; the cyanate has the NCO-stretching and the product amide-group is identifiable by the CO-stretching. For the mono-urethane reaction, only the CH-ol OH-stretching vibration has a frequency above the activation energy. Hence we will excite it to initiate the reaction. The energy of ν(NCO) is slightly (100 cm^{-1}) under the activation energy. However, when taking the thermal energy at room temperature into account (around 200 cm^{-1}), the energy may be still enough to go over the activation barrier. This experiment will be a likely candidate for future studies, particularly since the band has a six times higher extinction coefficient than the ν(OH)-band.

8.4 Aim of the Paper

Fig. 8.2 displays the steady-state IR spectra of the reagents and the product. The absorbance of strongest bands is outside the working range of the spectrometer for the used sample thickness and concentration. The bands common to all spectra belong to the THF solvent, which strongly absorbs around 2900 cm^{-1}.

To accelerate the reaction, we excite CH-ol at the OH-stretching band at 3500 cm^{-1}. To observe the reaction, we will probe PHI at the NCO-stretching of PHI at 2260 cm^{-1}, the ν(NCO) & δ(CH)-band of PHI at 1505 cm^{-1} as well as th the CO-stretch at 1735 cm^{-1} and the δ(NH) at 1520 cm^{-1} of the forming CC. Probing the CH-ol bands itself is not very useful, as any bleach could be either a result of the IVR induced band shift or due to product forma-

tion. Since we expect a low yield of product formation, detecting and distinguishing the bleaching caused by product formation from bleaching caused by hot-bands of Ch-ol seems not possible.

8.5 Methods

We applied two experiments to prove the acceleration of the reaction with IR-light.

In the first experiment, conducted by V. Kozich and F. Kössel, the reaction rates with and without mid-IR illumination were compared. Heating of sample is ruled out in two ways: By thermal imaging and by estimating the pump-induced heating. The former can rule out a steadily increased temperature in the sample volume. The latter gives the expected temperature rise in the focal volume when ignoring thermal diffusion. Multi-photon effects can be excluded by using a large spot size.

If an increase in the reaction rate under illumination is detected, we can calculate the temperature rise which would to achieve the same effect. By comparing this hypothetical temperature rise with the estimated temperature increase in the focal volume, we can prove or dismiss IR-acceleration. Additionally, we can vary the pump wavelength and compare the results. If pumping of solvent modes does not increase the reaction rate, we have another argument to dismiss the influence of laser-induced heating.

In the second experiment, IR-pump IR-probe spectroscopy, we want to observe the product formation directly. For that, we probe both vibrations belonging to the initially non-excited reagent and the product. If we measure rising bleaching signals of the reagent and rising product bands of the product, we would prove that reaction is initiated on an ultrashort timescale. Since we do not directly excite the reaction coordinate, the modes belonging to the RC need to be populated first. Thus, we expect the product build-up to fall on the same time-scale as intra-molecular redistribution and vibrational cooling. To distinguish spectral changes due to product formation and due to induced heating, the result is compared with IR pump-probe experiments on the reagents or product alone.

Theoretical calculations accompany the experiments. Since prior calculations could not predict the activation energy correctly, a method is used where the solvent molecules are included implicitly.

8.6 Summary

- For the first time, it was demonstrated that IR-excitation of a vibration connected to the reaction coordinate could initiate a bimolecular reaction.
- We achieved this by IR pump - IR probe spectroscopy, where the vibration of one reagent was excited and the vibrational bands of the second reagent and the product were probed.
- The data suggests that the energy of initially excited mode relaxes into the modes belonging to the reaction coordinate. It may be a general motif of efficient reactions at room temperature, that energy is funnelled into the RC.
- Theoretical calculation with implicit solvent molecules results in two populations with different activation energies. Only the minor population has an activation energy comparable with the experimentally value.
- The estimated quantum yield of 0.3 % is low but measurable and usable.

Chapter 9

Summary and Outlook

In this thesis, the results of femtosecond pump-probe experiments on four different systems were presented: the cyclic tetrapyrrole corrole; channelrhodopsin 1, a light-activated cation channel membrane protein; phytochrome, an important photosensing protein, and a ground-state reaction between phenylisocyanate and cyclohexanol.

For the three systems, we combined Vis-pump Vis-probe and Vis-pump IR-probe experiments to observe the reaction from two complementary perspectives. This combination of methods was especially fruitful for the proteins, where the electronic spectrum is practically blind to changes in the protein itself since it is dominated by the chromophore contributions.

I will first discuss the evolution of the used fs pump-probe spectrometer, before I give a summary of the results and a outlook of each system separately.

9.1 Experimental Setup

In the course of this work, I improved the existing fs-pump probe spectrometer in several key aspects. The improvements dramatically increased the signal to noise ration and data-collection rate. We can now record better data in less time than before, reducing the required sample amount.

For the IR-probe, this was achieved by better referencing and improved software. In the case of the visible probe, the reduction in time was achieved by expanding the spectral window simultaneously recorded. We also improved the supercontium generation by using water as the nonlinear medium, resulting in a bluer spectrum. Unlike other broader source like CaF, no mechanical movement is required to avoid photodamage.

There are still many available avenues to further improve the setup. The time-resolution could be improved by integrating pulses compressors, which could be combined with spatial light modulators. SLMs would also open the way for 2D-spectroscopy. Another way in which the setup is not yet optimal is the IR-detection. Only a small spectral window of the probe can be detected at once. Here, either a new MCT-array with more elements or using an up-conversion scheme to shift the IR-light in the visible region would help.

Piezo-mirrors and motorized kinematic-mounts could be used to automate the setup further, but this would also require new software development.

9.2 Corrole

By applying fs-pump-probe spectroscopy to brominated Al-corrole (Br-Al-cor) we could show that the attachment of the bromine introduced an intersystem crossing (ISC) from S_1 to a triplet state due to the increased spin-orbit coupling by the heavy Br-atoms. We estimate a triplet yield near unity. Therefore, Br-Al-Cor is a promising photosensitizer for photodynamic therapy.

Compared to currently used sensitizers, Ru- and Ir-pyridine complexes, corrole has a much stronger absorption in the red region of the spectrum. Longer wavelengths are preferred for light-applications in tissues since they allow for deeper light penetration. Similarly, we could show in a second paper that replacement of the Al-ligand with a heavier Sb atom is enough to introduce ISC with

300 ps in non-brominated corrole.

The ISC was detected by the decay of the stimulated emission signal belonging to the S_1-state. No bleach recovery accompanied the decay. Hence the observed decay is due to ISC with a time constant of approximately 95 ps. The IR transient spectrum of the triplet-state has a distinct shape in the C=C-stretching region around 1500 cm^{-1}. This distinct shape could allow the identification of priorly unknown triplet generating reaction pathways.

Another discovery was the increased rate of the Soret-band to Q-band transition, which happens in 200 fs for Br-Al-cor compared to 500 fs for Al-cor. The influence of the bromination on the electronic spectra is quite small, only shifting the spectrum by about 20 nm to longer wavelengths. This change is comparable to the difference of hexa- and pentacoordinated Al-corroles, where the rate of the Soret to Q-band transition is identical despite the spectral shift. Hence, it is tempting to assign the increased rate to the involvement of higher triplet-states partaking in the transition. Further studies are needed to see if this is true.

Additionally, the role of corrole as a photoactivated electron-donor is still unexplored. The combination of the Vis- and IR-probe is advantageous for the observation electron transfer processes since the changes in the donor, and the acceptor can be observed separately by probing molecule specific IR-bands.

9.3 Phytochrome

We applied fs-pump-probe spectroscopy to elude the photoreaction of Cph1 in the Pfr-state. We found three different time constants: 0.2 ps, 0.7 ps and 6 ps. The latter two were found in both visible and IR transient spectra. The shortest was only resolved in the visible spectra.

The central question, if the heterogeneity of the state influences the photoreaction, could be answered positively.

Compared to the other components, the decay-associated spectra of the 6 ps-component has a narrower bleaching band at the position of the ring D carbonyl stretching vibration. This is supported by the results of fitting the polarization resolved spectra: the narrow-component is well simulated by one band, while the other components need two bands for a reasonable simulation of the ring D carbonyl stretching vibration. The tdms of the resulting bands have slightly different relative angles to the electronic tdm, suggesting different ring configurations caused by different hydrogen bonds.

Due to the spectral shape of the 6 ps-component resembling a back reaction and its missing contribution to the final product, we assign the corresponding configuration to inactive. While this explains the low quantum yield of the Pfr photoreaction, it is not clear yet if the heterogeneity has biological relevance.

The low yield may be induced by the requirement of a thermal back-reaction, which is only possible if flat regions are connecting the two minima in the PES. This flat surface could have multiple flat minima near each minimum. For phytochrome, this results in an only slightly restricted ring D orientation, with serval minima in each ground-state.

What could be the biological relevance of a state heterogeneity lowering the quantum yield of a photo-sensor? From an evolutionary point of view, it could be a trade-off between the signaling strength and frequency. The inactive reservoir induced by the heterogeneity could be used for fine tuning the photo-response.

Also, the interplay between the ring isomerization and the later steps is still unclear. Are only the H-bond changes due to ring rotation functionally relevant or does the dipole change in the excited state also induces relevant changes?

Therefore, more research is necessary to understand the initial photoreaction of phytochrome. Our research shows that spectroscopy of the electronic transitions alone gives results which are difficult to interpret due to the similar spectra of the different electronic sub-states. Therefore, the increased structural sensitivity of in vibrational spectroscopy is essential to understand the reaction in detail.

9.4 Channelrhodopsin

For channelrhodopsin 1 we were able to elude the photoreaction in detail. By application of Vis-pump Vis-probe spectroscopy, we showed that the conical intersection, likely linked to all-*trans* to 13-

cis isomerization, is reached within 100 fs after excitation at 550 nm. Two further time-constants, 0.5 ps and 5 ps, were necessary for modelling the data. Since the spectra of these components are well described by derivatives of a peak function, we attributed them to cooling dynamics.

Tuning the pump-pulse to 500 nm resulted in different transient spectra for earlier delay timetimes. After 60 ps, both datasets look identical, and we, therefore, could extract the difference. We attribute the difference due to a population of the 13-cis ground-state, but we can not rule out other explanations.

Next, we analyzed the transient changes of the retinal in the so-called fingerprint region around 1200 cm^{-1} by Vis-pump IR-probe spectroscopy. The fingerprint region consists of coupled C-C stretching and H-wagging modes sensitive to the chromophore configuration. Our results confirmed the assumed all-trans to 13-cis reaction within less than 200 fs. From the comparison of the time-zero spectrum with our final spectrum, we estimated the yield of the reaction to about 60 %, which is very similar to the yield in BR, despite *Ca*ChR1 reaching the conical intersection much faster.

Exponential fitting resulted in time-constants identical to the one we found in the visible data, 0.5 ps and 5 ps. The 500 fs consists of unstructured positive features. We could not extract new information from its spectrum. In contrast, the 5 ps-spectrum revealed some fascinating traits: Firstmost the bleaching bands of the component look differently than the bleaching bands of the constant component. Secondly, the product is mostly unaffected on the 5 ps timescale, while the component explains the majority of the bleaching band loss.

Combined, this implies that the component is the non-reacting population, which has a slightly different spectrum in the fingerprint region than the reacting species. This is, to my knowledge, the first time the outcome of the retinal-isomerization can be directly linked to differences in the ground-state conformation.

In addition to the published work presented above, the thesis presents some unpublished results, the first being polarization resolved transient spectra of the fingerprint region.

Here we could show, that the transition dipole of the $C_{14}-C_{15}$-stretching vibration in the initial all-trans state is almost parallel to the electronic tdm. After isomerization, the angle between the tdm's changes to approximately 20°. The measurement of the orientation of tdms is useful for assessing and comparing the quality of different theoretical models since it gives additional parameters to compare the experimental results with the theoretical predictions. If the structure is available, the direction of individual tdm's can be estimated from it by simply observing the direction of the bonds.

The usefulness of the polarization-resolved spectra gets very apparent in the identification of the origin of the ultrafast protein response in the form of an ultrafast appearing amide I band, which is one of the main findings of our results in the amide region (1700 cm^{-1} to 1520 cm^{-1}).

This band, located around 1660 cm^{-1}, is observed in all retinal based rhodopsins investigated by ultrafast IR spectroscopy so far, including BR, SR2, and ChR2. From the polarization resolved spectra we deduce that the relative angle between the observed amide I tdm and the excited electronic tdm of the retinal is around 50°. This is quite unusual, the amide I tdm's are aligned in the direction of the alpha helices, which in rhodopsins typically have an angle of about 70° to the retinal axis. Since the electronic tdm is along the retinal axis, the number of possible candidate $\nu(C=O)_\alpha$ vibrations is small.

Both, in the C1C2 structure and the *Ca*ChR1 homology model based on the C1C2-structure, only one amino acid remains. The Trp 262 is located near at the turn of the transmembrane helix, which gives the unusual direction of the C=O group. While we could pin down the origin of the band, we are still missing the explanation for the lack of a positive band belonging the amide bleaching band.

Other bands in the amide region could also be tentatively assigned. The assignment differs from prior assignments in several details. Additionally, no signal in the 1700 cm^{-1} to 1800 cm^{-1} was observed, therefore our data excludes the protonation of E162 on the observed timescale and in the ground-state.

In summary, we now have a good picture of the initial photoreaction in *Ca*ChR1, but work remains. As for other retinal rhodopsins, the interplay of the initial reaction and the later steps is still unclear.

Does the attribution of the amide I response to the tryptophan generalize to the other rhodopsins? Is the isomerization relevant for the function? Why are reactions between the photoreaction of ChR1 and ChR2 so different? It would also be interesting to apply quantum chemical calculations to ChR1 to elude the origin of the different bleaching bands, since it could open the way for ChR variants with higher quantum yields.

9.5 Initiation of reaction with IR-light

We proved, by femtosecond IR-pump IR-probe spectroscopy on a cyclohexanol-isocyanate mixture, that a bimolecular ground-state reaction can be initiated by excitation of a mode connected to the reaction coordinate like transition state theory predicts it.

The use of ultrafast spectroscopy was necessary to rule out an increased reaction rate due to the pump-induced heating. I observed the product creation with a similar rate as the IVR, around 10 ps. We expected such a rate since we only excite one mode which is not directly the reaction coordinate. Therefore, the energy must first relax into the modes spanning the reaction coordinate before the product can be formed.

Even in the high concentration we used, the observed yield of 0.3 % is quite low. This likely the part of the explanation why nobody else reported an IR-activated reaction before.

Several points are responsible for low yield. Firstly, we only excite one molecule in the bimolecular reaction. It is likely that the reaction coordinate has contributions of both modes, requiring energy transfer from between the reagents.

Secondly, the theoretical calculations predict two configurations, with only the minor fraction having the experimental predicted activation energy while the major fraction has an activation energy is too high to be activated by the IR-excitation.

As we mentioned above, the modes of reaction coordinate are populated by thermal relaxation of other higher-energetic modes. The funneling of energy into the RC could be a general characteristic of all efficient reactions at room temperature. This question can be studied in further since our results offer an entirely new way to probe the reaction coordinate.

If the reported result generalizes to other reactions, the implications for chemical applications cannot be understated. Especially since nothing in our data indicates that an ultrashort pulse is necessary to initiate the reaction, our findings are amplified by the recent development of mid-IR CW lasers. One could cool down a mixture of reagents, slowing any reaction down to almost a halt. A suitable IR-excitation would then initiate only the desired reaction. Applications could make use of the temporal and spatial locality of the effect, creating chemical gradients in viscose solutions and forming laser shaped polymers.

Bibliography

(1) Stensitzki, T., Muders, V., Schlesinger, R., Heberle, J. & Heyne, K. The Primary Photoreaction of Channelrhodopsin-1: Wavelength Dependent Photoreactions Induced by Ground-State Heterogeneity. *Frontiers in Molecular Biosciences* **2.** ISSN: 2296-889X. pmid: 26258130 (July 22, 2015).

(2) Stensitzki, T., Yang, Y., Berg, A., Mahammed, A., Gross, Z. & Heyne, K. Ultrafast Electronic and Vibrational Dynamics in Brominated Aluminum Corroles: Energy Relaxation and Triplet Formation. *Structural Dynamics* **3.** ISSN: 2329-7778. pmid: 27226980 (May 12, 2016).

(3) Stensitzki, T., Yang, Y., Muders, V., Schlesinger, R., Heberle, J. & Heyne, K. Femtosecond Infrared Spectroscopy of Channelrhodopsin-1 Chromophore Isomerization. *Structural Dynamics* **3,** 043208. ISSN: 2329-7778 (July 1, 2016).

(4) Stensitzki, T., Yang, Y., Wölke, A. L., Knapp, E.-W., Hughes, J., Mroginski, M. A. & Heyne, K. Influence of Heterogeneity on the Ultrafast Photoisomerization Dynamics of Pfr in Cph1 Phytochrome. *Photochemistry and Photobiology* **93,** 703–712. ISSN: 1751-1097 (May 1, 2017).

(5) Stensitzki, T., Yang, Y., Kozich, V., Ahmed, A. A., Kössl, F., Kühn, O. & Heyne, K. Acceleration of a Ground-State Reaction by Selective Femtosecond-Infrared-Laser-Pulse Excitation. *Nature Chemistry* **10,** 126–131. ISSN: 1755-4349 (Feb. 2018).

(6) Zahn, C., Stensitzki, T., Gerecke, M., Berg, A., Mahammed, A., Gross, Z. & Heyne, K. Ultrafast Dynamics of Sb-Corroles: A Combined Vis-Pump Supercontinuum Probe and Broadband Fluorescence Up-Conversion Study. *Molecules* **22,** 1174 (July 13, 2017).

(7) Newville, M., Stensitzki, T., Allen, D. B. & Ingargiola, A. *LMFIT: Non-Linear Least-Square Minimization and Curve-Fitting for Python* Zenodo, Sept. 21, 2014.

(8) Boyd, R. W. *Nonlinear Optics* 3rd revised edition. 640 pp. ISBN: 978-0-12-369470-6 (Elsevier Ltd, Oxford, Amsterdam ; Boston, May 13, 2008).

(9) Zheltikov, A. M. Let There Be White Light: Supercontinuum Generation by Ultrashort Laser Pulses. *Physics Uspekhi* **49,** 605–628 (June 1, 2006).

(10) Dubietis, A., Tamošauskas, G., Šuminas, R., Jukna, V. & Couairon, A. Ultrafast Supercontinuum Generation in Bulk Condensed Media (Invited Review). arXiv: 1706.04356 [physics] (June 14, 2017).

(11) Hamm, P. & Zanni, M. T. *Concepts and Methods of 2d Infrared Spectroscopy* 286 pp. ISBN: 978-1-107-00005-6 (Cambridge University Pres, Cambridge ; New York, 2011).

(12) Kowalewski, M., Fingerhut, B. P., Dorfman, K. E., Bennett, K. & Mukamel, S. Simulating Coherent Multidimensional Spectroscopy of Nonadiabatic Molecular Processes: From the Infrared to the X-Ray Regime. *Chemical Reviews* **117,** 12165–12226. ISSN: 0009-2665 (Oct. 11, 2017).

(13) Parson, W. W. *Modern Optical Spectroscopy: With Examples from Biophysics and Biochemistry* OCLC: ocm77548352. 512 pp. ISBN: 978-3-540-37535-7 (Springer, Berlin ; New York, 2007).

(14) Linke, M., Theisen, M., von Haimberger, T., Madjet, M. E.-A., Zacarias, A., Fidder, H. & Heyne, K. Determining the Three-Dimensional Electronic Transition Dipole Moment Orientation: Influence of an Isomeric Mixture. *ChemPhysChem* **11.** 00008, 1283–1288. ISSN: 14394235 (Apr. 2010).

(15) Rubtsova, N. I. & Rubtsov, I. V. Vibrational Energy Transport in Molecules Studied by Relaxation-Assisted Two-Dimensional Infrared Spectroscopy. *http://dx.doi.org/10.1146/annurev-physchem-040214-121337* **Annunal Reviews** (Apr. 1, 2015).

(16) Heyne, K., Huse, N., Nibbering, E. T. J. & Elsaesser, T. Coherent Vibrational Dynamics of Intermolecular Hydrogen Bonds in Acetic Acid Dimers Studied by Ultrafast Mid-Infrared Spectroscopy. *Journal of Physics: Condensed Matter* **15,** S129. ISSN: 0953-8984 (2003).

(17) Heyne, K., Huse, N., Dreyer, J., Nibbering, E. T. J., Elsaesser, T. & Mukamel, S. Coherent Low-Frequency Motions of Hydrogen Bonded Acetic Acid Dimers in the Liquid Phase. *The Journal of Chemical Physics* **121,** 902–913. ISSN: 0021-9606. pmid: 15260622 (July 8, 2004).

(18) Yang, Y. *Echtzeitverfolgung der ultraschnellen Strukturänderungen der Pr und Pfr Photoisomerisierungen in Phytochrom* (Freie Universität Berlin, Freie Universität Berlin, Germany, 2017).

(19) Linke, M. *Analyse von Photorezeptoren und Antennenpigmenten mit Ultraschneller Polarisationsaufgelöster Infrarotspektroskopie* (Freie Universität Berlin, Freie Universität Berlin, Germany, 2012).

(20) Kaindl, R. A., Wurm, M., Reimann, K., Hamm, P., Weiner, A. M. & Woerner, M. Generation, Shaping, and Characterization of Intense Femtosecond Pulses Tunable from 3 to 20 Mm. *JOSA B* **17,** 2086–2094. ISSN: 1520-8540 (Dec. 1, 2000).

(21) Stenstitzki, T. Polarisationsaufgelöste Femtosekundenspektroskopie an Aluminium-Corrolen (2010).

(22) Wilhelm, T., Piel, J. & Riedle, E. Sub-20-Fs Pulses Tunable across the Visible from a Blue-Pumped Single-Pass Noncollinear Parametric Converter. *Optics Letters* **22,** 1494–1496. ISSN: 1539-4794 (Oct. 1, 1997).

(23) Wilson, G. *et al.* Best Practices for Scientific Computing. *PLoS Biology* **12** (ed Eisen, J. A.) e1001745. ISSN: 1545-7885 (Jan. 7, 2014).

(24) Fischler, M. A. & Bolles, R. C. Random Sample Consensus: A Paradigm for Model Fitting with Applications to Image Analysis and Automated Cartography. *Commun. ACM* **24,** 381–395. ISSN: 0001-0782 (June 1981).

(25) Seabold, S. & Perktold, J. *Statsmodels: Econometric and Statistical Modeling with Python* in *Proceedings of the 9th Python in Science Conference* **57** (2010), 61.

(26) Moler, C. & Van Loan, C. Nineteen Dubious Ways to Compute the Exponential of a Matrix, Twenty-Five Years Later. *SIAM Review* **45,** 3–49. ISSN: 0036-1445 (Jan. 1, 2003).

(27) Mullen, K. M. *Separable Nonlinear Models: Theory, Implementation and Applications in Physics and Chemistry* (Vrije Universiteit, Amsterdam).

(28) Marciniak, H. & Lochbrunner, S. On the Interpretation of Decay Associated Spectra in the Presence of Time Dependent Spectral Shifts. *Chemical Physics Letters* **609,** 184–188. ISSN: 00092614 (Aug. 2014).

(29) Holzwarth, A. R. in *Biophysical Techniques in Photosynthesis* 75–92 (Springer, Dordrecht, 1996). ISBN: 978-0-7923-3642-6 978-0-306-47960-1.

(30) Slavov, C., Hartmann, H. & Wachtveitl, J. Implementation and Evaluation of Data Analysis Strategies for Time-Resolved Optical Spectroscopy. *Analytical Chemistry* **87,** 2328–2336. ISSN: 0003-2700 (Feb. 17, 2015).

(31) Dorlhiac, G. F., Fare, C. & van Thor, J. J. PyLDM - An Open Source Package for Lifetime Density Analysis of Time-Resolved Spectroscopic Data. *PLoS computational biology* **13,** e1005528. ISSN: 1553-7358. pmid: 28531219 (May 2017).

(32) Groma, G. I., Heiner, Z., Makai, A. & Sarlós, F. Estimation of Kinetic Parameters from Time-Resolved Fluorescence Data: A Compressed Sensing Approach. *RSC Advances* **2.** 00006, 11481. ISSN: 2046-2069 (2012).

(33) Johnson, A. & Price, R. The Synthesis of Derivatives of Corrole (Pentadehydrocorrin). *Journal of the Chemical Society.* 00033, 1649–1653 (1960).

(34) Gross, Z., Galili, N. & Saltsman, I. Erste Direkte Synthese von Corrolen Aus Pyrrol. *Angewandte Chemie* **III.** 00064, 1530–1533. ISSN: 0044-8249 (May 1999).

(35) Paolesse, R., Mini, S., Sagone, F., Boschi, T., Jaquinod, L., Nurco, D. J. & Smith, K. M. 5,10,15-Triphenylcorrole: A Product from a Modified Rothemund Reaction. *Chemical Communications.* 00000, 1307–1308. ISSN: 13597345 (1999).

(36) Schweyen, P., Brandhorst, K., Wicht, R., Wolfram, B. & Bröring, M. The Corrole Radical. *Angewandte Chemie International Edition* **54,** 8213–8216. ISSN: 1521-3773 (July 6, 2015).

(37) Yadav, P., Rathi, P. & Sankar, M. Facile Generation of A2B Corrole Radical Using Fe(III) Salts and Its Spectroscopic Properties. *ACS Omega* **2,** 959–965. ISSN: 2470-1343 (Mar. 31, 2017).

(38) Aviv, I. & Gross, Z. Corrole-Based Applications. *Chemical Communications,* 1987. ISSN: 1359-7345 (2007).

(39) Teo, R. D., Hwang, J. Y., Termini, J., Gross, Z. & Gray, H. B. Fighting Cancer with Corroles. *Chemical Reviews* **117,** 2711–2729. ISSN: 0009-2665 (Feb. 22, 2017).

(40) Yang, Y. *et al.* Assignment of Aluminum Corroles Absorption Bands to Electronic Transitions by Femtosecond Polarization Resolved VIS-Pump IR-Probe Spectroscopy. *The Journal of Physical Chemistry A* **116,** 1023–1029. ISSN: 1089-5639 (Jan. 26, 2012).

(41) Rockwell, N. C. & Lagarias, J. C. A Brief History of Phytochromes. *Chemphyschem : a European journal of chemical physics and physical chemistry* **11,** 1172–1180. ISSN: 1439-4235. pmid: 20155775 (Apr. 26, 2010).

(42) Sharrock, R. A. The Phytochrome Red/Far-Red Photoreceptor Superfamily. *Genome Biology* **9,** 230. ISSN: 1465-6906. pmid: 18771590 (2008).

(43) Takala, H. *et al.* Signal Amplification and Transduction in Phytochrome Photosensors. *Nature* **509,** 245. ISSN: 1476-4687 (Apr. 30, 2014).

(44) Nagano, S. From Photon to Signal in Phytochromes: Similarities and Differences between Prokaryotic and Plant Phytochromes. *Journal of Plant Research* **129,** 123–135. ISSN: 0918-9440, 1618-0860 (Mar. 1, 2016).

(45) Yang, Y. *et al.* Real-Time Tracking of Phytochrome's Orientational Changes During Pr Photoisomerization. *Journal of the American Chemical Society* **134,** 1408–1411. ISSN: 0002-7863 (Jan. 25, 2012).

(46) Hegemann, P. Algal Sensory Photoreceptors. *Annual Review of Plant Biology* **59,** 167–189. ISSN: 1543-5008, 1545-2123 (June 2008).

(47) Hegemann, P. & Nagel, G. From Channelrhodopsins to Optogenetics. *EMBO Molecular Medicine* **5,** 173–176. ISSN: 1757-4676. pmid: 23339069 (Feb. 2013).

(48) Boyden, E. S. A History of Optogenetics: The Development of Tools for Controlling Brain Circuits with Light. *F1000Prime Rep* **3.** pmid: 21876722 (May 3, 2011).

(49) Lim, D. H., LeDue, J., Mohajerani, M. H., Vanni, M. P. & Murphy, T. H. Optogenetic Approaches for Functional Mouse Brain Mapping. *Frontiers in Neuroscience* **7.** ISSN: 1662-453X (2013).

(50) Kato, H. E. *et al.* Crystal Structure of the Channelrhodopsin Light-Gated Cation Channel. *Nature* **482,** 369–374. ISSN: 1476-4687. pmid: 22266941 (Jan. 22, 2012).

(51) Herbst, J. Femtosecond Infrared Spectroscopy of Bacteriorhodopsin Chromophore Isomerization. *Science* **297,** 822–825. ISSN: 00368075, 10959203 (Aug. 2, 2002).

(52) Moltke, S., Alexiev, U. & Heyn, M. P. Kinetics of Light-Induced Intramolecular Charge Transfer and Proton Release in Bacteriorhodopsin. *Israel Journal of Chemistry* **35,** 401–414. ISSN: 00212148 (1995).

(53) McCamant, D. W., Kukura, P. & Mathies, R. A. Femtosecond Stimulated Raman Study of Excited-State Evolution in Bacteriorhodopsin. *The Journal of Physical Chemistry B* **109,** 10449–10457. ISSN: 1520-6106, 1520-5207 (May 2005).

(54) Schenkl, S., van Mourik, F., van der Zwan, G., Haacke, S. & Chergui, M. Probing the Ultrafast Charge Translocation of Photoexcited Retinal in Bacteriorhodopsin. *Science* **309,** 917–920. ISSN: 0036-8075, 1095-9203. pmid: 16081732 (Aug. 5, 2005).

(55) Kawamura, I., Degawa, Y., Yamaguchi, S., Nishimura, K., Tuzi, S., Saitô, H. & Naito, A. Pressure-Induced Isomerization of Retinal on Bacteriorhodopsin as Disclosed by Fast Magic Angle Spinning NMR†. *Photochemistry and Photobiology* **83,** 346–350. ISSN: 1751-1097 (Mar. 1, 2007).

(56) Verhoefen, M.-K., Bamann, C., Blöcher, R., Förster, U., Bamberg, E. & Wachtveitl, J. The Photocycle of Channelrhodopsin-2: Ultrafast Reaction Dynamics and Subsequent Reaction Steps. *ChemPhysChem* **11,** 3113–3122. ISSN: 1439-7641 (Oct. 4, 2010).

(57) Neumann-Verhoefen, M.-K., Neumann, K., Bamann, C., Radu, I., Heberle, J., Bamberg, E. & Wachtveitl, J. Ultrafast Infrared Spectroscopy on Channelrhodopsin-2 Reveals Efficient Energy Transfer from the Retinal Chromophore to the Protein. *Journal of the American Chemical Society* **135,** 6968–6976. ISSN: 0002-7863 (May 8, 2013).

(58) Scholz, F., Bamberg, E., Bamann, C. & Wachtveitl, J. Tuning the Primary Reaction of Channelrhodopsin-2 by Imidazole, pH, and Site-Specific Mutations. *Biophysical Journal* **102,** 2649–2657. ISSN: 1542-0086. pmid: 22713581 (June 6, 2012).

(59) Muders, V., Kerruth, S., Lórenz-Fonfría, V. A., Bamann, C., Heberle, J. & Schlesinger, R. Resonance Raman and FTIR Spectroscopic Characterization of the Closed and Open States of Channelrhodopsin-1. *FEBS Letters* **588,** 2301–2306. ISSN: 1873-3468 (June 27, 2014).

(60) Ogren, J. I., Mamaev, S., Russano, D., Li, H., Spudich, J. L. & Rothschild, K. J. Retinal Chromophore Structure and Schiff Base Interactions in Red-Shifted Channelrhodopsin-1 from Chlamydomonas Augustae. *Biochemistry* **53,** 3961–3970. ISSN: 1520-4995. pmid: 24869998 (June 24, 2014).

(61) Lórenz-Fonfría, V. A. *et al.* Transient Protonation Changes in Channelrhodopsin-2 and Their Relevance to Channel Gating. *Proceedings of the National Academy of Sciences of the United States of America* **110,** E1273–1281. ISSN: 1091-6490. pmid: 23509282 (Apr. 2, 2013).

(62) Ogren, J. I., Mamaev, S., Russano, D., Li, H., Spudich, J. L. & Rothschild, K. J. Retinal Chromophore Structure and Schiff Base Interactions in Red-Shifted Channelrhodopsin-1 from *Chlamydomonas Augustae*. *Biochemistry* **53,** 3961–3970. ISSN: 0006-2960, 1520-4995 (June 24, 2014).

(63) Ogren, J. I. *et al.* Comparison of the Structural Changes Occurring during the Primary Phototransition of Two Different Channelrhodopsins from Chlamydomonas Algae. *Biochemistry* **54,** 377–388. ISSN: 0006-2960 (Jan. 20, 2015).

(64) Ogren, J. I., Yi, A., Mamaev, S., Li, H., Spudich, J. L. & Rothschild, K. J. Proton Transfers in a Channelrhodopsin-1 Studied by Fourier Transform Infrared (FTIR) Difference Spectroscopy and Site-Directed Mutagenesis. *Journal of Biological Chemistry* **290,** 12719–12730. ISSN: 0021-9258, 1083-351X. pmid: 25802337 (May 15, 2015).

(65) Heyne, K., Herbst, J., Dominguez-Herradon, B., Alexiev, U. & Diller, R. Reaction Control in Bacteriorhodopsin: Impact of Arg82 and Asp85 on the Fast Retinal Isomerization, Studied in the Second Site Revertant Arg82Ala/Gly231Cys and Various Purple and Blue Forms of Bacteriorhodopsin. *The Journal of Physical Chemistry B* **104,** 6053–6058. ISSN: 1520-6106, 1520-5207 (June 2000).

(66) Gross, R. *et al.* Primary Photoinduced Protein Response in Bacteriorhodopsin and Sensory Rhodopsin II. *Journal of the American Chemical Society* **131.** 00012, 14868–14878. ISSN: 0002-7863 (Oct. 21, 2009).

(67) Chattopadhyay, A. & Boxer, S. G. Vibrational Stark Effect Spectroscopy. *Journal of the American Chemical Society* **117,** 1449–1450. ISSN: 0002-7863 (Feb. 1, 1995).

(68) Dunning, G. T. *et al.* Reaction Dynamics. Vibrational Relaxation and Microsolvation of DF after F-Atom Reactions in Polar Solvents. *Science (New York, N.Y.)* **347.** 00000, 530–533. ISSN: 1095-9203. pmid: 25635095 (Jan. 30, 2015).

(69) J. Orr-Ewing, A. Taking the Plunge: Chemical Reaction Dynamics in Liquids. *Chemical Society Reviews* (2017).

(70) Zewail, A. H. Laser Selective Chemistry—Is It Possible? *Physics Today* **33,** 27–33. ISSN: 0031-9228, 1945-0699 (Nov. 1980).

(71) Kössl, F., Lisaj, M., Kozich, V., Heyne, K. & Kühn, O. Monitoring the Alcoholysis of Isocyanates with Infrared Spectroscopy. *Chemical Physics Letters* **621,** 41–45. ISSN: 0009-2614 (Feb. 4, 2015).

Chapter 10

Appendix

Note, the online version is missing the Nature Chemistry paper.

STRUCTURAL DYNAMICS **3**, 043210 (2016)

Ultrafast electronic and vibrational dynamics in brominated aluminum corroles: Energy relaxation and triplet formation

T. Stensitzki,[1] Y. Yang,[1] A. Berg,[2] A. Mahammed,[3] Z. Gross,[3] and K. Heyne[1,a)]

[1]*Institute of Experimental Physics, Free University Berlin, Arnimallee 14, 14195 Berlin, Germany*
[2]*Institute of Chemistry, The Hebrew University of Jerusalem, Jerusalem 91904, Israel*
[3]*Technion-Israel Institute of Technology, Schulich Faculty of Chemistry, Haifa 32000, Israel*

(Received 17 February 2016; accepted 29 April 2016; published online 12 May 2016)

We combined femtosecond (fs) VIS pump–IR probe spectroscopy with fs VIS pump–supercontinuum probe spectroscopy to characterize the photoreaction of the hexacoordinated Al(tpfc-Br_8)$(py)_2$ in a comprehensive way. Upon fs excitation at ∼400 nm in the Soret band, the excitation energy relaxes with a time constant of (250 ± 80) fs to the S_2 and S_1 electronic excited states. This is evident from the rise time of the stimulated emission signal in the visible spectral range. On the same time scale, narrowing of broad infrared signals in the C=C stretching region around 1500 cm^{-1} is observed. Energy redistribution processes are visible in the vibrational and electronic dynamics with time constants between ∼2 ps and ∼20 ps. Triplet formation is detected with a time constant of (95 ± 3) ps. This is tracked by the complete loss of stimulated emission. Electronic transition of the emerging triplet absorption band overlaps considerably with the singlet excited state absorption. In contrast, two well separated vibrational marker bands for triplet formation were identified at 1477 cm^{-1} and at 1508 cm^{-1}. These marker bands allow a precise identification of triplet dynamics in corrole systems. [http://dx.doi.org/10.1063/1.4949363]

I. INTRODUCTION

Corroles are developing class of photosensitizers with significant chemical and photophysical properties and relatively unexplored potential.[1,2] The simple and efficient procedure of corroles synthesis combined with readily tuned physical and chemical characteristics by varying the peripheral substituents,[3–6] central metal,[5,7] and axial ligands[8,9] has revived substantial interest in employing these contracted porphyrinoids in various fields. Examples for application of the corroles include dye-sensitized solar cells,[7,10] photodynamic therapy,[11–13] photodynamic detection,[14] photodynamic inactivation of mold fungi and green algae,[15,16] regular and sophisticated optical imaging,[17,18] formation of singlet oxygen for catalysis,[19–21] and corrole-based electron and energy transfer systems.[22–24] In this context, the ability to control the corrole's parameters such as fluorescence,[6,25] phosphorescence,[26–29] and singlet oxygen quantum yield,[30] energy,[31] and lifetime of their photoexcited states[26,32–34] is fundamental in optimizing the corrole based photocatalysts for their specific application.[35] However, there are very few in-depth reports on the physical and spectroscopic features of corroles. The most striking example is vibrational spectroscopy (IR, RR, and more sophisticated methods), very well established for porphyrins[36–39] but very limited for corroles.[40–43] What is more, there is only one prior publication that focused on the ultrafast vibrational processes involved therein.[44] A recent study on

a)Author to whom correspondence should be addressed. Electronic mail: Karsten.heyne@fu-berlin.de

other corrole systems investigated electronic dynamics from femtoseconds to microseconds, but a separation of singlet and triplet dynamics on the short time scale remained difficult.[45] An improved insight into the fundamental properties of post-transition metallocorroles is hence clearly required for learning how to utilize them in potentially practical applications.

II. RESULTS AND DISCUSSION

In this study, we investigated hexacoordinated aluminum(III) 2,3,7,8,12,13,17,18-octabromo-5,10,15-tris(pentafluorophenyl) corrole, Al(tpfc-Br_8)(py)$_2$, upon excitation at the high energy side of the Soret band at 400 nm. The absorption spectrum exhibits a Soret band maximum at 445 nm, and two maxima in the Q band at 600 nm and 637 nm, resulting from the $S_0 \rightarrow S_2$ transition and $S_0 \rightarrow S_1$ transition.[44] Fluorescence maxima were observed at 643 nm and 704 nm, as depicted in Fig. 1. Two pyridine ligands are located above and below the corrole plane, directly interacting with the aluminum (see Fig. 1 inset).

The electronic dynamics were studied by femtosecond VIS pump–supercontinuum probe spectroscopy on a time scale from femtoseconds to 280 ps. We investigated the dynamics in a broad spectral range from 500 nm to 975 nm with a system response of ∼100 fs. Figure 2(b) presents the difference absorbance change upon photoexcitation in a 2D map. Bleaching and stimulated emission signals (negative) are shown in blue, while increased absorption due to excited state and product bands as triplet absorption are colored in red. As displayed in Fig. 2(b), the positive signal from 500 nm to 574 nm, the positive signal from 670 nm to 975 nm, as well as the negative signal from 574 nm to 670 nm appear instantaneously upon excitation. We assign the positive signal to singlet excited state absorption, and the negative signal to bleaching absorption of the ground state. On a time scale of a few hundred femtoseconds, negative signals rise at the position of the fluorescence at around 650 nm and around 710 nm (see also Fig. 3). We assign these signals to stimulated emission. On a longer time scale of 100 ps, these stimulated emission signals vanish completely, indicating the decay of the electronic excited singlet state. On the same time scale, the bleaching signal from 570 nm to 625 nm increases, due to the loss of the singlet excited state absorption in this spectral range. This is well visible in Fig. 3 for long delay times. This demonstrates the triplet formation on a time scale of 100 ps, since the bleaching signal does not recover, while the stimulated emission signal, reflecting singlet excited state population, vanishes completely.

In Fig. 3, we display the absorbance difference spectra as a function of wavelengths at different delay times. The complete loss of stimulated emission signals around 650 nm and around 710 nm is clearly visible, enabling a definite assignment of the triplet state. Around 600 nm,

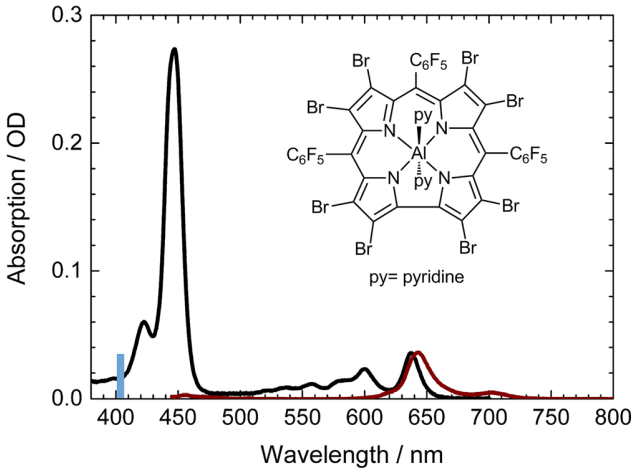

FIG. 1. Absorption spectrum (black) and emission spectrum (wine) of Al(tpfc-Br_8)(py)$_2$; excitation wavelength is indicated by a blue bar at 403 nm; inset: Molecular structure of Al(tpfc-Br_8)(py)$_2$.

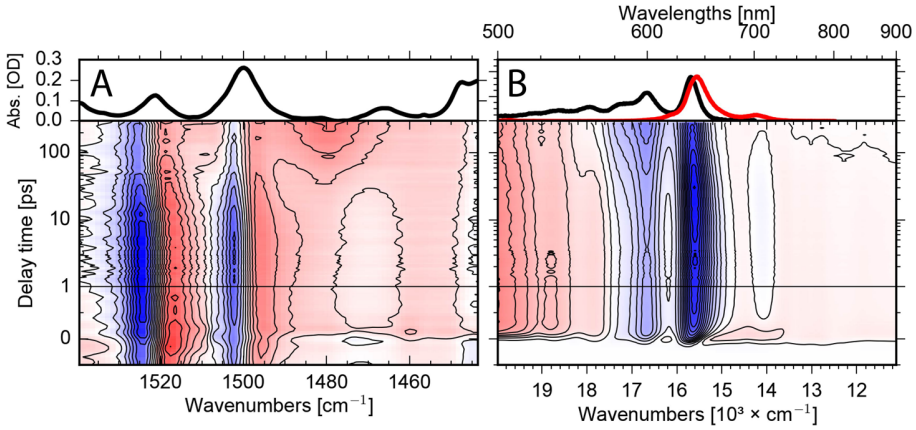

FIG. 2. A. Upper panel: Infrared absorption spectrum of Al(tpfc-Br_8)$(py)_2$ in the investigated spectral region. Lower panel: 2D map of the vibrational absorbance change upon excitation at ∼400 nm as a function of wavenumber and delay time. Negative signals (blue) indicate bleaching signals, while positive signals (red) are due to singlet excited state absorption and triplet absorption. B. Upper panel: Visible absorption spectrum of Al(tpfc-Br_8)$(py)_2$ (black line) and fluorescence signal (red line) in the investigated spectral region. Lower panel: 2D map of the absorbance change as a function of wavelengths and pump-probe delay time. Excitation at the same wavelength ∼400 nm. Positive signals (red) show excited state and triplet absorption; negative signals (blue) indicate bleaching and stimulated emission signals. The transient changes of both experiments can be compared directly.

a strong effect of the decaying singlet excited state absorption is displayed; while for wavelengths longer than ∼670 nm and for short wavelength around 500 nm, a significant positive signal remains. We attribute this remaining positive signal to triplet absorption. Triplet generation in Br_8Al(tpfc)$(py)_2$ was previously observed by the time resolved EPR studies.[5] Importantly, the spectral shape of singlet excited state absorption and triplet absorption are strongly overlapping, and thus difficult to separate.

Transients at selected wavelengths are presented in Fig. 4. At short wavelengths around 500 nm (red line, Fig. 4), the transient absorbance change is minor, because the loss of singlet excited state signal around 100 ps is compensated by the newly generated triplet signal on the same time scale. This indicates a reaction pathway from the singlet excited state to the triplet state. Transients at 550 nm (dark yellow line) and 590 nm (green line) in Fig. 4 illustrate the increase of the negative bleaching contribution on a time scale of ∼100 ps, due to the loss of

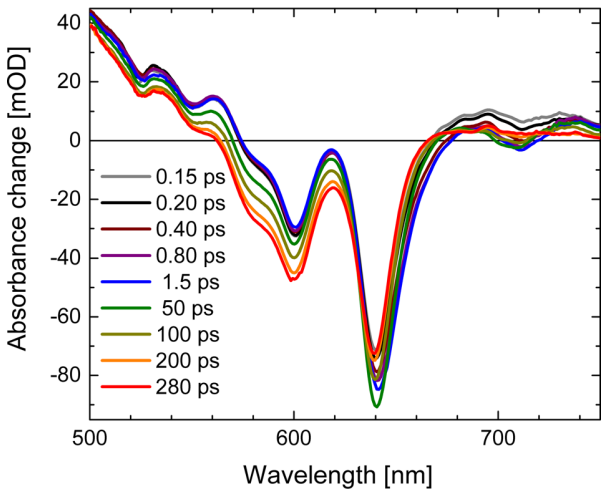

FIG. 3. Absorbance changes of Al(tpfc-Br_8)$(py)_2$ as a function of wavelength at different pump-probe delay times. Positive signals indicate increased absorption upon excitation at ∼400 nm, while negative signals are due to reduced absorption.

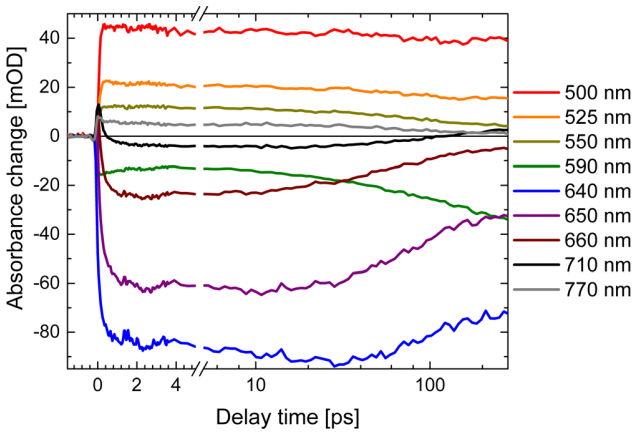

FIG. 4. Transients of the visible dataset upon excitation of Al(tpfc-Br_8)$(py)_2$ at ~400 nm (thick solid lines). Simulations of the transients are presented by thin lines.

singlet excited state absorption. In this spectral range, the triplet absorption is smaller than the singlet excited state absorption and cannot compensate the loss of positive signal anymore. At wavelengths of 640 nm (blue line), 650 nm (purple line), 660 nm (wine line), and 710 nm (black line), the negative signal rises within a few hundred femtoseconds, stays nearly constant, and decays on a time scale of ~100 ps. The transient at 770 nm (grey line) in Fig. 4 exhibits an instantaneous rise to a positive signal due to the singlet excited state absorption that decays on a time scale of ~100 ps to a smaller positive signal. The remaining positive signal is not vanishing, reflecting triplet absorption.

Global simulation of the dataset with a multi exponential approach results in three relevant time constants of $\tau_1 = (0.25 \pm 0.08)$ ps, $\tau_2 = (6 \pm 2)$ ps, $\tau_3 = (95 \pm 3)$ ps, and a constant τ_4. The decay associated spectra (DAS) for these time constants are shown in Fig. 5. Here, we can use a true sequential model with a sequence of several steps. Upon excitation, the singlet excited state in the Soret band is formed instantaneously, followed by transfer to the singlet excited state of the Q band accompanied with the rise of stimulated emission with 250 fs. On the picosecond time scale, energy relaxation processes occur in the singlet excited state, followed by a complete singlet excited state decay into the triplet manifold with 95 ps. The constant component in Figure 5 reflects the difference between ground state bleaching and triplet absorption.

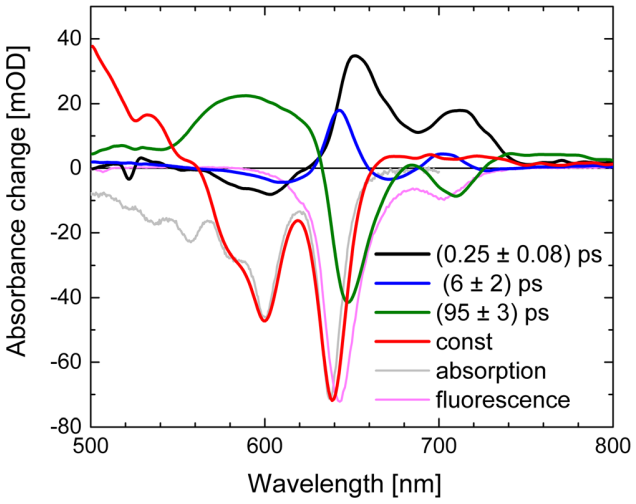

FIG. 5. Decay associated spectra (DAS) of the visible dataset upon excitation of Al(tpfc-Br_8)$(py)_2$ at ~400 nm. Absorption (grey line) and fluorescence (pink line) are scaled and plotted for comparison.

As a result of the sequential model, the presented decay associated spectra (DAS) in Figure 5 show the decay and rise of intermediate states with the given time constants.

The DAS of τ_1 (DAS_1) exhibits positive signals at the spectral positions of the fluorescence maxima, and small negative signals around 600 nm. This demonstrates that the stimulated emission rises with a time constant τ_1, and probably small excited state absorption increases around 600 nm. The DAS_2 exhibits a derivative like pattern with positive/negative contributions at 609 nm (−)/643 nm (+) and 674 nm (−)/702 nm (+) and a time constant of about 6 ps (blue line Fig. 5). This can be interpreted as cooling of vibrational modes coupled to the singlet excited state absorption, resulting in spectral shifts and narrowing of the stimulated emission. Extending the global fit to five exponentials results in splitting of DAS_2 in two contributions. This is presented in Fig. S1 with two time constants of 2 ps and 18 ps for cooling.[50] DAS_3 has negative signals at spectral positions of the fluorescence, significant positive signals around 600 nm, and small positive signals around 500 nm and 800 nm. We assign time constant τ_3 to the singlet excited state decay and triplet formation. Positive signals indicate decay of the singlet electronic excited state signal that is not compensated by the triplet absorption, and negative signals indicate the decay of the stimulated emission signal. Note that the stimulated emission signal vanishes completely, best visible at around 700 nm.

Since the stimulated emission and the electronic absorption spectra of excited state, triplet state, and ground state provide considerable spectral overlap, we decided to investigate the vibrational marker band region around 1500 cm^{-1} after excitation at ∼400 nm.[44]

The absorbance change upon excitation as a function of wavenumber and delay time is presented as a 2D map in Fig. 2(a) lower panel. Observed are pronounced bleaching signals at 1501 cm^{-1} and 1523 cm^{-1}, matching the positions of the absorption bands in Fig. 2(a) upper panel. These bleaching signals were assigned to C=C stretching vibrations $\nu(C{=}C)_1$ and $\nu(C{=}C)_2$ at 1501 cm^{-1} and 1523 cm^{-1}, respectively. The bleaching band around 1470 cm^{-1} in Fig. 2(a) is indicated by a small perturbed free induction decay signal[44] at delay times before time zero in Fig. 2(a). This negative signal is masked by positive contributions for all detected delay times up to 300 ps. Upon excitation, we observe strong positive signals red-shifted to the bleaching bands at 1501 cm^{-1} and 1523 cm^{-1} due to the vibrations in the singlet electronic excited state. We assign these vibrations to $\nu(C{=}C)_1$* and $\nu(C{=}C)_2$* vibrations in the S_1 electronic excited state. On a time scale of a few hundred femtoseconds, the positive bands show a significant broadening to lower energy frequencies. We assign this feature to excitation of higher low-frequency vibrational states in the S_1, i.e., a hot population of the observed vibrations due to fast energy redistribution of the excess energy. A striking feature in Fig. 2(a) is the decay of the $\nu(C{=}C)_1$* and $\nu(C{=}C)_2$* signals on a time scale of 100 ps, exactly the time scale when stimulated emission signal vanishes in Fig. 2(b). Accompanied with this decay, new positive signals rise at 1480 cm^{-1} and 1506 cm^{-1}. We assign the decay of the $\nu(C{=}C)_1$* and $\nu(C{=}C)_2$* absorption to a decay of the singlet excited state, and the rise of the positive signals at 1480 cm^{-1} and 1506 cm^{-1} to triplet formation. Hence, the new emerging bands at 1480 cm^{-1} and 1506 cm^{-1} represent the marker bands for a triplet state in $Al(tpfc\text{-}Br_8)(py)_2$.

In Fig. 6, the absorbance difference spectra at different delay times are presented. At early delay times, no signatures indicative of the triplet marker bands are visible. The positive signal around 1540 cm^{-1} exhibits a decay within a few picoseconds. This signal could reflect some population persisting longer in the electronic excited state of the Soret band, resulting in a strongly altered C=C stretching frequency. The early delay times from a few ps to about 30 ps are dominated by narrowing of the positive bands. The cooling effect is also visible by the spectral shift of the zero-crossings on the low energy side of the bleaching signals at 1499 cm^{-1} and 1520 cm^{-1}. These spectral shifts presented in Fig. S2 can be simulated with time constants of (1.4 ± 0.3) ps and (19 ± 3) ps.[50] This is corroborated by spectral shift of the bleaching and stimulated emission band around 650 nm (see Fig. S2) with the time constants of (1.2 ± 0.8) ps and (22 ± 2) ps.[50] The difference spectrum at 300 ps (red dots and line) in Fig. 6 mainly shows triplet absorption (positive signals) and bleaching bands (negative signals).

Fig. 7 presents the transients at selected wavenumbers: At 1516 cm^{-1} (green triangles) and 1522 cm^{-1} (yellow circles), a significant part of the dynamic changes in the sub picosecond

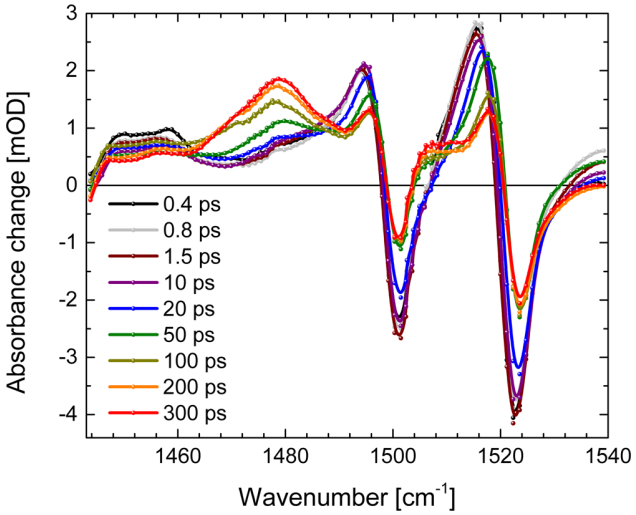

FIG. 6. Vibrational absorbance difference spectra of Al(tpfc-Br_8)$(py)_2$ as a function of wavenumber at different delay times. Positive signals are for increased absorption and negative signals for decreased absorption (bleaching bands).

time scale. On a time scale of about 20 ps positive/negative absorption pairs decay at 1495 cm^{-1} (+)/1501 cm^{-1} (−) and 1516 cm^{-1} (+)/1522 cm^{-1} (−). Positive absorption of the transients at 1480 cm^{-1} (black dots) and 1506 cm^{-1} (blue triangles) clearly increases around 100 ps, matching the triplet rise time of 95 ps in the visible data (Fig. 5).

In Fig. 8, we present DAS of the global fit of the vibrational data. We found at least five components to simulate the data. The fast component with (200 ± 100) fs decay time reflects signal decay around 1460 cm^{-1} and shifting of bands around 1500 cm^{-1} and 1520 cm^{-1}. Time constants of (2.0 ± 0.5) ps and (18 ± 3) ps show dispersive features around 1500 cm^{-1} and 1520 cm^{-1} reflecting cooling, narrowing, and spectral shifts of these bands. The spectral shifts of the zero-crossings are presented in Fig. S2.[50] Since vibrational dynamics are directly connected to its electronic dynamics, common decay times describe the same dynamics. Thus, the DAS with decay time of (80 ± 8) ps displays the decay of the singlet excited state (positive signals) and the rise of the triplet absorption (negative signals). We obtain the same results upon analyzing the lifetime map of the vibrational data (presented in Fig. S3).[50]

In summary, we propose the following photoreaction scheme presented in Fig. 9. After photoexcitation, the internal conversion in the Soret band is ultrafast, and energy relaxation into

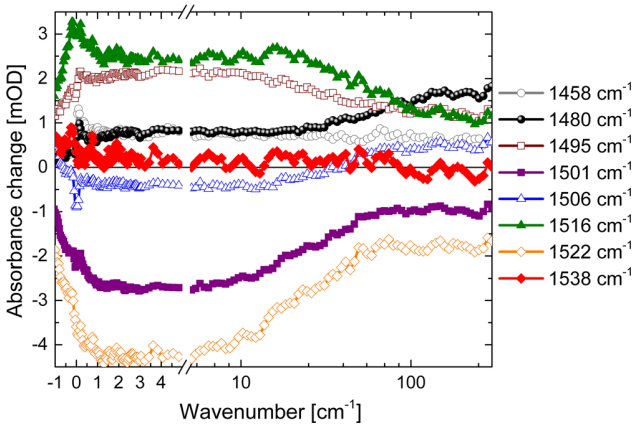

FIG. 7. Vibrational transient data at selected wavenumbers as a function of delay time upon excitation of Al(tpfc-Br_8)$(py)_2$ at ∼400 nm.

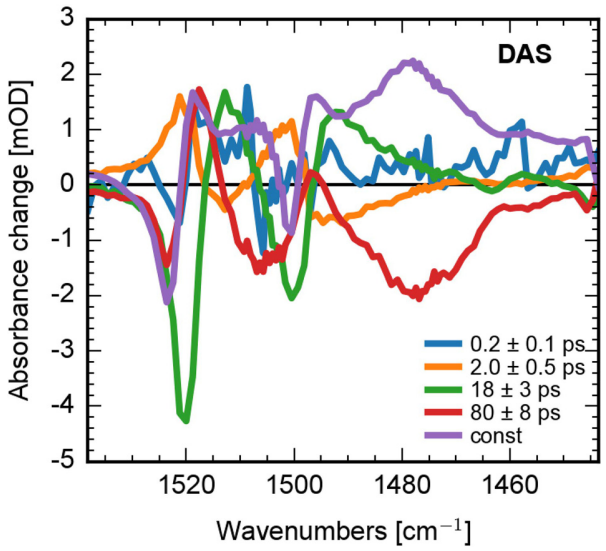

FIG. 8. Decay associated spectra of the vibrational dynamics of Al(tpfc-Br_8)$(py)_2$ upon excitation at ~400 nm. Our true sequential model allows to interpret the spectra as spectra of intermediate states increasing/decaying with the given time constant.

the Q band occurs with a time constant of 250 fs. In the Q band, energy relaxation processes on the picosecond time scale take place (see Fig. 9). With a time constant of 95 ps all population is transferred from the singlet excited state to the triplet state. We assume that this triplet state is the T_1 state, because we do not detect further relaxation processes on a time scale of 300 ps, but we cannot exclude that the populated triplet state is an excited triplet state. We conclude that 100% of the excited state population is transferred to the triplet state, since we do not observe any bleaching recovery in the 95 ps time scale, and the stimulated emission signal completely vanishes with this time constant.

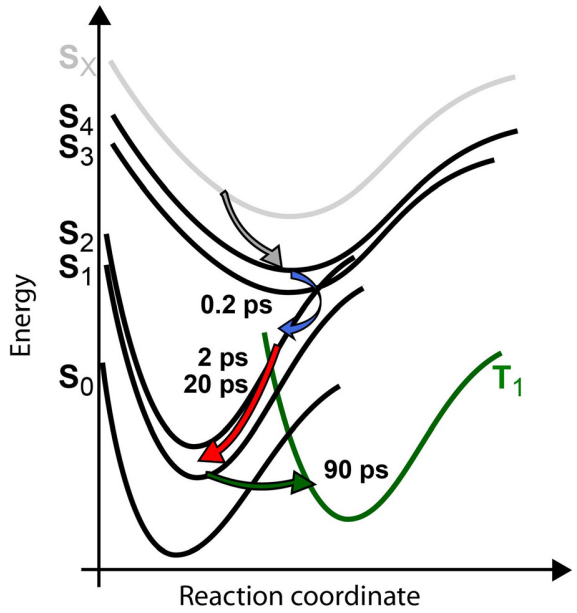

FIG. 9. Sketch of the proposed photoreaction pathways. Upon excitation, a fast relaxation to the Q band (S_1, S_2) with a time constant of 250 fs occurs, followed by energy redistribution processes with 2 ps and 20 ps. The complete excited population is transferred to the triplet state with a time constant of 95 ps.

III. CONCLUSION

We present the first comprehensive analysis of the photoreaction dynamics of a brominated corrole Al(tpfc-Br_8)$(py)_2$ by combining electronic and vibrational dynamics for the first time. We measured a very fast Soret to Q band transition with a time constant of 250 fs, which is fast compared to non-brominated Al(tpfc)py with a time constant of 500 fs,[34] and other corrole systems.[32,34,45] The energy redistribution processes occur on a picosecond time scale, similar to other corrole systems.[32,45]

Nevertheless, electronic absorption bands overlap significantly and thus prevent a clear assignment of triplet dynamics. We identified vibrational triplet marker bands at 1480 cm^{-1} and 1506 cm^{-1} as ideally suited for characterization of triplet formation and dynamics. In Al(tpfc-Br_8)$(py)_2$ triplet generation takes place with a time constant of 95 ps, significantly faster than intersystem crossing rates reported for free-base corroles and their germanium and phosphorus complexes,[32,45] and with an extraordinarily high yield of about 100%. This exceptional high triplet quantum yield can be explained by the bromine atoms introducing a strong spin-orbit coupling. Hence, Al(tpfc-Br_8)$(py)_2$ is a very promising candidate as a photosensitizer with an expected high singlet oxygen yield. The identification of vibrational marker bands for separation of singlet and triplet dynamic opens new strategies to investigate the triplet formation in corroles and related molecules.

IV. METHODS

Femtosecond laser pulses were generated starting from a fundamental femtosecond laser pulse delivered by a 1 kHz Ti:Sa laser system (Coherent Legend USP, 80 fs pulses at 800 nm). The fundamental beam was split into two parts for pump and probe pulse generation. The pump pulses were generated by second harmonic generation in a BBO crystal with a pulse energy of 0.25 μJ.

Angle balanced femtosecond polarization resolved VIS pump–IR probe measurements were applied as described elsewhere.[46,47] In short, the mid-IR probe beam is generated by a difference frequency mixing step from near-infrared signal and idler pulses generated by 800 nm fs pulses in a BBO crystal. Two reflections of the fs mid-IR pulse are taken as probe beams with different polarizations used at the same time in the same sample volume to detect absorbance changes. The system response was about 350 fs with pump focus of about 200 μm and probe focus of about 150 μm. Absorbance changes with mid-IR polarizations parallel (A_{pa}) and perpendicular (A_{pe}) to the VIS pump beam polarization were detected. Isotropic absorbance changes (A_{iso}) were calculated by $A_{iso} = (A_{pa} + 2\ A_{pe})/3$. Here, we presented only isotropic data. In the IR dataset, we observed a rising featureless background with a delay time. This background is subtracted in the presented data. The background is probably induced by long-lasting triplet generation.

For isotropic Vis pump–supercontinuum probe measurements, we used a sapphire white light supercontinuum with polarization angle between both beams set to the magic angle (54.7°). Both beams were focused into the sample cell by a curved mirror. Behind the sample, a filter (HR-800 mirror) was used to suppress the fundamental in the supercontinuum, and the beam was focused into a prism-spectrometer (Stresing GmbH) equipped with a 512 pixel InGaAs sensor. Every second pump beam was blocked by a chopper to record excited and not excited sample volumes alternatively.[48] The sample was moved perpendicular to the beam direction to minimize reexcitation. The system response was better than 100 fs (typically ~80 fs). The Al(tpfc-Br_8)$(py)_2$ was synthesized as reported previously.[5,49] Al(tpfc-Br_8)$(py)_2$ samples of about 0.008 mol/l were prepared with a maximal absorption of about 1 OD in the Q-band at 640 nm in d_8-toluene.

ACKNOWLEDGMENTS

Work performed at the Technion was supported by a grant from the Israel Science Foundation. The work at the Hebrew University of Jerusalem was supported by the KAMEA Foundation (A.B.). The work performed at the Free University of Berlin was supported by the SFB 1078, TP B3.

[1]I. Aviv and Z. Gross, Chem. Commun. **2007**, 1987.
[2]C. I. M. Santos, J. F. B. Barata, M. J. F. Calvete, L. S. H. P. Vale, D. Dini, M. Meneghetti, M. G. P. M. S. Neves, M. A. F. Faustino, A. C. Tome, and J. A. S. Cavaleiro, Curr. Org. Synth. **11**, 29 (2014).
[3]J. Vestfrid, M. Botoshansky, J. H. Palmer, A. C. Durrell, H. B. Gray, and Z. Gross, J. Am. Chem. Soc. **133**, 12899 (2011).
[4]L. Wagnert, R. Rubin, A. Berg, A. Mahammed, Z. Gross, and H. Levanon, J. Phys. Chem. B **114**, 14303 (2010).
[5]L. Wagnert, A. Berg, E. Stavitski, T. Berthold, G. Kothe, I. Goldberg, A. Mahammed, L. Simkhovich, Z. Gross, and H. Levanon, Appl. Magn. Reson. **30**, 591 (2006).
[6]C. M. Lemon, R. L. Halbach, M. Huynh, and D. G. Nocera, Inorg. Chem. **54**, 2713 (2015).
[7]B. J. Brennan, Y. C. Lam, P. M. Kim, X. Zhang, and G. W. Brudvig, ACS Appl. Mater. Interfaces **7**(19), 12728–12734 (2015).
[8]I. Aviv-Harel and Z. Gross, Coord. Chem. Rev. **255**, 717 (2011).
[9]J. Palmer, in *Molecular Electronic Structures of Transition Metal Complexes I*, edited by D. M. P. Mingos, P. Day, and J. P. Dahl (Springer, Berlin, Heidelberg, 2012), Vol. 142, p. 49.
[10]D. Walker, S. Chappel, A. Mahammed, B. S. Brunschwig, J. R. Winkler, H. B. Gray, A. Zaban, and Z. Gross, J. Porphyrins Phthalocyanines **10**, 1259 (2006).
[11]J. Y. Hwang, D. J. Lubow, J. D. Sims, H. B. Gray, A. Mahammed, Z. Gross, L. K. Medina-Kauwe, and D. L. Farkas, J. Biomed. Opt. **17**, 015003 (2012).
[12]J. F. B. Barata, A. Zamarrón, M. G. P. M. S. Neves, M. A. F. Faustino, A. C. Tomé, J. A. S. Cavaleiro, B. Röder, Á. Juarranz, and F. Sanz-Rodríguez, Eur. J. Med. Chem. **92**, 135 (2015).
[13]J. Y. Hwang, D. J. Lubow, D. Chu, J. Sims, F. Alonso-Valenteen, H. B. Gray, Z. Gross, D. L. Farkas, and L. K. Medina-Kauwe, J. Controlled Release **163**, 368 (2012).
[14]H. Agadjanian, J. Ma, A. Rentsendorj, V. Valluripalli, J. Y. Hwang, A. Mahammed, D. L. Farkas, H. B. Gray, Z. Gross, and L. K. Medina-Kauwe, Proc. Natl. Acad. Sci. U.S.A. **106**, 6105 (2009).
[15]A. Preuss, I. Saltsman, A. Mahammed, M. Pfitzner, I. Goldberg, Z. Gross, and B. J. Roder, Photochem. Photobiol. B **133**, 39 (2014).
[16]J. Pohl, I. Saltsman, A. Mahammed, Z. Gross, and B. J. Roder, Appl. Microbiol. **118**, 305 (2015).
[17]J. Y. Hwang, Z. Gross, H. B. Gray, L. K. Medina-Kauwe, and D. L. Farkas, Proc SPIE **7902**, 79020F (2011).
[18]J. Y. Hwang, S. Wachsmann-Hogiu, V. K. Ramanujan, J. Ljubimova, Z. Gross, H. B. Gray, L. K. Medina-Kauwe, and D. L. Farkas, Mol. Imaging Biol. **14**, 431 (2012).
[19]I. Luobeznova, M. Raizman, I. Goldberg, and Z. Gross, Inorg. Chem. **45**, 386 (2006).
[20]J. F. B. Barata, A. L. Daniel-da-Silva, M. G. P. M. S. Neves, J. A. S. Cavaleiro, and T. Trindade, RSC Adv. **3**, 274 (2013).
[21]L. M. Reith, M. Himmelsbach, W. Schoefberger, and G. J. Knör, Photochem. Photobiol. A: Chem. **218**, 247 (2011).
[22]L. Flamigni and D. T. Gryko, Chem. Soc. Rev. **38**, 1635 (2009).
[23]L. Giribabu, J. Kandhadi, R. K. Kanaparthi, and P. S. Reeta, J. Lumin. **145**, 357 (2014).
[24]L. Giribabu, J. Kandhadi, and R. K. Kanaparthi, J. Fluoresc. **24**(2), 569 (2014).
[25]L. Shi, H.-Y. Liu, H. Shen, J. Hu, G.-L. Zhang, H. Wang, L.-N. Ji, C.-K. Chang, and H.-F. Jiang, J. Porphyrins Phthalocyanines **13**, 1221 (2009).
[26]J. Vestfrid, I. Goldberg, and Z. Gross, Inorg. Chem. **53**, 10536 (2014).
[27]E. Rabinovich, I. Goldberg, and Z. Gross, Chem. Eur. J. **17**, 12294 (2011).
[28]J. H. Palmer, A. C. Durrell, Z. Gross, J. R. Winkler, and H. B. Gray, J. Am. Chem. Soc. **132**, 9230 (2010).
[29]J. H. Palmer, M. W. Day, A. D. Wilson, L. M. Henling, Z. Gross, and H. B. Gray, J. Am. Chem. Soc. **130**, 7786 (2008).
[30]W. Shao, H. Wang, S. He, L. Shi, K. Peng, Y. Lin, L. Zhang, L. Ji, and H. J. Liu, Phys. Chem. B **116**, 14228 (2012).
[31]A. Mahammed, B. Tumanskii, and Z. Gross, J. Porphyrins Phthalocyanines **15**, 1275 (2011).
[32]L. Zhang, Z.-Y. Liu, X. Zhan, L.-L. Wang, H. Wang, and H.-Y. Liu, Photochem. Photobiol. Sci. **14**, 953 (2015).
[33]D. Kowalska, X. Liu, U. Tripathy, A. Mahammed, Z. Gross, S. Hirayama, and R. P. Steer, Inorg. Chem. **48**, 2670 (2009).
[34]X. Liu, A. Mahammed, U. Tripathy, Z. Gross, and R. P. Steer, Chem. Phys. Lett. **459**, 113 (2008).
[35]A. Mahammed and Z. Gross, Angew. Chem. Int. Ed. **54**, 12370 (2015).
[36]S. C. Omapinyan, *Vibrational Spectroscopy of Porphyrins, Phthalocyanines and Tetraphenyl Derivatives of Group IV-A Elements* (University of East Anglia, 1997).
[37]B. M. Leu, M. Z. Zgierski, C. Bischoff, M. Li, M. Y. Hu, J. Zhao, S. W. Martin, E. E. Alp, and W. R. Scheidt, Inorg. Chem. **52**, 9948 (2013).
[38]L. M. Proniewicz, A. Bruha, K. Nakamoto, E. Kyuno, and J. R. Kincaid, J. Am. Chem. Soc. **111**, 7050 (1989).
[39]T. Kitagawa and Y. Ozaki, in *Metal Complexes with Tetrapyrrole Ligands I*, edited by J. Buchler (Springer, Berlin, Heidelberg, 1987), Vol. 64, p. 71.
[40]E. Steene, T. Wondimagegn, and A. J. Ghosh, Inorg. Biochem. **88**, 113 (2002).
[41]V. V. Mody, M. B. Fitzpatrick, S. S. Zabaneh, R. S. Czernuszewicz, M. Gałęzowski, and D. T. Gryko, J. Porphyrins Phthalocyanines **13**, 1040 (2009).
[42]I. Halvorsen, E. Steene, and A. Ghosh, J. Porphyrins Phthalocyanines **05**, 721 (2001).
[43]I. H. Wasbotten, T. Wondimagegn, and A. Ghosh, J. Am. Chem. Soc. **124**, 8104 (2002).
[44]Y. Yang, D. Jones, T. von Haimberger, M. Linke, L. Wagnert, A. Berg, H. Levanon, A. Zacarias, A. Mahammed, Z. Gross, and K. Heyne, J. Phys. Chem. A **116**, 1023 (2012).
[45]S. S. K. Raavi, J. Yin, G. Grancini, C. Soci, S. V. Rao, G. Lanzani, and L. Giribabu, J. Phys. Chem. C **119**, 28691 (2015).
[46]Y. Yang, M. Linke, T. von Haimberger, R. Matute, L. González, P. Schmieder, and K. Heyne, Struct. Dyn. **1**, 014701 (2014).
[47]L. Linke, Y. Yang, B. Zienicke, M. A. S. Hammam, T. von Haimberger, A. Zacarias, K. Inomata, T. Lamparter, and K. Heyne, Biophys. J. **105**, 1756 (2013).
[48]T. Stensitzki, V. Muders, R. Schlesinger, J. Heberle, and K. Heyne, Front. Mol. Biosci. **2**(41), 1 (2015).
[49]A. Mahammed and Z. Gross, J. Inorg. Biochem. **88**, 305 (2002).
[50]See supplementary material at http://dx.doi.org/10.1063/1.4949363 for a global fit of the visible data with four exponentials, an analysis of spectral shifts of visible and infrared data, and a lifetime map of vibrational dynamics.

Ultrafast electronic and vibrational dynamics in brominated Aluminum corroles: Energy relaxation and triplet formation

T. Stensitzki,[1] Y. Yang,[1] A. Berg,[2] A. Mahammed,[3] Z. Gross,[3] K. Heyne,[1,a)]

[1]Institute of Experimental Physics, Free University Berlin, Arnimallee 14, 14195 Berlin, Germany

[2]Institute of Chemistry, The Hebrew University of Jerusalem, Jerusalem, 91904, Israel

[3]Technion-Israel Institute of Technology, Schulich Faculty of Chemistry, Haifa, 32000, Israel

Visible data were also simulated by a global fit with five components and four decay times. The decay associated spectra (DAS) are presented in Fig. S1. The major findings are nearly identical with the results of a global fit with four components presented in Fig. 5. However, the cooling dynamics simulated by a single time constant of 6 ps in Fig. 5 (blue line) are now represented by two time constants of (0.9±0.5) ps (orange line in Fig. S1) and (16±4) ps (green line in Fig. S1). Spectrally shifting bands as observed by cooling are expected to be represented by several decay components with differing time constants.[REF] Thus, visible data and IR data can be simulated well by five components with four decay constants.

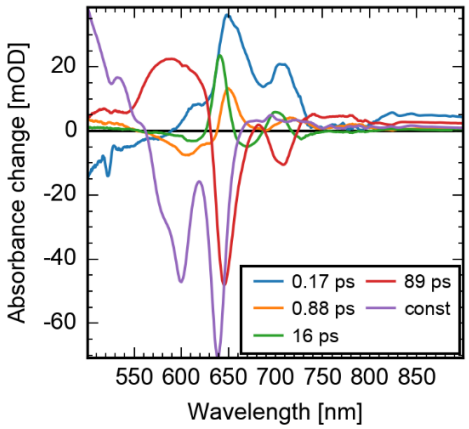

Figure S1: Decay associated spectra from a global fit with five exponentials.

Energy relaxation processes lead to cooling of electronic excited states and ground states. These hot states exhibit excess energy resulting in a non-Boltzmann population distribution of vibrational states. Low-frequency vibrational modes are excited resulting in an effective reduction of vibrational force constant, a broadening, and a frequency red shift of the observed vibration. Since excited low-frequency vibrations relax on a picosecond time scale the hot vibrational band cools down to a more narrow and blue-shifted band. This effect is presented in Fig. S2. The spectral position of the zero-crossings of the two major bleaching bands at 1520 cm^{-1} and 1499 cm^{-1} are displayed as a function of time in Fig. S2 upper panel. The zero-crossings at the low energy sides of the vibrational absorption bands show spectral shifts with time constants of (1.4±0.3) ps and (19±3) ps, matching the time constants assigned to cooling effects in Fig. 9.

In the visible data the bleaching and stimulated emission band in the spectral range from 643 nm to 660 nm show also a spectral shift visible in Fig. 3. The spectral shift of the center of mass of this spectral range is plotted as a function of time in Fig. S2 lower panel. A blue-shift of the center of mass by about 1 nm is observed with time constants of (1.2±0.8) ps and (22±2) ps. These time constants match the time constants of the cooling processes observed in the vibrational data very well, corroborating cooling processes on a time scale from 2 ps to 20 ps. Since we see no bleaching recovery in our measurement the cooling processes occur in the electronic excited state.

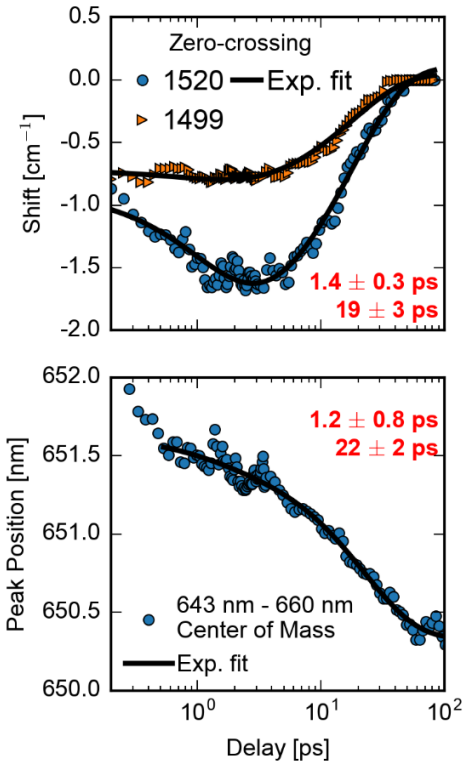

Figure S2: Upper panel: Spectral shifts of vibrations due to cooling. Lower panel: Spectral shifts of the bleaching and stimulated emission band due to cooling.

Information on the time constants of the vibrational dynamics are presented by the lifetime map in Fig. S3.The lifetime map was calculated by using the approach described in [1]. Only data with delay times longer than 300 fs was used. To generate the experimental matrix A, convoluted exponentials were simulated. Their decay constants are uniformly distributed on log-timescale going from 0.1 ps to 300 ps. With n being the number of data samples, each channel data y was fitted to the experimental matrix using L1-norm penalized least squares with the regularization parameter α:

$$\frac{1}{2n}\|y - Ax\|_2^2 + \alpha\|x\|_1$$

The choice of α = 0.004 was performed by increasing α to the point where the residuals start to show systematic behavior. The fitting was done with the Lasso-model of scikit-learn [2]. Lifetime maps are very useful for data with shifting bands [3]. The decay constants are depicted as a function of wavenumber for positive (red) and negative (blue) amplitudes. In the spectral region of about 1480 cm^{-1} we observe a negative amplitude for a decay constant of ~100 ps. This reflects the rising of a positive signal attributed to triplet formation. Similar decay constants and amplitudes are visible around 1508 cm^{-1} with negative values, and around 1520 cm^{-1} with positive values. This could indicate that the decaying positive $\nu(C{=}C)_2^*$ stretching vibration at ~ 1520 cm^{-1} is connected with the rising of the triplet $\nu(C{=}C)_2$ stretching vibration at ~ 1508 cm^{-1}. Parallel pairs of decay constants with similar slopes, positive amplitudes at lower wavenumbers, and negative amplitudes at higher wavenumbers reflect cooling processes of hot vibrational states. This can be seen around 1510 cm^{-1}, and 1520 cm^{-1} for decay constants in the range of 10 ps to 30 ps in Fig. S3. The low energy side of the positive excited state band decays, due to cooling, and the bleaching band is refilled. This results in a blue-shift of the positive vibrational absorption band and a relative blue-shift of the bleaching band, both with altering decay constants (see Fig. S3). In Figure S3 left panel the integrated amplitudes of the decay constants are plotted. Here, we observe major contributions at 90 ps, at 20 ps to 30 ps, at 2 ps, and a small contribution around 0.2 ps. These major contributions were reflected in the global analysis presented in Fig. 9.

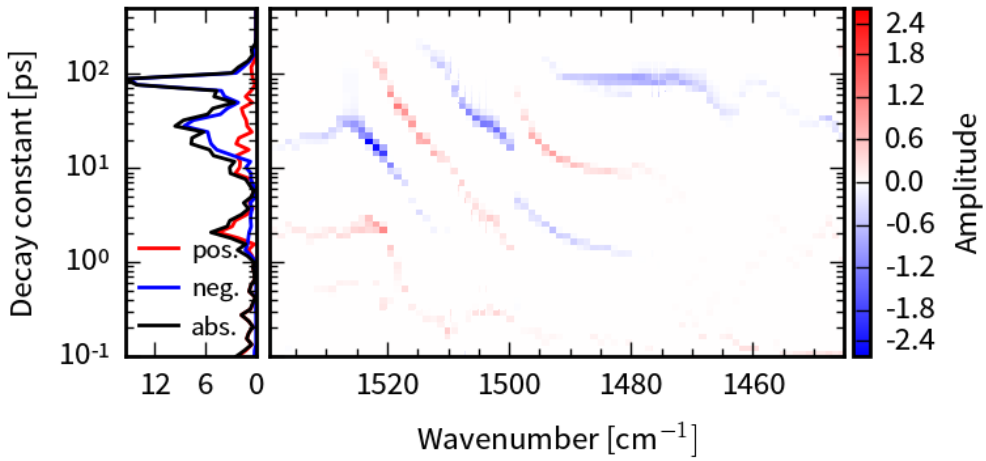

FIG. S3: Right panel: Lifetime map of the absorbance difference vibrational dynamics as a function of wavenumber and decay constants. Positive signals (red) indicate decaying positive or rising negative contributions; negative signals (blue) indicate decaying negative

or rising positive contributions. Left panel: Integrated signal over the entire wavenumber range. Strong signals represent major decay constant contributions.

REFERENCES

[1] Géza I. Groma, Zsuzsanna Heiner , András Makai and Ferenc Sarlós; Estimation of kinetic parameters from time-resolved fluorescence data: A compressed sensing approach; *RSC Adv.*, (2012) 2, 11481-11490.

[2] Pedregosa, F; Varoquaux, G; Gramfort,; Michel, V ; Thirion, B; Grisel, O; Blondel, M; Prettenhofer, P; Weiss, R; Dubourg, V; Vanderplas, J; Passos, A; Cournapeau, D; Brucher, M; Perrot, M; Duchesnay, E; Scikit-learn: Machine Learning in Python, *JMLR* (2011) 12, 2825-2830.

[3] Marciniak, H., Lochbrunner, S.; On the interpretation of decay associated spectra in the presence of time dependent spectral shifts, *Chem. Phys. Lett.,* (2014) 609, 184–188.

Photochemistry and Photobiology, 2017, 93: 703–712

Influence of Heterogeneity on the Ultrafast Photoisomerization Dynamics of Pfr in Cph1 Phytochrome†

Till Stensitzki[1], Yang Yang[1], Anna Lena Wölke[2], Ernst-Walter Knapp[2], Jon Hughes[3], Maria Andrea Mroginski[4] and Karsten Heyne*[1]

[1]Department of Physics, Free University Berlin, Berlin, Germany
[2]Institute of Chemistry and Biochemistry, Free University Berlin, Berlin, Germany
[3]Institut für Pflanzenphysiologie, Justus-Liebig Universität, Gießen, Germany
[4]Institut für Chemie, Technische Universität Berlin, Berlin, Germany

Received 12 October 2016, accepted 3 January 2017, DOI: 10.1111/php.12743

ABSTRACT

Photoisomerization of a protein-bound chromophore is the basis of light sensing and signaling in many photoreceptors. Phytochrome photoreceptors can be photoconverted reversibly between the Pr and Pfr states through photoisomerization of the methine bridge between rings C and D. Ground-state heterogeneity of the chromophore has been reported for both Pr and Pfr. Here, we report ultrafast visible (Vis) pump–probe and femtosecond polarization-resolved Vis pump–infrared (IR) probe studies of the Pfr photoreaction in native and $^{13}C/^{15}N$-labeled Cph1 phytochrome with unlabeled PCB chromophore, demonstrating different S_0 substates, Pfr-I and Pfr-II, with distinct IR absorptions, orientations and dynamics of the carbonyl vibration of ring D. We derived time constants of 0.24 ps, 0.7 ps and 6 ps, describing the complete initial photoreaction. We identified an isomerizing pathway with 0.7 ps for Pfr-I, and silent dynamics with 6 ps for Pfr-II. We discuss different origins of the Pfr substates, and favor different facial orientations of ring D. The model provides a quantum yield for Pfr-I of 38%, in line with ~35% ring D rotation in the electronic excited state. We tentatively assign the silent form Pfr-II to a dark-adapted state that can convert to Pfr-I upon light absorption.

INTRODUCTION

Phytochromes are a family of red/far-red photochromic biliprotein photoreceptors mediating photomorphogenesis and floral induction in plants and various light responses in bacteria and fungi (1–3). The bilin (linear tetrapyrrole) chromophore is covalently linked to the protein at a cysteine residue either in the GAF domain (as in plant and Cph1-like phytochromes from cyanobacteria) or near the N-terminus (as in bacteriophytochromes). Two thermodynamically stable parent states, namely the far-red-absorbing Pfr state and the red-absorbing lowest energy state Pr (4–7), are converted via distinct photoreactions. The chromophore adopts ZZZssa and ZZEssa geometries in the Pr and Pfr states, respectively. Upon Pr photoexcitation (ZZZssa → ZZEssa), photoisomerization is observed with a time constant of 30 ps, corresponding to Lumi-R formation (8). In contrast, photoexcitation of Pfr shows a much faster time constant of 0.7 ps for ZZEssa → ZZZssa photoisomerization, corresponding to Lumi-F formation. In both cases, isomerization of the C15=C16 double bond leads to rotation of ring D. In contrast to the extremely high extinction coefficients of the phytochrome family, commensurate with the biological role of photoreceptors, the measured quantum yield of photoconversion for both Pr→Pfr and Pfr→Pr is surprisingly low (~15%). In contrast, retinal based photoreceptors, that is rhodopsin, show quantum yields of about 60%. One explanation would be that phytochrome exhibits different ground states with distinct quantum yields, explaining the low average yield (5,9–11). Recent studies revealed ground-state heterogeneity of the Pr form in Cph1 from the cyanobacterium *Synechocystis* 6803 as well as oat phytochrome A3 (11–13) and identified an active conformation with photoreaction quantum yield of about 30% (8). Two Pfr substates (Pfr-I and Pfr-II) were found forming a temperature-dependent conformational equilibrium, differing in structural details of the *C-D* and *A-B* methine bridges: In Pfr-I, the angle between the rings *C* and *D* is ~10° larger than in Pfr-II, whereas the angle between rings A and B is smaller (14). Although ground-state heterogeneity was observed for Pfr, the connection between photodynamics and structural differences at the atomic level remains unclear. Whereas precise structural information is available for Cph1Δ2 (the N-terminal 1- to 514-residue sensory module of Cph1) as Pr from magic angle spinning NMR and X-ray diffraction studies (11,15), equivalent information for Pfr is not available. The electronic dynamics of the Pfr photoreaction were described by two decay times in the range from 300 fs to 600 fs and 2 ps to 5 ps (16,17), matching the reported photoreaction time constants in plant phytochrome phyA (18). The complex electronic Pfr photoreaction dynamics of Cph1 were described with a model involving two subpopulations with 6% and 94% occupancy, respectively. The major component showed a Lumi-F photoproduct generation with a time constant of 1.5 ps and a hot ground-state generation with decay constants of 770 fs and 2.8 ps (17). Because electronic state dynamics of phytochromes are spectrally complex, we analyzed the system by combining electronic state dynamics measured by femtosecond (fs) visible (Vis) pump–supercontinuum Vis probe spectroscopy with angle-balanced polarization-resolved femtosecond Vis pump–infrared (IR) probe spectroscopy (19). This

*Corresponding author e-mail: karsten.heyne@fu-berlin.de (Karsten Heyne)
†This article is a part of the Special Issue dedicated to Dr. Wolfgang Gärtner on the occasion of his 65th birthday.

allows us to separate electronic dynamics from photoproduct generation and hot ground-state relaxation (20,21). Ultrafast IR spectroscopy is an ideal tool to identify the appearance of photoproduct bands upon photoexcitation (22–25). Furthermore, polarization-resolved fs Vis pump–IR probe measurements provide additional information on the angle between electronic transition dipole moment (tdm) and the vibrational transition dipole moment (vtdm), fixed within a given molecular structure. In combination with structural models and DFT calculations, providing vibrational frequencies and vibrational tdms, polarization-resolved data can provide structural information on both ground and excited states and allow structural changes to be tracked. This was demonstrated by tracking ring D orientation during photoisomerization of Pr and Pfr in Cph1Δ2. Together with photoproduct generation, photoisomerization time constants were determined to be 30 ps and 0.7 ps for Pr and Pfr, respectively (8,26).

Upon excitation of Pfr, we investigated electronic dynamics in a broad spectral range from 500 nm to 1060 nm, as well as polarization-resolved vibrational dynamics from 1610 to 1740 cm^{-1}. In combination with structural models for the Pfr binding pocket and DFT calculations, we identified different excited-state dynamics related to distinct S_0 substates with differing hydrogen bond patterns or chromophore conformations.

MATERIALS AND METHODS

Model building. A structural model for the Pfr state of the photosensory domain of Cph1 was built by homology modeling using the 3D structure of PaBphB phytochrome from *Pseudomonas aeruginosa* (Protein Data Bank code 3C2W) as template (27). The MODELER suite was employed for this purpose (28). Initial structure alignment between Cph1 (UniProtKB entry:PHY1_SYNY3) and PaBphB (UniProtKB entry: BPHY_PSEAE), sharing 29% sequence identity, was based on PSI-BLAST sequence alignment. The biliverdin chromophore in PaBphB was manually modified into a phycocyanobilin (PCB) molecule. Two conformations of PCB were considered, namely with up- and down-orientations of the D ring N-H groups with respect to the coplanar rings A, B and C (see Figures S8, S9, S10 and S11).

Missing residues at the G462-K466 turn and P72-T82, M99-N102 and L147-N152 loops were added by hand. Their positions were optimized in the following modeling steps. Hydrogen atoms were added to the structural model of heavy atoms by means of the Karlsberg+ software (29), assuming pH 7. Within this procedure, the H260 that directly interacts with the PCB chromophore was protonated at Nε, in agreement with NMR observations (11). The entire system was solvated in a box of thermally equilibrated TIP3P water molecules. Water molecules whose oxygen atoms were closer than 2.8 Å to any nonhydrogen atom of the protein were removed. In a first step of structure relaxation, only water molecules were energy-minimized, while protein atoms were fixed. Next, all atoms of the system were included in energy minimization. Then, a 5 ns molecular dynamics simulation (MD) was performed for thermal equilibration. The MD simulations were carried out with the CHARMM32b2 program (30), using the CHARMM22 force field with periodic boundary conditions and an isothermal–isobaric (NTP) ensemble at 300K (31). During the equilibration phase, the backbone atoms of Cph1 were constrained to their positions after energy minimization and the geometry of the PCB chromophore was held fixed in a ZZEssa methine bridge geometry, as expected for a Pfr state.

The two structures of the PCB chromophore and its immediate environment were further optimized using a hybrid DFT/CHARMM approach using the Chemshell program (32). Here, the PCB chromophore together with the side chains of the ligating Cys259, Asp207, Tyr263, Ser474 and pyrrole water (117 atoms in total) was described at the B3LYP/6-31G* level of quantum chemical theory. The remaining residues as well as the solvent were modeled by the CHARMM22 force field. Only residues within a 20 Å sphere from the N(C) nitrogen of PCB were free to move during energy minimization following the laws of molecular mechanics, while the rest were kept fixed at their original positions.

Vibrational frequencies and transition dipole moments. The DFT/CHARMM optimized structures of PCB were used as input for frequency calculations and computation of electronic and vibrational transition dipole moments. In all these calculations, the protein environment is described as a cloud of atomic point charges from the CHARMM force field. This procedure has been described elsewhere (33,34). A listing of all calculated vibrational modes and their IR intensity is given in the Supporting Information (Figure S12). Transition dipole moments of electronic transitions were calculated by time-dependent (TD)-DFT theory. The relative angle between the electronic transition dipole moment (tdm) and specific vibrational transition dipole moments (vtdm) can be extracted directly from the calculations. These calculations were made using the Gaussian09 software (35).

Vis pump–IR probe spectroscopy. Pump and probe pulses were generated using nonlinear optical methods. By difference frequency mixing in various steps, we obtained mid-IR pulses of 200 fs (FWHM) or shorter at a repetition rate of 1.088 kHz. Simultaneously, laser pulses of 200 fs duration at 710 nm were generated and used to photoexcite the sample at Pfr λ_{max}, thus initiating the photoreaction. Photoselection experiments were performed using focal pump pulse diameters of ~500 μm, sample thickness of 50 μm, focal probe pulse diameters of 180 μm and pump pulse energies of 350 nJ. This resulted in excitation coefficients of below 10%. Angle-balanced polarization-resolved femtosecond Vis pump–IR probe spectroscopy was used in which transient absorption was simultaneously probed by two mid-IR pulses with polarizations oriented parallel and perpendicular to the pump pulse polarization at specific orientations (14,26). Probe pulses were dispersed with an imaging spectrograph and recorded with a 2 × 32 element MCT array detector (20). The system response was measured to be ~300 fs using a thin Ge plate in identical sample holders. Background illumination at ~640 nm by a diode laser yielded Pfr up to ~70% occupancy, whereas pump irradiation at ~710 nm specifically excited the Pfr fraction (see Figure S1). The high repetition rate required that the sample be moved across the focused laser beams with a Lissajous sample cell in order to avoid multiple excitation of a specific sample volume.

1 Isotropic conditions: Absorbance changes with mid-IR polarizations parallel ($A_{\parallel}$) and perpendicular ($A_{\perp}$) to the VIS pump beam polarization were detected. Isotropic absorbance changes (A_{iso}) were calculated by $A_{iso} = (A_{\parallel} + 2\,A_{\perp})/3$.
2 Polarization-resolved conditions: Absorbance changes with mid-IR polarizations parallel ($A_{\parallel}$) and perpendicular ($A_{\perp}$) to the VIS pump beam polarization were detected.
3 Sample preparation: We assembled $^{13}C/^{15}N$-labeled Cph1Δ2 apophytochrome with nonlabeled PCB chromophore to yield holoprotein which was then purified and concentrated in solution at an optical density of about 0.25 OD at 710 nm in D_2O, as described previously (36–38). Isotopic labeling of the protein results in shifting all ν(C=O), ν(C=C) and ν(C=N) stretching vibrations of the protein to frequencies lower than 1670 cm^{-1}. For Vis pump–Vis probe experiments unlabeled Cph1Δ2 in H_2O was prepared as described (39).

Vis pump–Vis supercontinuum probe spectroscopy. The sample was excited with femtosecond excitation pulses at 710 nm. These were generated starting from a fundamental femtosecond laser pulse delivered by a 1 kHz Ti:Sa laser system (Coherent Legend USP, 80 fs pulses at 800 nm). The fundamental beam was split into two parts for pump and probe pulse generation. The pump pulses were generated in a noncollinear optical parametric amplifier (NOPA). A sapphire white light supercontinuum was used as seed, amplified in a BBO crystal by frequency doubled pulses at 400 nm. The instrument response function was ~100 fs. We selected energies to excite the sample of about 400–500 nJ per pulse with a pump focus diameter of ~300 μm. At an optical density of ~0.25 OD in the absorption maximum, we thereby excited about 10% of the sample. The fundamental for the probe pulses was first directed over an optical delay line, then focused into a 2 mm Nd:YAG crystal inducing self-phase modulation and generating the broadband white light supercontinuum from ~480 nm to ~1300 nm for probing. A HR-800 mirror was used to filter out most of the 800 nm fundamental subsequently. Probe wavelengths from 499 nm to 1060 nm were selected. Both beams were focused into the sample cell, the probe by a 250 mm concave mirror and the pump with a 200 mm lens. The beam was than focused into a prism spectrometer (Stresing GmbH Berlin)

equipped with a CCD camera system equipped with two 512 pixel NIR-CCDs (Hamamatsu G9212-512). The spectral resolution ranged from 0.6 nm at 500 nm, to 3 nm at 1060 nm. Every second pump beam was blocked by a chopper to record excited and nonexcited sample volumes alternately. As polarization effects were found to be negligible, pump and probe beams were polarized perpendicularly to reduce stray light. The sample cell thickness was 100 µm, and the sample was rapidly moved perpendicular to the beam direction by a Lissajous scanner to provide a fresh sample at every shot.

RESULTS

Calculations

Two structural models were developed for the Pfr chromophore structure within the protein binding pocket, with the PCB N-H group of ring D in an up- and down-orientation, presented in Fig. 1b and a, respectively (see also Figures Figures S8, S9, S10 and S11). NMR data reported that (C=O)[207b], the backbone carbonyl group of Asp207, forms hydrogen bonds with the N-H groups at rings A, B and C (11). In the down-model (Fig. 1a), this corresponds to distances between the backbone oxygen of Asp207 and the hydrogen atoms of the N-H groups at rings A, B and C of 2.77 Å, 1.85 Å and 3.03 Å, respectively. Moreover, hydrogen bonds were reported between the carboxyl group oxygens of Asp207 and the N-H group of ring D, as well as between the hydroxyl group of Tyr263 (OH)[263] and the C_{19}=O carbonyl group of ring D (11). This is also reflected in the down-model with hydrogen bond distances of 1.85 Å and 3.15 Å between (COO^-)[207] and the hydrogen of the N-H group of ring D, and the OH[263] and the C_{19}=O group of ring D, respectively. The down-model agrees well with the reported NMR data. Both down- and up-models were used to investigate direct interactions between the chromophore and the surrounding protein. The excitation energy predicted at 2.03 eV (611 nm) is only 0.3 eV (105 nm) overestimated with respect to the experimental value of 1.76 eV (704 nm). The relative angle between the electronic transition dipole moment (tdm) and specific vibrational transition dipole moments (vtdm) was extracted from the calculations. For the lowest energy electronic excitation, the angle between the electronic tdm and vtdms of the carbonyl groups of the chromophore was determined to be 35° and 40°, and 41° and 48° for the stretching vibrations of $\nu(C_1{=}O)$ of ring A and of $\nu(C_{19}{=}O)$ of ring D of the down- and up-conformations, respectively. Moreover, the relative angle between electronic tdm and vtdm of the stretching vibration ν(C=O)[207b] of the backbone carbonyl vibration of Asp207 connected to the N-H groups of rings A, B and C was calculated to be 60.4° and 70.2° for the down- and up-conformations, respectively. This angle is for both conformations larger than the magic angle of 54.7°, resulting in different signal strengths for parallel and perpendicularly polarized absorption signals in polarization-resolved experiments. While the parallel signal is stronger than the perpendicular one for angles below the magic angle, the perpendicular signal is stronger in that range.

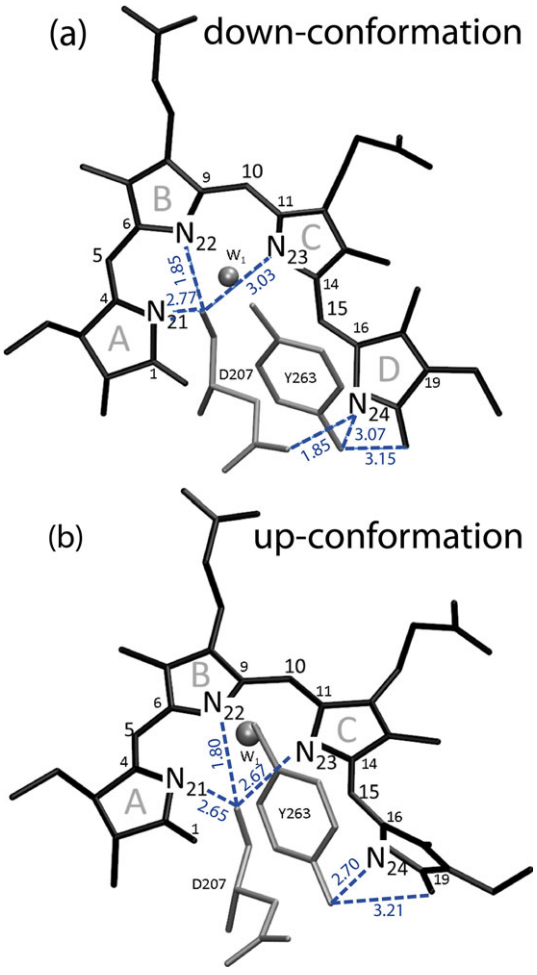

Figure 1. Structural models of the phycocyanobilin (PCB) chromophore, Asp207, Tyr263 and a pyrrole water W_1 (gray bullet). (a) Down-conformation; (b) up-conformation; hydrogen bonds and distances are indicated by blue dashed lines, and blue numbers in Å, respectively. (Stereo views are presented in Figures S8 and S9.)

Vis pump–IR probe spectroscopy

Steady-state FTIR difference spectroscopy on thermal stable and cryo-trapped intermediates provided essential information on the position of the C=O stretching vibrations of the PCB chromophore in D_2O (40). Experiments with a PCB chromophore isotopically labeled with ^{18}O at the carbonyl group of ring A identified the C_1=O stretching vibration at about 1722 cm^{-1} in the Pfr form (41). The C_{19}=O stretching vibration of ring D was found to absorb around 1700 cm^{-1} in the Pfr and Pr forms, and around 1720 cm^{-1} in the cryo-trapped Lumi-F intermediate (41,42). These frequency positions of the carbonyl vibrations of ring A and ring D were confirmed in femtosecond Vis pump–IR probe experiments on Cph1 (8,12,26). Thus, in Vis pump–IR probe experiments excitation of the Pfr form should result in instantaneous bleaching (negative) bands around 1700 cm^{-1} and 1722 cm^{-1} of ring D and ring A, respectively, while Lumi-F formation should be reflected by a rise of a product (positive) band around 1720 cm^{-1}. Femtosecond Vis pump–IR probe spectroscopy is based on difference signals between excited and unexcited photoreceptor states, and therefore only detects vibrational signals from groups changing their vibrational properties. Upon femtosecond excitation only the chromophore itself and groups of the protein directly interacting with the excited chromophore change; thus, femtosecond Vis pump–IR probe spectroscopy is a method specifically sensitive to changes in and around the chromophore. Contributions from the $^{13}C/^{15}N$-

labeled protein are not expected in the spectral range from 1670 cm^{-1} to 1800 cm^{-1}.

Isotropic conditions. Upon excitation of Pfr at 710 nm, infrared absorbance difference spectra as a function of wavenumber for different pump–probe delay times were measured (Fig. 2). The initial difference spectra at 350 fs after excitation show negative features from 1610 to 1638 cm^{-1}, from 1696 to 1717 cm^{-1} and from 1717 to 1734 cm^{-1}. The negative 1731 cm^{-1} spike at early delay times is due to water vapor absorption (20). The negative signals around 1630 cm^{-1} show negligible change at ~ 500 fs but decay on a picosecond time scale. The negative feature around 1705 cm^{-1} exhibits a sub-picosecond decay on the low-frequency side around 1701 cm^{-1}, while the high-energy side around 1708 cm^{-1} has a biphasic decay on a sub-picosecond and a picosecond time scale. A part of the negative signal remains at long delay times, indicating the loss of the initial Pfr ground state due to the forward reaction. The negative signal around 1725 cm^{-1} decays on the sub-picosecond and picosecond time scale resulting in a constant positive signal at long delay times of tens of picoseconds, indicating the absorption of the first photoproduct, Lumi-F (26). Positive signals are apparent in the range from 1638 cm^{-1} to 1696 cm^{-1}. The positive signals decay on a sub-picosecond and picosecond time scale, reflecting excited-state absorption. Global fitting of the transient signals with a biexponential model results in decay times of $\tau_1 = (0.7 \pm 0.3)$ ps and $\tau_2 = (5 \pm 2)$ ps, in agreement with earlier findings (26).

The quantum yield of the forward reaction can be estimated by inspection of the initial absorbance difference spectrum in comparison with the absorbance difference spectrum when the early photoreaction has been completed. In Fig. 3, both spectra at time zero (red curve) and the constant spectrum (black curve) were calculated from the global fit. The negative (bleaching) bands around 1705 cm^{-1} and 1725 cm^{-1} were assigned to the vibrations of the $\nu(C_{19}{=}O)$ of ring D and $\nu(C_1{=}O)$ of ring A, respectively (14,26). The signal from $\nu(C_{19}{=}O)$ comprises two overlapping bleaching bands whose decomposition leads to absorption bands at 1702 cm^{-1} (dotted gray lines) and 1708 cm^{-1} (dashed gray lines) (14). The difference between the negative bleaching signals at time zero and after the photoreaction is a measure of the proportion of molecules that change their ground-state properties. After the photoreaction, the remaining signal intensities of the bands at 1702 cm^{-1} and 1708 cm^{-1} are 15% and 17%, respectively. As two different vibrational bands for the same $\nu(C_{19}{=}O)$ vibration of ring D were observed, it seems clear that two (or more) different conformations of the PCB chromophore are present, differing at least at ring D. Assuming two chromophore ground states, the bleaching band recovery is a measure of the forward reaction quantum yield or of structural transitions between the Pfr S_0 substates.

Polarization-resolved conditions. To resolve the significance of the two Pfr S_0 substates on the dynamics, polarization-resolved decay-associated spectra (DAS) were derived for decay constants $\tau_1 = 0.7$ ps (DASτ_1) and $\tau_2 = 5.0$ ps (DASτ_2) for parallel (black circles and black line) and perpendicular (red circles and red line) polarization with respect to pump pulse polarization (Fig. 4). From the ratio $D{=}(A_\parallel/A_\perp)$ of parallel absorption ($A_\parallel$) and perpendicular absorption ($A_\perp$), the relative angle θ between electronic tdm and vtdm can be estimated directly from $\theta = \mathrm{acos}([(2D - 1)/(D + 2)]^{1/2})$. The angles were determined precisely by simulation of the DAS with a sum of Lorentzians (Figures S2, S3 and S4). In Fig. 4a, the DASτ_1 for $\tau_1 = 0.7$ ps is presented. A broad positive feature from 1610 to 1697 cm^{-1} is visible that we assign to the decay of the vibrational stretching $\nu(C_{19}{=}O)^*$ of ring D in S_1, and to a lesser extent the dynamics of $\nu(C_1{=}O)^*$ in S_1. The signal from 1660 to 1697 cm^{-1} with an average relative angle of 34° experiences an orientational change over time reflecting rotation of ring D in S_1 (26). This was not visible for

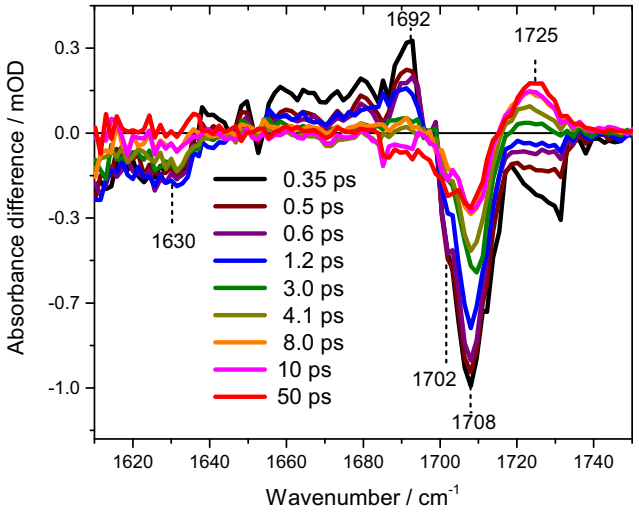

Figure 2. Absorbance difference spectra upon excitation of the Pfr form at 710 nm for various delay times. Bleaching signals are negative; positive signals reflect excited-state or photoproduct absorption. Bleaching signals of ring D carbonyl vibration at 1702 cm^{-1} and 1708 cm^{-1}, and ring A carbonyl vibration at 1721 cm^{-1}. Excited-state signal of ring D carbonyl vibration around 1680 cm^{-1}.

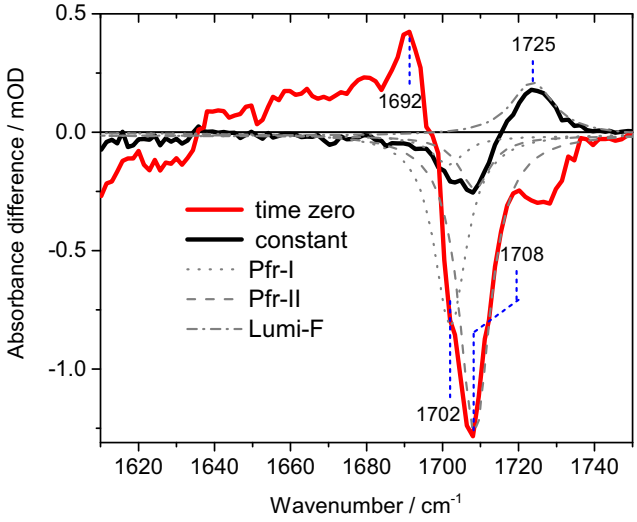

Figure 3. Absorbance difference spectra upon excitation of the Pfr form at 710 nm extracted from the decay-associated spectra for time zero (red line) and for delay times after photoreaction (black line). Simulated Lorentzian bleaching bands of Pfr-I and Pfr-II are plotted by gray dotted and gray dashed lines, respectively. Lumi-F absorption is also simulated (gray dash dotted line). From the ratio of the absorption strengths at zero (black line) and for delay times after photoreaction (red line), the quantum yield can be estimated.

the signal around 1640 cm^{-1} due to the poor signal-to-noise ratio. The negative features around 1705 cm^{-1} were assigned to the $\nu(C_{19}=O)$ stretching of ring D of two different S_0 substates Pfr-I and Pfr-II at 1702 cm^{-1} and 1708 cm^{-1} with relative angles of 47° (1σ error range: 45° to 50°) and 39° (1σ error range: 36–42°), respectively. Although the broad negative signal at 1725 cm^{-1} might comprise two substates Pfr-I and Pfr-II at 1718 cm^{-1} and 1727 cm^{-1}, with relative angles in the range from 25° to 54°, we were not able to resolve orientational differences between them. Thus, this negative band was assigned to one stretching vibration of ring A $\nu(C_1=O)$ with an angle of 40° (1σ error range: 25–54°). The relative angles between the electronic tdm and the vtdms of $\nu(C_1=O)$ and $\nu(C_{19}=O)$ of the Pfr-I substate are in agreement with calculated angles of the ZZEssa PCB up-model at 40° and 48°, respectively. Moreover, the relative angles of $\nu(C_1=O)$ and $\nu(C_{19}=O)$ of the Pfr-II substate are in agreement with calculated angles for the ZZEssa PCB down-model at 35° and 40°, respectively. Thus, our experimental data demonstrate Pfr-I and Pfr-II substates matching the ZZEssa PCB up- and down-models, respectively.

In Fig. 4b, the DASτ_2 for τ_2 = 5.0 ps is shown. The signatures for the bleaching bands of the $\nu(C_{19}=O)$ and $\nu(C_1=O)$ stretching vibrations differ from DASτ_1 significantly. While DASτ_1 exhibits two bleaching bands for the $\nu(C_{19}=O)$ stretching vibration at 1702 cm^{-1} and 1708 cm^{-1}, DASτ_2 has only one (at 1708 cm^{-1}). The absence of the 1702 cm^{-1} component indicates that the latter has only fast dynamics of 0.7 ps and no slow dynamics of 5 ps. Additionally, the broad feature of the $\nu(C_1=O)$ stretching vibration at 1725 cm^{-1} in DASτ_1 is much narrower in DASτ_2. The positive signal around 1695 cm^{-1} with a relative angle of 46° in the DASτ_2 reflects the dynamics of the $\nu(C_{19}=O)$*, and to a lesser extent the dynamics of $\nu(C_1=O)$* in S_1. Surprisingly, a new negative signal at 1635 cm^{-1} and a positive signal at 1660 cm^{-1} appear in the DASτ_2. Both signals exhibit stronger absorption for perpendicular than for parallel polarization, demonstrating a relative angle >54.7°. If this signal were to arise from chromophore vibrations, the only possible assignment would be to ν(C=C) stretching vibrations or the ν(C=O) or ν(COO^-) vibrations of the propionate side chains. However, in femtosecond excited state stimulated Raman spectroscopic (FSRS) experiments on Cph1Δ2, only very fast ν(C=C) stretching dynamics around 1600 cm^{-1} with a time constant of 260 fs were observed, with no dynamics in the spectral range up to 1800 cm^{-1} (26). In contrast to Raman experiments, IR experiments are sensitive to protein contributions. Typical vibrational frequencies of a protein in this spectral range are $\nu(^{13}C=O)$ stretching vibrations, with a frequency range from 1660 cm^{-1} to 1740 cm^{-1} for $\nu(^{12}C=O)$ in native proteins. Moreover, asymmetric stretching vibrations $\nu(COO^-)$ of the propionate side chains of the chromophore are predicted to absorb around 1650–1630 cm^{-1}. Thus, it is very likely that the feature at 1635 cm^{-1} (−)/1660 cm^{-1} (+) arises from the propionate side chain vibration or from the $^{13}C/^{15}N$-labeled protein.

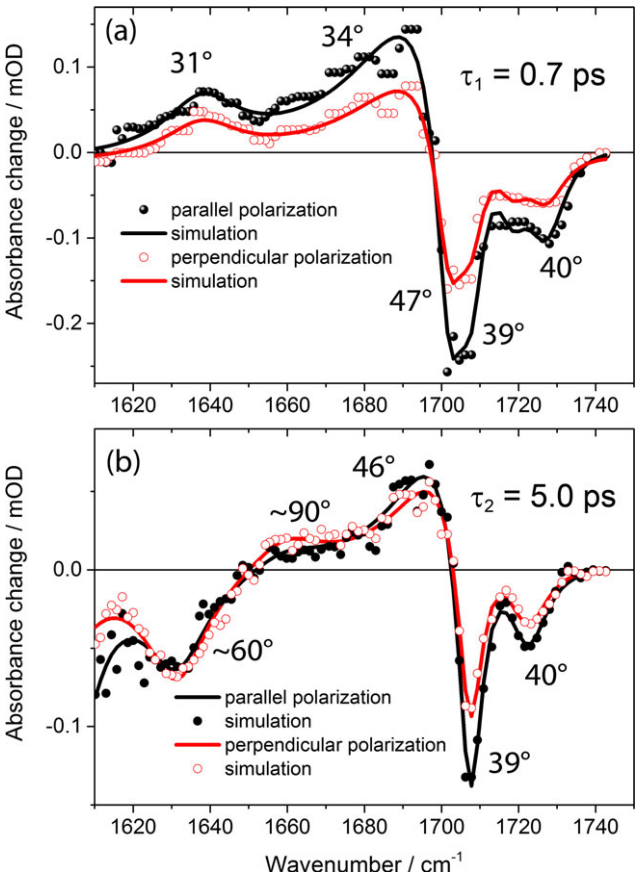

Figure 4. Decay-associated spectra of the (a) τ_1 = 0.7 ps and (b) τ_1 = 5.0 ps component. Signals taken for parallel (black circles) and perpendicular (red circles) polarization of the IR probe beam with respect to the Vis pump beam. Simulations with multiple Lorentzians are presented for parallel (black line) and perpendicular (red line) polarizations. Relative angles between tdm and vtdm derived from the simulations are plotted next to the peak positions (see Figures S4 and S5).

To further elucidate the origin of the feature at 1635/1660 cm^{-1}, structural models were evolved to address the impact of directly coupled amino acids on the chromophore. As reported, the Asp207 residue forms a tight hydrogen bond between its backbone C=O group and the N-H groups of rings A, B and C. Our structural models allow the calculated relative angle between electronic tdm and vtdm of the Asp207 backbone $\nu(^{13}C=O)^{207}$ stretching vibration to be determined. Angles of 60.4° and 70.2° were determined for the down- and up-models, respectively, both matching the measured angle of ~60° for the bleaching band at 1635 cm^{-1}. The asymmetric stretching vibration $\nu(COO^-)$ of the propionate side chain at ring C exhibits angles of 61.5° and 67.9° for the down- and up-conformations, respectively. The calculated angle for the propionate side chain at ring B is <20°. Moreover, the signal strength of the bleaching band at 1635 cm^{-1} is comparable to that of $\nu(C_1=O)$. This is in line with the calculated IR signal strengths for the $\nu(^{13}C=O)^{207b}$ of the backbone Asp207 as well as for the $\nu(COO^-)$ of the propionate side chain at ring C. Thus, both (1) the $\nu(^{13}C=O)^{207b}$ and (2) the $\nu(COO^-)$ of the propionate side chain at ring C are appropriate candidates for the signals at 1635 cm^{-1} (−) and 1660 cm^{-1} (+). Both assignments match with both conformations. In detail, the following two conclusions are possible:

1 On the basis of our structural model, we assign the signal at 1635 cm^{-1} to the bleaching band of the carbonyl backbone stretching vibration of Asp207 ($\nu(^{13}C=O)^{207b}$). As carbonyl vibrations experience a redshift at this frequency of up to some tens of wavenumbers, we assign the positive signal at 1660 cm^{-1} to the $\nu(^{13}C=O)^{207b+}$ vibration that is blueshifted due to weakening or breaking of the hydrogen bonds to the N-

H groups of rings A, B and C. This can be explained by a reallocation of electron density during the electronic excited state, facilitating the reduction of the C_{15}=C_{16} double bond. This change in electron density at ring D can result in a breaking of the strong hydrogen bond between the N-H group of ring D and the COO- group of Asp207. This would directly influence orientation of Asp207 and the character of the hydrogen bonds to rings A, B and C. The suggested change in orientation between the absorption of the $\nu(^{13}C{=}O)^{207b}$ at 1635 cm^{-1} and $\nu(^{13}C{=}O)^{207b+}$ at 1660 cm^{-1} could derive from the reduction in hydrogen bonding and deformation of the carbonyl orientation.

2 In S_1, the $\nu(COO^-)$ of the propionate side chain at ring C experiences a fast change of the electric field due to the reallocation of the electron density. This leads to a frequency shift and an orientational change of the COO- group that decays together with the electronic excited state. Under this assumption, we would also expect a contribution of the $\nu(COO^-)$ of the propionate side chain at ring B with a different angle, which, however, was not observed.

Thus, we favor the assignment of the $\nu(^{13}C{=}O)^{207b}$ stretching vibration to the bleaching band at 1635 cm^{-1}. As a result, it seems unlikely that excited-state proton transfer upon Pfr excitation takes place with protonation of the C=O group at Asp207 (43). This would cause the $\nu(^{13}C{=}O)^{207b}$ vibration to deplete and the new C-OH vibration to appear in a different spectral range. Here we see the $\nu(^{13}C{=}O)^{207b+}$ vibration at 1660 cm^{-1} as a result of the interaction with the electronic excited state, and no additional time scale for the $\nu(^{13}C{=}O)^{207b}$ vibration was observed.

The two different S_0 substates Pfr-I and Pfr-II differ in geometry and dynamics. Pfr-I exhibits a $\nu(C_{19}{=}O)$ stretching vibration of ring D at 1702 cm^{-1} with a relative angle θ_D between electronic tdm and vdm of 47°. The ring A absorption around 1725 cm^{-1} has an angle θ_A of 40°, and we found a broad vibrational signature of the electronic excited state ranging from 1610 cm^{-1} to 1697 cm^{-1} with an average angle θ_{ES} of ~34°. The signal is dominated by the $\nu(C_{19}{=}O)^*$ stretching vibration of ring D in S_1, changing its orientation with a time constant of 0.7 ps, indicating rotation of ring D with photoisomerization (26). We found no contributions of the protein in the observed spectral range with a time constant of 0.7 ps. As the bleaching signal of Pfr-I $\nu(C_{19}{=}O)$ exhibits only a single time constant of 0.7 ps and the photoisomerization takes place with the same time constant, it seems reasonable to assign the Pfr-I dynamics to a single decay time constant of 0.7 ps. It was reported that about ~35% of the chromophores rotate in the electronic excited state, while the remaining ~65% do not change orientation. This matches with the ratio of the initial bleaching signals at $t = 0$ at 1702 cm^{-1} (Pfr-I) and 1708 cm^{-1} (Pfr-II) of about ~0.6 (see Fig. 3) (14). However, it cannot be excluded that interconversion of Pfr-I* and Pfr-II* takes place in the electronic excited state on a time scale of hundreds of femtoseconds, before isomerization.

Pfr-II exhibits a $\nu(C_{19}{=}O)$ stretching vibration of ring D at 1708 cm^{-1} with a relative angle θ_D between electronic tdm and vdm of 39°. The ring A absorption around 1725 cm^{-1} has an angle θ_A of 40°. The electronic excited state shows a biexponential behavior. Starting from a broad vibrational pattern in the electronic excited-state from 1610 to 1697 cm^{-1} with a decay time of ~0.7 ps, the excited-state signal narrows to around 1695 cm^{-1} with a decay time of 5 ps. Transition from Pfr-II* in the electronic excited state to Pfr-I* seems not to occur in the 5 ps time range because no bleach recovery at 1702 cm^{-1} was detected. In addition to the chromophore signals, Pfr-II excitation induces changes in the surrounding protein assigned to weakening or breaking of the hydrogen bonds between carbonyl backbone of Asp207 and the N-H groups of rings A, B and C.

Vis pump–Vis supercontinuum probe spectroscopy

Vis pump–Vis supercontinuum probe spectroscopy reflects the dynamics of the electronic excited and ground states. In Fig. 5, the absorbance changes upon excitation from fs to 50 ps are plotted as a function of wavelength from 500 to 1050 nm, blue and red colors indicating negative and positive signals, respectively. Initially, a strong negative signal around 725 nm is seen, due to the bleaching band of Pfr absorption and stimulated emission accompanied by a strong positive signal from 500 to 650 nm representing excited-state absorption (ESA). At early delay times, the negative signal in the spectral range from 750 nm to 950 nm, reflecting stimulated emission (SE), and the major part of the positive signal from 500 to 650 nm (ESA) decay on a time scale of about 300 fs. This is accompanied by the emergence of a positive signal around 780 nm, well visible on a time scale of ~0.4–1.2 ps. The positive signal around 780 nm could either originate from a vibrationally excited Lumi-F photoproduct or from a long-lived S_1 absorption. For longer delay times, a blueshift of the positive signal around 780 nm is seen, resulting in a reduction in the positive and bleaching signal. This is in agreement with cooling effects observed for the Lumi-F vibrational band of ring D, as well as with a decay of an electronic excited state to the ground state (26). Global fitting and analysis of decay-associated spectra result in three decay constants of τ_{V1} = (0.24 ± 0.05) ps, τ_{V2} = (0.7 ± 0.1) ps and τ_{V3} = (6 ± 1) ps with decay-associated spectra (DAS) presented in Fig. 6. The fast dynamics of a few hundred femtoseconds corresponding to DASτ_{V1} is clearly visible in Fig. 5 and represented in Fig. 6 as a blue line. This exhibits a broad flat positive

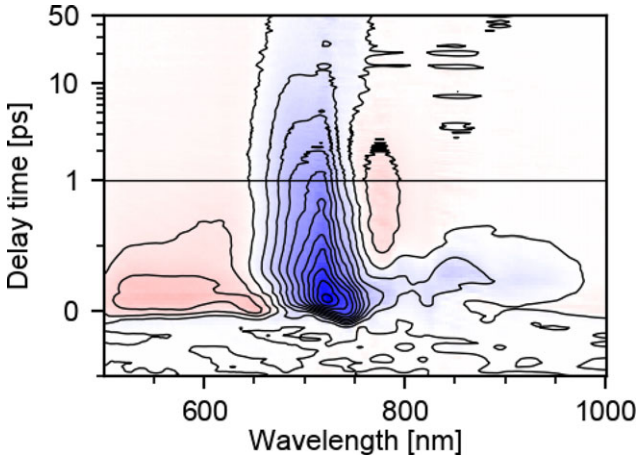

Figure 5. Absorbance difference signals from Vis pump–Vis probe experiments. Negative absorbance indicates bleaching and stimulated emission signals; positive absorbance shows excited-state and photoproduct signals. The signal strength of positive (red) and negative (blue) absorption is presented in a contour plot. Linear time axis up to 1 ps; logarithmic axis from 1 ps to 50 ps.

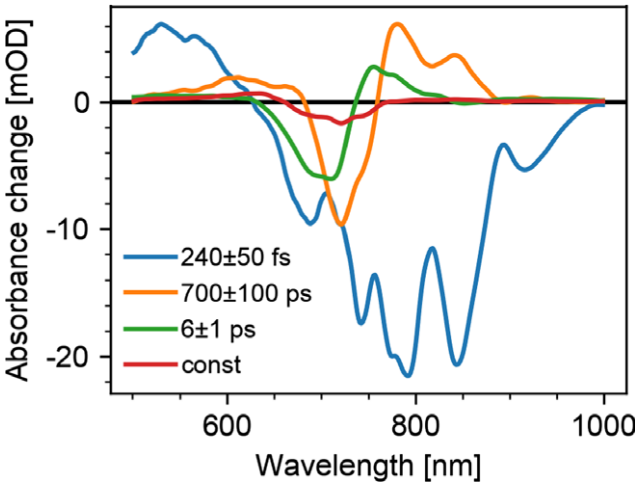

Figure 6. Decay-associated spectra of the Vis pump–Vis probe experiments in a spectral region from 499 nm to 1000 nm. The complete dataset is described by time constants of 240 fs (blue line), 700 fs (orange line), 6 ps (green line) and a constant contribution (red line). The constant contribution represents the signals after the photoreaction is completed on a time scale of 50 ps.

contribution from 500 nm to 630 nm and a negative part from 630 nm to 1000 nm with a maximum around 800 nm. Contributions from the bleaching band with peak at 704 nm are weak compared to the stimulated emission signal in this fast process. The observed time constant agrees with time-resolved Raman experiments (FSRS), where the 260 fs component is assigned to C=C stretching vibrational dynamics in the excited state as the preceding step for ring D rotation (26). The fast process can be explained by a strong and fast shift of the S_1 absorption to short wavelengths, due to fast relaxation on the excited-state surface increasing the transition energy to higher-order excited states. On the same time scale, the stimulated emission shifts to longer wavelengths with increasing delay time, visible by the small tilt of the fast negative signals from 780 nm to 950 nm in Fig. 5. These two processes reflect excited-state relaxation as reported for other systems, for example rhodopsin (44). This fast process was not observed in the time-resolved IR data due to limited time resolution of 300 fs.

The DASτ_{V2} in Fig. 6 (orange line) shows a broad positive signal from 550 nm to ~ 900 nm overlapped by a negative contribution around 720 nm. As the 0.7 ps time constant matches the IR time constant for photoisomerization, we assign this to the photoisomerization process accompanied by loss of excited state and stimulated emission signal. Lumi-F absorption is presented in Figure S2 and is very similar to Pfr absorption, resulting in negligible contributions to the DASτ_{V2}. Thus, the broad positive absorption from 550 nm to ~900 nm reflects excited-state absorption of the reacting and relaxing populations.

The DASτ_{V3} has a different shape with a broad negative signal with maximum ranging from 685 nm to 710 nm, and a positive contribution peaking at 760 nm. The negative signal is clearly stronger than the positive. We assign the positive and negative signals to $S_1 \rightarrow S_0$ decay and bleaching recovery, respectively. This matches the interpretation and time constant from the IR data. The absorption peaks in the absorption spectrum of Pfr provide information on the $S_0 \rightarrow S_1$ transitions with energy of 704 nm (14200 cm^{-1}) and to the S_2 state (Soret band absorption) with energy of 385 nm (26000 cm^{-1}). The resulting energy difference between the S_1 and S_2 states is about 847 nm (11800 cm^{-1}), that is excited-state absorption. Figure S3 shows three transient signals in this spectral range with positive absorption signals on a picosecond time scale, corroborating the existence of an electronic excited state on a picosecond time scale, after ring D photoisomerization. After decay of all excited states, the absorption signal arises from molecules in the photoproduct Lumi-F (positive signal) and their (negative) bleaching signals. As presented in Fig. 6 (constant, red line), the total signal is dominated by negative contributions, demonstrating a higher extinction coefficient of the Pfr ground state compared with the photoproduct Lumi-F in the visible spectrum.

The electronic and vibrational dynamics support a model of excited-state dynamics with a sub-picosecond time constant of 0.24 ps, followed by the photoisomerization with 0.7 ps. Not all molecules undergo photoisomerization, but stay in the electronic excited state and decay with a time constant of ~5 ps.

DISCUSSION

Two Pfr S_0 substates

Our time-resolved IR data show clearly the existence of two distinct S_0 substates of Pfr (Pfr-I and Pfr-II), with a Pfr-I/Pfr-II ratio between 0.6 and 0.7 (see Fig. 3 and Figures S4 and ST3). The substates probably differ in the orientation of ring D and their dynamics upon excitation. Both visible and IR data point to two different S_1 substates with distinct decay times and spectral features. By comparison of the bleaching recovery dynamics in the IR with the excited-state dynamics in the IR and visible data, we associate the excited state Pfr-I* with the fast decay time of 0.7 ± 0.3 ps, the time constant of photoisomerization (26), and Pfr-II* with the slow decay time of about 5 ± 2 ps. Hence, the slow time constant represents an inactive photoreaction pathway. We tentatively assign the 0.7 ps time constant observed for Pfr-II to a transition of Pfr-II* to a potential energy surface position close to Pfr-I*, followed by relaxation to the Pfr-I ground state. This would allow a fraction of the Pfr-II* population to relax to the Pfr-I ground state without forming Lumi-F. The total quantum yield was determined to be 17% (±7%, 3σ range), with bleaching recoveries of 15% and 17% for Pfr-I and Pfr-II, respectively. As we envisage a fast transition from Pfr-II* to Pfr-I, the individual bleaching recovery yields cannot be assigned to single conformations. However, considering that Pfr-II is inactive, the remaining bleaching signal of Pfr-II should originate from molecules undergoing Pfr-II* to Pfr-I transition. Under this assumption, ~45% of the Pfr-II* molecules are transferred to the Pfr-I substate, and the resulting photoreaction quantum yield of the active Pfr-I substate would be about 38%. In this scenario, all Pfr-I* chromophores show ring D rotation, about 60% forming Lumi-F. This model agrees with the observation that about 35% of all Pfr PCB chromophores show ring D rotation in the electronic excited state of Cph1 (26), and provides the first conclusive explanation of this fraction. The concept of a photoactive and a silent conformation was also suggested for the photoreaction of the Pr substates of Cph1 with different ring D conformations (12).

The two distinct S_0 substates of Pfr (Pfr-I and Pfr-II) can be well separated by femtosecond Vis pump–IR probe spectroscopy. On the time scale of solid-state NMR experiments, the separation

is not observed (6), suggesting that the substates are linked to dynamics faster than the microsecond time scale.

Possible origins of Pfr conformations. There are two different explanations possible for the Pfr-I and Pfr-II S_0 substates.

1 Similar to the Pr ground state of Cph1, the two Pfr substates described here might be associated with different PCB ring D conformations. We developed two structural models with the PCB N-H group of ring D in up- and down-orientations (Figs. 1, S7, S8, S9 and S10). The down-conformation exhibits a tilt angle between rings C and D of 146.6°, and a hydrogen bond between the N-H group of ring D and the COO^- group of Asp207, with distance of 1.85 Å. By contrast, in the up-conformation, the respective values are 139.3° and 3.94 Å, too far for a hydrogen bond. The calculated tilt angle difference of 7° between rings C and D of up- and down-conformations is in agreement with an angle difference of ~8° between Pfr-I and Pfr-II between electronic transition dipole moment and vibrational transition dipole moment of $\nu(C_{19}{=}O)$ stretching vibration of ring D (14). In contrast to the up-conformation, one would expect that the down-conformation would not participate in photoisomerization to the active Pr form (12), because of the additional barrier on the excited-state surface caused by the steric interaction of the methyl groups at rings C and D. This is supported by the observation that the Pfr-I substate shows only bleaching recovery on the time scale of 0.7 ps, clearly demonstrating that the substates have distinct dynamics. Distinct down- and up-conformational substates would lead to a system comprising both photoactive (up-conformation, Pfr-I) and silent (down-conformation, Pfr-II) substates, rather similar to the likely situation in Pr of Cph1 (12). The photoactive conformation would photoisomerize, while the silent conformation would partly transfer to the photoactive conformation upon excitation. The other part of the silent conformation would stay in the electronic excited state with a large amount of excess energy that induces distortions of the chromophore via energy redistribution. These distortions might lead to a breaking of the hydrogen bond between the COO^- group of Asp207 and the N-H group of ring D, as well as between $\nu(^{13}C{=}O)^{207b}$ and the N-H groups of rings A, B and C. Were the 1635 cm^{-1} (−)/1660 cm^{-1} (+) signal to reflect the $\nu(COO^-)$ absorption of the propionate side chain at ring C, a change in the hydrogen bonding network in that region might be induced that decays with the electronic excited state. High-level excited-state calculations or time-resolved CD experiments should be able to support or contradict the suggested system of down- and up-conformations.
2 The two substates Pfr-I and Pfr-II might result from a down-conformation with a different number of hydrogen bonds between ring D and the protein. It was reported that in Pfr the N-H group of ring D forms a hydrogen bond to the COO^- group of Asp207, and that hydrogen bonds exist between the backbone C=O group of Asp207 and the N-H groups of rings A, B and C. Additionally, a weak hydrogen bond between the OH group of Tyr263 and ring D is possible. The hydrogen bond has a distance of 3.15 Å between the oxygens of the Tyr263 and of the C_{19}=O group of ring D. The stronger the hydrogen bonding to the C_{19}=O group, the stronger the frequency down-shift. Because we found two substates Pfr-I and Pfr-II with $\nu(C_{19}{=}O)$ absorption at 1702 cm^{-1} and 1708 cm^{-1}, respectively, Pfr-II can be interpreted as a down-conformation with no or weaker hydrogen bond at the carbonyl group of ring D, and Pfr-I as a conformation with one hydrogen bond at ring D to Tyr263 (see Fig. 1). The additional or stronger hydrogen bond to ring D in Pfr-I increases the tilt angle between rings C and D, explaining the greater angle of the $\nu(C_{19}{=}O)$ vibration in Fig. 4a. Upon excitation, the hydrogen bond to the ring D carbonyl breaks, resulting in one broad $\nu(C_{19}{=}O)^*$ vibrational band in the electronic excited state (see Fig. 4a). Thus, in the electronic excited state, one can no longer distinguish between the conformations with different hydrogen bonding, and the single bleaching recoveries of Pfr-I and Pfr-II cannot be assigned to individual reaction dynamics. With a fast relaxation in the electronic excited state (~0.25 ps), the excited-state population splits into a fraction propagating to the conical intersection, where part of the molecules generate the photoproduct Lumi-F, while another part relaxes back to the ground state. The other fraction cannot isomerize and relaxes back to the ground state with a time constant of about 5 ps. This system can be tested by studying the dynamics of mutants at position 263. A loss of the additional hydrogen bonds should result in a disappearance of the two ground states. Up to now, only the photodynamics of the Pr form of Cph1 mutants at position 263 were investigated (45). The signals at 1635 cm^{-1} (−)/1660 cm^{-1} (+) were observed with a time constant of 5 ps only. Therefore, we assign these to a relaxation process not involved in the forward reaction. Either the broken hydrogen bond between $\nu(^{13}C{=}O)^{207b}$ and the N-H groups of rings A, B and C (see Fig. 1) reforms upon excited-state decay, or the broken hydrogen bond of the $\nu(COO^-)$ propionate side chain at ring C reforms upon excited-state decay. The origin of the 1635 cm^{-1} (−)/1660 cm^{-1} (+) signals can be investigated by experiments on native Cph1 protein with $^{13}C/^{15}N$-labeled PCB chromophore or by performing pH-dependent investigations. As the hydrogen bond between the carbonyl group at ring D and the OH group of Tyr263 is rather weak, we would expect a less pronounced separation of the two conformations. Consequently, we prefer the system with down- and up-oriented ring D chromophore conformations.

In summary, we combined femtosecond polarization-resolved Vis pump–IR probe and femtosecond Vis pump–supercontinuum Vis probe experiments to elucidate the complex dynamics of Pfr photoreaction in Cph1 phytochrome. We found consistent time constants of 0.24 ps, 0.7 ps and 6 ps, describing fast relaxation processes in the electronic excited state, the isomerization process and the excited-state decay of nonisomerizing molecules, respectively. We identified a new vibrational band pair at 1635 cm^{-1} (−)/1660 cm^{-1} (+) with tentative assignment to the $\nu(^{13}C{=}O)^{207b}$ backbone carbonyl vibration of Asp207 hydrogen bonded to rings A, B and C, or to the $\nu(COO^-)$ propionate side chain at ring C. Two Pfr S_0 substates were identified, with distinct $\nu(C_{19}{=}O)$ ring D absorption frequencies, different ring D orientations and different dynamics. We assigned the Pfr-I ground state to the $\nu(C_{19}{=}O)$ ring D absorption at 1702 cm^{-1} with an angle of 47° between its vibrational transition dipole moment (vtdm) and the electronic transition dipole moment (tdm). Pfr-II exhibits a $\nu(C_{19}{=}O)$ ring D absorption at 1708 cm^{-1} with an angle of 39°. According to the proposed system, Pfr-I is associated with photoisomerization, whereas Pfr-II is silent. This would explain why only about 35% of the

chromophores—the Pfr-I* population—exhibit rotation of ring D to form Lumi-F (26), whereas the Pfr-II fraction represents phytochrome in a S_0 Pfr state which can only become photoactive upon conversion to Pfr-I. The question arises as to the reason for ground-state heterogeneity in phytochromes. Although it might have simply physical origins, a possible biological purpose might be to detain a fraction of the Pfr population from photoconversion to Pr (the active kinase), extending the sensitivity range of the Cph1 photoreceptor.

Acknowledgements—The work performed at the Free University of Berlin was supported by SFB 1078 (B3 to K.H., C2 to E.-W.K and C3 to M.-A.M.). J.H. was supported by DFG Grant Hu702/8. We thank Peter Schmieder and Janina Hahn for preparation of the $^{13}C/^{15}N$-labeled Cph1 samples with unlabeled PCB. We thank J. Clark Lagarias and Nathan C. Rockwell from UC Davis for fruitful discussions on distinct geometries.

SUPPORTING INFORMATION

Additional Supporting Information may be found in the online version of this article:

Figure S1. Absorption spectrum of a Cph1 directly after illumination with a 640 nm diode (green) and spectrum of pump pulse (purple).

Figure S2. Decay-associated spectrum (DAS) for the time constant 0.7 ps in the IR spectral range.

Figure S3. Decay-associated spectrum (DAS) for the time constant 5.0 ps in the IR spectral range.

Figure S4. Decay-associated spectrum (DAS) for constant component in the IR spectral range, after photoisomerization.

Figure S5. Absorbance difference spectra from Fig. 5 with added bleaching spectrum (Pfr absorption).

Figure S6. Transient signals in the near infrared region around 900 nm.

Figure S7. Proposed reaction scheme sketch.

Figure S8. Stereo view of down-conformation of the chromophore PC, Asp207, and Tyr263 of Cph1 Pfr form.

Figure S9. Stereo view of up-conformation of the chromophore PC, Asp207, and Tyr263 of Cph1 Pfr form.

Figure S10. Definition of down-conformation of the chromophore PC, Asp207, and Tyr263 of Cph1 Pfr form.

Figure S11. Definition of up-conformation of the chromophore PC, Asp207, and Tyr263 of Cph1 Pfr form.

Figure S12. Calculated vibrational modes and intensities for both structural models presented as stick plots.

Table S1. Fit parameters for DAS time constant 0.7 ps as presented in Fig. S2.

Table S2. Fit parameters for DAS time constant 5.0 ps as presented in Fig. S3.

Table S3. Fit parameters for constant component in the DAS presented in Figure S4.

Data S1. PDB file of the Pfr down conformation.

Data S2. PDB file of the Pfr up conformation.

Data S3. Assignment of vibrations down conformation.

Data S4. Assignment of vibrations up conformation.

REFERENCES

1. Rockwell, N. C. and J. C. Lagarias (2010) A brief history of phytochromes. *ChemPhysChem* **11**, 1172–1180.
2. Rodriguez-Romero, J., M. Hedtke, C. Kastner, S. Muller and R. Fischer (2010) Fungi, hidden in soil or up in the air: Light makes a difference. *Annu. Rev. Microbiol.* **64**, 585–610.
3. Auldridge, M. E. and K. T. Forest (2011) Bacterial phytochromes: more than meets the light. *Crit. Rev. Biochem. Mol. Biol.* **46**, 67–88.
4. Braslavsky, S. E., W. Gärtner and K. Schaffner (1997) Phytochrome photoconversion. *Plant, Cell Environ.* **20**, 700–706.
5. Sineshchekov, V. A. (1995) Photobiophysics and photobiochemistry of the heterogeneous phytochrome system. *Biochim. Biophys. Acta* **1228**, 125–164.
6. Song, C., T. Rohmer, M. Tiersch, J. Zaanen, J. Hughes and J. Matysik (2013) Solid-state NMR spectroscopy to probe photoactivation in canonical phytochromes. *Photochem. Photobiol.* **89**, 259–273.
7. Song, P. S., M. H. Park and M. Furuya (1997) Chromophore: Apoprotein interactions in phytochrome A. *Plant, Cell Environ.* **20**, 707–712.
8. Yang, Y., M. Linke, T. von Haimberger, J. Hahn, R. Matute, L. Gonzalez, P. Schmieder and K. Heyne (2012) Real-time tracking of phytochrome's orientational changes during Pr photoisomerization. *JACS* **134**, 1408–1411.
9. Sineshchekov, V. A. and A. V. Sineshchekov (1995) Different photoactive states of red phytochrome form in the cells of etiolated pea and oat seedlings. *J. Photochem. Photobiol., B* **5**, 197–217.
10. Kandori, H., K. Yoshihara and S. Tokutomi (1992) Primary process of phytochrome – initial step of photomorphogenesis in green plants. *JACS* **114**, 10958–10959.
11. Song, C., G. Psakis, C. Lang, J. Mailliet, W. Gärtner, J. Hughes and J. Matysik (2011) Two ground state isoforms and a chromophore D-ring photoflip triggering extensive intramolecular changes in a canonical phytochrome. *PNAS* **108**, 3842–3847.
12. Yang, Y., M. Linke, T. von Haimberger, R. Matute, L. González, P. Schmieder and K. Heyne (2014) Active and silent chromophore isoforms for phytochrome Pr photoisomerization: An alternative evolutionary strategy to optimize photoreaction quantum yields. *Struct. Dyn.* **1**, 014701–014712.
13. Song, C., L.-O. Essen, W. Gärtner, J. Hughes and J. Matysik (2012) Solid-state NMR spectroscopic study of chromophore-protein interactions in the Pr ground state of plant phytochrome A. *Mol. Plant* **5**, 698–715.
14. Escobar, F. V., D. vonStetten, M. Günther-Lütkens, A. Keidel, N. Michael, T. Lamparter, L. O. Essen, J. Hughes, W. Gärtner, Y. Yang, K. Heyne, M. A. Mroginski and P. Hildebrandt (2015) Conformational heterogeneity of the Pfr chromophore in plant and cyanobacterial phytochromes. *Front. Mol. Biosci.* **2**, 1–13.
15. Essen, L. O., J. Mailliet and J. Hughes (2008) The structure of a complete phytochrome sensory module in the Pr ground state. *PNAS* **105**, 14709–14714.
16. Heyne, K., J. Herbst, D. Stehlik, B. Esteban, T. Lamparter, J. Hughes and R. Diller (2002) Ultrafast dynamics of phytochrome from the cyanobacterium synechocystis, reconstituted with phycocyanobilin and phycoerythrobilin. *Biophys. J* . **82**, 1004–1016.
17. Kim, P. W., N. C. Rockwell, S. S. Martin, J. C. Lagarias and D. S. Larsen (2014) Heterogeneous photodynamics of the Pfr state in the cyanobacterial phytochrome Cph1. *Biochemistry* **53**, 4601–4611.
18. Müller, M. B., I. Lindner, I. Martin, W. Gärtner and A. R. Holzwarth (2008) Femtosecond kinetics of photoconversion of the higher plant photoreceptor phytochrome carrying native and modified chromophores. *Biophys. J* . **94**, 4370–4382.
19. Stensitzki, T., Y. Yang, A. Berg, A. Mahammed, Z. Gross and K. Heyne (2016) Ultrafast electronic and vibrational dynamics in brominated aluminum corroles: Energy relaxation and triplet formation. *Struct. Dyn.* **3**, 043210–043219.
20. Linke, M., Y. Yang, B. Zienicke, M. A. S. Hammam, T. von Haimberger, A. Zacarias, K. Inomata, T. Lamparter and K. Heyne (2013) Electronic transitions and heterogeneity of the bacteriophytochrome Pr absorption band: An angle balanced polarization resolved femtosecond VIS pump–IR probe study. *Biophys. J* . **105**, 1756–1766.
21. Hamm, P., S. M. Ohline and W. Zinth (1997) Vibrational cooling after ultrafast photoisomerization of azobenzene measured by femtosecond infrared spectroscopy. *J. Chem. Phys.* **106**, 519–529.
22. Stensitzki, T., Y. Yang, V. Muders, R. Schlesinger, J. Heberle and K. Heyne (2016) Femtosecond infrared spectroscopy of channelrhodopsin-1 chromophore isomerization. *Struct. Dyn.* **3**, 043208-8.

23. Neumann-Verhoefen, M.-K., K. Neumann, C. Bamann, I. Radu, J. Heberle, E. Bamberg and J. Wachtveitl (2013) Ultrafast infrared spectroscopy on channelrhodopsin-2 reveals efficient energy transfer from the retinal chromophore to the protein. *JACS* **135**, 6968–6976.
24. Bonetti, C., T. Mathes, I. H. M. van Stokkum, K. M. Mullen, M.-L. Groot, R. van Grondelle, P. Hegemann and J. T. M. Kennis (2008) Hydrogen bond switching among flavin and amino acid side chains in the BLUF photoreceptor observed by ultrafast infrared spectroscopy. *Biophys. J* . **95**, 4790–4802.
25. Schumann, C., R. Groß, M. M. N. Wolf, R. Diller, N. Michael and T. Lamparter (2008) Subpicosecond midinfrared spectroscopy of the Pfr reaction of phytochrome Agp1 from *Agrobacterium tumefaciens*. *Biophys. J* . **94**, 3184–3197.
26. Yang, Y., K. Heyne, R. A. Mathies and J. Dasgupta (2016) Nonbonded interactions drive the sub-picosecond bilin photoisomerization in the Pfr state of phytochrome Cph1. *ChemPhysChem* **17**, 369–374.
27. Yang, X. and K. J. Moffat (2008) Crystal structure of *Pseudomonas aeruginosa* bacteriophytochrome: photoconversion and signal transduction. *PNAS* **105**, 14715–14720.
28. Sali, M. A., B. Webb, M. S. Madhusudhan, M.-Y. Shen, M. A. Marti-Renom, N. Eswar, F. Alber, M. Topf, B. Oliva, A. Fiser, R. Sanchez, B. Yerkovich, A. Badretdinov, F. Melo, J.P. Overington and E. Feyfant (2015) Program for protein structure modeling, University of California. Available at: https://salilab.org/modeller/9.15/manual.pdf. 10 April 2017.
29. Kieseritzky, G. and E. W. Knapp (2008) Optimizing pK(A) computation in proteins with pH adapted conformations. *Proteins-Struct. Funct. Bioinforma* **71**, 1335–1348.
30. Brooks, B. R., C. L. Brooks, A. D. MacKerell Jr, L. Nilsson, R. J. Petrella, B. Roux, Y. Won, G. Archontis, C. Bartels, S. Boresch, A. Caflisch, L. Caves, Q. Cui, A. R. Dinner, M. Feig, S. Fischer, J. Gao, M. Hodoscek, W. Im, K. Kuczera, T. Lazaridis, J. Ma, V. Ovchinnikov, E. Paci, R. W. Pastor, C. B. Post, J. Z. Pu, M. Schaefer, B. Tidor, R. M. Venable, H. L. Woodcock, X. Wu, W. Yang, D. M. York and M. Karplus (2009) CHARMM: The biomolecular simulation program. *J. Comput. Chem.* **30**, 1545–1614.
31. MacKerell, A. D. Jr, D. Bashford, M. Bellott, R. L. Dunbrack Jr, J. D. Evanseck, M. J. Field, S. Fischer, J. Gao, H. Guo, S. Ha, D. Joseph-McCarthy, L. Kuchnir, K. Kuczera, F. T. K. Lau, C. Mattos, S. Michnick, T. Ngo, D. T. Nguyen, B. Prodhom, W. E. Reiher, B. Roux, M. Schlenkrich, J. C. Smith, R. Stote, J. Straub, M. Watanabe, J. Wiórkiewicz-Kuczera, D. Yin and M. Karplus (1998) All-atom empirical potential for molecular modeling and dynamics studies of proteins. *J. Phys. Chem. B* **102**, 3586–3616.
32. Metz, S., J. Kästner, A. A. Sokol, T. W. Keal and P. Sherwood (2014) ChemShell-a modular software package for QM/MM simulations. *Wiley Interdiscip Rev. Comput. Mol. Sci.* **4**, 101–110.
33. Mroginski, M. A., F. Mark, W. Thiel and P. Hildebrandt (2007) Quantum mechanics/molecular mechanics calculation of the Raman spectra of the phycocyanobilin chromophore in alpha-c-phycocyanin. *Biophys. J* . **93**, 1885–1894.
34. Mroginski, M. A., D. von Stetten, S. Kaminski, F. V. Escobar, N. Michael, G. Daminelli-Widany and P. Hildebrandt (2011) Elucidating photoinduced structural changes in phytochromes by the combined application of resonance Raman spectroscopy and theoretical methods. *J. Mol. Struct.* **993**, 15–25.
35. Frisch, M. J., G. W. Trucks, H. B. Schlegel, G. E. Scuseria, M. A. Robb, J. R. Cheeseman, G. Scalmani, V. Barone, G. A. Petersson, H. Nakatsuji, X. Li, M. Caricato, A. Marenich, J. Bloino, B. G. Janesko, R. Gomperts, B. Mennucci, H. P. Hratchian, J. V. Ortiz, A. F. Izmaylov, J. L. Sonnenberg, D. Williams-Young, F. Ding, F. Lipparini, F. Egidi, J. Goings, B. Peng, A. Petrone, T. Henderson, D. Ranasinghe, V. G. Zakrzewski, J. Gao, N. Rega, G. Zheng, W. Liang, M. Hada, M. Ehara, K. Toyota, R. Fukuda, J. Hasegawa, M. Ishida, T. Nakajima, Y. Honda, O. Kitao, H. Nakai, T. Vreven, K. Throssell, J. A. Montgomery Jr, J. E. Peralta, F. Ogliaro, M. Bearpark, J. J. Heyd, E. Brothers, K. N. Kudin, V. N. Staroverov, T. Keith, R. Kobayashi, J. Normand, K. Raghavachari, A. Rendell, J. C. Burant, S. S. Iyengar, J. Tomasi, M. Cossi, J. M. Millam, M. Klene, C. Adamo, R. Cammi, J. W. Ochterski, R. L. Martin, K. Morokuma, O. Farkas, J. B. Foresman and D. J. Fox (2016) *Gaussian 09, Revision A.02*. Gaussian, Inc., Wallingford, CT.
36. Strauss, H. M., J. Hughes and P. Schmieder (2005) Heteronuclear solution-state NMR studies of the chromophore in cyanobacterial phytochrome Cph1. *Biochemistry* **44**, 8244–8250.
37. Hahn, J., H. M. Strauss and P. Schmieder (2008) Heteronuclear NMR investigation on the structure and dynamics of the chromophore binding pocket of the cyanobacterial phytochrome Cph1. *JACS* **130**, 11170–11178.
38. Roben, M., J. Hahn, E. Klein, T. Lamparter, G. Psakis, J. Hughes and P. Schmieder (2010) NMR spectroscopic investigation of mobility and hydrogen bonding of the chromophore in the binding pocket of phytochrome proteins. *ChemPhysChem* **11**, 1248–1257.
39. Hahn, J., H. M. Strauss, F. T. Landgraf, H. F. Gimenèz, G. Lochnit, P. Schmieder and J. Hughes (2006) Probing protein–chromophore interactions in Cph1 phytochrome by mutagenesis. *FEBS* **273**, 1415–1429.
40. Escobar, F. V., P. Piwowarski, J. Salewski, N. Michael, M. F. Lopez, A. Rupp, B. M. Qureshi, P. Scheerer, F. Bartl, N. Frankenberg-Dinkel, F. Siebert, M. A. Mroginski and P. Hildebrandt (2015) A protonation-coupled feedback mechanism controls the signalling process in bathy phytochromes. *Nature Chem.* **7**, 423–430.
41. Förstendorf, H., C. Benda, W. Gärtner, M. Storf, H. Scheer and F. Siebert (2001) FTIR studies of phytochrome photoreactions reveal the C=O bands of the chromophore: consequences for its protonation states, conformation, and protein interaction. *Biochemistry* **40**, 14952–14959.
42. Förstendorf, H., T. Lamparter, J. Hughes, W. Gärtner and F. Siebert (2000) The photoreactions of recombinant phytochrome from the cyanobacterium synechocystis: a low-temperature UV–Vis and FT-IR spectroscopic study. *Photochem. Photobiol.* **71**(5), 655–661.
43. Toh, K. C., E. A. Stojković, I. H. M. van Stokkum, K. Moffat and J. T. M. Kennis (2010) Proton-transfer and hydrogen-bond interactions determine fluorescence quantum yield and photochemical efficiency of bacteriophytochrome. *PNAS* **107**, 9170–9175.
44. Polli, D., P. Altoe, O. Weingart, K. M. Spillane, C. Manzoni, D. Brida, G. Tomasello, G. Orlandi, P. Kukura, R. A. Mathies, M. Garavelli and G. Cerullo (2010) Conical intersection dynamics of the primary photoisomerization event in vision. *Nature* **467**, 440–443.
45. Sineshchekov, V., J. Mailliet, G. Psakis, K. Feilke, J. Kopycki, M. Zeidler, L.-O. Essen and J. Hughes (2014) Tyrosine 263 in cyanobacterial phytochrome Cph1 optimizes photochemistry at the prelumi-R→lumi-R step. *Photochem. Photobiol.* **90**, 786–795.

Supporting Information

Influence of heterogeneity on the ultrafast photoisomerization dynamics of Pfr in Cph1 phytochrome

Till Stensitzki,[1] Yang Yang,[1] Anna Lena Wölke, [2] Ernst-Walter Knapp, [2] Jon Hughes, [3] Maria Andrea Mroginski, [4] Karsten Heyne*[1]

[1] Free University Berlin, Department of Physics, Arnimallee 14, 14195 Berlin, Germany.

[2] Free University Berlin, Inst. Chem & Biochem, Fabeckstr 36A, 14195 Berlin, Germany.

[3] Institut für Pflanzenphysiologie, Justus-Liebig Universität, 35390 Gießen, Germany.

[4] Technische Universität Berlin, Institut für Chemie, Sekr. PC14, Straße des 17.Juni135 D-10623 Berlin

*Corresponding author e-mail: karsten.heyne@fu-berlin.de (Karsten Heyne)

Visible spectra

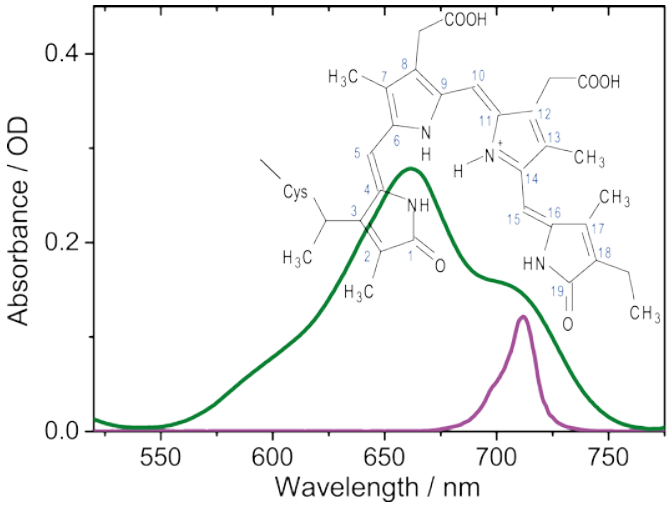

Figure S1: Absorption spectrum of a Cph1 directly after illumination with a 640nm diode (green) and spectrum of pump pulse (purple). Inset: structure of the photoreceptor PCB with numbered carbon atoms.

Simulation of the Vis-IR Decay Associated Spectra with Lorentzian bands To elude the nature of each decay-component, each polarization resolved decay associated spectra was fitted with the minimal number of Lorentzian-bands necessary for a reasonable fit. Constraints for the width and amplitude of the ring-D bleaching band was determined from the perturbed free induction decay, a coherent contribution detected for negative delay. While the width and the position of the bands was shared for both polarizations, the amplitude could differ between both polarizations. The errors presented here were estimated from the hessian of the residual function. The errors of the relative tdm angles as presented in paper were calculated by exhaustive search analysis, which is less effect by covariance between parameters. The optimization was done with Origin 8.

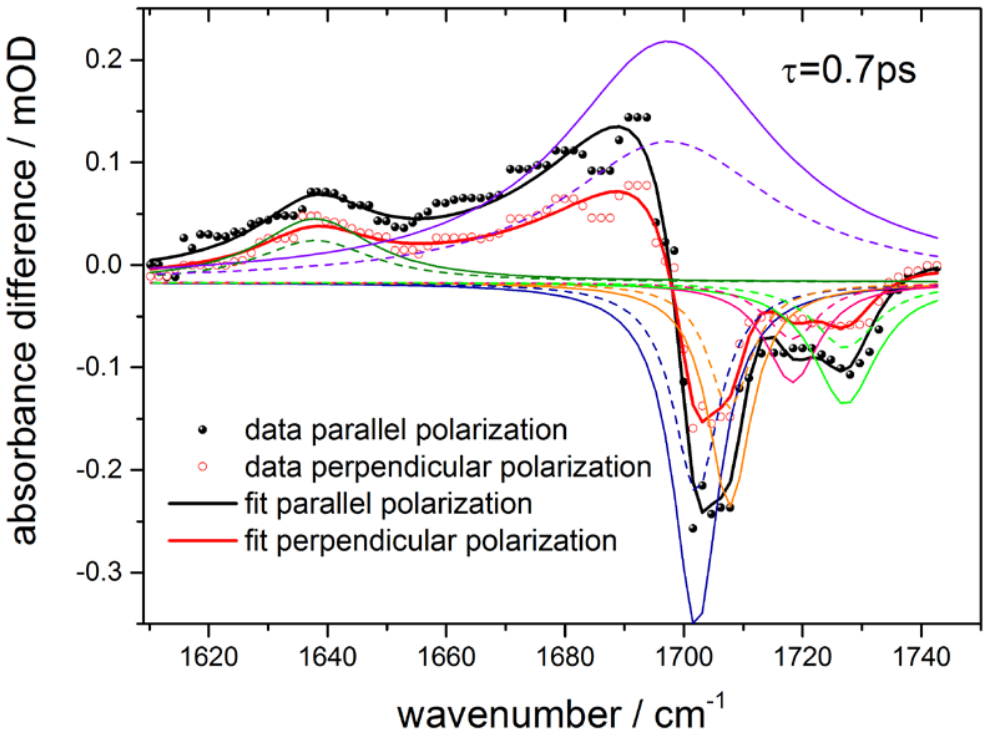

Figure S2: Decay associated spectrum (DAS) for the time constant 0.7 ps in the IR spectral range. Data and simulation for parallel polarization are presented as black circles and black line, respectively. Data and simulation for perpendicular polarization are presented as red circles and red line, respectively. Individual Lorentzians are plotted as solid and dashed lines for parallel and perpendicular polarizations, respectively.

Table ST1: Fit parameters for DAS time constant 0.7 ps as presented in Figure S2.

Frequency	pol	FWHM	Amplitude
1638	∥	19±5	1.6±0.4
1638	⊥		1.0±0.3
1698	∥	43±4	15±7
1698	⊥		9±4
1702	∥	9 ±2	-5±2
1702	⊥		-3±1
1708	∥	8±2	-3±2
1708	⊥		-2±1
1718	∥	12±7	-2±4
1718	⊥		-1±3
1727	∥	13	-3±4
1727	⊥		-2±2

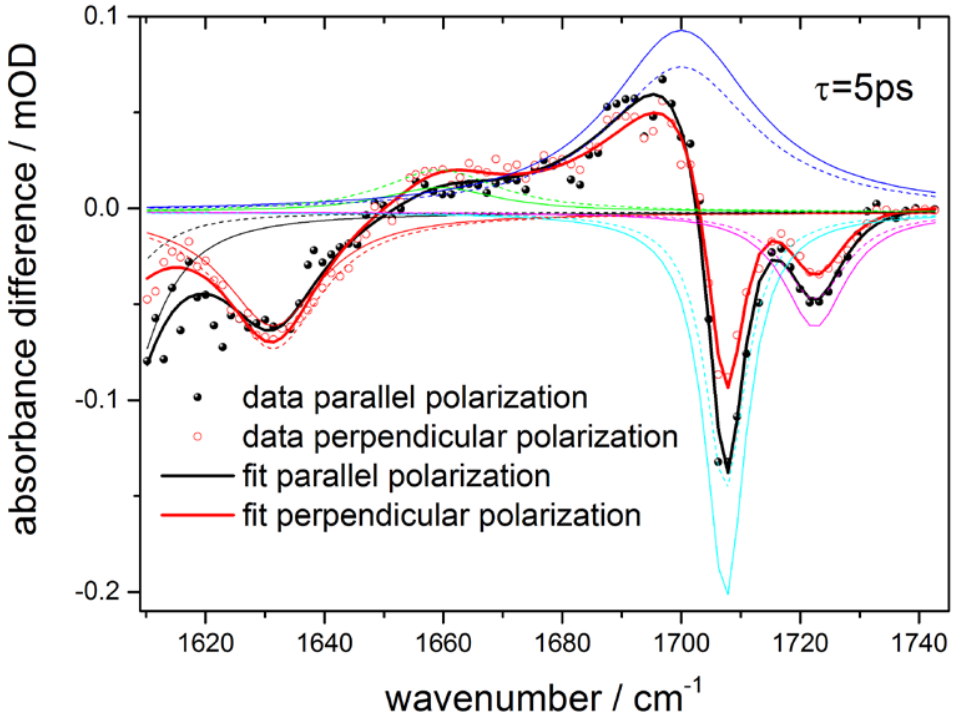

Figure S3: Decay associated spectrum (DAS) for the time constant 5.0 ps in the IR spectral range. Data and simulation for parallel polarization are presented as black circles and black line, respectively. Data and simulation for perpendicular polarization are presented as red circles and red line, respectively. Individual Lorentzians are plotted as solid and dashed lines for parallel and perpendicular polarizations, respectively.

Table ST2: Fit parameters for DAS time constant 5.0 ps as presented in Figure S3.

Frequency	pol	FWHM	Amplitude
1604	∥	17	-2.7±0.3
1604	⊥		-0.9±0.3
1632	∥	22±3	-2.1±0.6
1632	⊥		-2.6±0.8
1702	∥	28±3	5±2
1702	⊥		4±2
1708	∥	9±1	-3±1
1708	⊥		-2.1±0.7
1721	∥	14±7	-1.4±0.7
1721	⊥		-1.1±0.5

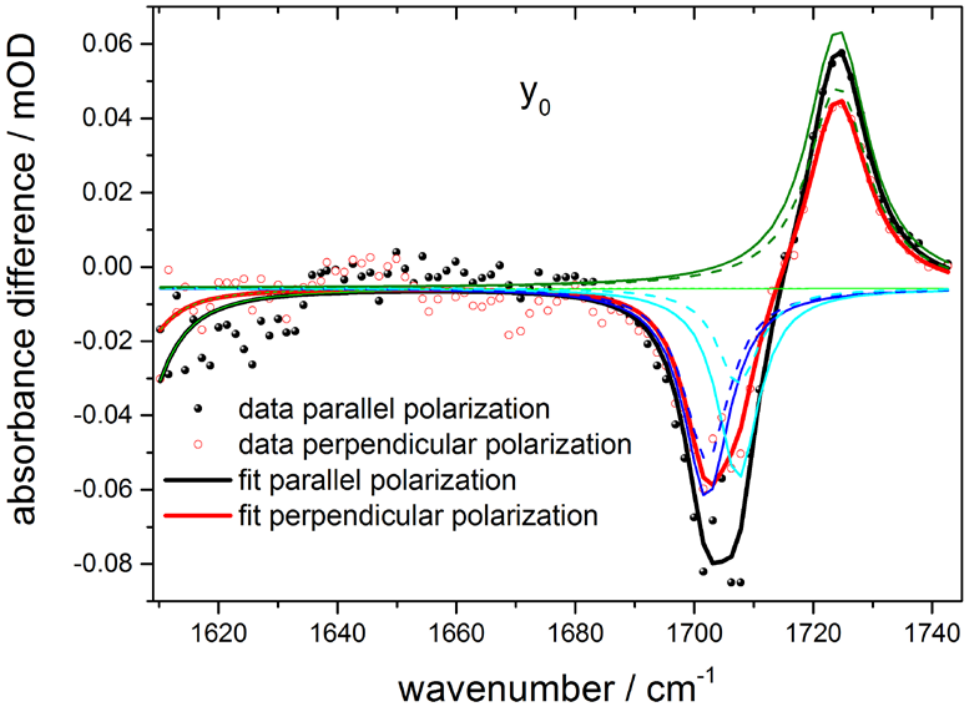

Figure S4: Decay associated spectrum (DAS) for constant component in the IR spectral range, after photoisomerization. Data and simulation for parallel polarization are presented as black circles and black line, respectively. Data and simulation for perpendicular polarization are presented as red circles and red line, respectively. Individual Lorentzians are plotted as solid and dashed lines for parallel and perpendicular polarizations, respectively.

Table ST3: Fit parameters for constant component in the DAS presented in Figure S4. Positions and FWHM for bleaching bands at 1702 cm^{-1} and 1708 cm^{-1} were taken from the other simulations.

Frequency	pol	FWHM	Amplitude
1702	∥	9	-0.83±0.06
1702	⊥		-0.68±0.06
1708	∥	8	-0.68±0.06
1708	⊥		-0.34±0.06
1724	∥	12±2	1.34 ±0.08
1724	⊥		1.05±0.07

Excited-state nature of the photoreaction

To further establish the ES-nature of the initial photoreaction of phytochrome, additional analysis of the Vis-vis data is presented here. In figure S5, the absorption spectra were subtracted from the data to remove the negative bleaching component. After removal, the positive band still shows a dip. The origin of the dip can be well explained by the presence of stimulated emission at the red edge of the initial bleaching band. Figure S6 shows selected transients from the NIR region, where the Q-band to Soret-band transition is observed. The observed signal is the region remains for some picoseconds. An assumed hot ground state with a spectral large shift of at least 2000 cm-1 would unlikely have such a long lifetime.

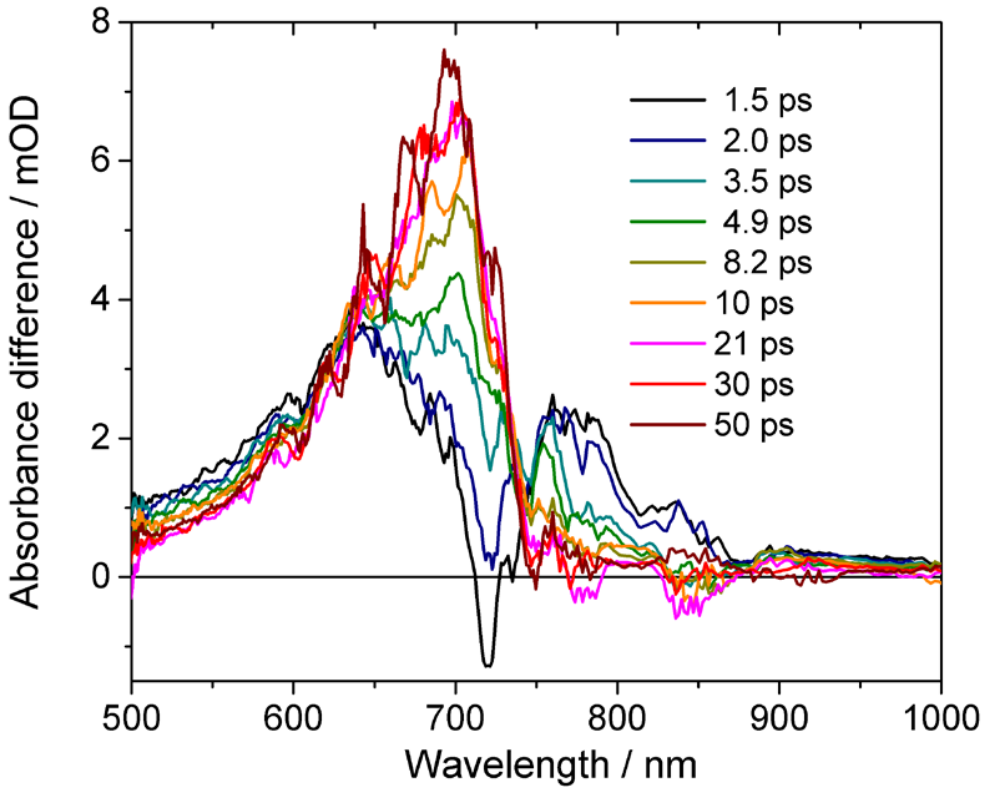

Figure S5: Absorbance difference spectra from Figure 5 with added bleaching spectrum (Pfr absorption). The amount of added Pfr absorption spectrum was increased to the point where the Lumi-F absorption at 50 ps was all positive. Since photoisomerization and Lumi-F formation takes place with ~ 0.7 ps, no additional photoproduct generation occurs from 1.5 ps to 50 ps. In Figure S2 we observe a broad absorption at a few picoseconds with a negative contribution peaking at 720 nm. This negative contribution is better described by the stimulated emission than the absorption of Pfr. This would indicate a contribution from an excited state on the picosecond time scale. Moreover, up to about 20 ps Lumi-F absorption narrows with increasing delay time, providing further evidence for photoproduct cooling.

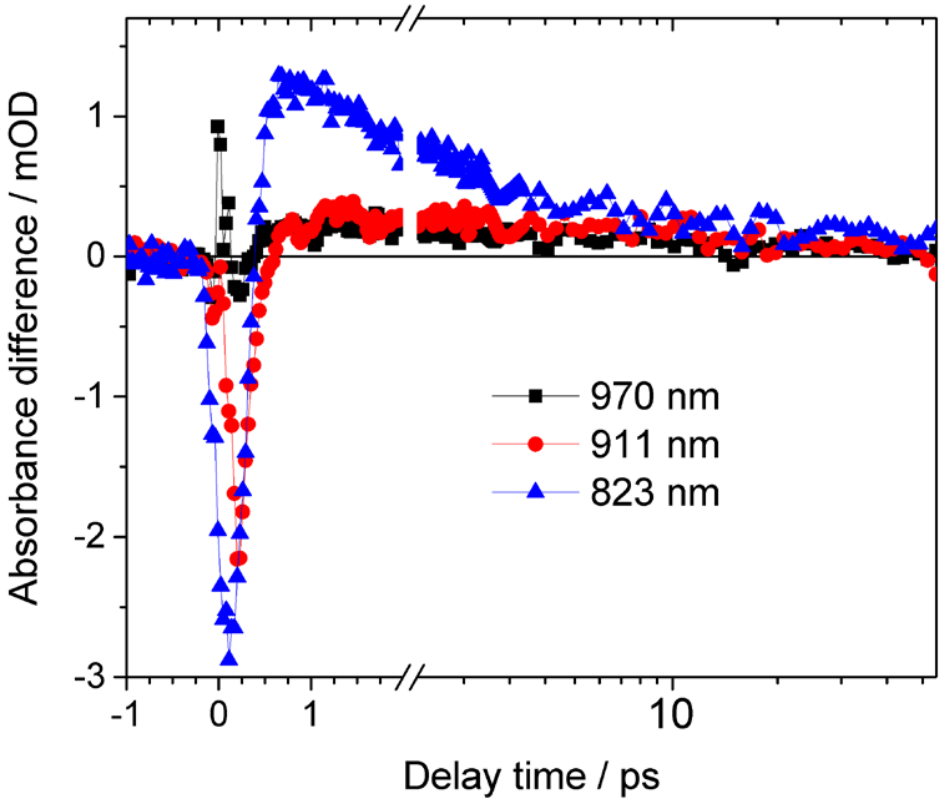

Figure S6: Transient signals in the near infrared region around 900 nm. The early negative signal displays stimulated emission, the positive signal on the picosecond time scale S1→S2 excited state absorption. The selected transients are far away from the absorption of Lumi-F. It is clearly visible that after decay of the stimulated emission the positive signal remains and stays on a picosecond time scale.

Proposed reaction scheme

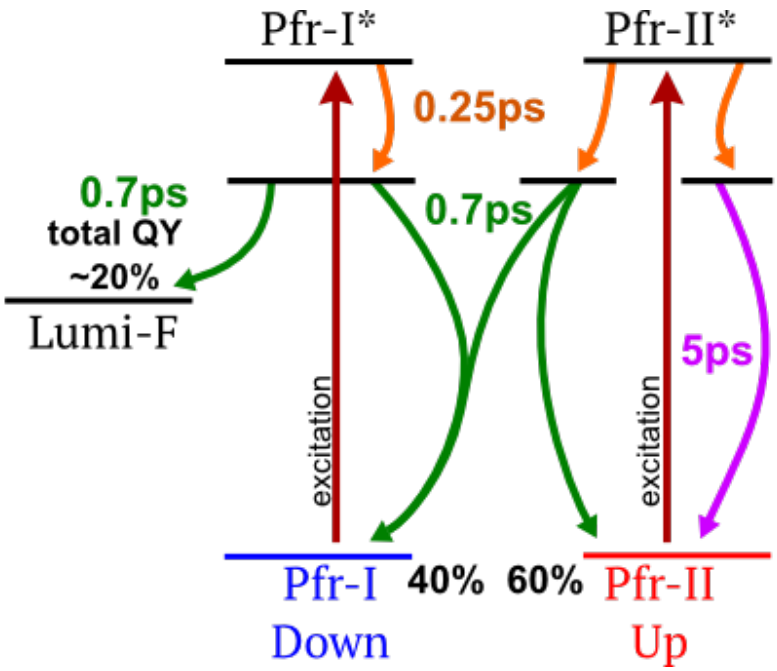

Figure S7: Proposed reaction scheme sketch. The given QY is relative to the initial total Pfr-I + Pfr-II population. Note that the shown model is not the only valid description of the data. Generation of the Lumi-F state from the Pfr-II state cannot be ruled out from our data. The relaxation time constant of Pfr-II was determined to 5 ps for the IR data and 6 ps for the visible data.

Calculated structural models, supplementary figures and data

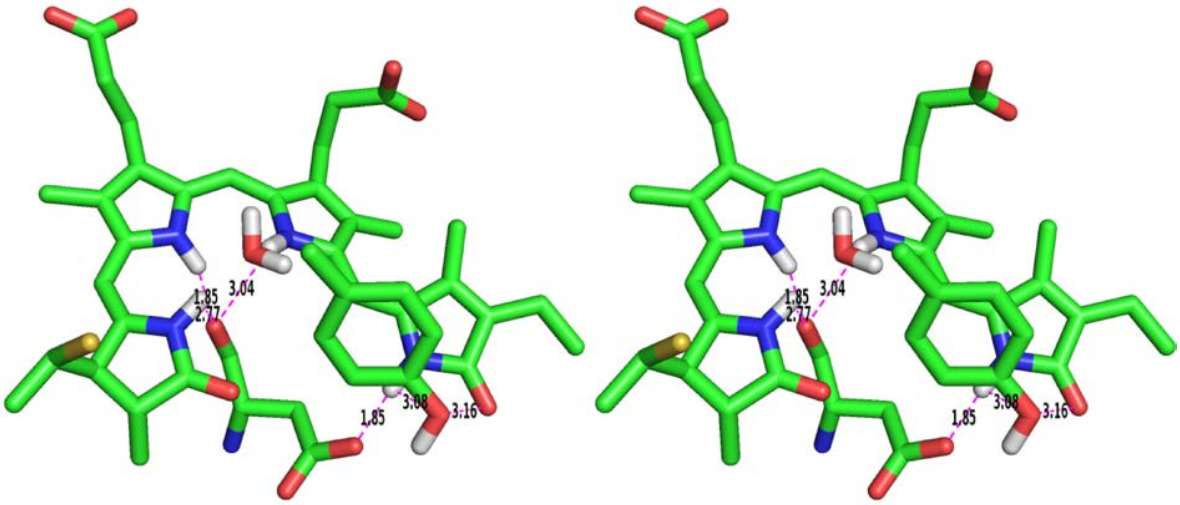

Figure S8: Stereo view of down conformation model showing the chromophore with ring *D* on the right, the pyrrole water, Asp207 (below), and Tyr263 (above).

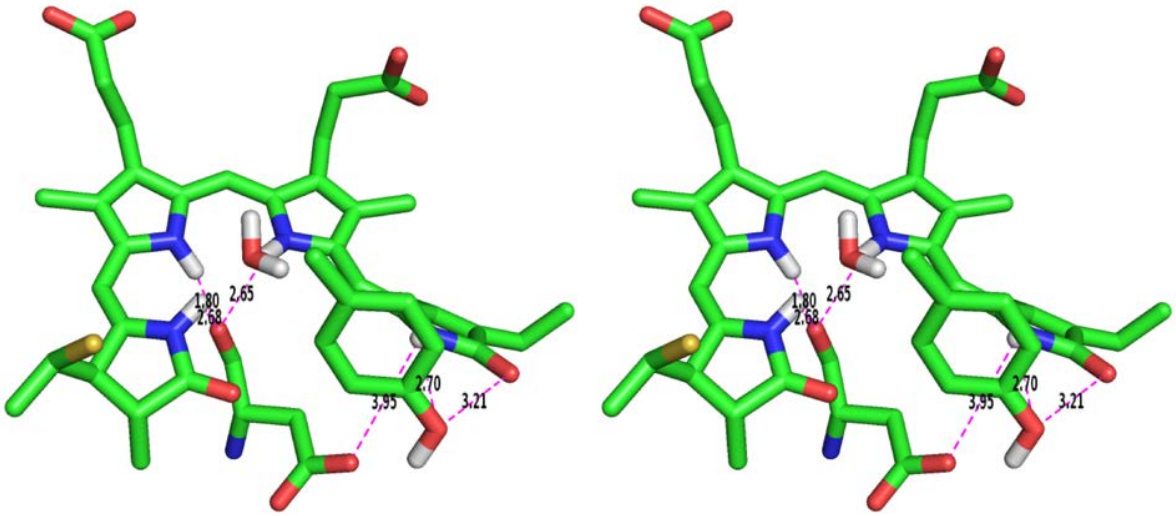

Figure S9: Stereo view of up conformation model showing the chromophore with ring *D* on the right, the pyrrole water, Asp207 (below), and Tyr263 (above).

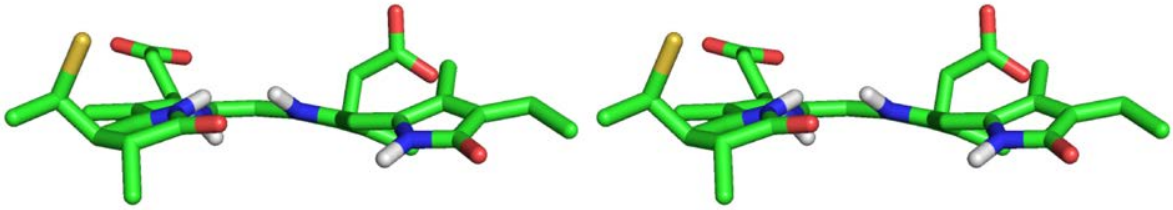

Figure S10: Definition of the down conformation model. The vector from the nitrogen of ring D (right) to its hydrogen is pointing downwards.

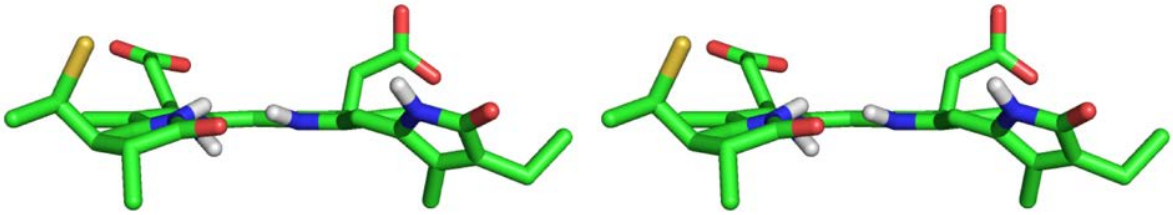

Figure S11: Definition of the up conformation model. The vector from the nitrogen of ring *D* (right) to its hydrogen is pointing upwards.

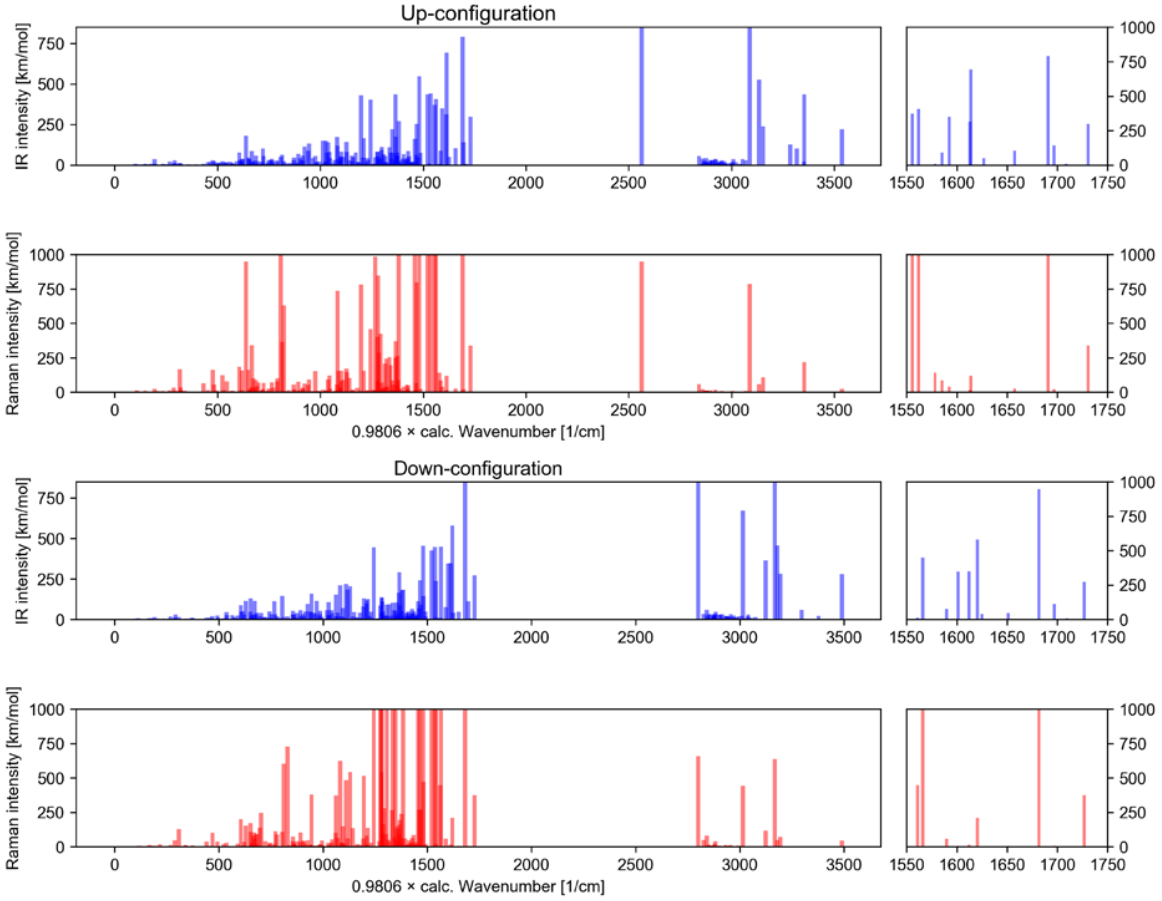

Figure S12: Calculated vibrational modes and intensities for both structural models presented as stick plots. Full information on the modes is given in the supplemental assign files.

frontiers in Molecular Biosciences

ORIGINAL RESEARCH
published: 22 July 2015
doi: 10.3389/fmolb.2015.00041

The primary photoreaction of channelrhodopsin-1: wavelength dependent photoreactions induced by ground-state heterogeneity

Till Stensitzki, Vera Muders, Ramona Schlesinger, Joachim Heberle and Karsten Heyne *

Institute of Experimental Physics, Free University Berlin, Berlin, Germany

The primary photodynamics of channelrhodopsin-1 from *Chlamydomonas augustae* (*Ca*ChR1) was investigated by VIS-pump supercontinuum probe experiments from femtoseconds to 100 picoseconds. In contrast to reported experiments on channelrhodopsin-2 from *Chlamydomonas reinhardtii* (*Cr*ChR2), we found a clear dependence of the photoreaction dynamics on varying the excitation wavelength. Upon excitation at 500 and at 550 nm we detected different bleaching bands, and spectrally distinct photoproduct absorptions in the first picoseconds. We assign the former to the ground-state heterogeneity of a mixture of 13-*cis* and all-*trans* retinal maximally absorbing around 480 and 540 nm, respectively. At 550 nm, all-*trans* retinal of the ground state is almost exclusively excited. Here, we found a fast all-*trans* to 13-*cis* isomerization process to a hot and spectrally broad P_1 photoproduct with a time constant of (100 ± 50) fs, followed by photoproduct relaxation with time constants of (500 ± 100) fs and (5 ± 1) ps. The remaining fraction relaxes back to the parent ground state with time constants of (500 ± 100) fs and (5 ± 1) ps. Upon excitation at 500 nm a mixture of both chromophore conformations is excited, resulting in overlapping reaction dynamics with additional time constants of <300 fs, (1.8 ± 0.3) ps and (90 ± 25) ps. A new photoproduct Q is formed absorbing at around 600 nm. Strong coherent oscillatory signals were found pertaining up to several picoseconds. We determined low frequency modes around 200 cm^{-1}, similar to those reported for bacteriorhodopsin.

Keywords: *Ca*ChR1, retinal, isomerization, femtosecond pump-probe spectroscopy, reaction model, ground-state heterogeneity

OPEN ACCESS

Edited by:
Tilo Mathes,
Vrije Universiteit Amsterdam, Netherlands

Reviewed by:
Josef Wachtveitl,
Goethe-University Frankfurt, Germany
Jose Luis Perez Lustres,
University of Santiago de Compostela, Spain

***Correspondence:**
Karsten Heyne,
Institute of Experimental Physics, Free University Berlin, Arnimallee 14, 14195 Berlin, Germany
karsten.heyne@fu-berlin.de

Specialty section:
This article was submitted to Biophysics, a section of the journal Frontiers in Molecular Biosciences

Received: *31 March 2015*
Accepted: *06 July 2015*
Published: *22 July 2015*

Citation:
Stensitzki T, Muders V, Schlesinger R, Heberle J and Heyne K (2015) The primary photoreaction of channelrhodopsin-1: wavelength dependent photoreactions induced by ground-state heterogeneity. Front. Mol. Biosci. 2:41. doi: 10.3389/fmolb.2015.00041

Introduction

Microbial rhodopsins comprise a large family of light-driven ion pumps and sensors. In 2002, a new functionality of microbial rhodopsins was introduced by the discovery of a light-gated ion channel (named channelrhodopsin) in the eyespot of the green algae *Chlamydomonas reinhardtii* (Nagel et al., 2002). A year later, a second channelrhodopsin (*Cr*ChR2) was characterized, Nagel et al. (2003) which paved the way for the new field of optogenetics where action potentials are elicited in neurons simply by remote illumination (Fenno et al., 2011).

Common to all rhodopsins, the polypeptide folds into the membrane in the form of a seven-helical bundle with the retinal chromophore covalently attached to a conserved lysine to form

a protonated Schiff base (SB). Electron microscopy provided the first structural information on *Cr*ChR2 and resolved the arrangement of the seven transmembrane helices (Muller et al., 2011). X-ray crystallography provided a high-resolution three-dimensional structural model of C1C2, a chimera of channelrhodopsin derived from *Cr*ChR1 (helices A–E) and *Cr*ChR2 (helices F, G) (Kato et al., 2012). It was shown by PELDOR spectroscopy that helices B and F move to open the cation channel under illumination (Krause et al., 2013; Sattig et al., 2013). Electron microscopy of the open state confirmed these helical movements among others (Muller et al., 2015).

All native channelrhodopsins (ChRs) are cation channels which share sequence homology and similar functionalities but differ in spectral sensitivity, photocurrent, and desensitization. The visible absorption of retinal in ChR1 from *Chlamydomonas augustae* (*Ca*ChR1) is red-shifted by 50 nm as compared to the widely employed *Cr*ChR2 (Hou et al., 2012). This spectral feature renders *Ca*ChR1 advantageous in optogenetic applications where an increased penetration depth of the excitation light is required.

Illumination of ChRs induces a cyclic reaction (Ritter et al., 2008; Lorenz-Fonfria and Heberle, 2014). Up to now, the photocycle of *Ca*ChR1 has been recorded only at ns time resolution. Akin to the photoreaction of *Cr*ChR2 (Bamann et al., 2008; Ernst et al., 2008) an early red-shifted P_1^{590} intermediate with absorption maximum at ~590 nm appears, which decays into the P_2^{380} intermediate with absorption peak at 380 nm. The long lifetime of the P_2^{380} state in *Ca*ChR1 is the most striking difference to *Cr*ChR2 (Sineshchekov et al., 2013) (our unpublished observations). As the lifetime of P_2^{380} correlates with the lifetime of the passive channel current, the P_2^{380} intermediate represents the conductive state of *Ca*ChR1. A P_3 intermediate is not observed in *Ca*ChR1 but minor contributions from an O-like intermediate at 600 nm appear (Sineshchekov et al., 2013). Intramolecular proton transfer occurs in *Ca*ChR1 (Sineshchekov et al., 2013; Ogren et al., 2015a) but with distinct differences to *Cr*ChR2 (Lorenz-Fonfria et al., 2013; Ogren et al., 2015b).

UV/VIS pump-probe spectroscopy shows *Cr*ChR2 relaxation on the S_1 potential energy surface by 150 fs, followed by a decay with a time constant of 400 fs into a hot ground state P_1 and the parent ground state. The hot P_1 relaxes with a time constant of 2.7 ps to a thermally equilibrated P_1, the first intermediate state of the photocycle (Verhoefen et al., 2010). This intermediate state is characterized by retinal in a 13-*cis* conformation and accompanied by conformational changes in the protein backbone (Neumann-Verhoefen et al., 2013). A slow relaxation pathway of 200 ps was observed (Verhoefen et al., 2010).

The configuration of retinal in the ground state of *Ca*ChR1 was identified by retinal extraction followed by isomer separation with high-performance liquid chromatography (HPLC). Similar to *Cr*ChR2, the retinal isomer composition of the ground state result in a mixture of ~70:30 all-*trans* to 13-*cis* retinal (Nack et al., 2009; Muders et al., 2014). Resonance Raman experiments showed that the vibrational bands in the C = C stretching region derive from a mixture of retinals, which were assigned to mostly all-*trans* and partially 13-*cis* retinal. The band assignment in the C–C stretching region to contributions of 13-*cis* retinal was inexplicit, therefore also 100% all-*trans* retinal in the ground state was discussed (Ogren et al., 2014).

Here, we present the first femtosecond VIS pump supercontinuum probe spectroscopic experiments on *Ca*ChR1. Blue-shifted and red-shifted excitations with respect to the visible absorption maximum were applied to resolve the early photoreactions of 13-*cis* and all-*trans* retinal containing populations of *Ca*ChR1.

Materials and Methods

*Ca*ChR1 was prepared as described (Lorenz-Fonfria et al., 2014; Muders et al., 2014). Briefly, the truncated *Ca*ChR1 gene (1–352 aa) was fused with a 10 × His-tag (GeneArt, Life Technologies) and was heterologously expressed in *Pichia pastoris* cells. The solubilized protein was purified on a Ni-NTA column (Macherey-Nagel, Germany) and concentrated to 46 mg/mL in buffer containing 20 mM Hepes, 100 mM NaCl, 0.05% DDM at pH 7.4. Two times 150 µL of the *Ca*ChR1 solution was placed between two CaF_2 windows. The sample cell thickness was 100 µm, and the sample was rapidly moved perpendicular to the beam direction by a Lissajous scanner to provide a fresh sample at every shot. The spectral shape of the two selected femtosecond excitation pulses are plotted with the absorption spectrum of *Ca*ChR1 in **Figure 1**. Femtosecond laser pulses were generated starting from a fundamental femtosecond laser pulse delivered by a 1 kHz Ti:Sa laser system (Coherent Legend USP, 80 fs pulses at 800 nm). The fundamental beam was split into two parts for pump and probe pulse generation. The pump pulses were generated in a non-collinear optical parametric amplifier (NOPA). A sapphire white light supercontiuum was used as seed, amplified in a BBO crystal by frequency doubled pulses at 400 nm. We selected energies to excite the sample of about 0.4–0.5 µJ per pulse with a pump focus diameter of about 300 µm.

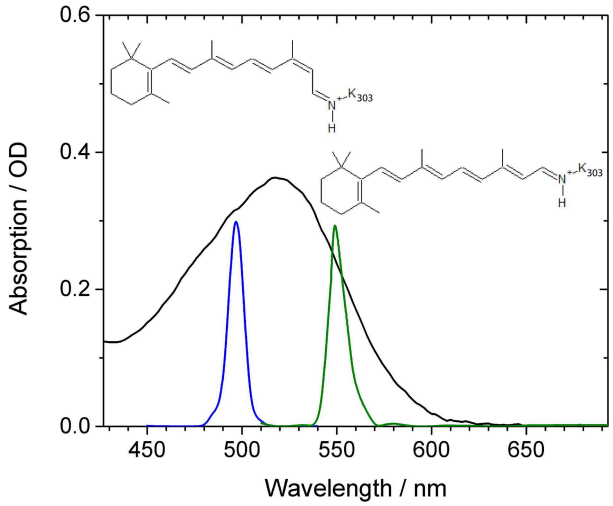

FIGURE 1 | Absorption spectrum of *Ca*ChR1 (black line) as a function of wavelength. Blue and green lines indicate the shape of the excitation pulses used in our experiments. The reported chromophore isomer structures of 13-*cis* retinal and all-*trans* retinal are inserted.

At an optical density of 0.25 OD in the absorption maximum we excite about 10% of the sample. The fundamental for the probe pulses were first directed over an optical delay line, then focused into a 1 cm water cell generating the broadband white light supercontinuum from ∼400 to ∼1100 nm for probing. We selected probe wavelengths from 427 to 693 nm. We achieved fluctuations of below 1% standard deviation with a properly aligned water white light setup. Both beams were focused into the sample cell by a curved mirror. Behind the cell, the probe beam is collimated and passed through a short-pass filter (<750 nm) and a polarizer. The beam is than focused into a fiber connected with a grating spectrometer (Andor Shamrock 303i, 600 l/cm) equipped with a CCD camera system (2000 × 5 pixel, 0.35 nm/pixel, Stresing GmbH Berlin). The spectral resolution was below 0.5 nm. We used step sizes of 30 fs from −1 to 5 ps, and step sizes of $\log_{10}$ for longer delay times, and 8000 averages per data point. Every second pump beam was blocked by a chopper to record excited and not excited sample volumes alternatively. Since we found negligible polarization effects, we selected perpendicular polarization between pump and probe beam to reduce stray light. The time-zero was determined by recording the signal in pure CaF_2 of the sample window. The delay with a maximal signal for each pixel was found and the resulting wavelength-delay curve was fitted with a 3rd order polynomial. For better visibility, the data shown in the contour plots in **Figure 2** were smoothed in the time domain with Gaussian windows with a width of 4 points of 30 fs step size (corresponding to FWHM of 200 fs). This strongly reduces the oscillatory features. The unfiltered dataset is available in Figure S2. The instrument response function (IRF) determined to be 90 fs is governed by the pump pulse length (see Figure S6) (Kovalenko et al., 1999). The chirped water white light supercontinuum has negligible influence on the IRF after mathematical chirp correction Hence, the low frequency mode at 316 cm^{-1} with an oscillation period of 104 fs of our CaF2 windows could be well-resolved, and was used as an internal standard.

Results

In **Figure 1** the absorption spectrum of *Ca*ChR1 is presented with two spectrally different excitation pulse positions, and the two retinal chromophore conformations. The absorption spectrum peaks at 518 nm, exhibits a steeper decline at longer wavelengths compared to shorter wavelengths, and has a shoulder at around 470 nm. Raman studies showed that the retinal chromophore in ground-state *Ca*ChR1 adopts a mixture of 13-*cis* and all-*trans* conformations with a fraction of ∼30 and ∼70%, respectively (Muders et al., 2014).

Thus, different absorptions are expected for *Ca*ChR1 harboring 13-*cis* and all-*trans* retinal (Muders et al., 2014). The displayed absorption profile is broad and covers about 100 nm similarly as it was reported for dark-adapted bacteriorhodopsin and some bacteriorhodopsin mutants (Mowery et al., 1979; Harbison et al., 1984; Heyne et al., 2000). Assuming the same protein surrounding, and a simple particle in a box approach for the direction of the electronic transition dipole moment, the 13-*cis* retinal is expected to absorb at lower wavelengths due to a reduced length in one direction of its bent conjugated π-electron system of the ethylenic moiety compared to all-*trans* retinal (Aton et al., 1977; Fodor et al., 1989). Therefore, we expect complex photoreaction dynamics of *Ca*ChR1 with 13-*cis* retinal and with all-*trans* retinal upon excitation at 500 nm, while upon excitation at 550 nm at the low energy side of the absorption

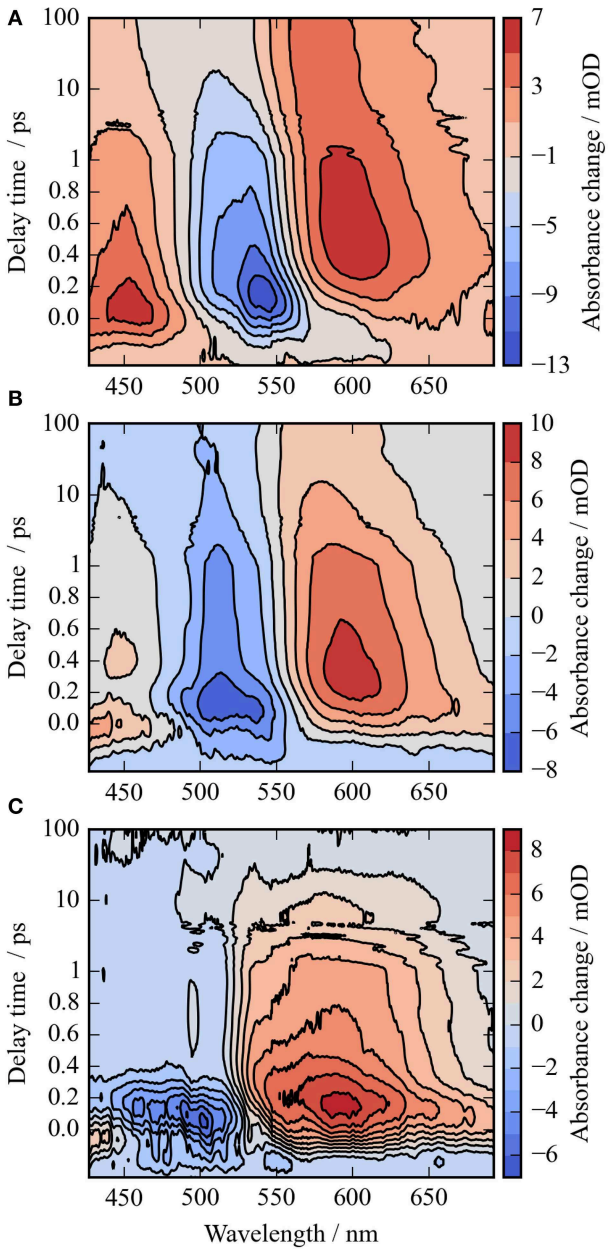

FIGURE 2 | Contour plots of the photoreaction dynamics of *Ca*ChR1 upon excitation at 550 nm (A), 500 nm (B), and the difference of both datasets (C). Blue colors indicate negative signals, red colors positive signals. The contour plots display the absorbance difference in mOD upon excitation as a function of delay time and wavelength. The contour plots were smoothed in the time domain with Gaussian windows with a width of 4 points (FWHM of ∼200 fs), the unfiltered dataset is depicted in Figure S2. The difference contour plot **(C)** is calculated by the direct difference of **(B)** and **(A)**.

spectrum the photoreaction dynamics of *Ca*ChR1 containing all-*trans* retinal will dominate.

In **Figure 2A** the absorbance change of *Ca*ChR1 upon excitation at 550 nm is presented as a function of probe wavelength from 427 to 693 nm for different pump probe delay times. In this contour plot positive signals are found in the spectral region around 450 and 600 nm, while negative signals are visible around 540 nm. Upon excitation the initial absorption increase of excited state absorption (ESA) is found around 450 nm. The transient at 450 nm is plotted in **Figure 3** (blue dots). The major part of the ESA signal exhibits a fast decay with time constant τ_1 of 100 fs accompanied with a spectral narrowing displayed in **Figure 2A**, in conflict with a blue shift of the ESA. This points to relaxation or isomerization on the electronic excited state potential energy surface. The negative signal in **Figure 2A** exhibits a blue shift and decays at longer wavelengths on the same time scale. The major fraction of the transient at 550 nm (**Figure 3**, green dots) decays with τ_1, a smaller fraction exhibits time constants of $\tau_2 = (0.5 \pm 0.1)$ and $\tau_3 = (5 \pm 1)$ ps. Decay associated spectra (DAS) representing decaying spectral features with a given time constant are displayed in **Figure 4**. The DAS of the time constant $\tau_1 = 100$ fs exhibits a positive signal from 427 to 490 nm, and a negative signal for longer wavelengths. At short wavelengths the positive signal shows the instantaneous ESA, while the negative signal represents stimulated emission decay and the rise of the first photoproduct. Note, there is no contribution matching the bleaching signal, indicating no back reaction to the parent ground state on this ultrafast time scale. We assign the time constant $\tau_1 = (100 \pm 50)$ fs to excited state decay accompanied by stimulated emission decay, and 13-*cis* photoproduct formation. The DAS for time constants of 500 fs and 5 ps exhibit very similar spectral features with a stronger signal for long and short wavelengths of the 500 fs component. This could be interpreted by involvement of the same electronic ground state showing broader spectral features of a hotter ground state at early delay times. A hot ground state is characterized by population of excited vibrations not relaxed to their thermal equilibrium. These populated non-thermal vibrations relax via intra- and intermolecular vibrational redistribution pathways on a picosecond time scale (Heyne et al., 2004a,b; Rey et al., 2004; Kozich et al., 2006; Shigeto et al., 2008). The positive signal contributions around 450 nm occur instantaneously upon excitation and persist up to 100 ps, as visible by the vanishing negative signal at 430 nm at 100 ps delay time (**Figures 4**, **5A**). Since the bleaching signal has negative contribution at this spectral position, a positive band is also contributing there. Thus, the first thermally relaxed photoproduct P_1 exhibits a broad spectral absorption from 427 to 693 nm with a maximum at about 560 nm (see Figure S1).

The rise of the vibrational excited (hot) photoproduct P_1 within 100 femtoseconds is visible at 600 nm, and at 650 nm in **Figures 2A**, **3**. After formation of the hot photoproduct P_1 a relaxation occurs on the low energy and high energy side of the absorption on a time scale of $\tau_2 = (500 \pm 100)$ fs to a more cooled, but still hot photoproduct, which relaxes further with a time constant of $\tau_2 = (5 \pm 1)$ ps to the thermally relaxed P_1. As a result of the cooling processes the positive absorption shifts to smaller wavelengths and the spectral feature narrows as displayed in **Figure 2A**. No stimulated emission signals were observed after 200 fs, corroborating the excited state decay with <100 fs.

The spectral integrated transient upon excitation at 550 nm is depicted in **Figure 7**. The spectral integrated transient provides information on the overall change in extinction coefficient. This assumption holds for integrated spectral ranges covering the whole contributing absorption band. This is fulfilled to a high extend in our measurements. Upon excitation at 550 nm a strong coherent contribution of the CaF_2 sample cell window is clearly

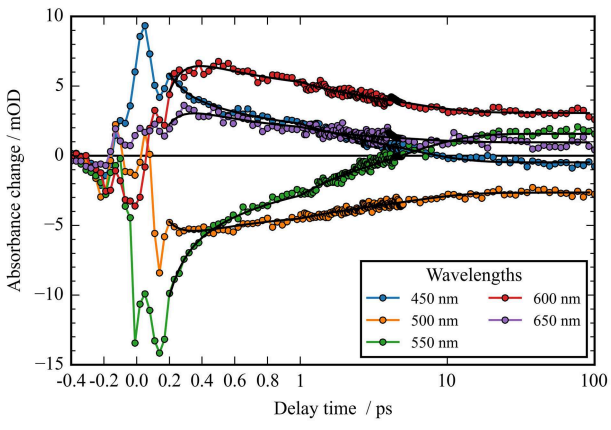

FIGURE 3 | Transients (dots) and simulated transients (black lines) upon excitation at 550 nm: the temporal change in absorption of *Ca*ChR1 is plotted as a function of delay time after excitation. Transient changes on the 100 femtosecond, sub picosecond, and picosecond time scales are directly visible.

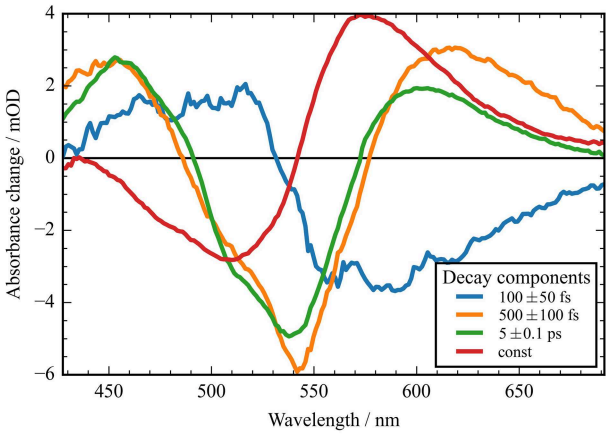

FIGURE 4 | Decay associated spectra (DAS) of the transient data upon excitation at 550 nm of *Ca*ChR1. Positive signals indicate decaying excited state and photoproduct absorption; negative signals indicate decaying bleaching absorption, rising photoproduct absorption, and stimulated emission decay. The fast component (blue line) exhibits no signature of the bleaching signal. The two components at 500 fs and 5 ps decay time exhibit similar spectral shapes with deviations at the high and low energy side. The red line displays the spectral difference between the bleaching signal and the photoproduct P_1.

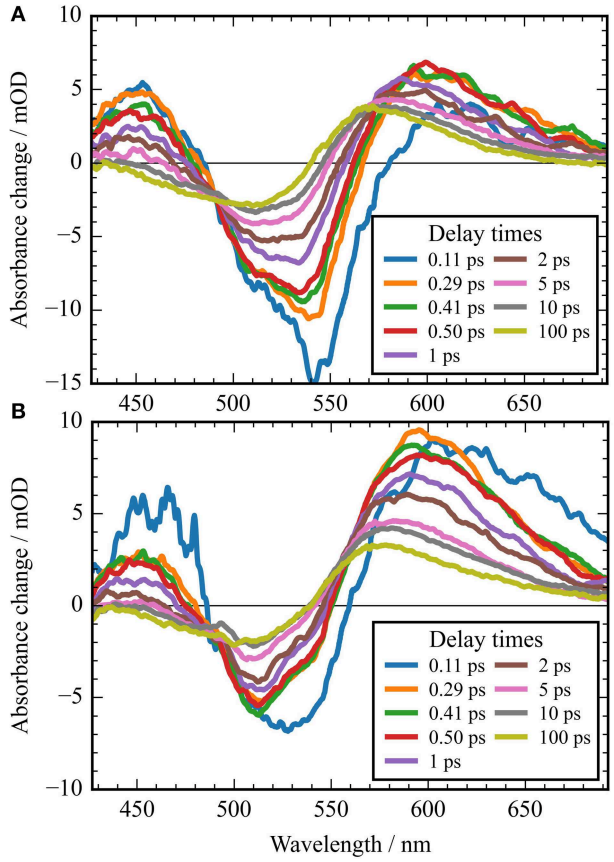

FIGURE 5 | Absorbance difference spectra of *Ca*ChR1 upon excitation at 550 nm (A), and upon excitation at 500 nm (B). The first spectra at 0.11 ps could still be influenced by the instrument response function. Comparison of both spectra displays striking differences in the photoproduct region around 600 nm at picosecond delay times.

visible in **Figure 7** around time zero. We observe coherent oscillations in the first picoseconds with a period of ∼100 fs. As shown in **Figure 7** the overall integrated transient rises within 100 femtoseconds to positive values, and stays nearly constant for picoseconds. Spectral integrated transients are not affected by spectral shifting, but are sensitive to new emerging species with different extinction coefficients. We see no significant signal change after 300 fs. Therefore, we assign the time constants of 500 fs and 5 ps to cooling processes of the photoproduct. As presented in **Figure 4**, the stimulated emission decays with a time constant of 100 fs. Since, the only detectable transition from the electronic excited state to another state is connected with the time constant of 100 fs, we assign this process to the all-*trans* to 13-*cis* isomerization.

It was reported that the initial photoreaction is independent of the excitation wavelength in *Cr*ChR2 (Verhoefen et al., 2010). For *Ca*ChR1, we see significant changes upon changing the excitation wavelength from the low energy side of the absorption band at 550 nm to the high energy side of the absorption band at 500 nm. The differences are best visible by comparing **Figures 5A,B**, as well as by comparing **Figures 2A,B**.

In **Figure 2B** the contour plot of the photoreaction dynamics upon 500 nm excitation is plotted. Again, there are instantaneous positive signals around 450 nm, instantaneous negative signals around 510 nm, and positive signals around 600 nm showing a delayed emergence. The negative signal exhibits features of a fast decaying fraction around 560 nm, pointing to a very small stimulated emission as compared to excitation at 550 nm. In addition, the bleaching signal peaks clearly at 510 nm continuing in position. The positive signal around 600 nm is much stronger compared to excitation at 550 nm. Since we expect to excite *Ca*ChR1 with 13-*cis* retinal as well as *Ca*ChR1 with all-*trans* retinal upon excitation at 500 nm, the photoreaction dynamics should consist of two parts. One part describes the photoreaction of *Ca*ChR1 with all-*trans* retinal, the other part the photoreaction of *Ca*ChR1 containing 13-*cis* retinal. Since the bleaching signals at 100 ps, where the primary photoreaction is nearly finished, shows identical spectral shape from 430 to 510 nm for excitation at 550 and 500 nm, we have a handle to compare both photoreactions directly. Therefore, the dataset excited at 500 nm was scaled by 1.4 to match the bleaching signals of both datasets at 100 ps delay time. Then, we subtracted the dataset upon excitation at 500 nm from the dataset upon excitation at 550 nm. The resulting difference is plotted as a contour plot in **Figure 2C**. The difference dataset has negative signals below ∼520 nm with a maximum around 480 nm, and positive signals above 520 nm. Within the first 100 femtoseconds ($\tau_1 < 300$ fs) the negative signal exhibits a strong decay, while the positive signal decays with a blue shift on this time scale (**Figure 2C**).

The remaining positive signal decays with time constants of $\tau_2 = (1.8 \pm 0.3)$ and $\tau_3 = (90 \pm 25)$ ps to zero. The corresponding decay associated spectra (DAS) and transients are presented in Figure S7. The positive signal corresponding to τ_2 exhibits a maximum at 590 nm and a broad absorption from 520 nm to wavelengths longer than 690 nm. A small negative contribution is found around 500 nm. The DAS corresponding to τ_3 (DAS_3) has a smaller amplitude with a maximum at 570 nm and positive signals from 490 to 690 nm. Small negative contributions are found around 450 nm. The spectral integrated signal in Figure S4 exhibits an instantaneous positive feature masked by oscillations, decaying with time constants <300 fs, 1.8 ps, and ∼90 ps. Since spectral integrated signals are insensitive to spectral shifts, three time constants indicate three transitions of electronic states. Thus, we assign the significant DAS_2 signal not to a cooling effect, but to a change of the electronic state properties.

The back reaction of the excited *Ca*ChR1 with 13-*cis* retinal to the parent ground state is nearly complete within 100 ps. This explains the nearly identical negative shapes of the absorption difference signals upon excitation at 500 and 550 nm.

At 100 ps delay time the spectral shape of the negative bleaching band signals are nearly identical for excitation at 500 and 550 nm (see Figure S5). Upon scaling of the bleaching bands for both excitations the photoproduct bands are rather similar, with band integrals differing by about 1.4, and absorption at longer wavelengths upon excitation at 500 nm. The intensity and spectral differences point to the existence of different photoproducts depending on the excitation energy. Increasing

the excitation energy by shorter wavelengths introduce a higher amount of excess energy into the *Ca*ChR1 protein allowing for formation of photoproducts with higher ground-state energy and consequently red-shifted absorption. Ground-state heterogeneity of chromophore structures were reported for several photoreceptors (Gervasio et al., 1998; Sineshchekov, 2004; von Stetten et al., 2008; Mailliet et al., 2011; Kim et al., 2012; Ritter et al., 2013).

Examination of the photoreaction quantum yield is difficult and can only be roughly estimated by our data.

We estimated a quantum yield for the *Ca*ChR1 with all-*trans* retinal upon excitation at 550 nm to be higher than 0.25 and lower than 0.7. Excitation of the *Ca*ChR1 at 500 nm is lower compared to excitation at 550 nm.

A striking property of the *Ca*ChR1 dynamics are the coherent oscillations visible in the transients (**Figure 3**), as well as in the contour plots (Figure S2). We obtained coherent oscillations up to 3 ps delay time by subtracting the simulated exponential dynamics from the dataset. The remaining residues were Fourier transformed and the amplitudes were plotted in **Figure 6A**. **Figure 6B** presents the spectral distribution of the Fourier components. Upon excitation at 550 nm we were able to identify oscillatory signals at about 80, 100, 150, 200, and 225 cm^{-1}. The vibrations around 100, 150, 200, and 225 cm^{-1} occur at spectral positions connected to the electronic excited state, and also to the photoproduct absorption at long wavelengths. This could be interpreted in a way that these four vibrations constitute a part of the reaction coordinate in *Ca*ChR1, transferring the electronic excited state population to the first hot photoproduct P_1. These vibrations at 100, 155, 200, and 225 cm^{-1} were assigned for all-*trans* retinal in solution to a ring torsion vibration, a chain methyl and ring torsion vibration, a methyl ring torsion vibration, and a chain bending and methyl ring torsion vibration, respectively (Prokhorenko et al., 2006). Two similar coherent vibrations at 195 and 226 cm^{-1} were reported to be crucial to optimize the photoisomerization reaction, while the coherent vibration of 155 cm^{-1} were reported to reduce the photoreaction quantum yield in bacteriorhodopsin (Polli et al., 2010; Johnson et al., 2014).

Discussion

Our model for the photoreaction of *Ca*ChR1 with all-*trans* retinal is presented in **Figure 8**:

Upon photoexcitation the all-*trans* retinal relaxes on the electronic excited state surface followed by an excited state decay and isomerization with a time constant of $\tau_1 = (100 \pm 50)$ fs via a conical intersection to the very hot photoproduct P_1. Our decay associated spectrum (DAS_1) in **Figure 4** with a time constant of $\tau_1 = (100 \pm 50)$ fs is the only signature explaining the rise of the delayed positive signal around 600 nm. The excess energy is located in retinal and protein vibrations strongly coupled to the reaction coordinate. We propose a reaction coordinate consisting of several vibrations including the low-frequency vibrations at 205 and 225 cm^{-1}. From the vibrational excited electronic hot P_1 the *Ca*ChR1 with 13-*cis* retinal relaxes via cascaded energy redistribution processes (Heyne et al., 2004a) to the relaxed photoproduct P_1 on a time scale of 500 fs and 5 ps. The initial P_1 photoproduct absorption band exhibits a very broad absorption ranging from 427 to 690 nm. A significant narrowing of the spectrum especially at the low-energy side of the photoproduct absorption is observed on a time scale of 500 fs, followed by a narrowing of the spectrum at the high-energy side of the photoproduct absorption on a time scale of 5 ps. These spectral shifts without a change of extinction coefficient are visible in the spectrally resolved data (**Figure 4**), but not in the spectral integrated transient (**Figure 7**). These processes are indicated by the change of the potential energy surface shapes of P_1 in **Figure 8**. Narrowing of P_1 absorption upon vibrational relaxation is accompanied with the narrowing of the photoproduct potential well. Despite the fact, that we cannot directly detect the photoisomerization process as by time-resolved infrared spectroscopy, we were able to identify the excited state decay with a time constant of 100 fs and the emerged absorption of the photoproduct within 200 fs (**Figure 2A**). Thus, we conclude that the photoisomerization process is an ultrafast process with a time constant of (100 ± 50) fs. The strong red-shift of P_1 absorption with 13-*cis* retinal can be explained by

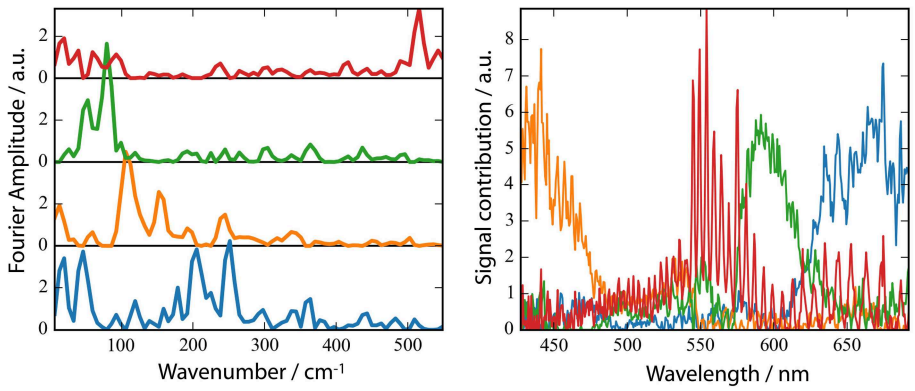

FIGURE 6 | Fast Fourier Transform (FFT) amplitudes of the residuals (A) and the spectral distribution of the components (B). (B) non-negative matrix factorization (NMF) of the 2D matrix presented in Figure S3 of the FFT amplitudes mapped to 4 components. The number of components was inferred from the singular values of the matrix.

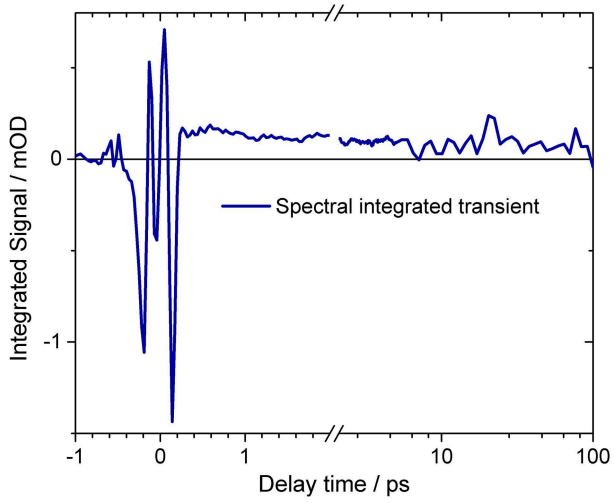

FIGURE 7 | Spectral integrated transient of the complete dataset upon excitation at 550 nm. At delay times around time zero and before 200 fs strong oscillatory signals are visible. The mean signal directly after excitation is negative, rising to about 500 fs. On a picosecond time scale the signal stays nearly constant. The transient is plotted on a logarithmic scale for long delay times. A small signal decrease is observed. Small oscillatory signals are also visible for delay times after 200 fs.

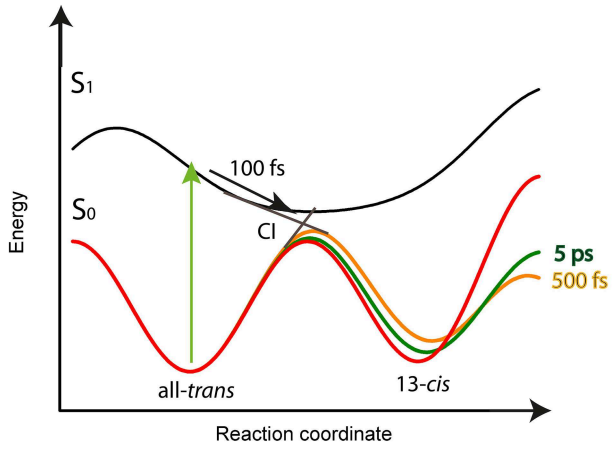

FIGURE 8 | Schematic potential energy surface as a function of the reaction coordinate for the *Ca*ChR1 with all-*trans* retinal. After excitation (green arrow) the molecules relax within 100 fs on the S_1 potential energy surface (black arrow) to the conical intersection (CI), indicated as straight lines from S_1 to S_0. Transition from S_1 to S_0 is accompanied with all-*trans* to 13-*cis* retinal photoisomerization. The excess energy excites vibrations of the chromophore and protein resulting in a softer ground-state potential energy surface (solid orange line) for the photoproduct P_1 with 13-*cis* retinal. Upon vibrational energy relaxation the ground-state potential energy surface becomes stiffer and more harmonic, thereby stabilizing the photoproduct (green line) until the fast relaxation process equilibrates (red curve). This process is connected with the same time constants as for parent ground-state recovery of 500 fs, and 5 ps.

protein surrounding that is not equilibrated. The structural change of the chromophore, change of electric fields around the chromophore, and redistribution of the excess energy into the protein surrounding promotes the energy of *Ca*ChR1 ground state, resulting in a red-shifted absorption. These changes lead to an energetically elevated photoproduct ground-state P_1 initiating the photocycle.

This early photoreaction mechanism is nearly identical to the photoreaction of rhodopsin (Schapiro and Ruhman, 2014). The chromophore relaxes from the Franck-Condon region within 100 fs and reaches the conical intersection. Within this time scale the stimulated emission vanishes completely in rhodopsin, as well as in *Ca*ChR1. In contrast, we see no ultrafast red-shift of the stimulated emission in *Ca*ChR1, probably due to a smaller extinction coefficient in *Ca*ChR1. With the disappearance of the stimulated emission the photoproduct absorption appears and shifts to higher energies in rhodopsin and in *Ca*ChR1.

The thermally equilibrated photoproduct P_1 in *Ca*ChR1 absorbs maximally around 560 nm (Figure S1). The quantum yield of the forward reaction is roughly estimated to be between 0.25 and 0.7, as expected for retinal proteins. The photoproduct P_1 is the first activated protein state of the photocycle of *Ca*ChR1.

The photoreaction is strongly influenced by coherent oscillations. Due to limited time resolution with an IRF of at least 90 fs we are able to identify strong coherent signals up to $\sim$320 cm^{-1}. We found oscillations resulted from low-frequency vibrations coupled to the photodynamics of *Ca*ChR1 with all-*trans* retinal at 205, 225, and 320 cm^{-1}. We assign the vibration around 320 cm^{-1} to Raman vibrations of the CaF_2 windows. The other low-frequency modes could be assigned to all-*trans* retinal vibrations (Prokhorenko et al., 2006) but further experiments with higher time resolution have to be performed to allow a precise assignment of frequency and phase of the involved vibrational oscillations.

In bacteriorhodopsin constructive and destructive interference effects of coherent vibrations drives the ultrafast isomerization process (Polli et al., 2010; Johnson et al., 2014). We expect a similar photoreaction mechanism for *Ca*ChR1 with all-*trans* retinal. Whether the quantum yield of the *Ca*ChR1 photoreaction can be optimized by coherent pulse shaping, has to be investigated in the future. As a result of the very fast isomerization process and formation of the hot electronic ground-state photoproduct, the chromophore and protein surrounding cannot follow this fast reaction speed. Thus, intra- and intermolecular energy redistribution processes on the sub picosecond and picosecond time scale transforms the system to the thermally equilibrated first photoproduct P_1. Whether the different time scales can be assigned to intramolecular redistribution within the 13-*cis* chromophore and intermolecular redistribution between chromophore and protein has to be investigated by time-resolved infrared spectroscopy.

Comparison with reported photoreaction of *Cr*ChR2 reveals several similarities and differences. The photoproduct absorbs red-shifted to the bleaching band in *Ca*ChR1, and in *Cr*ChR2. In *Cr*ChR2 the excited state relaxes with 150 fs similar to the fast time constant in *Ca*ChR1 of 100 fs, but decays with a longer time constant of 400 fs to the photoproduct. The photoproduct cooling was determined to 2.7 ps, in contrast to *Ca*ChR1, where

we observed two cooling processes with 500 fs and 5 ps. As visible in **Figure 2A** the spectral shifting in *Ca*ChR1 has not stopped completely at long delay times. In *Cr*ChR2 a similar spectral shift with a time constant of 200 ps was assigned to protein relaxation. For both systems the primary photoreaction process is assigned to all-*trans* to 13-*cis* retinal isomerization. Due to the blue-shifted absorption of *Cr*ChR2 with absorption maximum around 450 nm no positive signals from the ESA could be observed on the high energy side of the bleaching signal. In *Ca*ChR1, we detected the ESA on the high energy side of the bleaching signal, allowing for a direct separation of electronic excited state and photoproduct absorption. In contrast to *Cr*ChR2 we found strong oscillatory signals in *Ca*ChR1 and a dependence of the photoreaction dynamics on the excitation wavelength (Verhoefen et al., 2010).

Upon excitation at 550 nm we observe the expected photoisomerization of *Ca*ChR1 with all-*trans* retinal to the first photoproduct P_1 cooling down on the picosecond time scale. Changing the excitation energy to 500 nm, results in significantly different photoreaction dynamics. The initial bleaching band is blue-shifted with respect to excitation at 550 nm, demonstrating heterogeneity of the *Ca*ChR1 ground state. Whether the origin of heterogeneity is due to differences in the chromophore structure or differences in the protein strongly interacting with the chromophore can be assessed by electronic or vibrational dynamics. The dynamics of the electronic states show distinct differences in band positions, time scales, and extinction coefficients upon excitation at 500 nm and 550 nm. It was reported that two chromophore conformations appear with all-*trans* and 13-*cis* retinal of 70 and 30% abundance, respectively. Raman stretching vibrations of the C = C were determined at 1533 cm^{-1} for *Ca*ChR1 with all-*trans* retinal and at 1550 cm^{-1} for *Ca*ChR1 with 13-*cis* retinal (Muders et al., 2014). Thus, the differences in the photoreaction dynamics can be explained by ground-state heterogeneity of the *Ca*ChR1 retinal chromophore.

We determined the absorption maxima of *Ca*ChR1 with all-*trans* retinal, and 13-*cis* retinal to be at 540, and ~480 nm, respectively. This is in accordance with the reported linear correlation between the frequency of the retinal C = C stretching vibration ν(C = C) and the maximum of the visible absorption spectrum λ_{max} for equilibrated ground-state structures (Aton et al., 1977; Fodor et al., 1989).

Excitation at 500 nm triggers the photoreaction of *Ca*ChR1 with all-*trans* retinal, and of *Ca*ChR1 with 13-*cis* retinal. After subtraction of the *Ca*ChR1 with all-*trans* retinal dynamics we observed the *Ca*ChR1 with 13-*cis* retinal. We found an ultrafast photoreaction with a positive signal around 600 nm, which decays on a time scale of <300 fs. This is indicated by the decay of the negative and positive signals in **Figure 2C**, S7A at early delay times around 480 and 600 nm, respectively. A significant positive signal of the photoproduct Q with a maximum around 590 nm indicates absorption, decaying with a time constant $\tau_2 = (1.8 \pm 0.3)$ ps. The remaining positive absorption Q' with maximum around 570 nm decays with $\tau_3 = (90 \pm 25)$ ps. The bleaching signals around 480 nm are weak compared to the strong positive signals around 600 nm, indicating a smaller extinction coefficient for the bleaching signals. This explains the poor dynamics of the bleaching signal that might overlap with the high-energy part of the Q spectrum of similar strength. Hence, bleaching recovery of the Q population result in negligible changes of the bleaching signal. The dynamics of *Ca*ChR1 with 13-*cis* retinal show three time constants also visible in the spectral integrated transient in Figure S4A. Thus, we expect all time constants to be connected with changes of electronic state properties.

Since the bleaching signals are the same for excitation at 550 and 500 nm after 100 ps, we expect the photoreaction of *Ca*ChR1 with 13-*cis* retinal to be recovered to its parent state at this time. Thus, several photoreaction mechanism can be discussed:

A photoreaction without isomerization would promote the *Ca*ChR1 13-*cis* ground state (*cis*) to its electronic excited state *cis**, followed by a fast relaxation in the electronic excited state, decays to *cis*' ground state with vibrational excited protein surrounding, and relaxed back to its parent state *cis*. The first time constant of 200 fs (see Figure S7C) would correspond to the relaxation process, the second time constant $\tau_2 = (1.8 \pm 0.3)$ ps to the *cis** → *cis*' transition, and the 90 ps time constant to the recovery of the parent state. The only remaining question is why is the extinction coefficient so different in *cis** and *cis*' compared to *cis*. It seems to be more plausible that the difference of extinction coefficient is due to different chromophore structures induces by isomerization.

Possible photoreactions with two isomerizations start with the promotion of the *Ca*ChR1 13-*cis* ground state (*cis*) to its electronic excited state *cis**, followed by a fast relaxation in the electronic excited state. The first isomerization can occur either in the electronic excited state (*cis** → *trans**), or can be accompanied by the transition from the excited to the ground state *cis** → *trans** or *trans** → *cis*'. If a ground state with *trans*' is formed, an isomerization to *cis* has to take place in the ground state. The first time constant of 200 fs can be connected with an excited state relaxation or a *cis** → *trans** isomerization. The second time constant of 1.8 ps can be due to transitions from *cis** → *trans*' or *trans** → *cis*'. The third time constant of 90 ps reflects the recovery to the parent *Ca*ChR1 13-*cis* ground state from *trans*' → *cis* or *cis*' → *cis*.

Since isomerization processes in the electronic ground state are seldom, we prefer the photoreaction with a *cis** → *trans** isomerization in the electronic excited state on a time scale of <300 fs inducing a strong signal change (Q), followed by a back-isomerization (*trans** → *cis*') with 1.8 ps accompanied with the transition from the electronic excited to the ground state cis' (Q'), that recovers to its parent state by 90 ps. A small fraction can also decay to a *trans*' ground state (*trans** → *trans*').

This would explain the positive signal above 520 nm, upon excitation at 500 nm, with a significantly higher extinction coefficient than upon excitation at 550 nm for long delay times. We tentatively assign this positive signal to a photoproduct *Ca*ChR1 with all-*trans* retinal. For Anabaena Sensory Rhodopsin, it was reported that excitation of the ground state with 13-*cis* retinal, leads to formation of a first K-like photoproduct with all-*trans* retinal, decaying back to ground state with all-*trans* retinal (Anderson et al., 2004). The photoreaction of *Ca*ChR1 with 13-*cis* retinal is completed after some 100 picoseconds. Whether this photoreaction induces dynamics and structural changes of the

protein with possible biological function remains unclear, and has to be clarified in other studies.

In summary, we determined the primary photoreaction of *Ca*ChR1 for the first time. Ground-state heterogeneity of two isomers of the chromophore, all-*trans* retinal and 13-*cis* retinal leads to deviating photoreaction upon changing the excitation wavelength. Shorter wavelengths result in an increase of *Ca*ChR1 with 13-*cis* retinal dynamics, while excitation at longer wavelength increase the photoreaction of *Ca*ChR1 with all-*trans* retinal. Our data for *Ca*ChR1 with all-*trans* retinal are best explained by an all-*trans* to 13-*cis* retinal isomerization and hot photoproduct P_1 formation with a time constant of ∼100 fs. The photoreaction of *Ca*ChR1 with all-*trans* retinal turns out to be faster than in *Cr*ChR2, and exhibit strong oscillatory signals as reported for bacteriorhodopsin. Our data demonstrate a heterogeneity of isomers in the ground state with different photodynamics, but only one reaction pathway seems to be relevant for biological function.

Acknowledgments

We thank the Deutsche Forschungsgemeinschaft (SFB-1078, projects B3 to JH and KH and B4 to RS) for financial support and Dorothea Heinrich and Kirsten Hoffmann for excellent technical assistance. We also thank Yang Yang for sample preparation and setup alignment.

Supplementary Material

The Supplementary Material for this article can be found online at: http://journal.frontiersin.org/article/10.3389/fmolb.2015.00041

References

Anderson, S., Srajer, V., and Moffat, K. (2004). Structural heterogeneity of cryotrapped intermediates in the bacterial blue light photoreceptor, photoactive yellow protein. *Photochem. Photobiol.* 80, 7–14. doi: 10.1562/2004-03-15-RA-115.1

Aton, B., Callender, R. H., Becher, B., and Ebrey, T. G. (1977). Resonance raman studies of purple membrane. *Biochemistry* 16, 2995–2999. doi: 10.1021/bi00632a029

Bamann, C., Kirsch, T., Nagel, G., and Bamberg, E. (2008). Spectral characteristics of the photocycle of channelrhodopsin-2 and its implication for channel function. *J. Mol. Biol.* 375, 686–694. doi: 10.1016/j.jmb.2007.10.072

Ernst, O. P., Sanchez Murcia, P. A., Daldrop, P., Tsunoda, S. P., Kateriya, S., and Hegemann, P. (2008). Photoactivation of channelrhodopsin. *J. Biol. Chem.* 283, 1637–1643. doi: 10.1074/jbc.M708039200

Fenno, L., Yizhar, O., and Deisseroth, K. (2011). The development and application of optogenetics. *Annu. Rev. Neurosci.* 34, 389–412. doi: 10.1146/annurev-neuro-061010-113817

Fodor, S. P. A., Gebhard, R., Lugtenburg, J., Bogomolni, R. A., and Mathies, R. A. (1989). Structure of the retinal chromophore in sensory rhodopsin-I from resonance Raman-spectroscopy. *J. Biol. Chem.* 264, 18280–18283.

Gervasio, F. L., Cardini, G., Salvi, P. R., and Schettino, V. (1998). Low-frequency vibrations of all-trans-retinal: far-infrared and Raman spectra and density functional calculations. *J. Phys. Chem. A* 102, 2131–2136. doi: 10.1021/jp9724636

Harbison, G. S., Smith, S. O., Pardoen, J. A., Winkel, C., Lugtenburg, J., Herzfeld, J., et al. (1984). Dark-adapted bacteriorhodopsin contains 13-cis, 15-syn and all-trans, 15-anti retinal Schiff bases. *Proc. Natl. Acad. Sci. U.S.A.* 81, 1706–1709. doi: 10.1073/pnas.81.6.1706

Heyne, K., Herbst, J., Dominguez-Herradon, B., Alexiev, U., and Diller, R. (2000). Reaction control in bacteriorhodopsin: impact of arg82 and asp85 on the fast retinal isomerization, studied in the second site revertant arg82ala/gly231cys and various purple and blue forms of bacteriorhodopsin. *J. Phys. Chem. B* 104, 6053–6058. doi: 10.1021/jp992877u

Heyne, K., Huse, N., Dreyer, J., Nibbering, E. T. J., Elsaesser, T., and Mukamel, S. (2004b). Coherent low-frequency motions of hydrogen bonded acetic acid dimers in the liquid phase. *J. Chem. Phys.* 121, 902–913. doi: 10.1063/1.1762873

Heyne, K., Nibbering, E. T. J., Elsaesser, T., Petkovic, M., and Kuhn, O. (2004a). Cascaded energy redistribution upon O-H stretching excitation in an intramolecular hydrogen bond. *J. Phys. Chem. A* 108, 6083–6086. doi: 10.1021/jp048653f

Hou, S. Y., Govorunova, E. G., Ntefidou, M., Lane, C. E., Spudich, E. N., Sineshchekov, O. A., et al. (2012). Diversity of chlamydomonas channelrhodopsins. *Photochem. Photobiol.* 88, 119–128. doi: 10.1111/j.1751-1097.2011.01027.x

Johnson, P. J. M., Halpin, A., Morizumi, T., Brown, L. S., Prokhorenko, V. I., Ernst, O. P., et al. (2014). The photocycle and ultrafast vibrational dynamics of bacteriorhodopsin in lipid nanodiscs. *Phys. Chem. Chem. Phys.* 16, 21310–21320. doi: 10.1039/C4CP01826E

Kato, H. E., Zhang, F., Yizhar, O., Ramakrishnan, C., Nishizawa, T., Hirata, K., et al. (2012). Crystal structure of the channelrhodopsin light-gated cation channel. *Nature* 482, 369–374. doi: 10.1038/nature10870

Kim, P. W., Freer, L. H., Rockwell, N. C., Martin, S. S., Lagarias, J. C., and Larsen, D. S. (2012). Femtosecond photodynamics of the red/green cyanobacteriochrome NpR6012g4 from Nostoc punctiforme. 1. Forward dynamics. *Biochemistry* 51, 608–618. doi: 10.1021/bi201507k

Kovalenko, S. A., Dobryakov, A. L., Ruthmann, J., and Ernsting, N. P. (1999). Femtosecond spectroscopy of condensed phases with chirped supercontinuum probing. *Phys. Rev. A* 59, 2369–2384. doi: 10.1103/PhysRevA.59.2369

Kozich, V., Dreyer, J., Ashihara, S., Werncke, W., and Elsaesser, T. (2006). Mode-selective O-H stretching relaxation in a hydrogen bond studied by ultrafast vibrational spectroscopy. *J. Chem. Phys.* 125, 074504-1–074504-9. doi: 10.1063/1.2219111

Krause, N., Engelhard, C., Heberle, J., Schlesinger, R., and Bittl, R. (2013). Structural differences between the closed and open states of channelrhodopsin-2 as observed by EPR spectroscopy. *FEBS Lett.* 587, 3309–3313. doi: 10.1016/j.febslet.2013.08.043

Lorenz-Fonfria, V. A., and Heberle, J. (2014). Channelrhodopsin unchained: structure and mechanism of a light-gated cation channel. *Biochim. Biophys. Acta* 1837, 626–642. doi: 10.1016/j.bbabio.2013.10.014

Lorenz-Fonfria, V. A., Muders, V., Schlesinger, R., and Heberle, J. (2014). Changes in the hydrogen-bonding strength of internal water molecules and cysteine residues in the conductive state of channelrhodopsin-1. *J. Chem. Phys.* 141, 22D507. doi: 10.1063/1.4895796

Lorenz-Fonfria, V. A., Resler, T., Krause, N., Nack, M., Gossing, M., Fischer von Mollard, G., et al. (2013). Transient protonation changes in channelrhodopsin-2 and their relevance to channel gating. *Proc. Natl. Acad. Sci. U.S.A.* 110, E1273–E1281. doi: 10.1073/pnas.1219502110

Mailliet, J., Psakis, G., Feilke, K., Sineshchekov, V., Essen, L. O., and Hughes, J. (2011). Spectroscopy and a high-resolution crystal structure of Tyr263 mutants of cyanobacterial phytochrome Cph1. *J. Mol. Biol.* 413, 115–127. doi: 10.1016/j.jmb.2011.08.023

Mowery, P. C., Lozier, R. H., Chae, Q., Tseng, Y. W., Taylor, M., and Stoeckenius, W. (1979). Effect of acid pH on the absorption spectra and photoreactions of bacteriorhodopsin. *Biochemistry* 18, 4100–4107. doi: 10.1021/bi00586a007

Muders, V., Kerruth, S., Lorenz-Fonfria, V. A., Bamann, C., Heberle, J., and Schlesinger, R. (2014). Resonance Raman and FTIR spectroscopic characterization of the closed and open states of channelrhodopsin-1. *FEBS Lett.* 588, 2301–2306. doi: 10.1016/j.febslet.2014.05.019

Muller, M., Bamann, C., Bamberg, E., and Kuhlbrandt, W. (2011). Projection structure of channelrhodopsin-2 at 6 angstrom resolution by electron crystallography. *J. Mol. Biol.* 414, 86–95. doi: 10.1016/j.jmb.2011.09.049

Muller, M., Bamann, C., Bamberg, E., and Kuhlbrandt, W. (2015). Light-induced helix movements in channelrhodopsin-2. *J. Mol. Biol.* 427, 341–349. doi: 10.1016/j.jmb.2014.11.004

Nack, M., Radu, I., Bamann, C., Bamberg, E., and Heberle, J. (2009). The retinal structure of channelrhodopsin-2 assessed by resonance Raman spectroscopy. *FEBS Lett.* 583, 3676–3680. doi: 10.1016/j.febslet.2009.10.052

Nagel, G., Ollig, D., Fuhrmann, M., Kateriya, S., Musti, A. M., Bamberg, E., et al. (2002). Channelrhodopsin-1: a light-gated proton channel in green algae. *Science* 296, 2395–2398. doi: 10.1126/science.1072068

Nagel, G., Szellas, T., Huhn, W., Kateriya, S., Adeishvili, N., Berthold, P., et al. (2003). Channelrhodopsin-2, a directly light-gated cation-selective membrane channel. *Proc. Natl. Acad. Sci. U.S.A.* 100, 13940–13945. doi: 10.1073/pnas.1936192100

Neumann-Verhoefen, M. K., Neumann, K., Bamann, C., Radu, I., Heberle, J., Bamberg, E., et al. (2013). Ultrafast infrared spectroscopy on channelrhodopsin-2 reveals efficient energy transfer from the retinal chromophore to the protein. *J. Am. Chem. Soc.* 135, 6968–6976. doi: 10.1021/ja400554y

Ogren, J. I., Mamaev, S., Russano, D., Li, H., Spudich, J. L., and Rothschild, K. J. (2014). Retinal chromophore structure and Schiff base interactions in red-shifted channelrhodopsin-1 from *Chlamydomonas augustae*. *Biochemistry* 53, 3961–3970. doi: 10.1021/bi500445c

Ogren, J. I., Yi, A., Mamaev, S., Li, H., Spudich, J. L., and Rothschild, K. J. (2015a). Proton transfers in a channelrhodopsin-1 studied by Fourier transform infrared (FTIR) difference spectroscopy and site-directed mutagenesis. *J. Biol. Chem.* 290, 12719–12730. doi: 10.1074/jbc.M114.634840

Ogren, J. I., Yi, A., Mamaev, S., Li, H., Lugtenburg, J., DeGrip, W. J., et al. (2015b). Comparison of the structural changes occurring during the primary phototransition of two different channelrhodopsins from *Chlamydomonas algae*. *Biochemistry* 54, 377–388. doi: 10.1021/bi501243y

Polli, D., Altoe, P., Weingart, O., Spillane, K. M., Manzoni, C., Brida, D., et al. (2010). Conical intersection dynamics of the primary photoisomerization event in vision. *Nature* 467, 440–443. doi: 10.1038/nature09346

Prokhorenko, V. I., Nagy, A. M., Waschuk, S. A., Brown, L. S., Birge, R. R., and Miller, R. J. D. (2006). Coherent control of retinal isomerization in bacteriorhodopsin. *Science* 313, 1257–1261. doi: 10.1126/science.1130747

Rey, R., Moller, K. B., and Hynes, J. T. (2004). Ultrafast vibrational population dynamics of water and related systems: a theoretical perspective. *Chem. Rev.* 104, 1915–1928. doi: 10.1021/cr020675f

Ritter, E., Piwowarski, P., Hegemann, P., and Bartl, F. J. (2013). Light-dark adaptation of channelrhodopsin C128T mutant. *J. Biol. Chem.* 288, 10451–10458. doi: 10.1074/jbc.M112.446427

Ritter, E., Stehfest, K., Berndt, A., Hegemann, P., and Bartl, F. J. (2008). Monitoring light-induced structural changes of channelrhodopsin-2 by UV-visible and fourier transform infrared spectroscopy. *J. Biol. Chem.* 283, 35033–35041. doi: 10.1074/jbc.M806353200

Sattig, T., Rickert, C., Bamberg, E., Steinhoff, H. J., and Bamann, C. (2013). Light-induced movement of the transmembrane HelixB in channelrhodopsin-2. *Angew. Chem. Int. Ed. Engl.* 52, 9705–9708. doi: 10.1002/anie.201301698

Schapiro, I., and Ruhman, S. (2014). Ultrafast photochemistry of anabaena sensory rhodopsin: experiment and theory. *Biochim. Biophys. Acta* 1837, 589–597. doi: 10.1016/j.bbabio.2013.09.014

Shigeto, S., Pang, Y., Fang, Y., and Dlott, D. D. (2008). Vibrational relaxation of normal and deuterated liquid nitromethane. *J. Phys. Chem. B* 112, 232–241. doi: 10.1021/jp074082q

Sineshchekov, O. A., Govorunova, E. G., Wang, J., Li, H., and Spudich, J. L. (2013). Intramolecular proton transfer in channelrhodopsins. *Biophys. J.* 104, 807–817. doi: 10.1016/j.bpj.2013.01.002

Sineshchekov, V. A. (2004). Phytochrome A: functional diversity and polymorphism. *Photochem. Photobiol. Sci.* 3, 596–607. doi: 10.1039/b315430k

Verhoefen, M. K., Bamann, C., Blocher, R., Forster, U., Bamberg, E., and Wachtveitl, J. (2010). The photocycle of channelrhodopsin-2: ultrafast reaction dynamics and subsequent reaction steps. *Chemphyschem* 11, 3113–3122. doi: 10.1002/cphc.201000181

von Stetten, D., Gunther, M., Scheerer, P., Murgida, D. H., Mroginski, M. A., Krauss, N., et al. (2008). Chromophore heterogeneity and photoconversion in phytochrome crystals and solution studied by resonance Raman spectroscopy. *Angew. Chem. Int. Ed. Engl.* 47, 4753–4755. doi: 10.1002/anie.200705716

Conflict of Interest Statement: The authors declare that the research was conducted in the absence of any commercial or financial relationships that could be construed as a potential conflict of interest.

frontiers

Supplementary Material

The primary photoreaction of channelrhodopsin-1: Wavelength dependent photoreactions induced by ground-state heterogeneity

Till Stensitzki, Vera Muders, Ramona Schlesinger, Joachim Heberle, Karsten Heyne*

Freie Universität Berlin, Institut für Experimentalphysik, Arnimallee 14, 14195 Berlin, Germany

*** Correspondence:** Karsten Heyne, Freie Universität Berlin, Institut für Experimentalphysik, Arnimallee 14, 14195 Berlin, Germany.
Karsten.heyne@fu-berlin.de

Keywords: *Ca*ChR1, retinal, isomerization, femtosecond pump-probe spectroscopy, reaction model, ground state heterogeneity

1. Supplementary Data

Examination of the photoreaction quantum yield is difficult and can only be roughly estimated by our data. Upon excitation at 550 nm the DAS at 100 fs indicates no change of the ground-state bleaching signal, but a positive signal contribution of ~ 1.5 mOD at 510 nm (Figure 4). At the same time the absorption difference spectrum in Figure 5A displays a negative signal of ~ 9.5 mOD. This results in a bleaching signal of 11 mOD at 510 nm. For 100 ps the remaining bleaching signal is 2.8 mOD. From this ratio a maximal bleaching recovery, and a minimal quantum yield of ~ 0.25 can be estimated. This analysis uses directly the negative signal of the absorption difference at 100 ps delay time. Since the broad positive P_1 absorption band superimposes the bleaching band, the original contribution of the bleaching band should be higher. Assuming a P_1 absorption profile with a smooth shape connecting the positive contributions at 560 nm and 430 nm, we had to scale the bleaching contribution by 2.8 (Figure S1). This results in 2.8 fold contribution of the bleaching signal at 100 ps, and an increase of the quantum yield to ~ 70%. The same rough estimation leads to a quantum yield higher than ~ 25 % and smaller than ~ 40% for excitation at 500 nm. This can be explained by the additional 13-*cis* retinal reaction pathway that does not contribute to the forward reaction.

Supplementary Material

Figure S1: Calculated thermally relaxed photoproduct spectrum (blue line): The absorption difference at 100 ps (black line) is displayed together with an absorption spectrum of *Ca*ChR1. We scaled the absorption spectrum by 2.8, and added it to the absorption difference at 100 ps. The result was the photoproduct spectrum of P_1 (blue line). Smaller scaling factors lead to a double peak structure of the photoproduct with peaks at 560 nm and 440 nm.

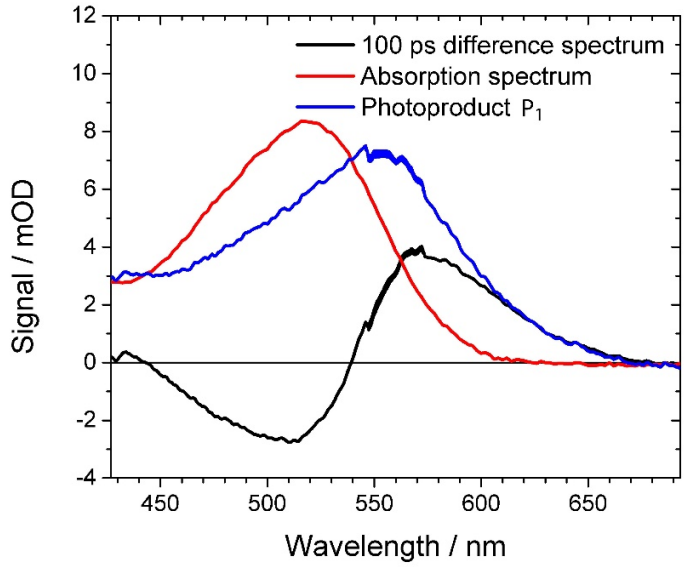

Figure S2: Contour plots of the photoreaction dynamics of *Ca*ChR1 upon excitation at 550 nm (A), 500 nm (B), and the difference of both datasets (C). Blue colors indicate negative signals, red colors positive signals. The contour plots display the absorbance difference in mOD upon excitation as a function of delay time and wavelength. The difference contour plot (C) is calculated by the direct difference of (B)-(A).

.

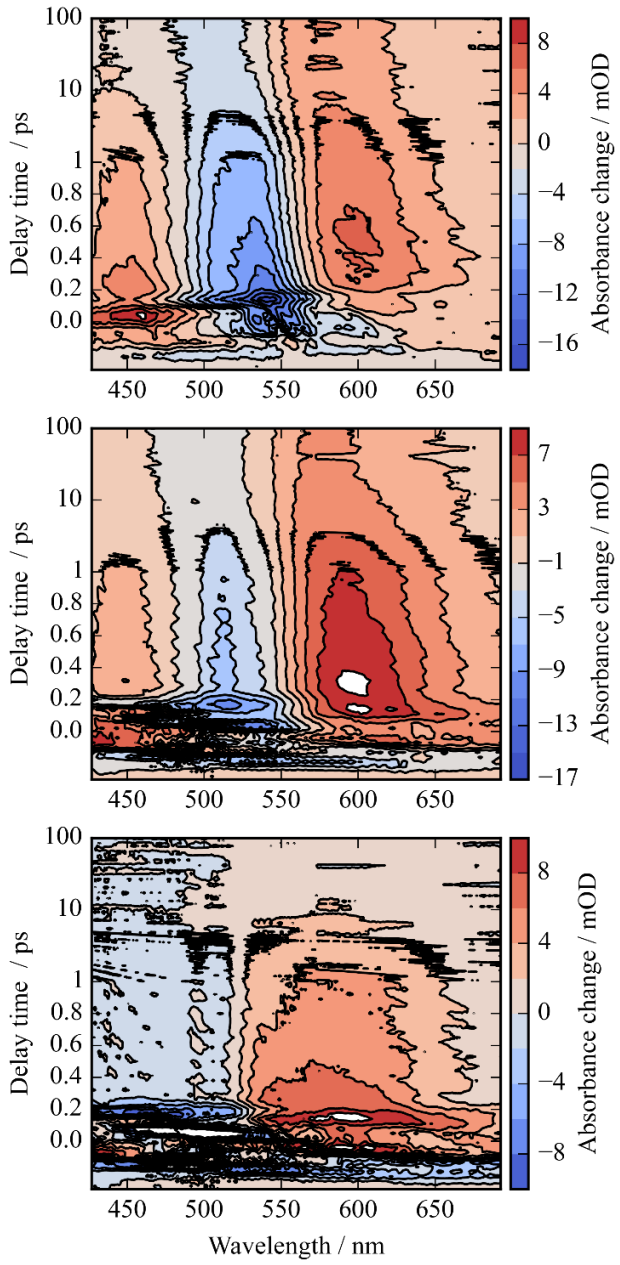

Supplementary Material

Figure S3: FFT amplitudes of the residues as a function of wavelength and wavenumber for a time window of 3 ps. Contributions around 7cm^{-1}, 100 cm^{-1}, 150 cm^{-1}, 200 cm^{-1}, and 225 cm^{-1} are clearly visible.

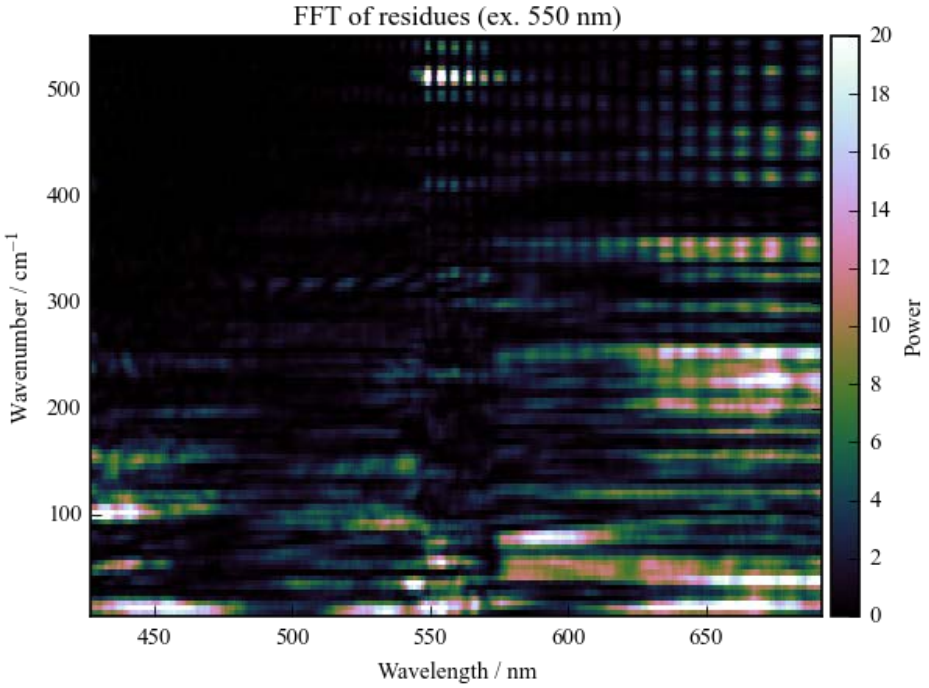

Figure S4: Spectral integrated signals upon excitation at 500 nm (A),(B), and at 550 nm (C). For all integrations the spectral axis was transferred to wavenumbers and the different spectral resolutions were taken into account. (A) T(1)ransient of the complete spectral integrated signal (blue line), and a simulation (orange line) with time constants of (170±70) fs, (1.3±0.5) ps, and 30 ps. The strong coherent oscillations around time zero are dominated by nonlinear signals of the CaF2 windows. (B) All positive, and negative signals of the dataset were spectral integrated; the P/N transient (blue line) is the ratio of the integrated positive to integrated negative transient. P/N signals are sensitive to spectral shifts of bands with different extinction coefficient, while the integrated signal is not. The sub picosecond and picosecond time components are clearly visible, as well as oscillatory behavior with a period of 100 fs. (C) Integrated positive (black line), integrated negative (red line), and integrated P/N transient (green line) plotted as a function of delay time. The P/N transient exhibits a small signal increase up to 500 fs and stays nearly constant for longer delay times.

Supplementary Material

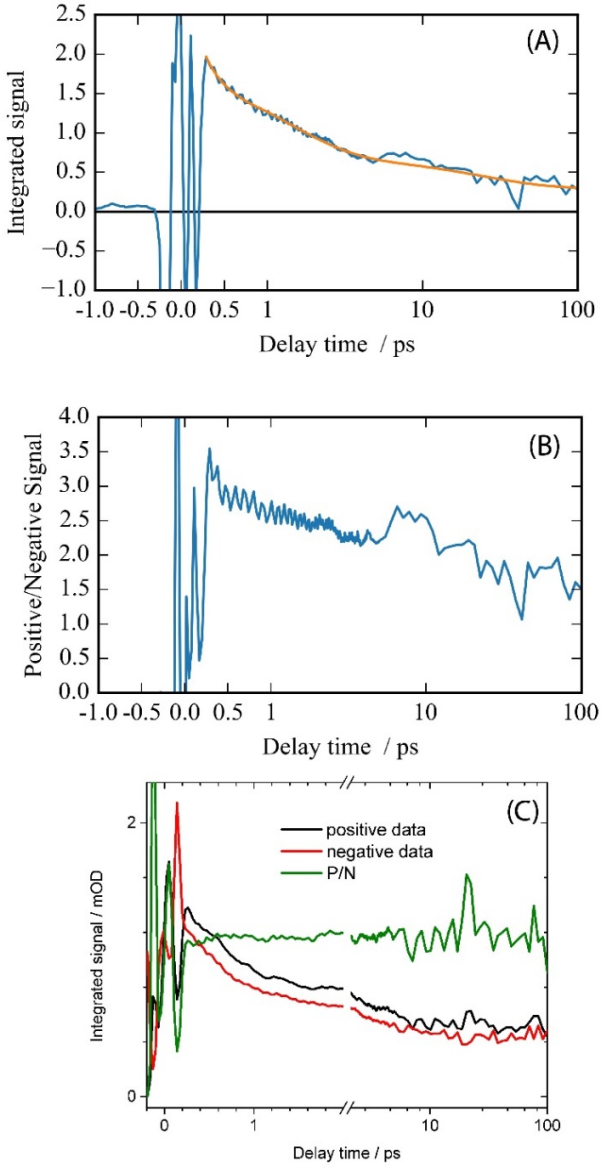

Figure S5: Absorption difference spectra at 100 ps upon excitation at 500 nm (blue line), 550 nm (orange line), and its difference scaled by a factor of 3 (green line). The shape of the bleaching signal is nearly identical from 430 nm to 510 nm, indicating not remaining bleaching signal from *Ca*ChR1 with 13-*cis* retinal. The difference shows signatures of a broad absorbing species with maximum around 610 nm.

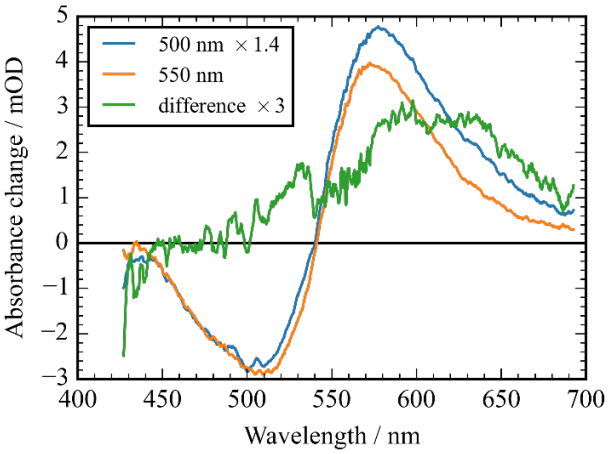
500 nm ×1.4
550 nm
difference ×3
Absorbance change / mOD
Wavelength / nm
5
4
3
2
1
0
−1
−2
−3
400
450
500
550
600
650
700

Supplementary Material

Figure S6: Nonlinear signal in the CaF_2 windows at 550 nm probe wavelength. The "glass signal" (blue dots) represents the nonlinear signal of the empty sample cell with CaF_2 windows. The signal can be well simulated (orange line) by a Gaussian ($\exp(-t^2/\sigma^2)$) and its first and second derivative as reported by Kovalenko et al.(1) This simulation results at an instrument response function (IRF) and cross-correlation of σ=90 fs. Note, using a standard Gaussian ($\exp(-t^2/[2\ \sigma^2])$) would result in an even shorter IRF. Hence, the time resolution, given by the IRF or cross-correlation is better than 100 fs. Therefore, small oscillatory features of the ~320 cm^{-1} vibration with an oscillation period of 104 fs of the windows are visible, only possible with an IRF below 100 fs.

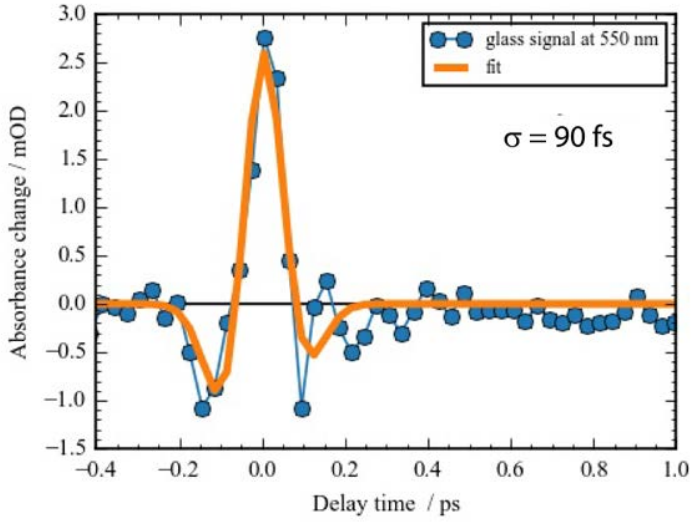

Figure S7: Dynamics of *Ca*ChR 1 with 13-*cis* retinal derived from the data by direct subtraction of the dataset excited at 500 nm from the dataset excited at 550 nm. Positive signals are new emerging bands, while negative signals show bleaching bands and stimulated emission. (A) Absorbance difference spectra for different delay times. For 100 ps delay time a positive signal remains around 650 nm, indicating the difference between 500 nm and 550 nm excitation at 100 ps delay time (Figure S5, green signal). (B) Transients at selected wavelengths on a logarithmic time scale. Three time constants are well visible. Solid lines represent the fits with three time constants of τ_1=200 fs, τ_2=1.8 ps, and τ_3=90 ps. (C) Decay associated spectra. The positive bands are stronger than the negative bands indicating higher extinction coefficients for the new emerging bands compared to the bleaching band.

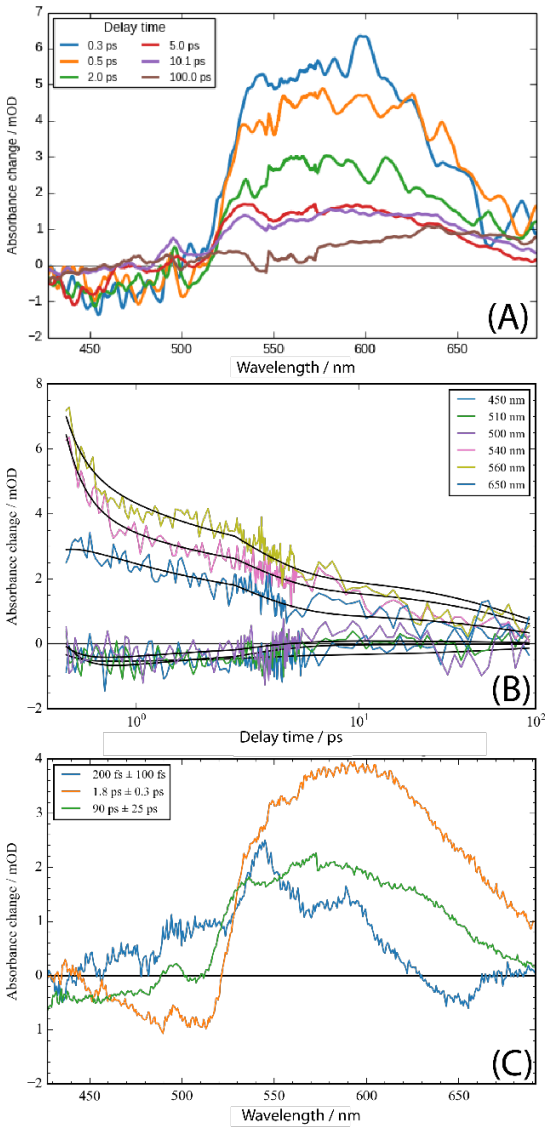

Supplementary Material

1. Kovalenko SA, Dobryakov AL, Ruthmann J, Ernsting NP. Femtosecond spectroscopy of condensed phases with chirped supercontinuum probing. *Phys Rev A* (1999) **59**:2369-84.

Femtosecond infrared spectroscopy of channelrhodopsin-1 chromophore isomerization

T. Stensitzki,[1] Y. Yang,[1] V. Muders,[2] R. Schlesinger,[2] J. Heberle,[3] and K. Heyne[1,a)]

[1]*Department of Physics, Institute of Experimental Physics, Freie Universität Berlin, Arnimallee 14, 14195 Berlin, Germany*
[2]*Genetic Biophysics, Department of Physics, Freie Universität Berlin, Arnimallee 14, 14195 Berlin, Germany*
[3]*Experimental Molecular Biophysics, Department of Physics, Freie Universität Berlin, Arnimallee 14, 14195 Berlin, Germany*

(Received 1 March 2016; accepted 15 April 2016; published online 29 April 2016)

Vibrational dynamics of the retinal all-*trans* to 13-*cis* photoisomerization in channelrhodopsin-1 from *Chlamydomonas augustae* (*Ca*ChR1) was investigated by femtosecond visible pump mid-IR probe spectroscopy. After photoexcitation, the transient infrared absorption of C-C stretching modes was detected. The formation of the 13-*cis* photoproduct marker band at 1193 cm^{-1} was observed within the time resolution of 0.3 ps. We estimated the photoisomerization yield to (60 ± 6) %. We found additional time constants of (0.55 ± 0.05) ps and (6 ± 1) ps, assigned to cooling, and cooling processes with a back-reaction pathway. An additional bleaching band demonstrates the ground-state heterogeneity of retinal. [http://dx.doi.org/10.1063/1.4948338]

I. INTRODUCTION

Light excitation of rhodopsins lead to various functionalities like sensing, ion pumping and channeling across the biological membrane. Channelrhodopsins (ChR) are the only light-gated ion channels in nature found so far. Originally, they are located in the eyespot of green algae to mediate phototaxis. In these days, channelrhodopsins are used in the vibrant field of optogenetics[1] where the protein is used to elicit action potentials in nerve cells by light. ChR have been applied to unravel neuronal connectivity[2] and to manipulate behavior in ChR-expressing animals like worms and rodents.[3,4] Due to their application in living organisms, the detailed understanding of the molecular mechanism after light excitation is of high interest.

Common to all rhodopsins, the initial step of photo-activation of channelrhodopsin involves isomerization of the retinal chromophore. Most spectroscopic analysis has been performed on channelrhodopsin-2 from *Chlamydomonas reinhardtii* (*Cr*ChR2).[5] Ultrafast pump-probe experiments[6] provided evidence for retinal isomerization and formation of the first photoproduct to take place with a time constant τ of 400 fs. Due to the fast deactivation of the excited state, the impact of retinal isomerization on the protein surrounding was observed with a time constant of 0.5 ps by Vis-pump/mid-IR probe spectroscopy.[7]

Much less is known about the photoreaction of the other light-activated cation channel of *C. reinhardtii*, *Cr*ChR1, due to the difficulties in overexpression. However, channelrhodopsin-1 from related *Chlamydomonas augustae* (*Ca*ChR1) achieves high expression yields in the yeast *Pichia pastoris*.[8,9] Interestingly, *Ca*ChR1 comes with two distinct advantages for optogenetic application. It has a slower inactivation under sustained illumination than *Cr*ChR1 and a

a)Author to whom correspondence should be addressed. Electronic mail: Karsten.heyne@fu-berlin.de

red-shifted absorption maximum as compared to *Cr*ChR2. Thus, *Ca*ChR1 can be activated with the light of longer wavelength, which is able to penetrate deeper into biological tissue.[8]

Like in *Cr*ChR2, the ground state of *Ca*ChR1 exhibits a heterologous retinal isomer composition. Retinal extraction and analysis of the isomers by high performance liquid chromatography reveals a 70:30 ratio of all-*trans* to 13-*cis* retinal. Resonance Raman experiments of the C=C stretching modes of the retinal embedded in the functional protein confirmed that mainly all-*trans* and to a minor amount 13-*cis* retinal exists.[9] Recently, the heterogeneity of the ground state was again verified by UV/Vis absorption experiments with femtosecond time resolution which exhibit different photoreaction dynamics of *Ca*ChR1 on varying the excitation wavelength.[10] These experiments revealed an ultrafast isomerization of the all-*trans* retinal to a hot and spectrally broad P_1 photoproduct with a time constant of (100 ± 50) fs, followed by the photoproduct relaxation with time constants of (500 ± 100) fs and (5 ± 1) ps.[10] UV/Vis absorption experiments with nanosecond time resolution showed that the appearance of a red-shifted intermediate P_1 absorbing at around 560 nm arises, followed by the rise of a biphasic P_2 intermediate matching the time for ion conduction of the channel.[11] After the decay of the P_2 intermediate, only faint traces of a red-shifted intermediate (P_3-like) and a P_4 intermediate have been detected.[11]

In this study, we focus on identification of the retinal all-*trans* photoreaction by vibrational spectroscopy. Time-resolved vibrational spectroscopy proved to be a very reliable method for characterization of photoisomerization dynamics.[12,13] In particular, vibrational modes of retinal chromophores in photoreceptors are well studied. Vibrational marker bands for the all-*trans*, 15-*anti* retinal around 1163 cm^{-1}, 1200 cm^{-1}, and ~1240 cm^{-1} were assigned to mixed C-C stretching modes of the chromophore. The vibration at ~1240 cm^{-1} was assigned to a vibration with significant C_{12}-C_{13} stretching mode character, while the vibration at ~1200 cm^{-1} was assigned to a mode with significant C_{14}-C_{15} stretching character.[14] In *Ca*ChR1, these modes were observed in FTIR-difference spectra at 1163 cm^{-1}, 1205 cm^{-1}, and 1240 cm^{-1}.[15] Upon photoisomerization, the expected photoproduct has a 13-*cis*, 15-*anti* retinal conformation. A specific vibrational marker band was reported at about 1195 cm^{-1}, assigned to a vibration with a significant C_{14}-C_{15} stretching component.[16] This marker band for a 13-*cis* photoproduct was also observed in *Ca*ChR1 by FTIR-difference spectroscopy and, very recently, by impulsive vibrational spectroscopy,[17] confirming all-*trans* to 13-*cis* isomerization.[15] Here, we focused on the time-resolved observation of the all-*trans* marker bands at 1200 cm^{-1} and 1240 cm^{-1}, as well as on the 13-*cis*, 15-*anti* marker band at ~1195 cm^{-1}.

II. RESULTS AND DISCUSSION

In Fig. 1, the visible absorption spectrum of *Ca*ChR1 is plotted. We excited the sample at ~530 nm, where the absorption spectrum is dominated by *Ca*ChR1 with retinal all-*trans* configuration.

For tracking the retinal photoisomerization from all-*trans* to 13-*cis* configuration around the C_{13}=C_{14} double bond, we applied angle-balanced polarization-resolved femtosecond visible (VIS) pump–IR probe spectroscopy[18] to determine the vibrational dynamics on *Ca*ChR1 in H_2O in the vibrational fingerprint region from 1174 cm^{-1} to 1257 cm^{-1} with a high spectral resolution of 1.5 cm^{-1}. The spectral range around 1200 cm^{-1} exhibits well-characterized vibrational marker bands for retinal all-*trans* conformation, and retinal 13-*cis* conformation. These vibrational modes are dominated by the C_{14}-C_{15} stretching vibration of the retinal chromophore, the position where photoisomerization is supposed to induce strongest alterations. Since electronic spectra of stimulated emission, electronic excited state, product, and ground-state absorption overlap considerably, the vibrational marker band at 1190 cm^{-1} is a very suitable tool for 13-*cis* photoproduct identification.

Upon photoexcitation at 530 nm, spectral changes in the fingerprint region are presented in Fig. 2 for selected pump–probe delay times. An instantaneous strong negative signal is observed at 1203 cm^{-1}, reflecting the ground-state bleaching of the C_{14}-C_{15} stretching vibration of retinal in the all-*trans* conformation. A strong positive signal is visible at 1190 cm^{-1},

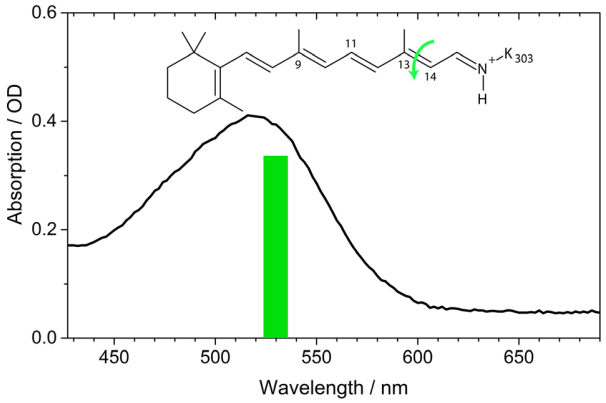

FIG. 1. Absorption spectrum of *Ca*ChR1. The green bar shows the excitation wavelength. Inset: Retinal all-*trans*, 15-*anti* configuration with protonated Schiff base. Green arrow indicates the photoisomerization.

representing the C_{14}-C_{15} stretching vibration of the 13-*cis* conformation. At time zero, this positive signal is absent, but at a delay time of 0.35 ps the signal has reached its maximum. This points to a very fast formation of the retinal 13-*cis* photoproduct, which is faster than 0.3 ps. Upon excitation, strong mixing of the C=C double and C-C single bond vibrations takes place in the electronic excited state. Thus, we observe no strong positive signal from retinal excited state absorption in the investigated spectral region. Another significant negative signal is visible at 1239 cm^{-1}, displaying the bleaching band of C_{12}-C_{13} stretching vibration in the retinal all-*trans* conformation. This band is spectrally shifted in the 13-*cis* conformation, and has negligible spectral overlap with strong positive absorption bands. Hence, we can use the bleaching recovery of this band to estimate the forward quantum yield of the photoreaction. The high spectral resolution of 1.5 cm^{-1} allows for identification of spectral substructures. A closer inspection of the bleaching band around 1239 cm^{-1} shows that a negative shoulder in the bleaching band at around 1230 cm^{-1} exists. Furthermore, we observe a broad positive feature from 1215 cm^{-1} to 1257 cm^{-1} at early delay times, which decays within a picosecond completely. In contrast, a remaining positive band at 1220 cm^{-1} is observed in the FTIR-difference spectra at 80 K.[19] This could point to the trapping of a transient intermediate state at low temperatures which relaxes back to the parent all-*trans* ground state on a picosecond time scale at room

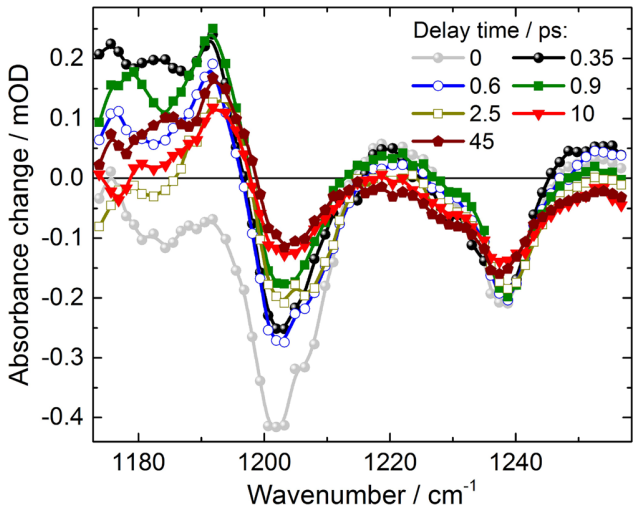

FIG. 2. Absorbance difference spectra of *Ca*ChR1 upon excitation at 530 nm at specific pump-probe delay times. Negative signals are bleaching signals; positive signals show vibrational absorption of hot ground-states, excited states, or product bands.

temperature. The transients at selected spectral positions plotted in Fig. 3 provide information on the photoreaction dynamics. At negative delay times, i.e., when the probe pulse arrives at the sample before the pump pulse, we observe signals from the perturbed free induction decay (PFID).[20] This results in an exponential increase at spectral positions of the strong bleaching bands at 1239 cm^{-1} and 1203 cm^{-1} (plotted as red and green lines in Fig. 3), reflecting the dephasing of these vibrations. The exponential rise of the PFID signal at 1239 cm^{-1} corresponds to a line width (FWHM) of (10 ± 2) cm^{-1},[20] matching the line width of the bleaching signal at 45 ps in Fig. 2, after completion of cooling processes. This supports the absence of a positive signal superimposed at 1239 cm^{-1} for long delay times. At time zero, the pump pulse arrives and populates excited states. Within the system response of 0.3 ps (grey line in Fig. 3) the all-*trans* bleaching signal at 1203 cm^{-1} (green line) appears and decays on a sub-picosecond to picosecond time scale. This bleaching recovery can reflect either repopulation of the ground state, or a blue-shift of the adjacent positive C_{14}-C_{15} stretching vibration of the 13-*cis* conformation around 1190 cm^{-1}. The latter is supported by narrowing of the spectral width of the C_{14}-C_{15} stretching vibration around 1180 cm^{-1}, and the blue-shift of the zero-crossing around 1197 cm^{-1} for increasing delay times in Fig. 2.

The transient of the C_{14}-C_{15} stretching vibration of the 13-*cis* conformation ($\nu(C_{14}$-$C_{15})^{13cis}$) at ∼1190 cm^{-1} (black circles in Fig. 3) displays a positive signal, which rises within the system response of 0.3 ps. Since the band at 1190 cm^{-1} is a marker band for 13-*cis* conformation, we can conclude that photoproduct formation due to all-*trans* isomerization is finished after 0.3 ps. This is in line with recent studies on electronic transitions.[10] The transient stays nearly constant in amplitude within the observed time window. All data are well-simulated by the sum of three exponentials.

We found decay constants of $\tau_1 = (0.55 \pm 0.05)$ ps, $\tau_2 = (6 \pm 1)$ ps, and a decay constant τ_3 much longer than our observation time window. We assign τ_3 to the remaining and constant signal in our time window of 200 ps. The simulated curves are presented in Fig. 3 as solid lines, and at spectral positions of 1203 cm^{-1} and 1239 cm^{-1} simulations of the PFID are also displayed. The transient of the $\nu(C_{14}$-$C_{15})^{trans}$ bleaching band at 1203 cm^{-1} (green line, Fig. 3) exhibits a significant decay with 0.55 ps and 6 ps. In contrast, the transient of the $\nu(C_{12}$-$C_{13})^{trans}$ bleaching band at 1239 cm^{-1} shows only a small amplitude changes with a decay constant of 6 ps. The decay associated spectra (DAS) of the decay constants τ_1 ($DAS_{\tau 1}$), τ_2 ($DAS_{\tau 2}$), and τ_3 ($DAS_{\tau 3}$) are plotted in Fig. 4.

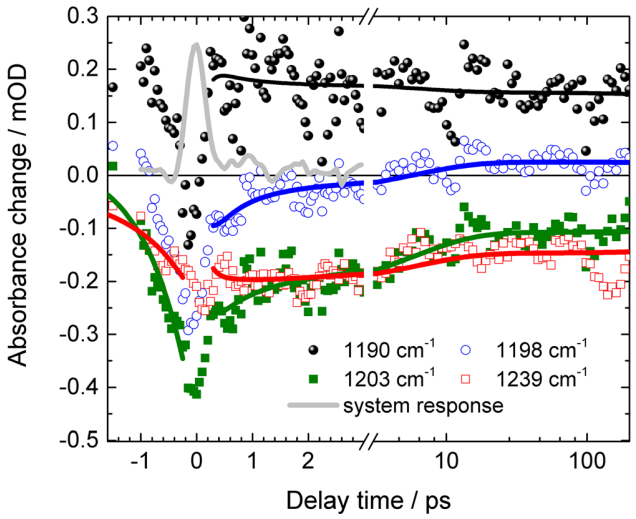

FIG. 3. Transients of *Ca*ChR1 upon excitation at 530 nm for selected wavenumbers. Positive delay times: Solid lines represent simulations with a sum of three exponentials; negative delay times: Solid lines represent PFID signals at 1203 cm^{-1} (green line) with a time constant of (0.80 ± 0.08) ps, and at 1239 cm^{-1} (red line) with a time constant of (1 ± 0.2) ps.

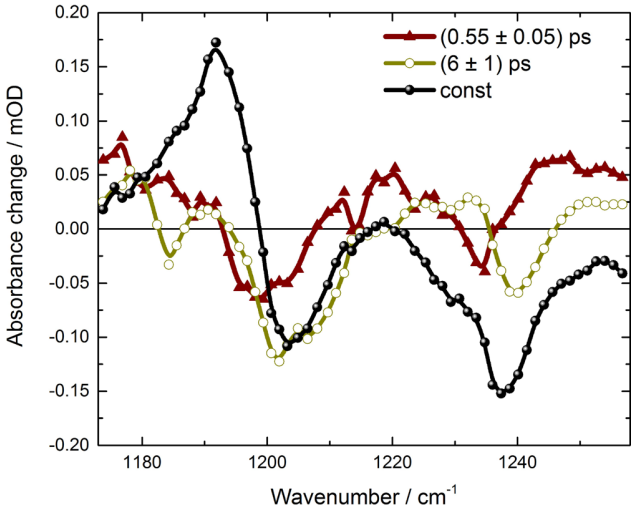

FIG. 4. Decay associated spectra of *Ca*ChR1. The constant $DAS_{\tau 3}$ (black) represents the difference spectra on a time scale of hundreds of ps. The fast $DAS_{\tau 1}$ (brown) shows dispersive features of vibrational cooling. $DAS_{\tau 2}$ (dark yellow) exhibits dispersive features and features of the bleaching bands.

The fast component $DAS_{\tau 1}$ exhibits a broad positive signal from 1173 cm^{-1} to 1193 cm^{-1}, and a negative signal with similar strength from 1193 cm^{-1} to 1208 cm^{-1}. The zero-crossing is exactly at the maximum of the $\nu(C_{14}\text{-}C_{15})^{13cis}$ absorption, indicating vibrational cooling of the 13-*cis* product band. Moreover, a broad positive signal from 1208 cm^{-1} to 1258 cm^{-1} is visible, with a negative peak around 1234 cm^{-1}. This feature could be caused by cooling of a vibration absorbing at higher wavenumbers than 1258 cm^{-1}. We assign the 0.55 ps component solely to the cooling processes. The slower component $DAS_{\tau 2}$ has also a positive component below 1193 cm^{-1}, and negative contributions from 1193 cm^{-1} up to 1220 cm^{-1}. In contrast to the fast component $DAS_{\tau 1}$, the negative signal has more amplitude than the positive one. For pure vibrational cooling processes, one would expect a stronger positive signal compared to the negative signal of the same vibration, since the oscillator strength is typically increased by vibrational excitation. This could point to the cooling processes, overlapped by ground-state recovery. This is supported by the positive/negative feature at 1228 cm^{-1} (+)/1239 cm^{-1} (−) in $DAS_{\tau 2}$. Again, a positive signal is observed at higher wavenumbers (around 1250 cm^{-1}). Moreover, the $DAS_{\tau 2}$ has negligible contributions at 1193 cm^{-1}, but strong contributions at 1203 cm^{-1} indicating no increase of the 13-*cis* photoproduct, but recovery of the all-*trans* bleaching band with a decay time of 6 ps. This supports the assignment of back-reaction processes with a time constant of 6 ps. The constant signal $DAS_{\tau 3}$ shows the clear positive/negative signature at 1192 cm^{-1} (+)/1204 cm^{-1} (−) of all-*trans* to 13-*cis* photoisomerization with amplitude ratio of 3:2, similar to those observed in light-induced FTIR-difference spectra of *Ca*ChR1 at cryogenic temperature.[19]

Since the $\nu(C_{14}\text{-}C_{15})^{trans}$ bleaching band at 1203 cm^{-1} is strongly masked by the $\nu(C_{14}\text{-}C_{15})^{13cis}$ absorption, we analyzed the $\nu(C_{12}\text{-}C_{13})^{trans}$ bleaching band at 1239 cm^{-1} to estimate the quantum yield of the forward photoisomerization reaction. In Fig. 5, we present the different absorption spectrum at delay time zero (black line) together with the constant component $DAS_{\tau 3}$ from the simulations. At 1239 cm^{-1}, we see negligible contributions of non-linear spectral features, but a broad positive background at delay time zero. By subtracting the background approximated by a straight line (grey line in Fig. 5), the bleaching signal strength is calculated at time zero (green line in Fig. 5). The constant DAS in Fig. 5 (red line) shows the pure bleaching signal at 1239 cm^{-1} without overlapping the positive contributions. The bleaching signal strength after the photoreaction is calculated and presented in Fig. 5 (blue line). The ratio of the two bleaching signals reveals the proportion of *Ca*ChR1 not reacting back to the all-*trans*

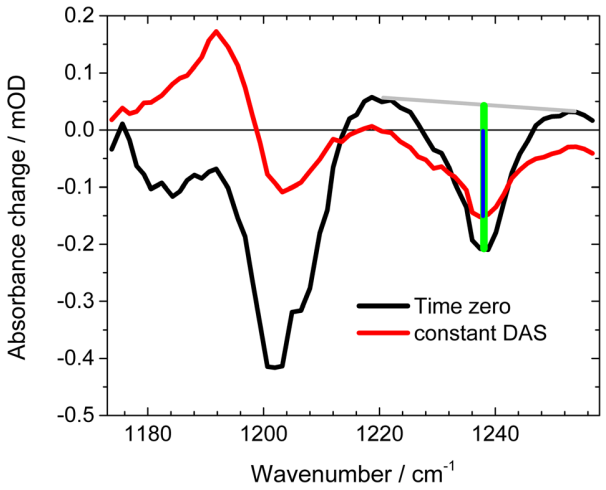

FIG. 5. Absorbance difference spectra at time zero (black line), and at long delay times represented by $DAS_{\tau 3}$ (red line). At 1239 cm^{-1} the amplitudes are taken at time zero and for long delay times, represented by the green and blue bars, respectively. Grey line: Baseline for subtraction of the positive broad background at time zero.

ground state, but undergo a forward reaction. Thus, the forward reaction quantum yield can be determined from our data to (0.60 ± 0.06).

Closer inspection of the spectral shape of the bleaching band at 1239 cm^{-1} displays a shoulder at 1230 cm^{-1}. This shoulder is visible in all difference spectra (Fig. 2) indicating an additional bleaching band. Whether this bleaching band reflects retinal ground state heterogeneity in all-*trans*, 15-*anti* conformation, i.e., due to different hydrogen bonding, or is caused by a sub-population of 13-*cis*, 15-*syn* retinal[10,21] of ground-state *Ca*ChR1 will be investigated in future studies.

III. CONCLUSION

We present the first femtosecond time-resolved IR study of the photoisomerization of channelrhodopsin-1 from *Chlamydomonas augustae* (*Ca*ChR1) in the vibrational fingerprint region of the C-C stretching vibrations. The vibrational dynamics of the retinal chromophore isomerization from all-*trans* to 13-*cis* was investigated by polarization-resolved VIS pump mid-IR probe spectroscopy at a high time resolution (about 300 fs). After photoexcitation at 530 nm, the transient infrared absorption was probed in a spectral region with dominant C-C stretching mode absorption. The photoproduct C_{14}-C_{15} vibrational marker mode at 1190 cm^{-1} that is indicative for a 13-*cis*, 15-*anti* configuration of the chromophore rises within the time resolution. Investigations in the visible spectral range reported photoisomerization time constants of 100 fs.[10] This is in line with our observations that provide direct evidence for the isomerization taking place faster than 0.3 ps, faster than in bacteriorhodopsin[13] or in channelrodopsin-2[7] from *Chlamydomonas reinhardtii* (*Cr*ChR2). Vibrational dynamics show additional time constants of (0.55 ± 0.05) ps and (6 ± 1) ps, identical to those observed in ultrafast VIS pump supercontinuum probe experiments.[10] We assigned the 0.55 ps time constant predominantly to vibrational cooling, while the longer time constant of 6 ps probably also consists of a back-reaction pathway. We estimated the photoisomerization reaction yield by the bleaching signal of the C_{12}-C_{13} stretching band at 1239 cm^{-1} to (60 ± 6)%, very similar to other rhodopsins. Our high spectral resolution of 1.5 cm^{-1} allows for identification of an additional bleaching component at 1230 cm^{-1}. This finding strongly supports ground state heterogeneity of the retinal chromophore. Further studies should be performed to assign this bleaching band to either heterogeneity of the all-*trans*, 15-*anti* retinal or to a 13-*cis*, 15-*syn* (dark-adapted) retinal conformation. Our study clearly demonstrates various different photoreaction processes in retinal photoreceptors. *Ca*ChR1shows a significantly faster isomerization dynamics as *Cr*ChR2 at a high yield. Further

studies will be performed to identify the molecular origin of these differences, in order to truly understand the optimization of photoreactions in photoreceptors.

IV. METHODS

*Ca*ChR1 was prepared as described previously.[9,22] Briefly, the truncated *Ca*ChR1 gene (1-352 aa) was fused with a 10xHis-tag (GeneArt, Life Technologies) and was heterologously expressed in *Pichia pastoris* yeast cells. The solubilized protein was purified on a Ni-NTA column (Macherey-Nagel, Germany) and concentrated to 46 mg/ml in a buffer containing 20 mM Hepes, 100 mM NaCl, 0.05% dodecyl maltoside at pH 7.4. Two times 150 μl of the *Ca*ChR1 solution was placed between two CaF_2 windows. The spectral line-width of the femtosecond excitation pulses is sketched with the absorption spectrum of *Ca*ChR1 in Figure 1.

Femtosecond laser pulses were generated starting from a fundamental femtosecond laser pulse delivered by a 1 kHz Ti:Sa laser system (Coherent Legend USP, 80 fs pulses at 800 nm). The fundamental beam was split into two parts for pump and probe pulse generation. The pump pulses were generated in a non-collinear optical parametric amplifier (NOPA). A sapphire white light supercontinuum was used as seed, amplified in a β-barium borate (BBO) crystal by frequency doubled pulses at 400 nm. We selected energies to excite the sample of about 0.4–0.5 μJ per pulse with a pump focus diameter of about 300 μm.

Angle balanced femtosecond polarization resolved VIS pump–IR probe measurements were applied as described elsewhere.[18] In short, the mid-IR probe beam is generated by a difference-frequency mixing of near-infrared signal and idler pulses generated by 800 nm fs pulses in a BBO crystal. Two reflections of the fs mid-IR pulse are taken as probe beams with different polarizations used at the same time in the same sample volume to detect absorbance changes. The system response was about 300 fs (shown in Fig. 3, grey line). We measured the system response in a thin Ge plate in identical sample holders, as were used for the experiments on *Ca*ChR1. Absorbance changes with mid-IR polarizations parallel (A_{pa}) and perpendicular (A_{pe}) to the VIS pump beam polarization were detected. Isotropic absorbance changes (A_{iso}) were calculated by $A_{iso} = (A_{pa} + 2\ A_{pe})/3$. Here, we presented only isotropic data.

ACKNOWLEDGMENTS

The work performed at the Free University of Berlin was supported by the SFB 1078, TP B3 to J.H. and K.H. and B4 to R.S. We are thankful to Dorothea Heinrich and Kirsten Hoffmann for excellent technical assistance.

[1]K. Deisseroth, "Optogenetics: 10 years of microbial opsins in neuroscience," Nat. Neurosci. **18**(9), 1213–1225 (2015).
[2]L. Petreanu, D. Huber, A. Sobczyk, and K. Svoboda, "Channelrhodopsin-2-assisted circuit mapping of long-range callosal projections," Nat. Neurosci. **10**(5), 663–668 (2007).
[3]G. Nagel, M. Brauner, J. F. Liewald, N. Adeishvili, E. Bamberg, and A. Gottschalk, "Light activation of channelrhodopsin-2 in excitable cells of *Caenorhabditis elegans* triggers rapid behavioral responses," Curr. Biol. **15**(24), 2279–2284 (2005).
[4]B. R. Arenkiel, J. Peca, I. G. Davison, C. Feliciano, K. Deisseroth, G. J. Augustine, M. D. Ehlers, and G. Feng, "*In vivo* light-induced activation of neural circuitry in transgenic mice expressing channelrhodopsin-2," Neuron **54**(2), 205–218 (2007).
[5]V. A. Lorenz-Fonfria and J. Heberle, "Channelrhodopsin unchained: Structure and mechanism of a light-gated cation channel," Biochim. Biophys. Acta **1837**(5), 626–642 (2014).
[6]M. K. Verhoefen, C. Bamann, R. Blocher, U. Forster, E. Bamberg, and J. Wachtveitl, "The photocycle of channelrhodopsin-2: Ultrafast reaction dynamics and subsequent reaction steps," Chemphyschem **11**(14), 3113–3122 (2010).
[7]M. K. Neumann-Verhoefen, K. Neumann, C. Bamann, I. Radu, J. Heberle, E. Bamberg, and J. Wachtveitl, "Ultrafast infrared spectroscopy on channelrhodopsin-2 reveals efficient energy transfer from the retinal chromophore to the protein," J. Am. Chem. Soc. **135**(18), 6968–6976 (2013).
[8]S. Y. Hou, E. G. Govorunova, M. Ntefidou, C. E. Lane, E. N. Spudich, O. A. Sineshchekov, and J. L. Spudich, "Diversity of Chlamydomonas channelrhodopsins," Photochem. Photobiol. **88**(1), 119–128 (2012).
[9]V. Muders, S. Kerruth, V. A. Lorenz-Fonfria, C. Bamann, J. Heberle, and R. Schlesinger, "Resonance Raman and FTIR spectroscopic characterization of the closed and open states of channelrhodopsin-1," FEBS Lett. **588**(14), 2301–2306 (2014).
[10]T. Stensitzki, V. Muders, R. Schlesinger, J. Heberle, and K. Heyne, "The primary photoreaction of channelrhodopsin-1: Wavelength dependent photoreactions induced by ground-state heterogeneity," Front. Mol. Biosci. **2**, 41 (2015).
[11]O. A. Sineshchekov, E. G. Govorunova, J. Wang, H. Li, and J. L. Spudich, "Intramolecular proton transfer in channelrhodopsins," Biophys. J. **104**(4), 807–817 (2013).

[12]Y. Yang, K. Heyne, R. A. Mathies, and J. Dasgupta, "Non-bonded interactions drive the sub-picosecond bilin photoisomerization in the Pfr state of phytochrome Cph1," Chemphyschem **17**(3), 369–374 (2016).
[13]J. Herbst, K. Heyne, and R. Diller, "Femtosecond infrared spectroscopy of bacteriorhodopsin chromophore isomerization," Science **297**(5582), 822–825 (2002).
[14]I. Palings, J. A. Pardoen, E. van den Berg, C. Winkel, J. Lugtenburg, and R. A. Mathies, "Assignment of fingerprint vibrations in the resonance Raman spectra of rhodopsin, isorhodopsin, and bathorhodopsin: Implications for chromophore structure and environment," Biochemistry **26**(9), 2544–2556 (1987).
[15]J. I. Ogren, S. Mamaev, D. Russano, H. Li, J. L. Spudich, and K. J. Rothschild, "Retinal chromophore structure and Schiff base interactions in red-shifted channelrhodopsin-1 from *Chlamydomonas augustae*," Biochemistry **53**(24), 3961–3970 (2014).
[16]S. O. Smith, J. Lugtenburg, and R. A. Mathies, "Determination of retinal chromophore structure in bacteriorhodopsin with resonance Raman spectroscopy," J. Membr. Biol. **85**(2), 95–109 (1985).
[17]C. Schnedermann, V. Muders, D. Ehrenberg, R. Schlesinger, P. Kukura, and J. Heberle, "Vibronic dynamics of the ultrafast all-trans to 13-cis photoisomerization of retinal in channelrhodopsin-1," J. Am. Chem. Soc. **138**(14), 4757–4762 (2016).
[18]M. Linke, Y. Yang, B. Zienicke, M. A. Hammam, T. von Haimberger, A. Zacarias, K. Inomata, T. Lamparter, and K. Heyne, "Electronic transitions and heterogeneity of the bacteriophytochrome Pr absorption band: An angle balanced polarization resolved femtosecond VIS pump-IR probe study," Biophys. J. **105**(8), 1756–1766 (2013).
[19]J. I. Ogren, A. Yi, S. Mamaev, H. Li, J. Lugtenburg, W. J. DeGrip, J. L. Spudich, and K. J. Rothschild, "Comparison of the structural changes occurring during the primary phototransition of two different channelrhodopsins from Chlamydomonas algae," Biochemistry **54**(2), 377–388 (2015).
[20]P. Hamm, "Coherent effects in femtosecond infrared-spectroscopy," Chem. Phys. **200**(3), 415–429 (1995).
[21]S. O. Smith, I. Palings, V. Copie, D. P. Raleigh, J. Courtin, J. A. Pardoen, J. Lugtenburg, R. A. Mathies, and R. G. Griffin, "Low-temperature solid-state 13C NMR studies of the retinal chromophore in rhodopsin," Biochemistry **26**(6), 1606–1611 (1987).
[22]V. A. Lorenz-Fonfria, V. Muders, R. Schlesinger, and J. Heberle, "Changes in the hydrogen-bonding strength of internal water molecules and cysteine residues in the conductive state of channelrhodopsin-1," J. Chem. Phys. **141**(22), 22D507 (2014).

Acceleration of a ground-state reaction by selective femtosecond-infrared-laser-pulse excitation

Till Stensitzki, Yang Yang, Valeri Kozich, Ashour A. Ahmed, Florian Kössl, Oliver Kühn and Karsten Heyne

https://doi.org/10.1038/nchem.2909

Acceleration of a ground-state reaction by selective femtosecond-infrared-laser-pulse excitation

Till Stensitzki, Yang Yang, Valeri Kozich, Ashour A. Ahmed, Florian Kössl, Oliver Kühn and Karsten Heyne

https://doi.org/10.1038/nchem.2909

Acceleration of a ground-state reaction by selective femtosecond-infrared-laser-pulse excitation

Till Stensitzki, Yang Yang, Valeri Kozich, Ashour A. Ahmed, Florian Kössl, Oliver Kühn and Karsten Heyne

https://doi.org/10.1038/nchem.2909

Acceleration of a ground-state reaction by selective femtosecond-infrared-laser-pulse excitation

Till Stensitzki, Yang Yang, Valeri Kozich, Ashour A. Ahmed, Florian Kössl, Oliver Kühn and Karsten Heyne

https://doi.org/10.1038/nchem.2909

Acceleration of a ground-state reaction by selective femtosecond-infrared-laser-pulse excitation

Till Stensitzki, Yang Yang, Valeri Kozich, Ashour A. Ahmed, Florian Kössl, Oliver Kühn and Karsten Heyne

https://doi.org/10.1038/nchem.2909

Acceleration of a ground-state reaction by selective femtosecond-infrared-laser-pulse excitation

Till Stensitzki, Yang Yang, Valeri Kozich, Ashour A. Ahmed, Florian Kössl, Oliver Kühn and Karsten Heyne

https://doi.org/10.1038/nchem.2909

nature chemistry

SUPPLEMENTARY INFORMATION

DOI: 10.1038/NCHEM.2909

In the format provided by the authors and unedited.

Acceleration of a ground-state reaction by selective femtosecond-infrared-laser-pulse excitation

T. Stensitzki,[1] Y. Yang,[1] V. Kozich,[1] A. A. Ahmed,[2,3] F. Kössl,[1] O. Kühn,[3] & K. Heyne[1]*

[1] Freie Universität Berlin, Department of Physics, Arnimallee 14, 14195 Berlin, Germany

[2] University of Cairo, Faculty of Science, Department of Chemistry, 12613 Giza, Egypt

[3] University of Rostock, Institute of Physics, Albert Einstein-Str. 23-24, 18059 Rostock, Germany

1. Schematic View of Alcoholysis Reactions

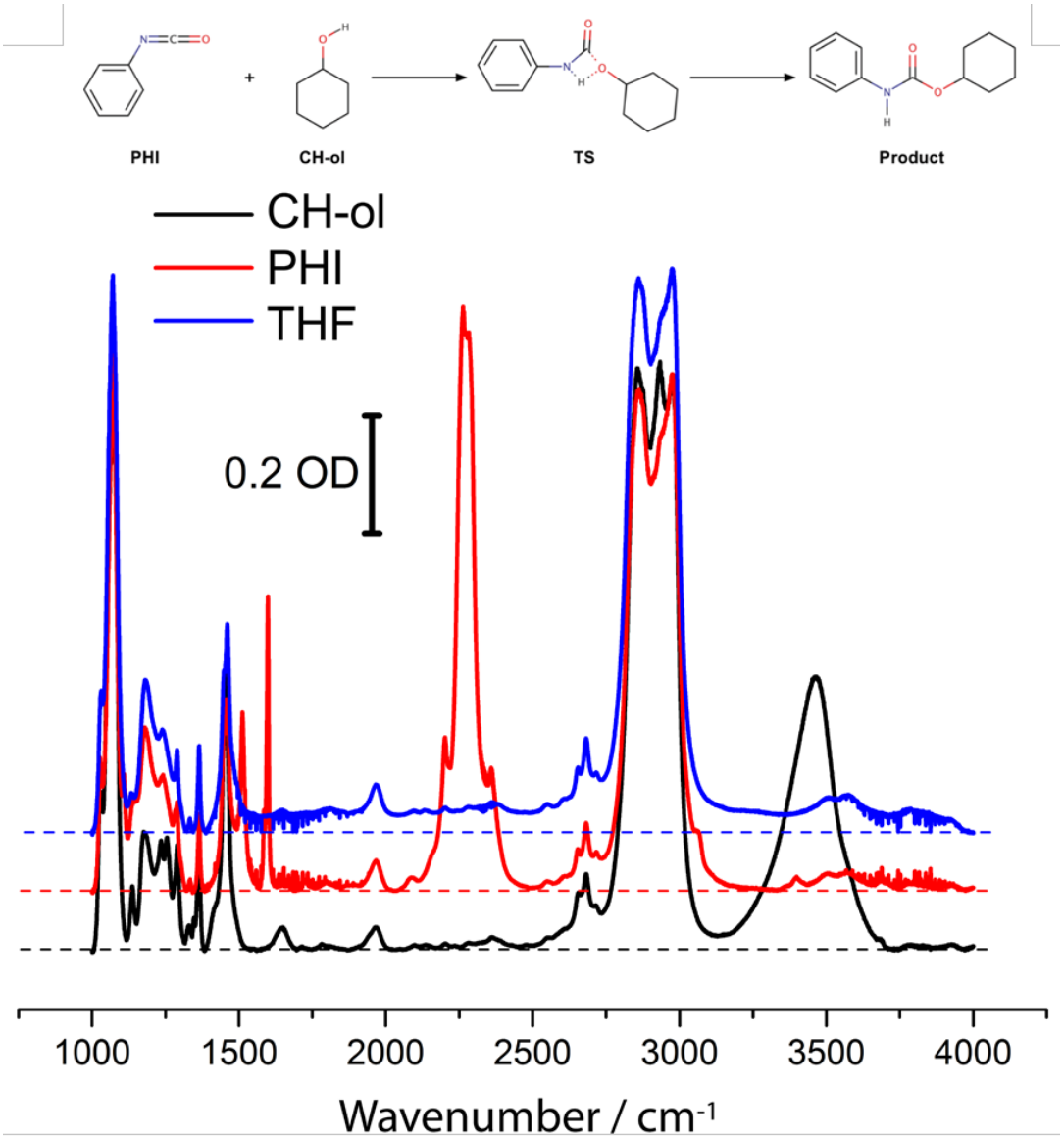

Supplementary Figure 1: Upper panel: Sketch of the alcoholysis reaction of phenylisocyanate (PHI) with cyclohexanol (CH-ol) forming the product cyclohexyl-carbanilate (CC). Lower panel: Absorption spectra of PHI solved in tetrahydrofuran (THF, red curve), CH-ol solved in THF (black curve), and the pure solvent THF (blue curve).

The alcoholysis reaction of phenylisocyanate (PHI) and cyclohexanol (CH-ol) is a thermal driven reaction and occurs upon mixing of PHI and CH-ol. Strong vibrational marker bands were found for CH-ol, the OH-stretching vibration, measured at 3500 cm^{-1} and calculated at 3816 cm^{-1}, and for PHI, the NCO stretching vibration, at 2270 cm^{-1} (calc. 2362 cm^{-1}), the CH bending vibration at 1600 cm^{-1} (calc. 1648 cm^{-1}), and the NCO stretching vibration and CH bending vibration at 1512 cm^{-1} (calc. 1560 cm^{-1}). These vibrations are visible in Supplementary Fig. 1 and 2 and are not masked by tetrahydrofuran (THF) vibrations and can be used to follow the reaction time-resolved.

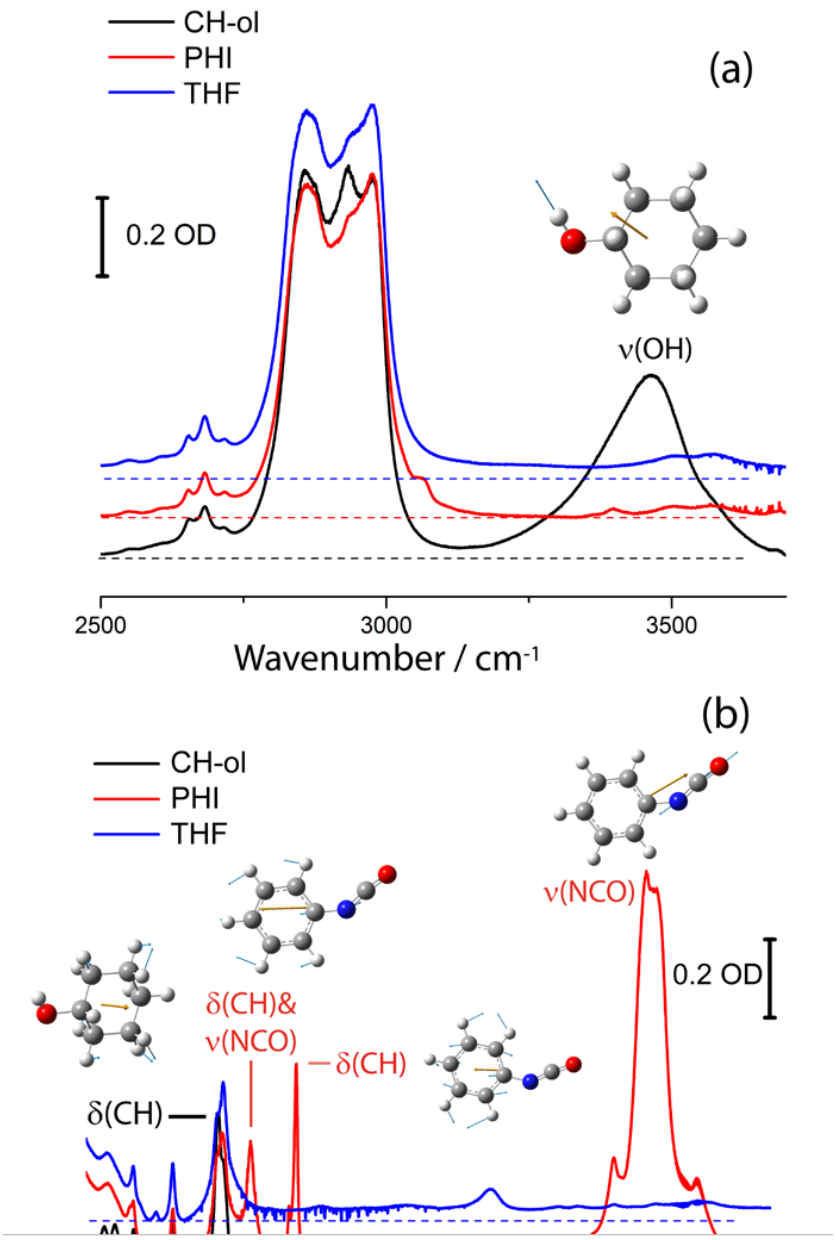

Supplementary Figure 2: (a) Absorption spectra of CH-ol in THF (black line), PHI in THF (red line), and THF (blue line) in the spectral range around 3000 cm^{-1} (a) and around 2000 cm^{-1} (b). (a) The OH-stretching vibration of CH-ol at 3500 cm^{-1}. The calculated IR transition dipole moment (orange arrow), and the displacement of the atoms (blue arrows) of this normal mode is shown next to the absorption band. (b) The NCO-stretching vibration of PHI at 2270 cm^{-1}. Moreover, the CH-bending vibration of PHI at 1600 cm^{-1}, the NCO-stretching & CH-bending vibration of PHI at 1512 cm^{-1}, and the CH-bending vibration of CH-ol at 1450 cm^{-1}. The calculated dipole derivative unit vectors (orange arrows), and the displacement vectors (blue arrows) of the normal modes are shown next to the absorption bands.

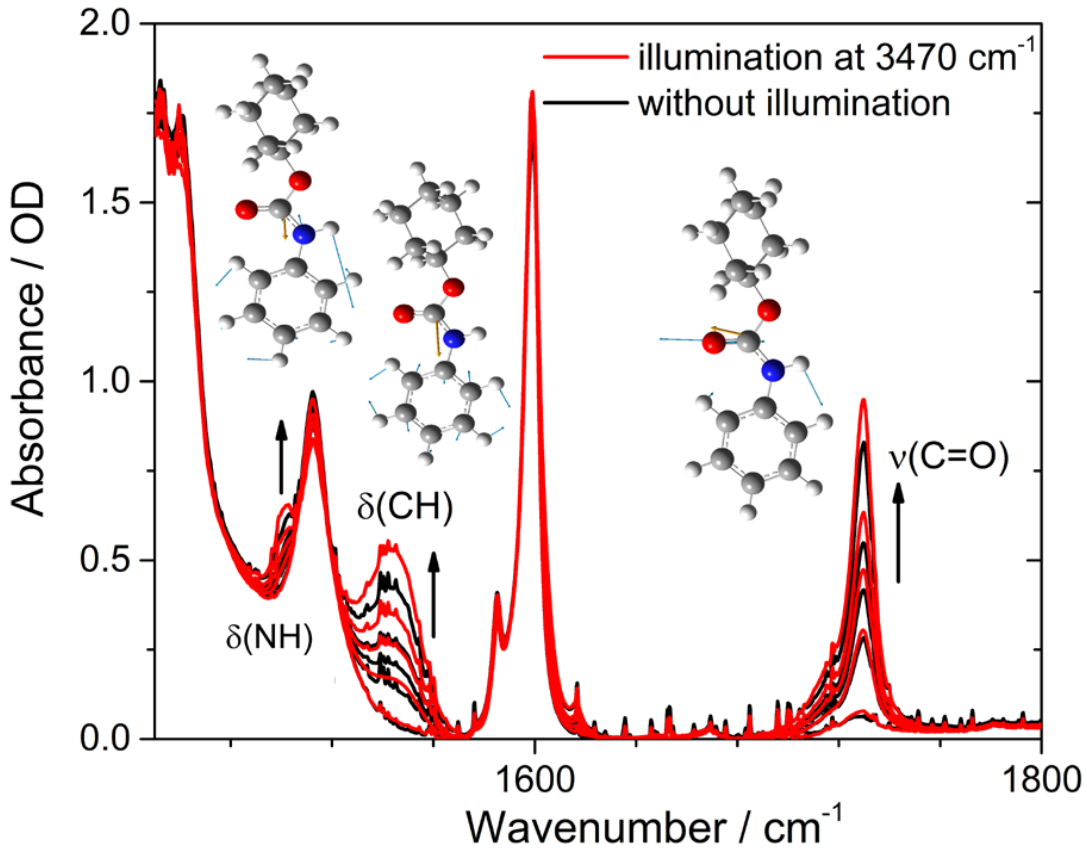

Supplementary Figure 3: Absorption spectra of a 1:1 mixture of CH-ol and PHI in THF for different waiting times of 0 min, 60 min, 120 min, 180 min, and 300 min after mixing. Two identical samples were mixed, one was illuminated at ~ 3470 cm^{-1} (FWHM ~ 50 cm^{-1}) at a repetition rate of 2 kHz (red lines), the other one was not illuminated (black lines).With increasing waiting time the cyclohexyl-carbanilate (CC) product rises. CC marker bands were identified: at 1730 cm^{-1} (calculated 1784 cm^{-1}) the CO stretching vibration; at 1545 cm^{-1} (calc. 1653 cm^{-1}) the CH-bending vibration, and at 1505 cm^{-1} (calc. 1566 cm^{-1}) mainly the NH-bending vibration.

The progress of the alcoholysis reaction can be monitored by the CC product absorption bands at 1730 cm^{-1}, 1545 cm^{-1}, and 1505 cm^{-1} presented in Supplementary Fig. 3. In addition, the NH-stretching vibration at 3300 cm^{-1} (calc. 3630 cm^{-1}) (not shown in Supplementary Fig. 3) can also be used to follow CC formation. The CC absorption bands increase, while the PHI and CH-ol bands decrease. Illumination around 3470 cm^{-1} accelerates the otherwise thermal driven reaction as can be seen by comparison of the illuminated sample (red lines) with the not illuminated sample (black lines).

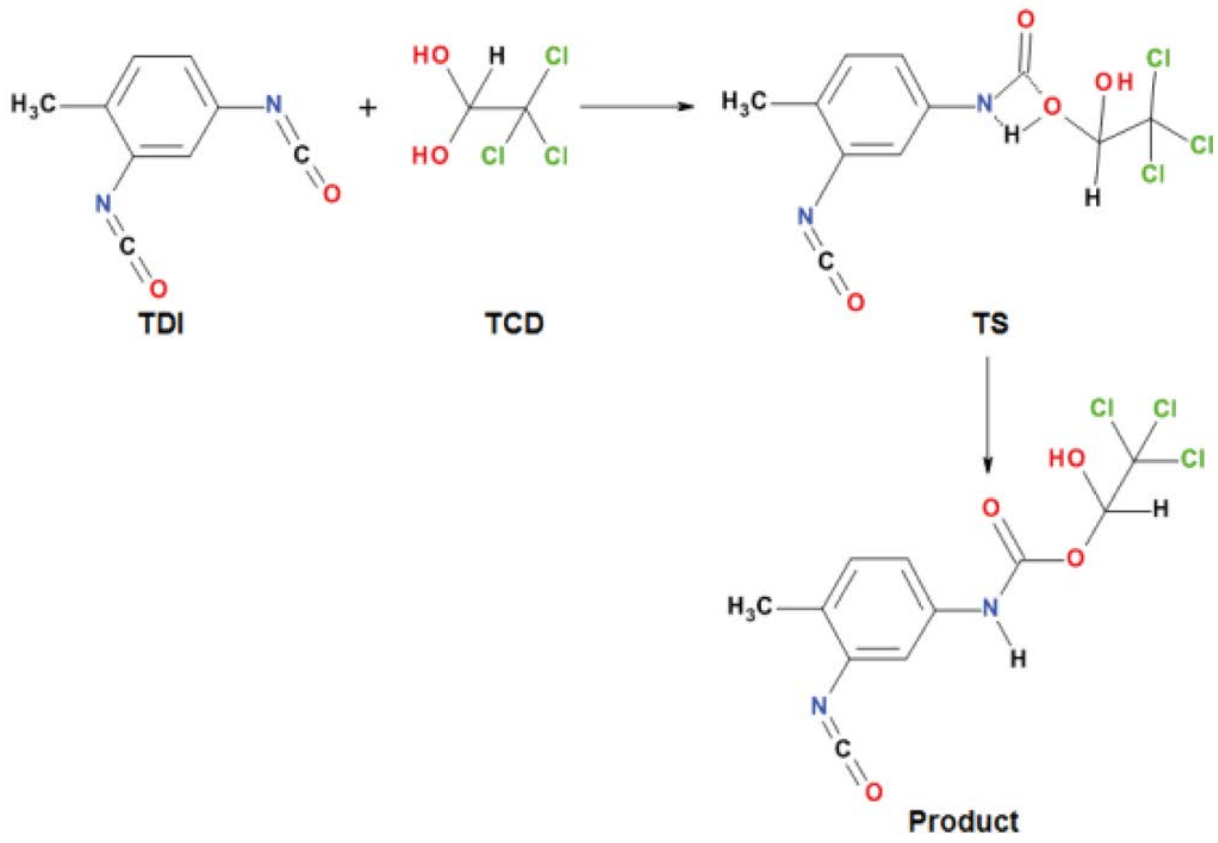

Supplementary Figure 4: Alcoholysis reaction of toluene-2,4-diisocyanate (TDI) and 2,2,2-trichloroethane-1,1-diol (TCD) and the first step towards a polymer by chain elongation.

2. Theoretical Methods and Additional Results

The initial step of the polymerization reaction has been mimicked by the alcoholysis reaction of PHI with CH-ol in explicit THF. Here, the experimental Arrhenius activation energy was found to be 6.7 kcal/mol [1]. First, geometry optimization and thermochemistry of stationary points, i.e. reactant, transition state, and product, have been performed in gas phase using DFT/B3LYP/6-31++G(d,p) [2]. The results are summarized in Supplementary Fig. 5 and Supplementary Tab. 1. Two different spatial conformations for the reactant (**R1** and **R2**), one transition state (**TS**), and one product (**P**) have been obtained (see Supplementary Fig. 6). It was observed that the two reactant (or precursor) geometries for the reactive system (PHI + CH-ol), **R1** and **R2** are almost isoenergetic (their energy difference is around 1.4 kcal/mol). However, their structure is rather different. While **R1** has a (nonlinear) N-H-O Hydrogen bond, **R2** is similar to the **TS,** which has a cyclic, -C-O-H-O-, structure. Apart from this fact, the structures differ by the orientation of the CH-ol. We did not locate a transition state between **R1** and **R2**, but it can be anticipated to exist. Similar to data reported in literature, the calculated

activation energies for **R1** and **R2** are found to be 30.1 to 31.5 kcal/mol, that is, 4.5 to 4.7 times the experimental values [1].

Due to this manifest discrepancy between the experimental results and the corresponding theoretical ones in gas phase, we included the effect of an explicit solvent, i.e. THF in the present case. Specifically, the stationary structures (PHI + CH-ol) of reactant, transition state, and product have been solvated with 26 THF molecules using a cluster model. Full geometry optimization for each system has been performed using the hybrid ONIOM model [3]. Here, the reactive molecular system (PHI + CH-ol) is studied at the B3LYP/6-31++G(d,p) level of theory, while the solvent molecules (THF) are described by the semi-empirical PM3 method.

For the ONIOM model the total energy is calculated as

$$E^{tot} = E^{react}_{B3LYP} + E^{solvent}_{PM3} + E^{int} \quad (1)$$

which can be rewritten as

$$E^{tot} = E^{react}_{B3LYP} + E^{react+solvent}_{PM3} - E^{react}_{PM3} \quad (2)$$

where E^{tot} is the total electronic energy, E^{react}_{B3LYP} is the electronic energy of the reactive system (PHI + CH-ol) using DFT/B3LYP, $E^{solvent}_{PM3}$ is the electronic energy of the solvent (THF) using PM3, $E^{react+solvent}_{PM3}$ is the electronic PM3 energy of the reactive system and solvent molecules (PHI + CH-ol + THF), and E^{int} is the interaction energy between the reactive system and solvent.

During the optimization process, structural changes occur for the solvent molecules that are not directly related to the reaction coordinate, but, e.g., reflect the flexibility at the surface of the cluster model. To avoid spurious effects due to such changes, the energy of the solvent is omitted from the total energy, thus giving the corrected energy

$$E = E^{react}_{B3LYP} + E^{react+solvent}_{PM3} - E^{react}_{PM3} - E^{solvent}_{PM3}. \quad (3)$$

Thermochemical calculations are performed for the reactive system only, assuming the validity of the harmonic approximation. The results of the ONIOM calculations are summarized in Supplementary Tabs. 1-5.

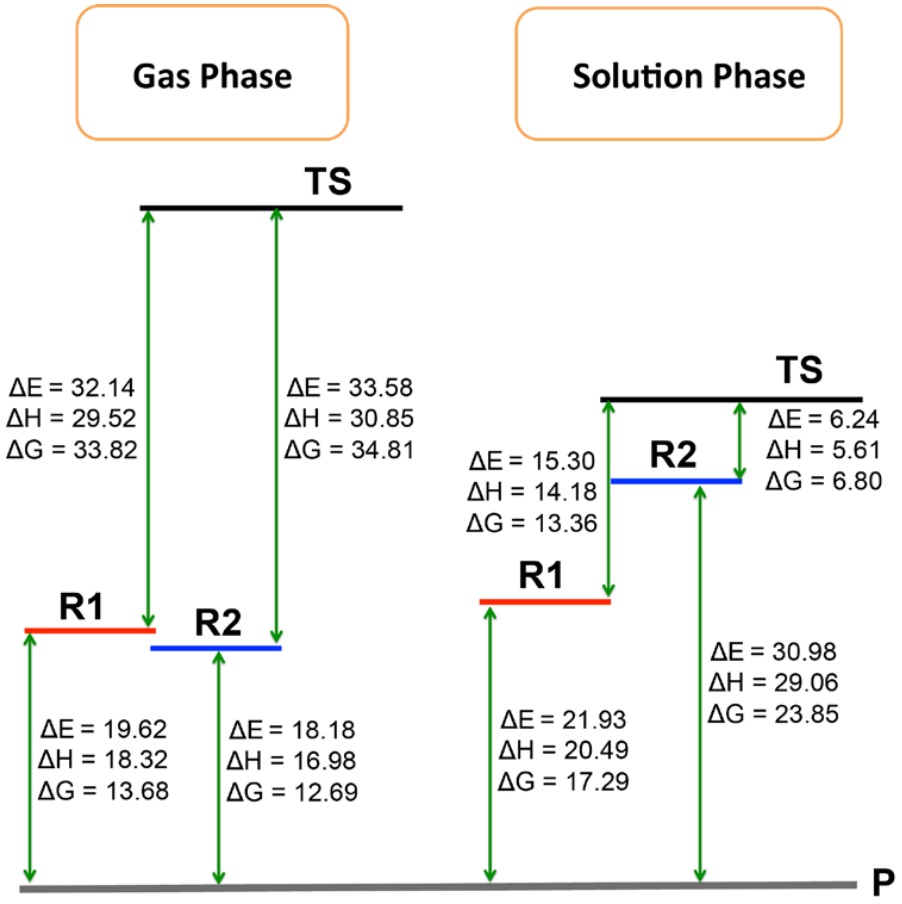

Supplementary Figure 5: Energetics of the reaction of PHI and CH-ol at the DFT/B3LYP/6-31++G(d,p) level in gas phase and in solution (treated by the ONIOM approach); numbers are given in kcal/mol.

In solution, Supplementary Figs. 5 and 7 show that there are also two reactant geometries for the reactive system (PHI + CH-ol), **R1** and **R2**. However, **R1** is more stable than **R2** (using the corrected energy, Eq. (3)) by about 9 kcal/mol. This means that in solution the cyclic nuclear conformation **R2** is the minor fraction, whereas **R1** is the major fraction. Given the similarity in structure between **R2** and **TS,** as depicted in Supplementary Fig. 7, we expect that these are the relevant configurations that give rise to the rather low activation energy observed in experiment for this reaction (6.7 ± 0.2 kcal/mol) [1]. This is in accord with the observed small urethane product yield that points to either an ineffective excitation process or a minor fraction of nuclear conformations capable of reacting. Further support for the responsibility of **R2** for the observed activation energy in experiment is the conformational change between **R2** and **TS**. This change is mainly negligible for CH-ol compared to PHI (see the dipole moments of PHI and CH-ol in Supplementary Tab. 2). Conformational changes from **R2** to **TS** show an NCO angle change of 0.6° (see Supplementary Tab. 3), a shortening of the distance between the NCO carbon and the OH oxygen by 0.1 Å, and a shortening of the distance between the NCO nitrogen and the OH hydrogen by 0.02 Å (see Supplementary Fig. 7). Moreover,

the interaction of the solvent with the R2 and TS conformations is stronger for CH-ol than for PHI (see Supplementary Tab. 4). These findings indicate to the stronger influence of the NCO-stretching vibration to the reaction coordinate as compared with the OH-stretching vibration, in accord with experiment. Furthermore, the shortening of the C-O distance is more pronounced than that of the N-H distance due to the stronger electrostatic interaction between the C and O atoms as compared with the N and H atoms (see the Mulliken partial atomic charges in Supplementary Tab. 5)

Concerning the energetics, we note that there is a substantial difference between the gas phase and solution results. Given the experimental activation energy of about 6.7 ± 0.2 kcal/mol the gas phase results are too large by factor of about 4.6. It turns out that the present ONIOM approach almost quantitatively reproduces the experimental value. In view of the various approximations such a quantitative agreement could be rather fortunate. However, it can be taken as an indication that the essential aspects of this part of the reaction are covered by the model.

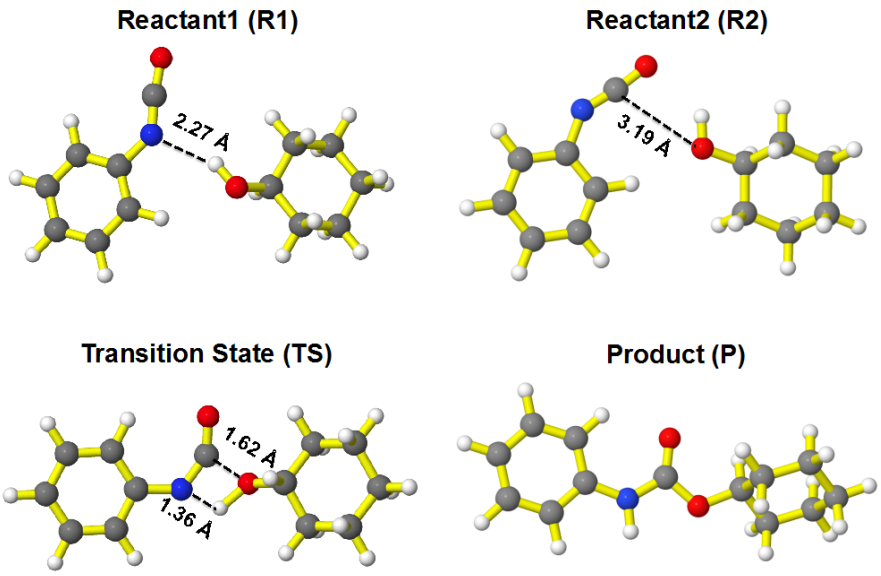

Supplementary Figure 6: Geometries of the reaction of PHI and CH-ol at the DFT/B3LYP/6-31++G(d,p) level in gas phase.

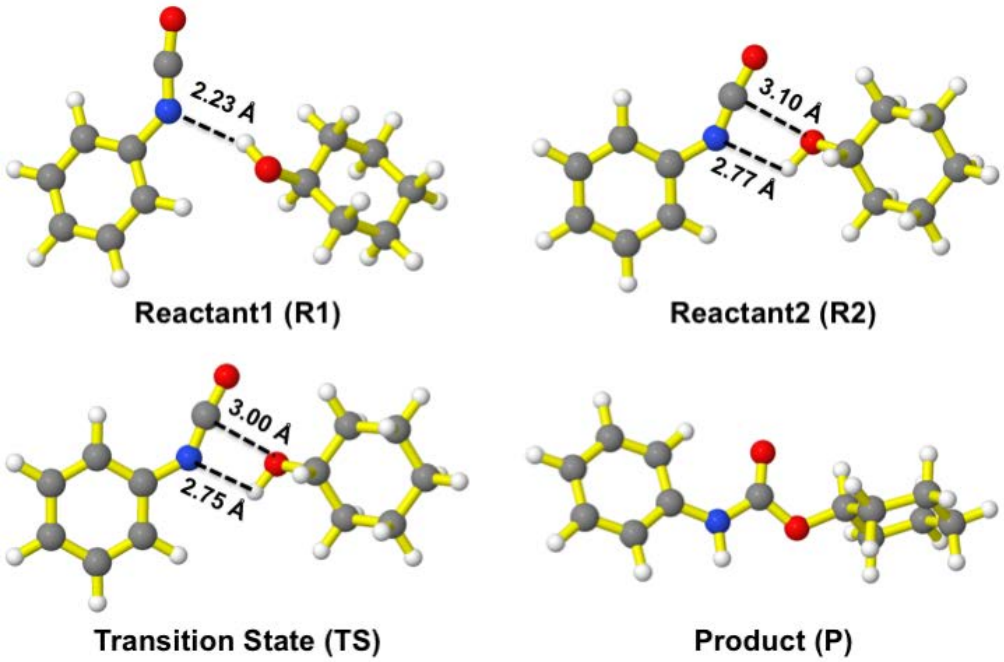

Supplementary Figure 7: Geometries of the reaction of PHI and CH-ol at the DFT/B3LYP/6-31++G(d,p) level in THF solution described by the ONIOM model.

Comparing the reactive systems in gas phase and in solution, one notices that the structural changes follow the order **P** < **R1** < **TS** < **R2**. This can be seen by comparing the geometries in Supplementary Figs. 6 and 7. In addition, the change in dipole moments of gas phase and solution reactive systems (Supplementary Tab. 2) and the root mean square deviation (RMSD) of geometries between gas phase and solution reactive systems (Supplementary Tab. 3) confirm the same order. In addition, much of the change of the dipole moment of PHI is due the structure and here most notably the NCO angle, which changes from 145° (gas phase) to 174° (solution). An interesting observation concerns the **TS** geometry, which is much tighter in gas phase as compared with the solution phase. For instance, the C-O distance in the TS changes from 1.6 Å to 3.0 Å upon solvation. This also can be observed from the Mulliken partial atomic charges on the interacting atoms (see Supplementary Tab. 5).

It is important to mention that all configurations **R1**, **R2**, **TS** and **P** are stabilized in solution as compared with the gas phase. This is due to the strong interaction between the solvent molecules and the reactive systems (PHI + CH-ol) and their constituents PHI and CH-ol. This reactive system-solvent-interaction increased in the order **TS** < **R2** < **R1** < **P**. Therefore, if we calculate the energy of reactive systems (**R1**, **R2**, and **TS**) relative to energy of **P** according to Eq. 3, we observe a stabilization of **TS** and a destabilization of **R2** (see Supplementary Fig. 5), leading to the observed experimental activation energy.

In a more detailed analysis of the reactive system (PHI + CH-ol) itself, it was observed that the CH-ol-solvent-interaction is stronger than the PHI-solvent-interaction for all reactive systems (see Supplementary Tab. 4). Further, the solvation shell around CH-ol is tighter as compared to PHI, thus pointing to the stronger (attractive) interaction.

Supplementary Table 1: Energetics (in kcal/mol) of the reaction between PHI and CH-ol in gas phase and in THF solution (according to Eq. (3); the uncorrected energies are given in parentheses).

		R1 → TS → P reaction pathway		**R2 → TS → P** reaction pathway	
		R1 to **TS**	**R1** to **P**	**R2** to **TS**	**R2** to **P**
gas phase	ΔE	32.1	-19.6	33.6	-18.2
	ΔH	29.5	-18.3	30.9	-17.0
	ΔG	33.8	-13.7	34.8	-12.7
	E_{act}	30.1	-	31.5	-
solution	ΔE	15.3 (2.2)	21.9 (27.1)	**6.2 (7.5)**	**-31.0 (-21.7)**
	ΔH	14.2 (1.0)	20.5 (25.7)	**5.6 (6.9)**	**-29.1 (-19.8)**
	ΔG	13.4 (0.2)	17.3 (22.5)	**6.8 (8.1)**	**-23.9 (-14.6)**
	E_{act}	14.8 (1.6)	-	**6.2 (7.5)**	**-**

Supplementary Table 2: Dipole moment of reactive system (PHI + CH-ol) and its constituents in gas phase as well as in THF solution.

dipole moment (Debye)			
		gas phase	solution
R1	reactive system	2.27	2.56
	PHI	2.64	2.61
	CH-ol	1.78	1.77
R2	reactive system	1.72	3.45
	PHI	2.86	2.77
	CH-ol	1.78	1.76
TS	reactive system	3.62	3.29
	PHI	0.99	2.74
	CH-ol	1.63	1.76
P	reactive system	2.50	2.54

Supplementary Table 3: NCO angle for reactive system in gas and solution as well as root mean square deviation (RMSD) between gas phase and solution reactive systems.

	NCO angle		RMSD (Å)
	gas phase	solution	
R1	173.2	173.3	0.33
R2	173.7	173.4	0.89
TS	145.9	174.0	0.60
P	126.5	126.1	0.25

Supplementary Table 4: Interaction energy of reactive system (PHI + CH-ol) and its constituents with the solvent (in kcal/mol).

	reactive system-solvent-interaction	PHI-solvent-interaction	CH-ol-solvent-interaction
R1	-29.9	-10.5	-19.5
R2	-23.2	-7.8	-15.5
TS	-17.3	-5.6	-11.9
P	-32.6	-	-

Supplementary Table 5: Mulliken partial atomic charges on the interacting atoms for reactive system in gas phase and in THF solution.

	Mulliken partial charges							
	gas				solution			
	PHI		CH-ol		PHI		CH-ol	
	N	C	O	H	N	C	O	H
R1	-0.39	0.66	-0.44	0.47	-0.37	0.67	-0.42	0.50
R2	-0.28	0.73	-0.46	0.42	-0.29	0.60	-0.42	0.40
TS	-0.45	0.58	-0.30	0.49	-0.26	0.62	-0.42	0.40
P	-0.44	0.43	-0.22	0.37	-0.42	0.39	-0.22	0.36

3. Experimental Methods and Additional Results

The formation of urethanes is a thermally driven reaction, which starts immediately after the components are mixed. CH-ol and PHI react forming the urethane product CC. For all experiments, we used equimolar concentration of CH-ol and PHI in THF with various concentrations and sample thicknesses.

The formation of polyurethanes is a thermally driven step-growth reaction, which starts immediately after the components are mixed. At the first step, TCD and TDI react forming the urethane product. The remaining unreacted functional OH and NCO groups allow a strain elongation by further urethane formation. In subsequent reaction steps a polyurethane polymer is formed. To get as large as possible polymer molecules the reactants should be of the equimolar concentration.

3.1. Sample preparation

3.1.1. Sample preparation for acceleration measurements of CH-ol & PHI

We dissolved 163 µl PHI in 337 µl THF resulting in a concentration of 3 mol/l. Accordingly 158 µl CH-ol were mixed with 342 µl THF to a concentration of 3 mol/l. For measurements with lower concentrations, we reduced the amount of PHI and CH-ol accordingly.

For the acceleration measurements 200 µl of both solutions were taken and mixed in a CaF_2 sample cell with 0.1 mm spacer thickness. The sample for the experiment had a concentration of 0.75 mol/l. The absorption of the ν(OH) vibration of CH-ol was about 1 OD at 3470 cm^{-1} (see Fig. 3a in the article). In the acceleration measurements, we tracked the formation of the ν(CO) of CC to determine the reaction rate upon excitation around 3470 cm^{-1} (with a laser pulse of 50 cm^{-1} FWHM). Typical absorptions are depicted in Fig. 3b. The absorption change at 1512 cm^{-1} of the ν(NCO)&δ(CH) of PHI was used to estimate absorption changes in the fs IR-pump IR-probe experiments (see Section 3.5.5). In these samples the ν(NCO) absorption was above 10 OD.

3.1.2. Sample preparation for acceleration measurements of TCD & TDI

TCD mother solution:

We dissolved 82,7 mg of TCD (165.4g/mol) in 500 µl of nitrobenzene yielding a mother solution with 1 mol/l.

TDI mother solution:

We mixed 71.9 µl of TDI (174.2g/mol) with 428.1 µl solvent, consisting of $CHCl_3$:CH in a ratio of 1:1. The resulting mother solution has a concentration of 1 mol/l.

We mixed 100 µl of both mother solutions (TDI and TCD) and diluted them with 400 µl nitrobenzene and 400 µl of the mixture $CHCl_3$:CH resulting in a concentration of 0.1 mol/l of both reactants. This solution was used for the acceleration measurements with pumping at 2270 cm^{-1} and at 3070 cm^{-1}. The dilution was necessary to track the vibrational NCO absorption band decrease within some hours.

The acceleration measurements upon excitation of the ν(OH) of TCD at 3470 cm^{-1} had to be performed in a mixture consisting of 100 µl of each mother solution (TDI and TCD), diluted with 100 µl of $CHCl_3$:CH and 100 µl of nitrobenzene (total volume of 400 µl) resulting in a reactant concentration of 0.25 mol/l. The adaption was necessary because the absorption in the 0.1 mol/l sample was too low for measuring any differences in the reaction rate.

3.1.3. Sample preparation for fs IR-pump IR-probe experiments

In all ultrafast measurements, the concentration ratio of CH-ol and PHI was the same (1:1). The extinction coefficient in the maximum of the ν(OH) absorption band of CH-ol is about 14 times and 6 times smaller than the extinction coefficient of the ν(NCO) absorption band of PHI, and the ν(CO) absorption band of CC, respectively. Thus, different concentrations and thicknesses were used for measurements in different spectral observation windows, otherwise the sample would absorb nearly all probe photons.

- In the 1500 cm^{-1} region, 50 µm of 0.75 mol/l CH-ol and 0.75 mol/l PHI solved in THF were used.
- For the measurements of the PHI NCO-band at 2260 cm^{-1}, 50 µm of 0.375 mol/l CH-ol and 0.375 mol/l PHI in THF were used.
- The rise of CO-band at 1730 cm^{-1} was detected within 100 µm of 1.5 mol/l CH-ol and 1.5 mol/l PHI in THF.

3.1.4. Drawing of polyurethane squares

Solution for photolithography:

We mixed 250 µl of both mother solutions (TDI and TCD), yielding in a concentration of 0.5 mol/l. From the resulting mixture 100 µl were taken and filled in a home build cuvette (two CaF_2 windows) with a 50 µm (or 25 µm) thick PTFE spacer (see Supplementary Fig. 8).

3.2. Cuvette for acceleration measurements

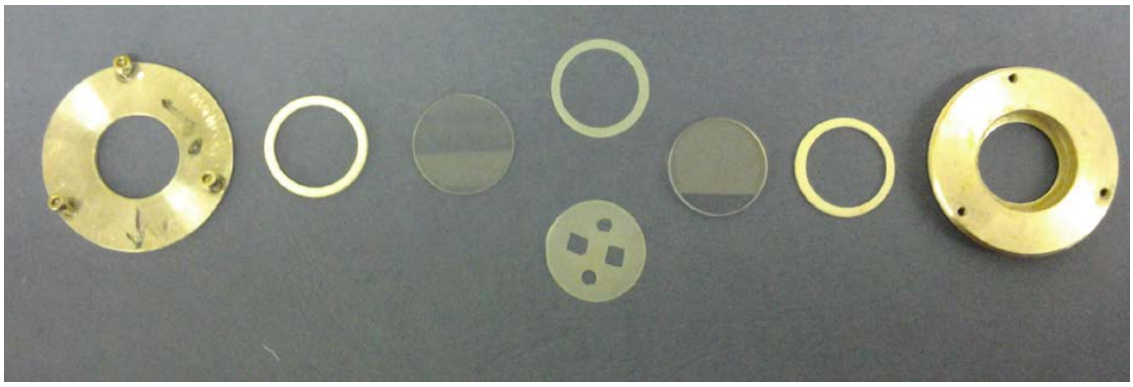

Supplementary Figure 8: Home built cuvette for acceleration and photolithography measurements. Two different spacers were tested: (i) One spacer exhibits two chambers filled with the same sample. One of the chambers is excited with IR light, the other one is not illuminated. (ii) One spacer exhibits only one big chamber. Here, two identical samples and cells were used, one was excited with IR light, the other one was not.

3.3. Acceleration measurements

All acceleration measurements were performed in the following way: The sample mixture was merged and within one to two minutes the sample was filled into two identical sample cells both consisting of two CaF_2 windows (25 mm diameter) with a Teflon spacer of 100 µm (or sometimes 50 µm) thickness. (i) The IR spectrum of both samples were taken (0 min) and then sample A was illuminated with the already running IR pulse OPA [4]. The other sample B was put next to the sample scanner, keeping the conditions as similar as possible. After a given time (e.g. 60 min) the procedure (i) was repeated. The acceleration measurements were stopped when about 30%-40% of the sample was consumed. The absorption of the investigated band was always smaller or about 1 OD.

Concentrations of CH-ol and PHI were in the range of about 0.75 mol/l in THF with a 0.1 mm spacer thickness, providing a reasonable absorption around 3500 cm^{-1} and 1730 cm^{-1}. Here, we chose a high concentration because the high activation energy results in a slower reaction.

Concentrations of TCD and TDI were in the range of about 100 mmol/l, resulting in a concentration of NCO and OH groups of about 200 mmol/l. Since absorption of the NCO stretching vibration is stronger than the OH stretching vibration, we increased the concentrations by 2.5 times to get reasonable absorption strengths for excitation at 3490 cm^{-1} (50 cm^{-1} FWHM).

We developed a sample holder for the IR spectrometer Bruker Equinox 55 to ensure a very reproducible positioning of the sample.

The reaction rates were determined by

- CH-ol & PHI mixtures: following the integral increase of the CO absorption at 1730 cm^{-1} upon excitation around 3470 cm^{-1} for CH-ol and PHI mixtures (see Fig. 3b in the article)
- TCD & TDI mixtures: following the decrease of the NCO absorption band (at 2270 cm^{-1}) upon excitation around 2270 cm^{-1} (Supplementary Fig. 11a) or the integral decrease of the OH absorption band (at 3500 cm^{-1}) upon excitation around 3070 cm^{-1} (Supplementary Fig. 10) or around 3490 cm^{-1} (Supplementary Fig. 9a and 9b).

The IR laser pulses were generated by a home built OPA. The IR pulses had energies between 2 µJ and 4 µJ, a repetition rate of 2 kHz and a spectral width (FWHM) of 50 cm^{-1} around its central frequency. A typical IR pulse spectrum is plotted in Supplementary Fig. 11a. For more information on the IR pulses see Kozich et al. [4]

For more information on analysis of the reaction rates and how we determined the activation energy see Kössl et al. [1]

The acceleration of the reaction was determined by calculating the ratio of the rate constants with illumination and without illumination. Since experimental errors or sample fluctuations can occur, we repeated the measurements several times by following the same procedure to obtain a statistic for the results. The distribution of results is presented in Supplementary Fig. 11c-e and 11g.

Changing the IR pulse focus in the sample from 150 µm to 75 µm or to 1-2 mm does not influence the acceleration of the reaction. Thus, we conclude that the observed acceleration effect is not due to a multi-photon process.

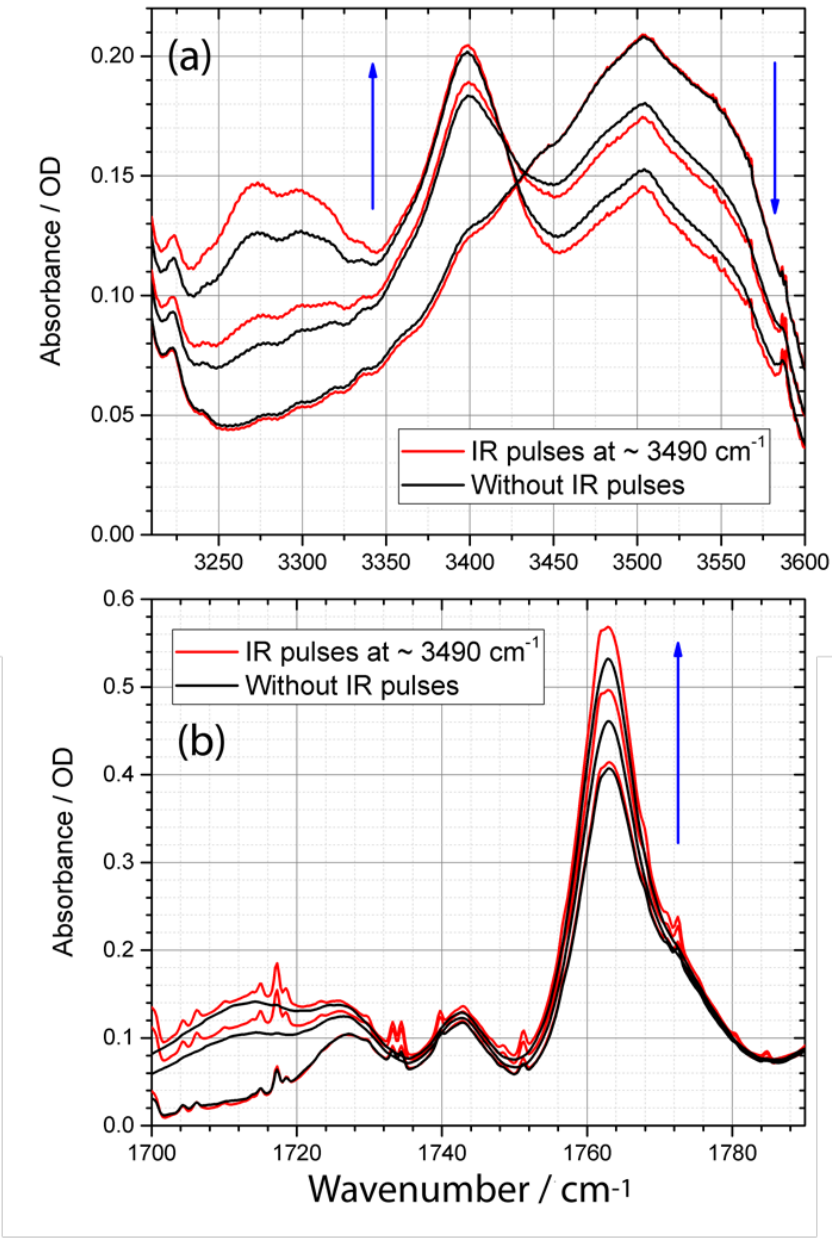

Supplementary Figure 9: Absorption spectra of a 1:1 mixture of TDI and TCD in nitrobenzene at delay times of 0 min, 45 min, and 90 min after merging without (black curves) and with IR pulse excitation at around 3490 cm^{-1} (red curves); a) the OH stretching vibration of TCD around 3500 cm^{-1} decreases, while the NH stretching vibration of the urethane product around 3300 cm^{-1} increases with time and illumination; b) the CO stretching vibration of the urethane group around 1760 cm^{-1} increases with time and illumination.

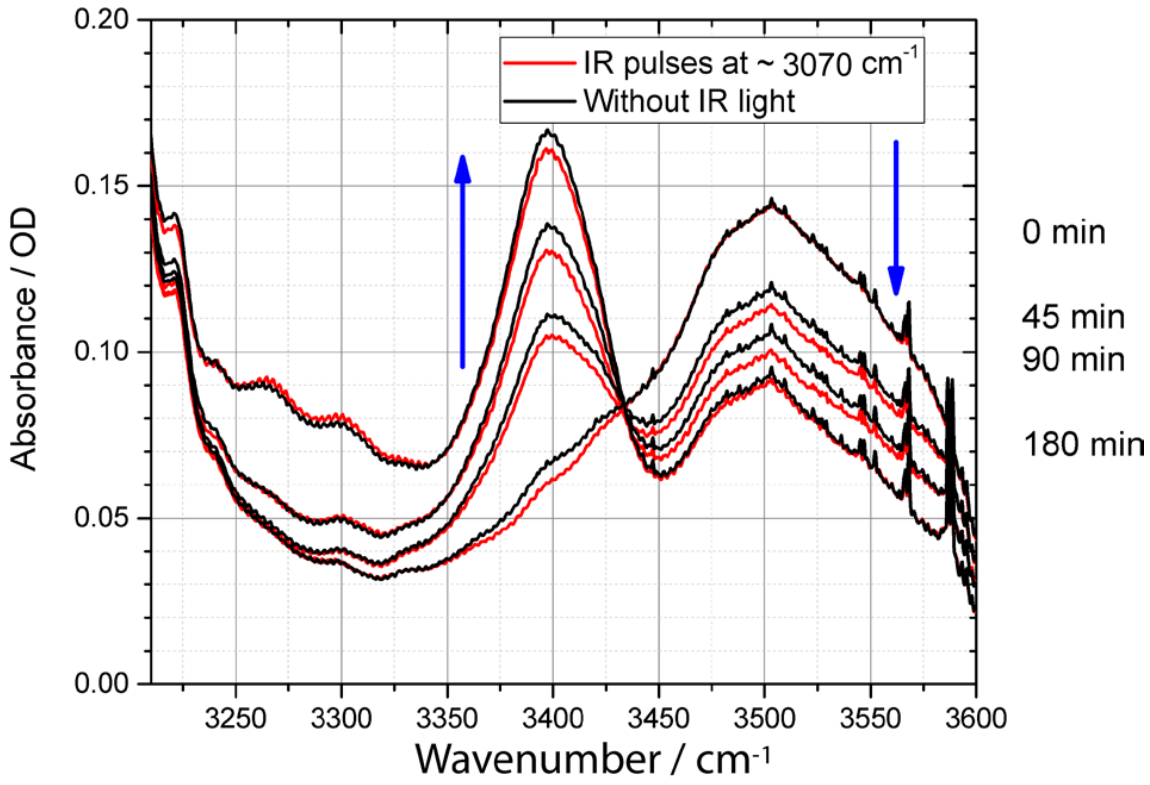

Supplementary Figure 10: Absorption spectra of a 1:1 mixture of TDI and TCD in nitrobenzene at delay times of 0 min, 45 min, 90 min, and 180 min after merging without (black curves) and with IR pulse excitation at around 3070 cm^{-1} (red curves); the OH stretching vibration of TCD around 3500 cm^{-1} decreases, while the NH stretching vibration of the urethane product around 3300 cm^{-1} increases with time. Illumination has no or negligible effect on the increase or decrease of the absorption bands.

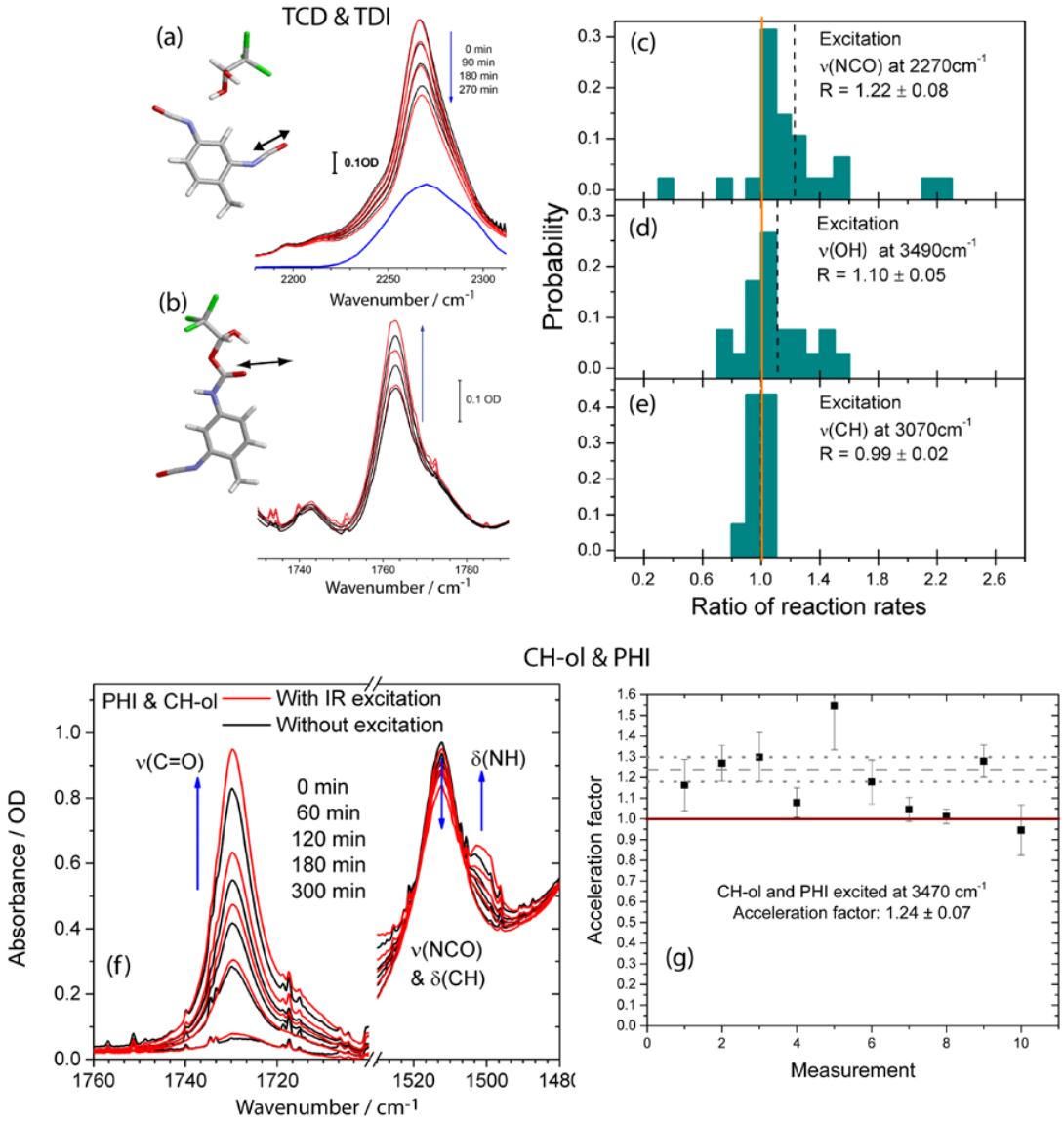

Supplementary Figure 11: Acceleration measurements: TCD & TDI upper panel, CH-ol & PHI lower panel. (a) Reaction as a function of time with IR pulse excitation (red lines) at 2270 cm^{-1} and without illumination (black lines); pump pulse spectrum (blue line), structures of TCD and TDI; (b) Reaction as a function of time with IR pulse excitation (red lines) at 3490 cm^{-1} and without illumination (black lines); structure of the formed urethane product; (c)-(e) measured acceleration ratios upon excitation at different vibrations. CH excitation is dominated by the solvent absorption at 3070 cm^{-1}, and leads to no acceleration. (f) Reaction as a function of time; illumination with IR pulses at 3470 cm^{-1} (red lines), without (black lines); vibrations are indicated. (g) Measured reaction rates.

3.4. Temperature effects

3.4.1. Thermal Imaging

To check whether the sample is heated by the IR excitation pulses at a repetition rate of 2 kHz over time, we measured the spatially resolved average temperature distribution within the sample with a FLIR A600 thermal imaging camera, while exciting the sample. For this experiment the sample was not moved, and the IR pulses illuminated the same sample spot. The thermal sensitivity of the camera from spot to spot was better than 0.05°C. We observed no temperature increase of the sample at the illuminated spot higher than 0.1 °C. Thus, no average thermal heating of the sample over time takes place. Note, this does not show whether a transient temperature change on a ps to ns time scale occurs, that completely equilibrates on a time scale of 0.5 ms to 33 ms.

Supplementary Figure 12: Temperature scan of the sample upon IR illumination; resolution (0.1 x 0.1 mm, frame rate 30 Hz); diameter of IR focus of 0.3 mm. The IR pulse with energy of 4 µJ hits the sample at the spot SP5. The measured average temperature was 22.2°C, not deviating from other spots in the sample (22.2 °C – 22.3 °C, see upper left inset). The camera measures the temperature with a frame rate of 30 Hz.

3.4.2. Thermal CO-band shift

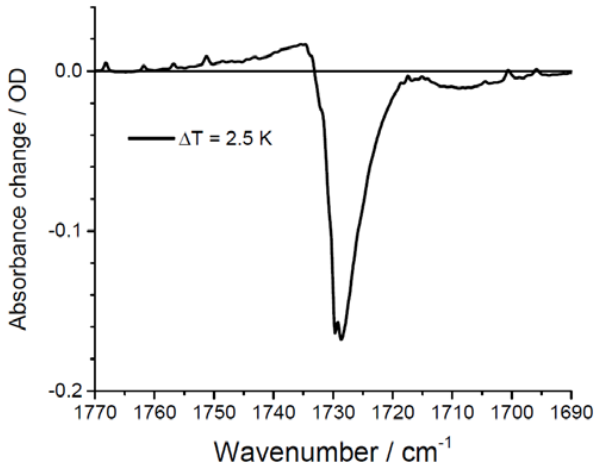

Supplementary Figure 13: Difference spectra of the CO-stretching vibration after heating the sample by 2.5K. The CO-band shifts to higher energies.

3.5. Estimates

3.5.1. Calculation of the temperature effect of 6°C for 24% acceleration (CH-ol & PHI)

The reaction rate k is given by the Arrhenius equation

$$k = Ae^{\frac{-E_a}{k_b T}}$$

where E_a is the activation energy, k_b the Boltzmann constant and A the pre-exponential factor. The influence of the temperature on the reaction rate changes Δk are given by

$$\Delta k = \frac{E_a}{k_b T^2} A e^{\frac{-E_a}{k_b T}} \cdot \Delta T$$

A change of 24% reaction rate for an activation energy of about 2300 cm^{-1} is

$$\frac{\Delta k}{k} = 0.24 = \frac{E_a}{k_b T} \cdot \frac{\Delta T}{T}$$

$$\Delta T = 0.24 \cdot \frac{200\ cm^{-1}}{2300\ cm^{-1}} \cdot 295\ K \approx 6\ K$$

From this estimation, we can conclude that an increase in reaction rate of 24% can be achieved by heating the sample by some Kelvin.

3.5.2. Heating the CH-ol & PHI in THF by fs IR pulses acceleration measurements

The heat capacity of THF Cp(THF) is 124 J/(molK), and of PHI Cp(CH-ol) is 157 J/(molK). The IR pulse energy can be calculated that is necessary to increase the temperature of the sample by 6 K. For simplicity, we assume only THF molecules to be in the volume (adding CH-ol or PHI does not

change the results significantly). In the acceleration experiments the focal radius was 0.15 mm, the sample thickness 0.1 mm, resulting in an excited volume V = 0.007 mm^3 per IR pulse.

The amount of substance in this volume is n = 8.72 $\times 10^{-8}$ mol, and the effective heat capacity $C_{eff} = C_p(THF) \times n(THF)$ is ~ 11 µJ/K. Since we excited the sample with about 3 µJ, we would expect an average temperature increase of 0.3 K, in agreement with our temperature measurements (see Supplementary Fig. 12).

Upon increasing the focal radius, the temperature increase is strongly reduced at constant IR pulse energy. Since we observed no change in reaction acceleration upon increasing the focal diameter to 1-2 mm, we can exclude heating effects as the origin of reaction acceleration.

3.5.3. Heating the CH-ol & PHI in THF during fs IR-pump IR-probe experiments

The heat capacity of THF $C_p(THF)$ is 124 J/(mol K), and of PHI C_p(CH-ol) is 157 J/(mol K). The IR pulse energy can be calculated that is necessary to increase the temperature of the sample by 6 K. For simplicity, we assume only THF molecules in the volume (adding CH-ol or PHI does not change the results significantly). In the IR-pump IR-probe experiments (probing the ν(NCO) range, Fig. 4b) the focal radius was bigger or equal to 0.075 mm, and the sample thickness 0.05 mm resulting in an excited volume V = 0.00088 mm^3 per IR pulse.

The amount of substance in this volume is n=1.1 $\times$ 10^{-8} mol, and the effective heat capacity $C_{eff} = C_p(THF) \times n(THF)$ is ~ 1.33 µJ/K. We excited the sample with about 3 µJ at an optical density of ~0.2 OD at 3500 cm^{-1} (the pump pulse spectrum in shown in Supplementary Fig. 14a), resulting in an effective pulse energy of 1.1 µJ. This would lead to a temperature increase of 0.8 K.

Experiments probing the ν(CO) (Fig. 4c) were performed with 0.1 mm spacer thickness and focal radius of 0.095 mm (and optical density of the ν(OH) of about 2OD).

3.5.4. Number of photons per OH group

Here, we estimate how many photons per OH group are available at the IR focus during the fs IR-pump IR-probe experiments.

We used CH-ol and PHI concentrations of 0.75 mol/l (probing the ν(NCO)& δ(CH) around 1500 cm^{-1}, Fig. 4a), 0.375 mol/l, or 1.5 mol/l and sample thicknesses of 0.05 mm, 0.05 mm, or 0.1 mm, respectively. For the OH groups with 0.75 mol/l we have to $4.5*10^{20}$ groups per cm^3. The volume that we excited by the pump pulse with focal radius of about 0.075 mm or bigger at a sample thickness of 0.05 mm is $V = \pi(0.0075)^2$ $cm^2 \times 0.005$ cm = 8.8×10^{-7} cm^3. This results in a number of OH groups in the pump pulse volume of about 4×10^{14} or more.

With an average pump energy of 3 mW at 1 kHz repetition rate (3×10^{-6} J/pulse) at 3500 cm^{-1}, and an absorption of 1.0 OD we have an effective pump energy per pulse of 2.7 µJ. We get the number of photons per pump pulse N from the energy per photon E_p:

$E_p = h \times \upsilon = h \times c \times 3500\ cm^{-1} = 7 \times 10^{-20}$ J/photon results in $N = 3.9 \times 10^{13}$

On average, less than every 10^{th} OH group was excited by a photon.

3.5.5. Estimation of fs IR-pump IR-probe signal strength

Here, we roughly estimate the signal change by a single IR pulse. At the beginning of the reaction between CH-ol and PHI the change of optical density of PHI is at least ~0.04 OD / hour. This change is directly visible from Supplementary Fig. 14b. We illuminated the sample (radius of 12 mm) with fs IR pulses of ~0.3 mm (0.25 mm – 0.35 mm) focal diameter and 2 kHz repetition rate by scanning the sample volume line by line. Thus, the illumination is spatially and temporally (on a minute time scale) averaged over the complete sample by this method, resulting in an averaged reaction rate increase of 24% (see Supplementary Fig. 11g). The average OD change due to illumination is at least 0.24 x 0.04 OD/hour ~0.01 OD / hour.

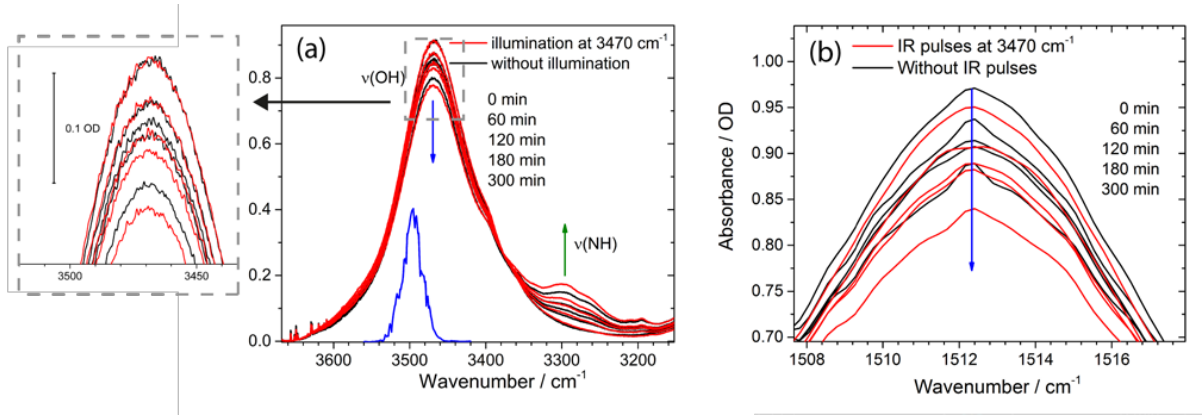

Supplementary Figure 14: Absorbance change as a function of time (acceleration measurements) of a CH-ol and PHI mixture in THF with IR pulse illumination at 3470 cm^{-1} (red lines) and without illumination (black lines). (a) Magnification of the spectral range of the ν(OH) and ν(NH) (from Fig. 3a). Pump pulse spectrum at 3500 cm^{-1} (blue line) of the fs IR pump – IR probe experiments presented in Fig. 4. (b) Magnification of the peak at 1512 cm^{-1} of Fig. 3b. Here, the decrease in absorption with (red lines) and without illumination (black lines) as a function of time are clearly visible. Without illumination, we see an absorption change from 0.97 OD to 0.93 OD in the first hour (0.04 OD / hour).

In our fs IR-pump IR-probe experiment we used a focal beam radius of about (0.075±0.01) mm and a cell radius of 12 mm. We illuminate the complete sample cell by scanning the pump beam over the sample line by line. The laser repetition rate is 1 kHz with every second pump pulse is blocked. The expected OD change in the illuminated volume could be a factor of ~2.5×10^4 higher, if the light intensity in the focus would be applied to the complete sample volume at the same photon density.

With this photon density we can compare the signal from the acceleration measurement with the signal from the fs IR-pump – IR-probe measurement.

During the measurement of 1 hour we emit about 0.5x 1000 × 3600 = 1.8 ×10^6 pump pulses, while scanning the sample. The estimated change in OD per pulse is about

$$Absorption\ change = \frac{0.01\ OD/hour \cdot 2.5 \cdot 10^4}{1.8 \cdot 10^6\ pulses/hour} \sim 0.14 \cdot 10^{-3}\ OD/pulse$$

Thus, we **expect a signal change** in the ν(NCO)&δ(CH) bleaching band at 1512 cm^{-1} **in the order of** some tenth of mOD, (**~ 0.1 mOD**) as observed in Fig. 4a.

Another possible way to estimate the signal strength of the ν(NCO)&δ(CH) bleaching band at 1512 cm^{-1} is to assume that only the number of photons and the number of illuminated molecules are responsible for the acceleration.

In the acceleration measurements we used a pump pulse with 2 kHz and a pulse energy of 3 µJ at 3470 cm^{-1} (50 cm^{-1} FWHM). The focal diameter was about 0.3 mm and the sample thickness 0.1 mm at a concentration of 0.75 mol/l of PHI and 0.75 mol/l of CH-ol in THF. The observed signal change due to acceleration was 0.01 OD in the first hour. We already concluded that every reaction was initiated by absorption of one photon.

Now, we can simply compare the number of photons and number of molecules in the excited volume in the acceleration and fs IR-pump – IR-probe measurements (fs IR-IR):

The repetition rate of the pump pulses in the acceleration measurements is 4 times higher than in the fs IR-IR. The focal Volume is 8 times bigger in the acceleration measurements. This results in an **estimated signal change of** 0.01 OD / 32 = 0.0003 OD = **0.3 mOD** in good agreement with the results displayed in Fig. 4a.

3.5.6. Estimation of the overall quantum yield upon fs excitation at 3500 cm^{-1}

Here, we estimate the overall quantum yield upon fs excitation at 3500 cm^{-1} from Fig. 4c displaying the rise of the ν(CO) vibration of CC. In Fig. 4c the final ν(CO) signal is about 0.75 mOD. In this experiment, we used CH-ol and PHI concentrations of 1.5 M and a sample thickness of 0.1 mm. The focal pump diameter was about 0.19 mm and the probe diameter was smaller about 0.13 mm. We do not take the different diameter sizes of pump and probe beam into account and estimate the number of OH groups in the excited volume. The volume is V=π$(0.0095)^2$ cm^2 x 0.01 cm = 2.8 x 10^{-6} cm^3. Since

we used a concentration of 1.5 mol/l = 1.5 x 10^{-3} mol/cm^3, with 6.023 x 10^{23} OH groups per mol, we had 9.0 x 10^{20} OH groups per cm^3. The number of OH groups N in the excited volume is

N = 2.5 x 10^{15}.

The pump beam had an excitation energy of 3 x 10^{-6} J. We assume all photons to be absorbed. Thus, about 4.3 x 10^{13} photons (see Sec. 3.5.4) were absorbed. About every 60 th OH group absorbs a photon. Since the total absorption of the OH-stretching vibration at 3500 cm^{-1} in the sample was about 2.0 OD, we would expect a total bleaching signal of about 33 mOD.

The observed signal at 1730 cm^{-1} was about 0.75 mOD. The extinction coefficient of the CC ν(CO) vibration is about 6 times higher than that of the ν(OH), hence the corresponding signal at the ν(OH) vibration resulting from the alcoholysis reaction is expected to be about 0.125 mOD.

The comparison of 33 mOD and 0.125 mOD results in a overall quantum yield of about 0.3 %.

Note, this is an estimation of the overall quantum yield. The error of this estimation is huge and we expect the overall quantum yield to be in the range of 0.05% to 0.6%. The main error source is the focal diameter.

Direct comparison of the absorption strengths of the ν(OH) vibration at 3500 cm^{-1} and the ν(NCO)&δ(CH) at 1512 cm^{-1} (see Supplementary Fig. 14a, 14b, and 3) shows, that both are of similar strength. Thus, the estimated bleaching signal is about 0.1 mOD, in agreement with the bleaching signal in Fig. 4a.

3.6. Femtosecond IR pump – IR probe results

3.6.1. Hydrogen bonding between CH-ol and CC

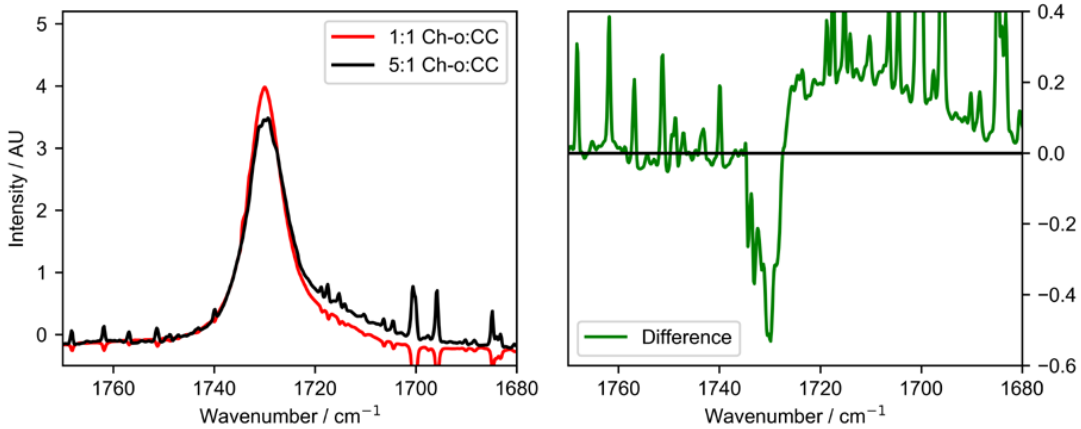

Supplementary Figure 15: Left: Comparison of the CC CO-stretching vibration for two different CH-ol:CC ratios, both solvated in THF. The sharp features in both spectra are caused by vapor water lines and can be ignored. Increasing the amount of CH-ol leads to a rise of the red-shifted and broadened shoulder. This is a strong indicator for H-bond formation. Right: The difference of both is presented. The H-bonding causes a peak shift of around 10 cm^{-1} and broadens the band by factor of 2 to 3.

3.6.2. Comparison to pure relaxation dynamics (IVR)

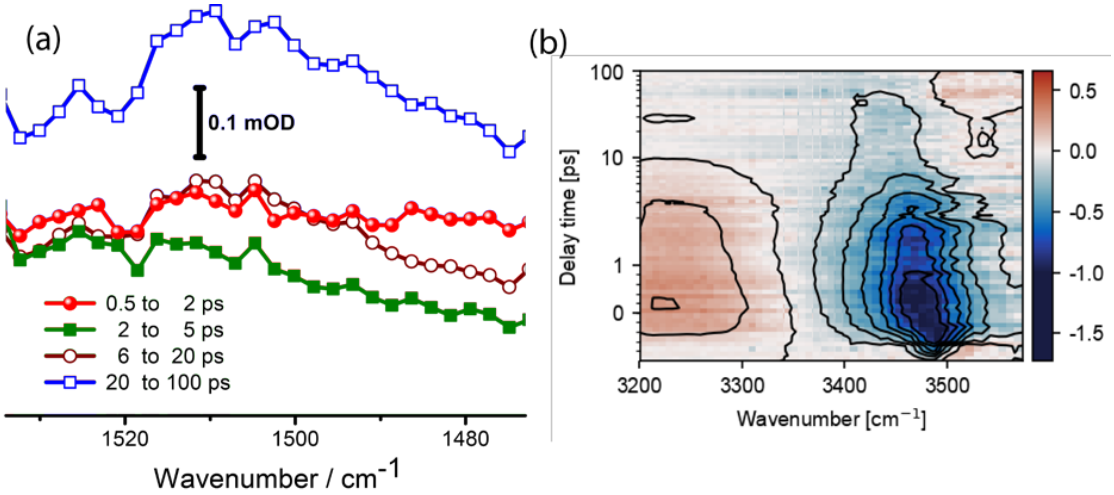

Supplementary Figure 16: (a) Transient spectra of CH-ol in THF after excitation of the OH-stretching vibration at 3500 cm^{-1}. We assign the broad feature as the tail of changes of δ(CH)-vibration at 1450 cm^{-1} (Supplementary Fig. 2b), or δ(OH)-vibration at lower wavenumbers. No sharp features are observed, neither at 1515 cm^{-1} nor at 1505 cm^{-1}. Right: IR pump – IR probe data at magic angle. (b) Transient data of CH-ol in THF upon excitation of the OH stretching vibration at 3500 cm^{-1}. The time axis is linear up to 1 ps, logarithmic from 1 ps to 100 ps. Excited state absorption (positive signal) is visible around 3250 cm^{-1}, bleaching signals at 3470 cm^{-1}, and 'hot' ground state absorption around 3530 cm^{-1} for longer delay times. Excitation energy of 1.5 µJ, 0.75 M CH-ol concentration, focal pump diameter about 200 µm, probe diameter about 150 µm, 0.05 mm thickness.

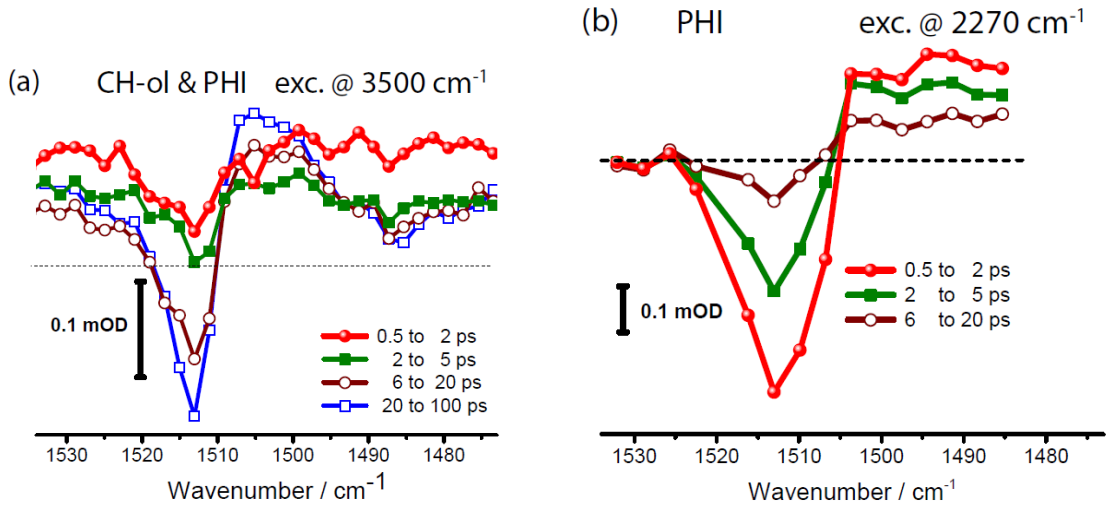

Supplementary Figure 17: *a)* Transient spectra of CH-ol & PHI in THF after excitation of the OH-stretching vibration at 3500 cm^{-1} as shown in the article (Fig 4a). b) Transient spectra of PHI in THF after excitation of the NCO-stretching vibration at 2270 cm^{-1}. The positive band of pure PHI is nearly featureless and decays on a fast time scale. Hence, the observed signals in the mixture is not due to heating of the PHI or excitation of the NCO-stretching via VER.

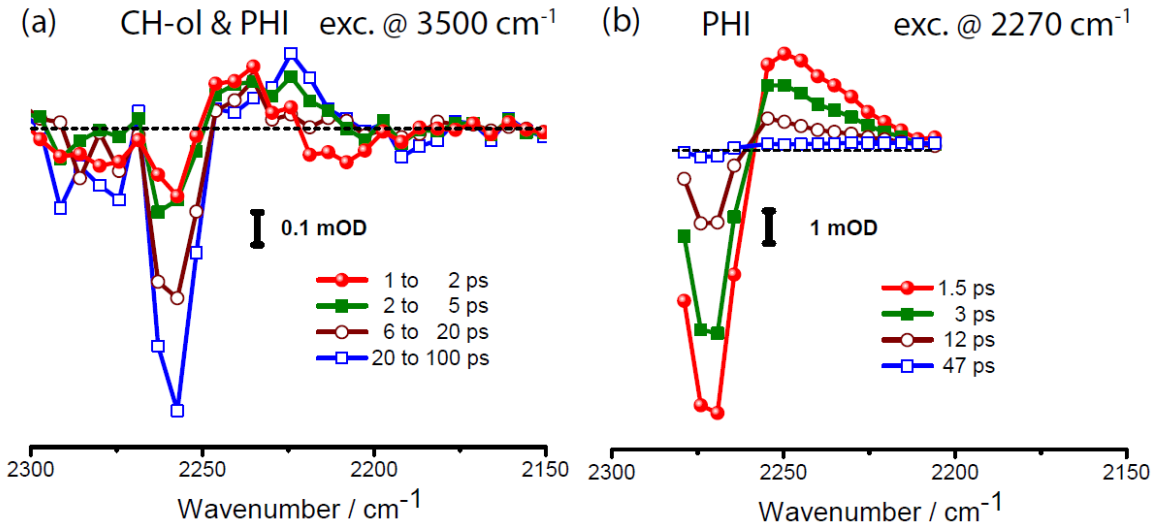

Supplementary Figure 18: *a)* Transient spectra of CH-ol & PHI in THF after excitation of the OH-stretching vibration at 3500 cm^{-1} as shown in the article (Fig. 4b). b) Transient spectra of PHI in THF after excitation of the NCO-stretching vibration at 2270 cm^{-1}. The positive and the negative band of pure PHI exhibit a different shape and decay much faster within some ps. Additionally, the bleaching position is different due to the different ESA. Thus, we conclude that the observed signal in the mixture it not due excitation of the NCO mode, or heating the NCO mode via VER.

3.6.3. Subtraction of the CH-ol & CC relaxation dynamic

As shown in Section 3.6.1, CH-ol and CC are forming an H-bond. The H-bond leads to an effective coupling between both molecules. This coupling causes visible signals in the ultrafast dynamics even for small concentrations of CC as presented in Supplementary Fig. 19 and 20.

We mixed a 10:1 mixture of CH-ol and CC to record the pure CC relaxation dynamics (Supplementary Fig. 19a, and Supplementary Fig. 19b red line). In Supplementary Fig. 19a the ν(CO) vibration of CC upon excitation of the ν(OH) of CH-ol at 3500 cm^{-1} is shown. Since, we observe clear signals, energy is transferred from the CH-ol ν(OH) to the CC ν(CO) via the H-bond coupling: We observe a fast positive component around 1700 cm^{-1} decaying on a time scale of ~ 4 ps. On this time scale the bleaching band has negligible strength, and we attribute the positive signal to the decay of the excited ν(CO)* vibrational mode of CC overlapping with the bleaching band. With the decay of the ν(CO)* vibration, the bleaching band increases and a blue-shifted band emerges around 1740 cm^{-1} with about 8 ps. We assign this process to heating of CC via IVR (see Supplementary Fig. 13).

Since, no formation of a product occurs in the CH-ol & CC mixture, we compared the dynamics of CH-ol & CC with CH-ol & PHI upon excitation of the OH-stretching vibration at 3500 cm^{-1}.The transient signal of the CH-ol & PHI mixture was subtracted from the transient PHI & CH-ol data. Prior subtraction, the spectra were scaled to have the same strength at the blue-shifted hot band around 1740 cm^{-1}. This is shown in Supplementary Fig. 19b. As a result, we receive the formation of the ν(CO) vibration of CC due to alcoholysis of CH-ol and PHI.

To give more validity to this approach, we also compared the first half of our scans from the PHI & CH-ol data with the second half (see Supplementary Fig. 20, left column). In Supplementary Fig. 20 left column, the absorbance difference spectra of the first half (thick lines), and second half (thin lines) are presented for different delay time intervals. Since the CC product concentration is increasing with time, the signal around 1700 cm^{-1} is stronger in the second half of the experiment (thin lines). Moreover, a significant difference between the first and second half of the experiment is observed at 1730 cm^{-1} with a strongly reduced bleaching signal in the first half of the experiment. After scaling of the first half of the experiment (Supplementary Fig. 20, left column) to the same signal strength around 1740 cm^{-1} (and 1700 cm^{-1}) of the second half of the experiment (see also Supplementary Fig. 19b), and subtraction of the second half a new absorption rises at the CO position indicating product formation, shown in Supplementary Fig. 20, last column. Due to short time difference between both halves, the resulting signal is weaker compared to the CC&CH-ol subtraction presented in Supplementary Fig. 19b, because part of the rising product signal is also subtracted.

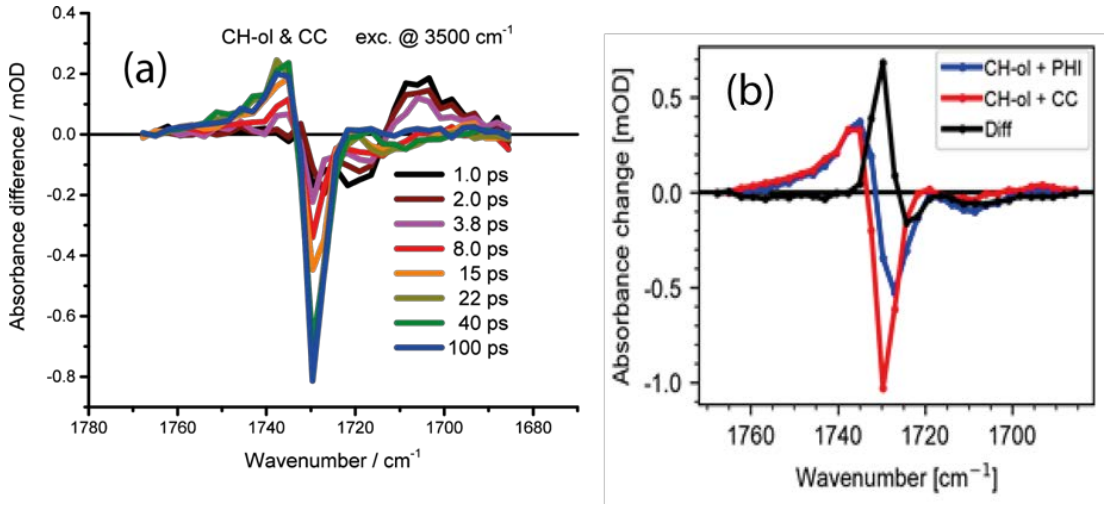

Supplementary Figure 19: (a) Transient spectra of CH-ol & CC upon excitation at 3500 cm^{-1} for different delay times. (b) Transient spectra of CH-ol & PHI and CH-ol & CC, both solved in THF after excitation of the OH-stretching vibration at 3500 cm^{-1}. The spectra were averaged from 30 ps to 100 ps to minimize noise; both signals are constant over the averaged time range. A scaling factor of 1.5, determined by minimizing the difference of the positive bands, was used to compensate for variations in the sample concentrations. After scaling, both signals are almost identical except at 1730 cm^{-1}. By subtracting CH-ol & CC from the CH-ol & PHI signal, we removed the unwanted contribution of the CH-ol & CC interaction. Thus, the resulting difference mainly shows the formation of the CO-stretching band.

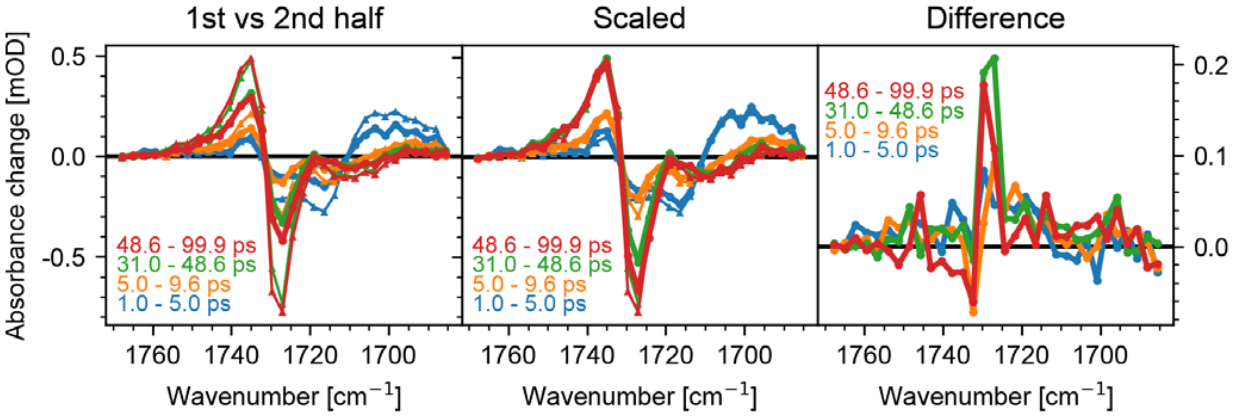

Supplementary Figure 20: Comparison of the averaged transient spectra of the first half hour and second half hour of measurement. *Left*: Unscaled averaged spectra, thick lines display the first half and thin lines the second half. The gross of the signal, attributed to the CC relaxation, grows with time. This is expected, as the CC concentration rises with time. *Middle*: The same signals, scaled to match in the hot-band of CC, small differences are only observed around 1730 cm^{-1}. *Right*: Subtraction of the scaled scans (fresh sample – old sample) shows a positive signal at the position of the ν(CO) mode, revealing the rise of the product. The time constant of the rise is consistent with the other data ((10 ± 3) ps.).

3.6.4. Selected transients

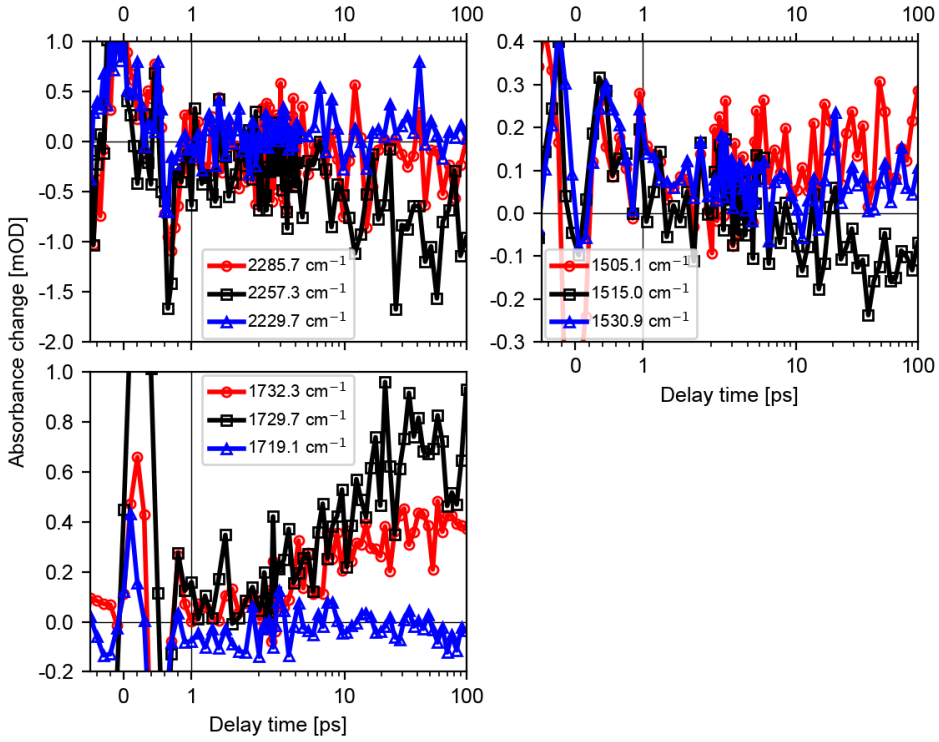

Supplementary Figure 21: Selected transients of CH-ol & PHI after excitation of the OH-stretching vibration at 3500 cm^{-1}. *Top left:* PHI υ(NCO) bleach increases around 2260 cm^{-1}, no rise of a hot-band is observed. *Top right:* Rise of the PHI υ(NCO)&δ(CH) bleach at 1515 cm^{-1} and rise of the CC δ(NH) band at 1505 cm^{-1}. *Bottom left:* Difference of the measurements of CH-ol and PHI and CH-ol and CC: Rise of the CC υ(CO)-stretch at 1730 cm^{-1}. All observed bands show changes with a (10±3) ps time constant. The larger noise for the NCO-bleach at 2260 cm^{-1} originates in the high absorption of the band and is due to a lower number of shots (only 4000 shots) compared to the other spectral ranges (around 30 000 shots).

3.6.5. Reproducibility – NCO region 24h old sample

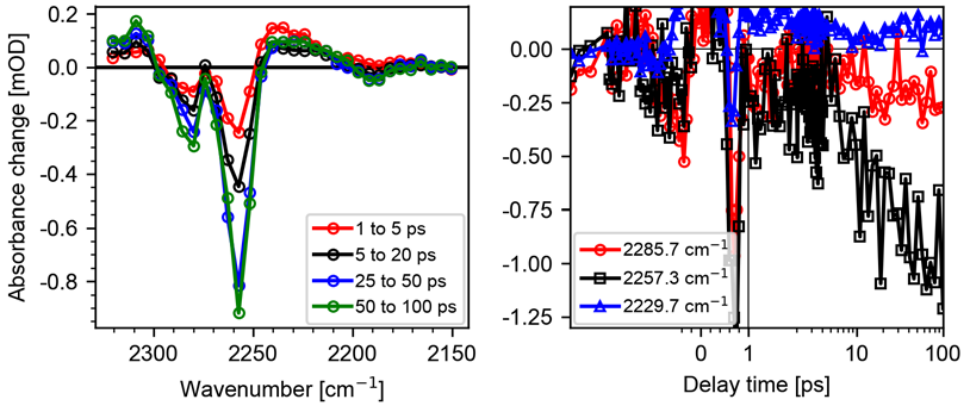

Supplementary Figure 22: Selected transients and averaged spectra of 24h old CH-ol & PHI sample after excitation of the OH-stretching vibration at 3500 cm^{-1}. The concentration of CH-ol and PHI of the fresh was two times higher than after 24 h. Since, around 2260 cm^{-1} there are no contributions of the CC product, these data should show the same dynamics as presented in Fig. 4b. The absorbance difference spectra agree well with the spectra in Fig. 4b, but exhibit a better signal to noise ratio due to longer averaging. Transients also corroborate the data shown in Fig. 4b and Supplementary Fig. 21.

3.7. Photolithography

Polyurethane squares were written in a solution of TCD/TDI mixture solved in nitrobenzene, cyclohexane, and chloroform. This specific solution enabled us to solve TCD and TDI, but the polymer was poorly solved. The polymer square is not visible in the sample cell if the solvent is still present, due to low scattering. Thus, we opened the cell and removed the solvent (see Supplementary Fig. 23). The special alcohol with three Cl groups were chosen, because of their strong electronegativity and scattering cross-section. Electron microscopy experiments enable to visualize the chlorine atoms. Unfortunately, the polymer structure was not detectable, since the sample melted during the experiment.

Measurements with a Raman microscope are presented in Supplementary Fig. 24. We determined 20 times higher Raman signals with the focus located on the polymer square compared to measurements with the focus next to the polymer square.

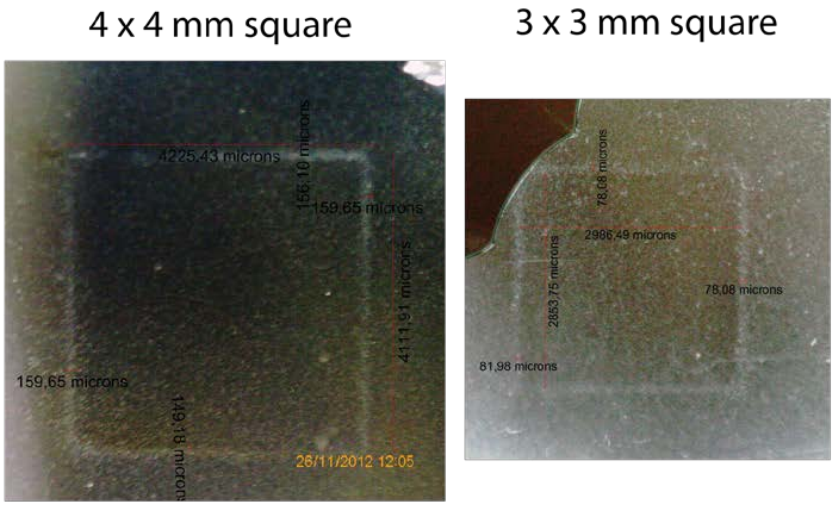

Supplementary Figure 23: Polymer squares generated by femtosecond IR pulse illumination at 2270 cm^{-1}. Distances were determined with the dnt DigiMicro Mobile camera. The solvent is removed to visualize the squares. Left panel: 4 x 4 mm square written with a focal diameter of 150 µm. Right panel: 3 x 3 mm square written with a focal diameter of 75µm. A small remaining part of the solvent and its effect on the transparency of the sample is visible in the upper left corner.

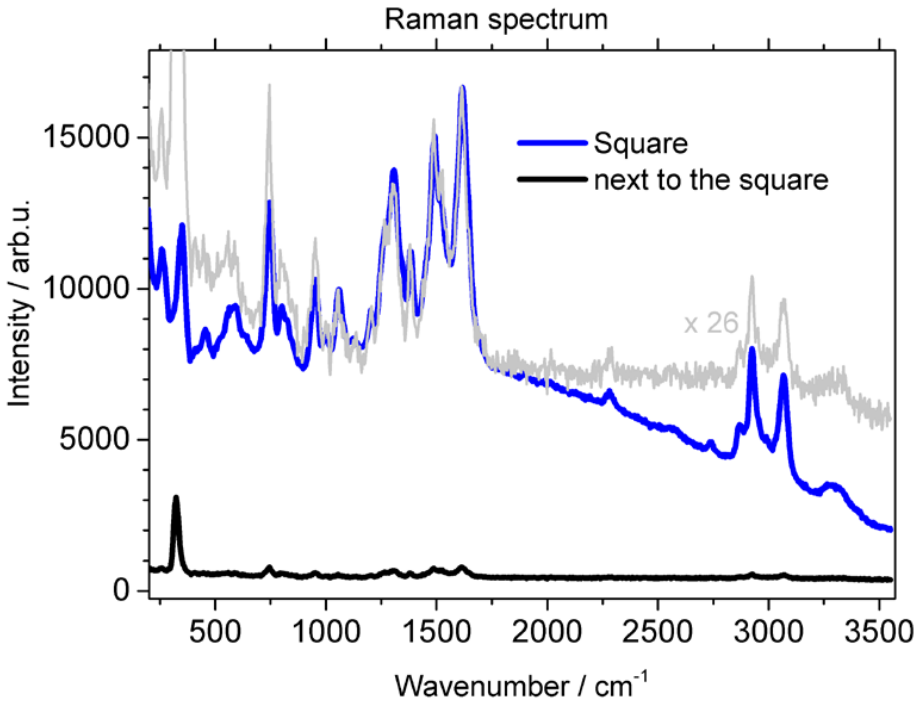

Supplementary Figure 24: Raman intensities on the polymer square (blue line) and next to the polymer square (black line) measured by a Raman microscope. The grey line displays the 26 times amplified intensities of the black line.

4. References

[1] F. Kössl, M. Lisaj, V. Kozich, K. Heyne, O. Kühn, Monitoring the alcoholysis of isocyanates with infrared spectroscopy, *Chem. Phys. Lett.* **621** (2015) 41.

[2] M. J. Frisch et al. Gaussian 09, Revision D.01, Wallingfort, CT (2009).

[3] S. Dapprich, I. Komáromi, K. S. Byun, K. Morokuma, M. J. Frisch, A New ONIOM Implementation in Gaussian 98. 1. The Calculation of Energies, Gradients and Vibrational Frequencies and Electric Field Derivatives, *J. Mol. Struct. (Theochem)* **462** (1999) 1.

[4] V. Kozich, A. Moguilevski, K. Heyne, High energy femtosecond OPA pumped by 1030 nm Yb:KGW laser, *Opt. Commun.* **285 (**2012) 4515.chrome

Selbstständigkeitserklärung

Hiermit bestätige ich, dass die vorliegende Doktorarbeit von mir allein und nur unter Nutzung der angegebenen Hilfsmittel verfasst wurde. Ferner bestätige ich, dass diese Arbeit nicht in einem früheren Promotionsverfahren angenommen oder als ungenügend beurteilt wurde.

Berlin, den 22.5.2018

_____

Till Stensitzki